eman ta zabal zazu

Universidad del País Vasco

Euskal Herriko Unibertsitatea

Insight into the crystallization of multi-phasic polymers

Valentina Chiquinquira Pirela Wilhelm

Ph.D. Thesis

Donostia-San Sebastian, 2024

eman ta zabal zazu

Universidad del País Vasco

Euskal Herriko Unibertsitatea

POLYMAT

Basque Center for Macromolecular Design and Engineering

Insight into the crystallization of multi-phasic polymers

Valentina Chiquinquira Pirela Wilhelm

Ph.D. Thesis

Department of Polymers and Advanced Materials:
Physics, Chemistry and Technology,
University of the Basque Country UPV/EHU
Donostia-San Sebastian, 2024

Acknowledgements

The words *"We're happy, free, confused, and lonely in the best way"* from Taylor Swift's song "22" beautifully encapsulate the journey of the last few years. This journey has been comprised of many moments of joy and satisfaction, the freedom of exploration and discovery with the occasional confusion in the face of complex challenges, and the sometimes self-imposed loneliness that comes with deep diving into projects. At the end of this chapter of my life, I am compelled to extend my heartfelt thanks to everyone who has supported and guided me.

En primer lugar, me gustaría expresar mi sincero agradecimiento a mis supervisores, el Dr. Jaime Martín y el Prof. Alejandro J. Müller, por el apoyo y la supervisión brindados a lo largo de estos años. A pesar de los numerosos cambios provocados por la pandemia, traslados, entre otros, su compromiso ha sido fundamental para la evolución sin contratiempos de estos proyectos. Por otro lado, me gustaría agradecer a POLYMAT y a la Universidad del País Vasco (EHU/UPV) por permitirme llevar a cabo mi tesis doctoral en sus reconocidos y excelentes centros.

Me gustaría extender mi más profundo agradecimiento a Edgar, mi postdoc, sin quien esta tesis no habría llegado a existir. Gracias por tu amistad, apoyo, por todo lo que me has enseñado y por impulsarme siempre a ser mejor y aprender más. Recordaré con mucho cariño nuestras noches eternas de sincrotrón y nuestras noches de cena en Talent House. También quiero expresar mi gratitud a Nico, no habríamos llegado hasta el final sin apoyarnos mutuamente en los momentos difíciles.

I would also like to thank all of my labmates: Eider, Ainhoa, Maria, Alessandra, Sebastian, Andromeda, Juan, Mario, Yilong, Ricardo, Leire, Jorge,

and Nico. En especial a Jorge por infinitos momentos de risas y a Sebas, los momentos de café y todo lo que hablamos por fin han llegado.

A mis italianas: Maria, Alessandra y Andromeda. Maria, mi bella italiana, gracias por todo tu cariño y ser una gran amiga desde el momento que nos conocimos. Muchas gracias a Alessandra, mi capsulina, estuviste poco tiempo pero sin nuestras noches de masajes y Alerta Policial este doctorado no habría sido lo mismo. Thank you Andromeda, for being a great friend, I will miss our mental health walks with coffee. Hold with diamond hands! We made it.

Ich möchte mich auch bei meiner Deutschklasse für ihre Unterstützung bedanken. Sie haben mir einen Ort gegeben, an dem ich mich ausruhen und lernen könnte. Steffi, ich danke dir für alles. Du bist eine Lehrerin, die es nicht so häufig gibt.

To my friends, I cannot possibly express every special moment I have shared with you here, so I will just say thank you, and I will forever be grateful to have met all of you. Thank you to Sebas, Fede, Kari, Justine, Gisela, Jorge, Maria, Andromeda, Meli, Alessandra, Andrea (Hermano!), Sofia, Kelly, Thijs, Janne, Julia, Joel, Masip, Ainhoa and many more.

Me gustaría dedicar mi tesis a mi madre y padre, Ramón y Yuraima, quienes siempre me han apoyado incondicionalmente en todo lo que me he propuesto y por ser un constante en mi vida en los que siempre he podido contar. Mami y Papi os quiero mucho y os estaré infinitamente agradecida por toda la educación que me habéis brindado. También me gustaría agradecer al resto de mi familia, abuela, hermanos, cuñados, sobrinos, primos y tios quienes siempre han mostrado su cariño a pesar de la distancia. En especial queria mencionar a mi tio Jorge quien siempre ha sido un verdadero impulsor de mis metas académicas a lo largo de mi carrera científica. Estoy profundamente agradecida por su presencia en mi vida, y no puedo expresar con palabras lo significativo

que ha sido su apoyo.

Finally, I want to take a moment to express my deepest gratitude to my partner, Timo, whose unwavering love, patience, understanding, and support have been essential for me during this journey. Your presence in my life has brought me immense love, joy, comfort, and strength, especially during the most challenging times. You have been my rock, and I treasure our memories together. I love you more than I can say with words, and I look forward to creating new memories together.

Thank you. Gracias. Danke.

TABLE OF CONTENTS

List of Abbreviations

AFM	atomic force microscopy
CB	chlorobenzene
C_p	heat capacity
Đ	polydispersity
DAP	diallyl phthalate
DMDS	2,2'-dimercaptodiethyl sulfide
DMF	N,N-dimethylformamide
DSC	differential scanning calorimetry
FSC	fast scanning chip calorimetry
GIWAXS	grazing incidence wide angle X-ray scattering
GPC	gel permeation chromatography
ΔG	free energy barrier
G	growth rate
G_o	growth rate constant
k	overall crystallization rate constant
LC	liquid crystal
μ-DSC	micro differential scanning calorimetry
ΔH_m	melting enthalpy
iPP	isotactic polypropylyne
M_n	number average molecular weight
M_w	weight average molecular weight
MD	molecular dynamics
n	Avrami index
n_n	nucleation rate component
n_d	growth dimensionally
PBTTT	poly[2,5-bis(3-dodecylthiophen-2-yl)thieno[3,2-b]thiophene]

PBC	periodic boundary conditions
PFO	poly(9,9-di-n-octylfluorenyl-2,7-diyl)
PL	photoluminescence
PLOM	polarized light optical microscope
PP	polypropylene
SAXS	small-angle X-ray scattering
SDS	sodium dodecyl sulfate
ΔT	supercooling
t_o	induction time
$\tau_{50\%}$	half crystallization time
T_a	annealing temperature
T_{cc}	cold crystallization temperature
T_c	crystallization temperature
T_g	glass transition temperature
T_m	melting temperature
THF	tetrahydrofuran
$\Delta H(t)$	enthalpy variation as a function of time
ΔH_{total}	maximum enthalpy value
V_c	relative volumetric transformed fraction
WAXS	wide angle X-ray scattering
W_c	mass fraction
ρ	density

Summary

The thesis aims to understand how the solidification process occurring in multi-phasic materials affects the behavior of these polymers. It aims to provide insight into how the initial molecular arrangement of a material can affect the crystallization kinetics, in addition to characterizing and understanding the changes in the material and its electronic and optical properties. This research is structured across eight chapters and delves specifically into understanding the crystallization kinetics of semicrystalline semiconducting polymers PFO and PBTTT, which exhibit a nematic liquid crystal and a smectic liquid crystal, respectively. This work establishes reliable thermal protocols to monitor the crystallization of said materials and characterize the microstructure by a range of techniques including but not limited to fast scanning calorimetry (FSC), wide angle X-ray scattering (WAXS), atomic force microscopy (AFM) amongst others. Our findings reveal that preexisting molecular order significantly influences the crystallization of PFO, accelerating early-stage crystallization kinetics but requiring longer times to reach full crystallization than samples crystallized from isotropic (disordered) states. Analysis with the Avrami model unveils distinct crystallization mechanisms, impacting semicrystalline morphology and photoluminescence properties. Additionally, in this thesis, the thermotropic behavior of PBTTT is explored along the crystallization kinetics; we find that the preexisting order given by the liquid crystal state promotes nucleation, accelerating early-stage kinetics, similarly to PFO. Moreover, our analysis uncovers complex crystallization kinetics in PBTTT, differing from typical behavior in commodity polymers in the late stages of crystallization.

This thesis also showcases the behavior of newly synthesized polythioethers with high sulfur content (DMDS-*alt*-DVE, DMDS-*alt*-TEGDVE, and DMDS-*alt*-BDDVE), presenting multiple phases, from

characterizing and establishing thermal protocols for the isolation or combination to exploring the kinetics of some of the different phases. Molecular dynamic simulations shed light on the diffusion capabilities, flexibility, and chain mobility among these polythioethers, with DMDS-*alt*-BDDVE resulting in the fastest diffusion and crystallization kinetics. These findings enhance our understanding of how subtle variations in chemical structure influence polymer behavior. This work contributes crucial insights into the influence of preexisting molecular arrangements or the existence of multiple polymorphic phases in the resulting crystallization kinetics and the microstructure.

Chapter 1

Structure and Objectives

1.1 Background and Objectives

To achieve technological development, it is of utmost importance to understand the behavior of polymers and how the solidification processes occur within this specific class of material[1–3]. For instance, the study of crystallization of conjugated polymers is essential to understand organic electronic devices, such as organic field effect transistors or photovoltaic cells[4–7] and the study of non-conjugated polymers such as polypropylene (PP) is essential for the improvement of packaging materials[8–10].

While there are numerous approaches to analyzing a particular material, the main scope of the research presented in this thesis focuses on bulk and thin-film methodologies. The study of polymers in the bulk polymers is the first step in analyzing newly-synthesized materials in order to provide a macroscopic view of the material properties as well as giving insight into the overall behavior and characteristics. Therefore, bulk polymer analysis serves as a foundational stage in the development process for subsequent research towards optimizing material's performance, functionality, and potential applications. On the other hand, thin-film architectures are the bases of the majority of organic electronic devices which are often used in a wide range of technologies including flexible electronics, organic photovoltaics, electrochemical and thin-film transistors, photodetectors and sensors[11–13]. The thin-film architecture can have an effect in a material that could not be achieved by the polymer in the bulk form as the confinement effects occurring in a polymer thin-film can give rise to unique physical properties due to the restrictive polymer chains conformation, motion and diffusivity. That is, it can lead to changes in the phase behavior, morphology, kinetics and crystallization compared to the material in the bulk. Because of this there is an imperative need to understand how crystallization and vitrification processes occur in these materials.

Many semicrystalline polymers can present polymorphism which can give rise to different properties[14–16]. An added trait to these materials is that they are often of complex structure making their phase behavior not straightforward and depending on the processing conditions or thermal pathways they will form one polymorph or another. These types of polymers have also received attention in recent years as the ability to form multiple structures will in turn result in different properties, which could lead to new applications for the same material.

For these reasons, this thesis aims to provide a deeper insight into these solidification processes and connect the kinetics of crystallization to the microstructure of these materials systems.

Devoted to understanding the crystallization of semiconducting polymers, the work will focus on understanding the crystallization kinetics from a liquid state, which can be isotropic or anisotropic. That is, the goal is to show how the initial molecular arrangement of a material can affect the crystallization kinetics, in addition to characterizing and understanding the changes in the material and their electronic and optical properties.

More specifically:

- Understand the crystallization kinetics of semicrystalline semiconducting polymers PFO and PBTTT, which exhibit a nematic liquid crystal and a smectic liquid crystal, respectively.
- Establish a reliable experimental protocol to monitor crystallization kinetics of semiconducting polymer thin-films via fast scanning calorimetry from the melt, an isotropic, and a liquid crystal state.
- Characterize of the inner microstructure of the crystallized materials by grazing incidence wide angle X-ray scattering (GIWAXS), fast scanning calorimetry (FSC), polarized optical light microscopy (PLOM) and atomic force microscopy (AFM).

For the chapters about non-conjugated polymers, in which we will discuss newly synthesized polythioethers with a high sulfur content presenting multiple phases, one of the aims will be to gain a deep understanding on how one can achieve each phase found in each material through thermal treatment. Additionally, the study will focus on each phase's crystallization kinetics and characterization.

More specifically,

- Establish and characterize each polymorphic phase of a family of novel polythioethers.

- Characterize and establish reliable protocols for the isolation or combination of each phase through techniques such as FSC, AFM, PLOM, differential scanning calorimetry (DSC), wide angle X-ray scattering (WAXS), etc.

- Study the crystallization kinetics of each phase and verification of the underlying physical phenomena using computational methods.

Additionally, in Chapter 2 and Chapter 3, some equations and schemes are identical to those in Chapters 4 through Chapter 7. However, for clarity and ease of reference within each chapter, these are reiterated in Chapters 4 through Chapter 7.

1.2 References for Chapter 1

(1) Cavallo, D.; Müller, A. J. Polymer Crystallization. In *Macromolecular Engineering*; John Wiley & Sons, Ltd, 2022; pp 1–57.

(2) Van Krevelen, D. W.; Te Nijenhuis, K. *Properties of Polymers*; 2009.

(3) De Rosa, C.; Scoti, M.; Di Girolamo, R.; de Ballesteros, O. R.; Auriemma, F.; Malafronte, A. Polymorphism in Polymers: A Tool to Tailor Material's Properties. *Polym Cryst* **2020**, *3* (2), 1–29.

(4) Chen, X.-L.; Huang, H.-L.; Shi, J.-G.; Liu, Y.-L.; Wang, L.-M. Isothermal Crystallization Kinetics and Melting Behavior of a Luminescent Conjugated Polymer, Poly(9,9-Dihexylfluorene-Alt-2,5-Didodecyloxybenzene). *J. Macromol. Sci. Part B* **2012**, *51* (6), 1049–1056.

(5) Jumali, M. H. H.; Al-Asbahi, B. A.; Yap, C. C.; Salleh, M. M.; Alsalhi, M. S. Optoelectronic Property Enhancement of Conjugated Polymer in Poly(9,9′-Di-n-Octylfluorenyl-2.7-Diyl)/Titania Nanocomposites. *Thin Solid Films* **2012**, *524*, 257–262.

(6) Baklar, M.; Barard, S.; Sparrowe, D.; Wilson, R. M.; McCulloch, I.; Heeney, M.; Kreouzis, T.; Stingelin, N. Bulk Charge Transport in Liquid-Crystalline Polymer Semiconductors Based on Poly(2,5-Bis(3-Alkylthiophen-2-Yl)Thieno[3,2-b]Thiophene). *Polym. Chem.* **2010**, *1* (9), 1448–1452.

(7) Cochran, J. E.; Junk, M. J. N.; Glaudell, A. M.; Miller, P. L.; Cowart, J. S.; Toney, M. F.; Hawker, C. J.; Chmelka, B. F.; Chabinyc, M. L. Molecular Interactions and Ordering in Electrically Doped Polymers: Blends of PBTTT and F4TCNQ. *Macromolecules* **2014**, *47* (19), 6836–

6846.

(8) Garbarczyk, J.; Paukszta, D.; Borysiak, S. Polymorphism of Isotactic Polypropylene in Presence of Additives, in Blends and in Composites. *J Macromol Sci Phys B* **2007**, *41* (4–6), 1267–1278.

(9) Schyns, Z. O. G.; Shaver, M. P. Mechanical Recycling of Packaging Plastics: A Review. *Macromol. Rapid Commun.* **2021**, *42* (3), 2000415.

(10) Rahman, S.; Gogoi, J.; Dubey, S.; Chowdhury, D. Animal Derived Biopolymers for Food Packaging Applications: A Review. *Int. J. Biol. Macromol.* **2024**, *255*, 128197.

(11) Griesser, H. J. *Thin Film Coatings for Biomaterials and Biomedical Applications*, 1st ed.; Woodhead Publishing, 2016.

(12) Zhang, X.; Hudson, S. D.; Delongchamp, D. M. Thin Film Morphology of Organic Electronic Materials. *Polym. Mater. Sci. Eng.* **2010**, *102*, 210.

(13) Elanjeitsenni, V. P.; Vadivu, K. S.; Prasanth, B. M. A Review on Thin Films, Conducting Polymers as Sensor Devices. *Mater. Res. Express* **2022**, *9* (2), 022001.

(14) Brog, J.-P.; Chanez, C.-L.; Crochet, A.; Fromm, K. M. Polymorphism, What It Is and How to Identify It: A Systematic Review. *RSC Adv.* **2013**, *3* (38), 16905.

(15) Brittain, H. G. *Polymorphism in Pharmaceutical Solids*; Brittain, H. G., Ed.; CRC Press: Milford, 2009; Vol. 192.

(16) Cocca, M.; Lorenzo, M. L. D.; Malinconico, M.; Frezza, V. Influence of Crystal Polymorphism on Mechanical and Barrier Properties of Poly(l-Lactic Acid). *Eur. Polym. J.* **2011**, *47* (5), 1073–1080.

Chapter 2

Multiphasic polymers

&

Polymer Crystallization

2.1 General Introduction

Polymers are intriguing and versatile materials composed of repeating subunits known as monomers[1,2]. Due to their large size, the polymer chains become intertwined with each other, creating a tangled structure. This entanglement may be completely disordered, without any long or short-range correlation, or may present crystalline regions between amorphous boundaries. For this, polymers are often considered to be amorphous or semicrystalline materials, that is, some regions are amorphous and other regions are crystalline (see Figure 2.1).

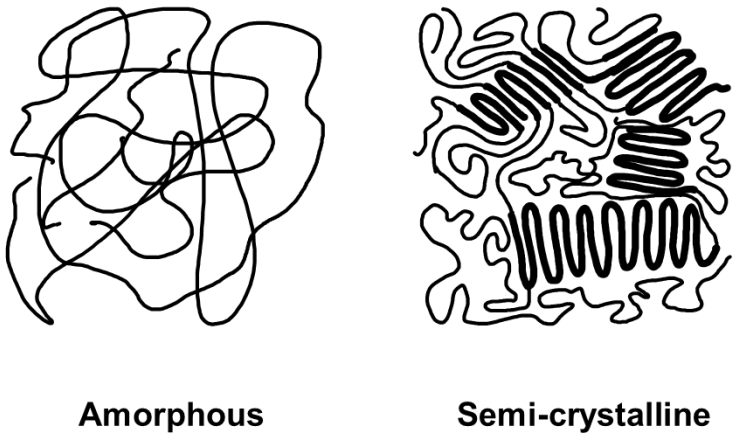

Figure 2.1. Schematic representation of an amorphous and semicrystalline material.

Crystallization of a polymer occurs within a specific temperature range, defined by the glass transition temperature (T_g) as the lower limit and the melting temperature (T_m) as the upper limit. Below T_g, the polymer chains become less mobile, impeding the crystallization process. On the other hand, near T_m, the nucleation process is hindered and crystallization does not occur. Taking this into consideration, typically when cooling from the melt the rate of crystallization increases (*i.e.,* the polymer crystallizes faster) as the

crystallization temperature decreases up to a maximum point. This is because the energy barrier required for the transformation from amorphous to crystalline region to occur is lower. As temperature decreases, melt viscosity also increases, and the diffusion of the chains to the crystallization front is hindered, thus causing a decrease in crystallization rate. As we approach T_g, the diffusion is greatly reduced to the point where the rate of crystallization approaches zero. Thus, when crystallizing from the melt, at first the rate of crystallization will be slow near T_m due to the difficulty of forming nuclei, as the crystallization temperature continues to decrease the crystallization rate will increase until a maximum crystallization rate is reached (thermodynamic control). Lastly, the crystallization rate will decrease due to the slow diffusion of the chains (diffusion control).

2.2 Multi-phase Polymers

All materials investigated in the present thesis exhibit an extraordinarily complex crystallization behavior through the presence of multiple and/or uniquely ordered or semi-ordered states. The main objective of this work is to comprehensively investigate the crystallization process and the kinetics and morphological aspects of these diverse materials. Additionally, the final properties of the material are directly related to the crystallization process, which is influenced to different degrees by various factors such as temperature, cooling rate, molecular weight, polymer composition, and processing conditions[3,4]. For this, understanding and controlling the formation of each polymorph or semi-ordered state is essential for tailoring material properties to meet specific requirements in industries such as packaging, automotive, textiles, and electronics[5,6].

2.2.1 Liquid-Crystals (LC)

Early investigations claimed the observation of flexible and flowing shapes in nerve fibers under a microscope[7–9], which seemed to exhibit the fluid properties of a liquid but the optical properties of solids. However, these works did specify the reason for the unusual behavior. Hence, the discovery of liquid crystals is usually attributed to the botanist Friedrich Reinitzer in 1888, as he observed two distinct melting points in a cholesterol mixture[10]. However, it was not until the sixties that the interest in liquid crystals (LC) went from a low level to exponential field advance and rapid development as technological applications for liquid crystals were found[9,10]. Nowadays, liquid crystals are well understood and are used for different commercial uses such as displays (*e.g.*, calculators, wristwatches, etc.)[10,11] or even biomedical applications (*e.g.*, drug delivery, bioimaging etc.)[12].

Crystalline solids are usually ordered in an orientational and positional manner and have optical, electrical, and magnetic anisotropy. Liquids, on the other hand, are isotropic (*i.e.*, all directions in the liquid are equivalent) and diffuse freely within the available space[7]. In other words, liquids flow and take the shape of space, while a crystalline solid has long-range positional and orientational order in three dimensions. Therefore, a liquid crystal will have some fluidity while retaining a certain degree of order. This orientational order that the liquid crystal retains can have a large effect on the electrical and optical properties of the material due to the anisotropic nature of the liquid crystal. That is, the main characteristic that all types of liquid crystals possess is their anisotropy; they are often called mesophases as they are considered to be an intermediate state between a crystalline solid and an isotropic/amorphous liquid[8]. Hence, mesogens are compounds that can form mesophases.

Polymers exhibiting a liquid crystalline state are often composed of

aromatic rings as they must have rigid sections for the mesophase to form. These materials can retain some order above the melting point instead of having a completely disordered (isotropic) state, whereas polymers that do not exhibit a liquid crystalline state, after crystallization, above the melting point (T_m) will transition into a disordered (liquid) state.

Three main categories can be used to differentiate the types of liquid crystals based on their physical parameters that allow the liquid crystal to exist: lyotropic liquid crystals, thermotropic liquid crystals and amphotropic liquid crystals. Lyotropic liquid crystals emerge from an amphiphilic mesogens (hydrophobic group at one end with a hydrophilic group at the other) being dissolved in a suitable solvent to form a liquid crystal phase under specific concentration and temperature conditions[7–9]. On the other hand, liquid crystals obtained by melting a crystalline solid are called thermotropic liquid crystals. They are stable for a particular temperature interval and will be stable according to the temperatures submitted to them[7–9]. Finally, those that can exhibit both lyotropic and thermotropic mesophases are known as amphotrophic liquid crystals[7–9]. Many classes of liquid crystal phases are subdivided into nematics, cholesterics, smectics, and columnar mesophases; however, this thesis will focus on the nematic and smectic phases distinguished by their structural and physical characteristics.

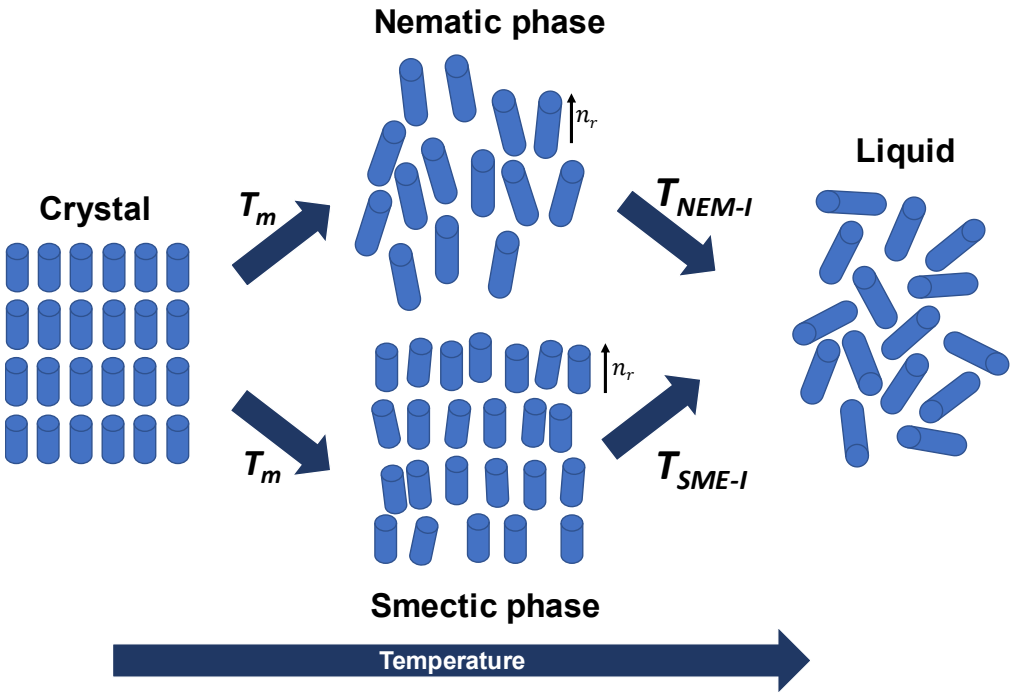

Figure 2.2. Schematic representation of the thermal transitions between a crystal (solid), a nematic or smectic phase (LC) and a liquid.

The nematic phase comes from the word "thread" in Greek, is the most widely studied liquid crystal phase[7,9,13]. In this phase, the molecules possess a long-range orientational order along a preferred direction. They retain a preferred orientational order but no positional order, as seen in Figure 2.2 (the director is represented by a unit vector, n_r). Additionally, it can often be easily identified by the birefringent texture under a light optical microscope with crossed polarizers as the nematic phase is fluid and exhibits a distinct texture and shine.

For the smectic phase, there are a few subclassifications according to the positional and directional arrangements of the molecules; they exhibit a type of polymorphism as different types of phases can be found depending upon whether the molecules are tilted or not[4,7]. The smectic phase, meaning "soap-like" in Greek, is more ordered than the nematic phase as it retains both

orientational and positional order to some degree but no translational correlation. That is, within the layers, there is no positional order. This thesis will refer to the smectic phase as presenting a lamellar nature without considering the layers tilting.

The generation of liquid crystal phases occurs within a defined subset of materials, often with rigid molecular backbones that define the long axes of molecules[13]. Therefore, having an overview of the relationship between structure and property is crucial in understanding the importance of liquid crystals. For instance, the nematic mesophase is considered the most relevant phase in commercial applications as it is used in mid-size displays. Additionally, these mesogens often contain π-conjugated segments which can facilitate charge transport making them organic semiconductors. Some of them can be thermally activated; depending on the temperature conditions to which the liquid crystal state is subjected, it could yield different charge carrier mobilities. Generally, the more ordered the liquid crystal phase is, the higher mobilities will be obtained. This is why smectic phases, due to their layered arrangement, provide a transport network beneficial for field-effect transistors and organic solar cells[14–17].

2.2.2 Polymorphism

The ability of a material to solidify in more than one form or crystal structure is called polymorphism[4,18,19]. Controlling the crystallization mechanism is crucial as it can profoundly influence a material's properties (*e.g.*, conductivity or tensile strength) and potential applications[4,18,20–22]. Polymorphs are studied in many fields, from material science to chemistry to pharmaceutical sciences. For instance, in the industrial processing of isotactic polypropylene (iPP) and polyvinylidene fluoride (PVDF), control over which polymorph forms has been demonstrated to directly relate to the resulting physical properties of

the materials, thereby allowing tunability in their characteristics. Therefore, a comprehensive understanding of how each polymorph is formed and the intricacies via which thermal or mechanical treatment one can control them is imperative. A recent shift in perspective has emerged regarding the challenges of controlling polymorphism thanks to the advancements in the ability to control the polymorphism exhibited by some materials, as opposed to it being perceived solely as an unintended result in the desired product[22]. Typically, only one of the polymorphs is stable under equilibrium conditions while the others are metastable, implying the possibility to transform into more stable ones by proper thermal treatments[23,24].

Usually, semicrystalline polymers, during crystallization, can produce different polymorphs. It is important to note that the exploited form does not necessarily correspond to the most kinetically stable form and hence, it is essential to identify that the polymorph with the highest melting point is the polymorph with the lowest free energy, which is the most thermodynamically stable polymorph[18,21].

Upon crystallization or polymorph formation, even though different polymorphs can crystallize, typically, one of the polymorphs will be the more thermodynamically stable among polymorphic polymers. In other words, a more unstable or metastable polymorph will eventually transform into a more thermodynamically stable form.

These less stable polymorphs are designated as the metastable phases, which often stems from the kinetic contribution, resulting in the metastable phase having a faster crystallization rate than the stable phase[25]. Phase transitions between one polymorph and another can occur through different mechanisms such as direct solid-to-solid phase transitions, in which, for instance, the material could evolve overtime transforming into another phase

(*e.g.,* isotactic poly(1-butene) (iPB)) or by introducing nucleating agents (isotactic polypropylene (iPP))[26]. Other phase transitions occur during the thermal treatment of the material, which can be influenced by the heating and cooling rates and the crystallization temperature, amongst others. On the other hand, during the crystallization of a polymer, which will be discussed in greater detail in the sections below, the nucleation and diffusion of polymer chains are significantly influenced by the degree of supercooling (ΔT). Supercooling is defined as $\Delta T = T_m^o - T_c$ where T_m^o is the melting temperature at the thermodynamic equilibrium. Consequently, polymers exhibit diverse crystallization kinetics as supercooling or the crystallization temperature (T_c) varies. Under high supercooling, *i.e.,* lower $T_c s$ many polymers crystallize faster, often resulting in the formation of metastable polymorphs. More recently, experiments using extremely fast temperature ramps have shown that metastable polymorphs can be isolated and crystallized under significant supercooling[25–27].

In this thesis, a combination of such techniques was used to isolate new polymorphs and analyze the occurrence and kinetics of different phase transitions of metastable and stable polymorphs in various semicrystalline polymers[4,18,19]. As mentioned above, this may grant access to unique physical properties, including thermal and mechanical properties, biodegradability, kinetics, etc.[25].

2.3 Crystal Structure and Morphology

Polymer crystallization is an intricate non-equilibrium process that involves the transition of polymers from an amorphous to an ordered state. The crystal structure, that is, the atomic and molecular arrangement can be influenced by many factors such as the crystallization temperature, cooling rate, presence of impurities, etc.; which can significantly influence the final structure

and the mechanical, physical, optical, and thermal properties of materials. Given that crystallization can offer precise and direct control over the final properties of a material as it can have a large effect on the mechanical, optical, and thermal properties. It is therefore important, to understand the development of the crystalline structure, the morphology and the crystallization behavior. Fortunately, this is possible through structural, morphological, and thermal characterization.

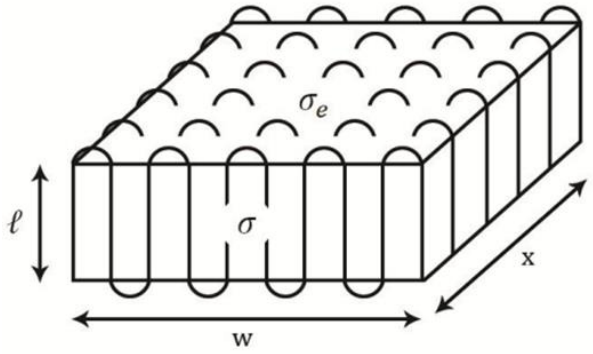

Figure 2.3. Schematic representation of a lamellar crystal with chain folds (l, w, x: lamellar thickness, length and width; σ and σ_e: lateral and fold surface free energies of the lamellae, respectively)[28].

Crystallization typically occurs by cooling from the melt state (non-isothermal crystallization) or by rapidly cooling the sample to a crystallization temperature (T_c) and allowing the material to crystallize over time (isothermal crystallization). However, crystallization of a polymer can also occur during the synthesis of the polymer, by mechanical stretching, solvent evaporation or even in solution[29,30]. During crystallization from the melt, long macromolecular chains disentangle from each other, and thin segments called lamellae form because polymer chains are aligned and folded together with thickness d_c separated by amorphous regions with thickness d_a. The sum of both is the long period (L), with a typical size on the order of a few nm (*e.g.*, 10 nm), see Figure

2.3[28].

Flexible polymers have the ability to crystallize, typically forming spherically symmetric aggregates characterized by radial lamellae, commonly referred to as spherulites. However, other supramolecular structures such as axialites or hedrites can also form.

The morphology and size of a spherulite will vary depending on the nature of the polymer and the crystallization conditions and will highly impact the final properties of the material.

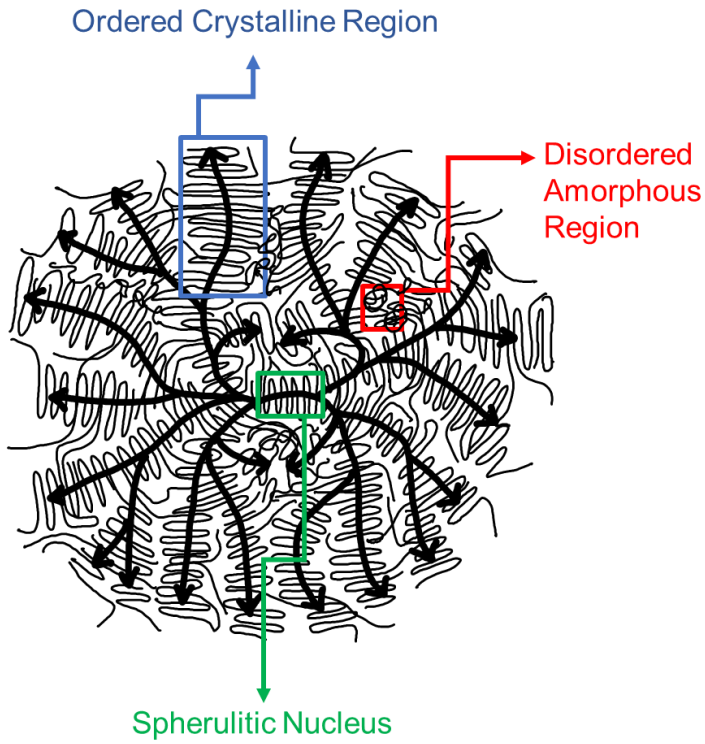

Figure 2.4. Radial growth of spherulite in two dimensions.

Figure 2.4 shows a representation of a grown spherulites in which three distinct regions can be observed: (i) and ordered crystalline region composed of stacked lamellae (ii) a disordered amorphous region composed of entangled polymer chains in the interspace between crystalline lamellae and (iii) the

spherulitic nucleus representing the centre of nucleation from which the spherulite grows[31–33].

These formations manifest as birefringent spheres, observable through *e.g.,* polarized light optical microscopy (PLOM), exhibiting distinctive extinction patterns known as Maltese crosses. These patterns emerge in alignment with both parallel and perpendicular orientations to the polarization direction (Figure 2.4 illustrates a representative instance of spherulites).

2.4 Crystallization Kinetics

The rate at which a polymer transforms from its amorphous state to a crystalline state refers to the crystallization kinetics of a material, which can be influenced by various factors such as molecular weight, cooling rate, temperature, and polymer structure. Crystallization in polymers is a thermal process which can be divided into two processes: primary crystallization and secondary crystallization. Additionally, primary crystallization can be broken down into primary nucleation, commonly referred to as nucleation, and secondary nucleation, commonly known as crystal growth. In this section, the intricacies of both primary and secondary crystallization in polymers and exploring their underlying mechanisms will be explained.

2.4.1 Primary Crystallization

Primary Crystallization is the initial stage of crystallization in polymers; during this process, the polymer chains begin to order themselves in a structured and ordered manner, forming a three-dimensional lattice, known as a crystallite, which occurs when a material is cooled from the melt (*i.e.,* amorphous state). Primary Crystallization can be broken down into two steps: nucleation (*i.e.,* primary nucleation) and growth (*i.e.,* secondary nucleation).

2.4.1.1 Nucleation

Primary nucleation is a fundamental process that plays a crucial role in the crystallization of polymers. It consists of the formation of small crystalline structures known as nuclei or nucleation sites. These nuclei serve as starting points for the growth of larger crystalline structures[34].

Primary nucleation can occur through two mechanisms: homogeneous nucleation and heterogeneous nucleation. Homogeneous nucleation consists in the spontaneous aggregation of parallel polymeric chain segments; that is, nucleation takes place uniformly throughout the polymer melt or solution without the involvement of any foreign particles or nucleating agents. For this to occur, the polymer chains in the melt or solution reach a critical level of supersaturation. Supersaturation refers to the state when the concentration of polymer chains exceeds the saturation concentration required for crystallization[29]. Once the critical supersaturation level is reached, polymer chains aggregate and form nuclei. If the particle size does not achieve the critical saturation level the grains disappear[1,35].

On the contrary, heterogenous nucleation occurs when foreign particles such as impurities or nucleation agents provide a favorable environment for the aggregation and orientation of polymer chains, promoting the formation of nuclei. These impurities reduce the free energy barrier for nucleation, making the process more efficient and predictable compared to homogeneous nucleation. Heterogeneous nucleation is more common than homogeneous nucleation in practical polymer processing scenarios due to the abundance of foreign particles and interfaces, and it can either occur sporadically or instantaneously. Sporadic nucleation refers to the formation of crystalline nuclei as a function of time during primary crystallization within the polymer melt, whereas instantaneous nucleation occurs when all nuclei appear at the same

time[1,35]. This change can be induced by various factors, including temperature quenching, pressure changes, or the addition of a nucleating agent. Instantaneous nucleation results in the rapid formation of nuclei, which then grow into crystalline domains typically occurring during high supercooling.

2.4.1.2 Growth

As it has been established, the crystallization of polymers is described in terms of nucleation and growth. The growth process, also known as secondary nucleation, involves the growth of crystalline regions from existing crystal nuclei. These nuclei act as templates for the attachment and ordering of additional polymer chains, leading to the enlargement of the crystal structure. It is considered that primary crystallization ends when the crystals have impinged on one another, typically at the 50% conversion mark of the entire crystallization process[36]. Commonly, the lamellae grow in a radial manner, forming, spherulites of $1-100\ \mu$m[37]. The growth rate (G) of secondary nucleation is influenced by factors such as temperature, cooling rate, the diffusion of polymer chains, and the alignment or rearrangement of the amorphous regions. The dependence of G on the isothermal crystallization temperature or supercooling can be represented as a bell-shaped curve (see Figure 2.5)[38] because of the dynamic interaction of two processes: diffusion and the secondary nucleation term. Additionally, a similar dependence on temperature can be observed for primary nucleation. On the left side of the curve (high supercooling), the growth of the crystals is dominated by the slow diffusion of the chains; hence, G increases as T_c increases, whereas the right side of the curve is controlled by secondary nucleation activation energy; hence, as T_c increases the G decreases as fewer nuclei are generated.

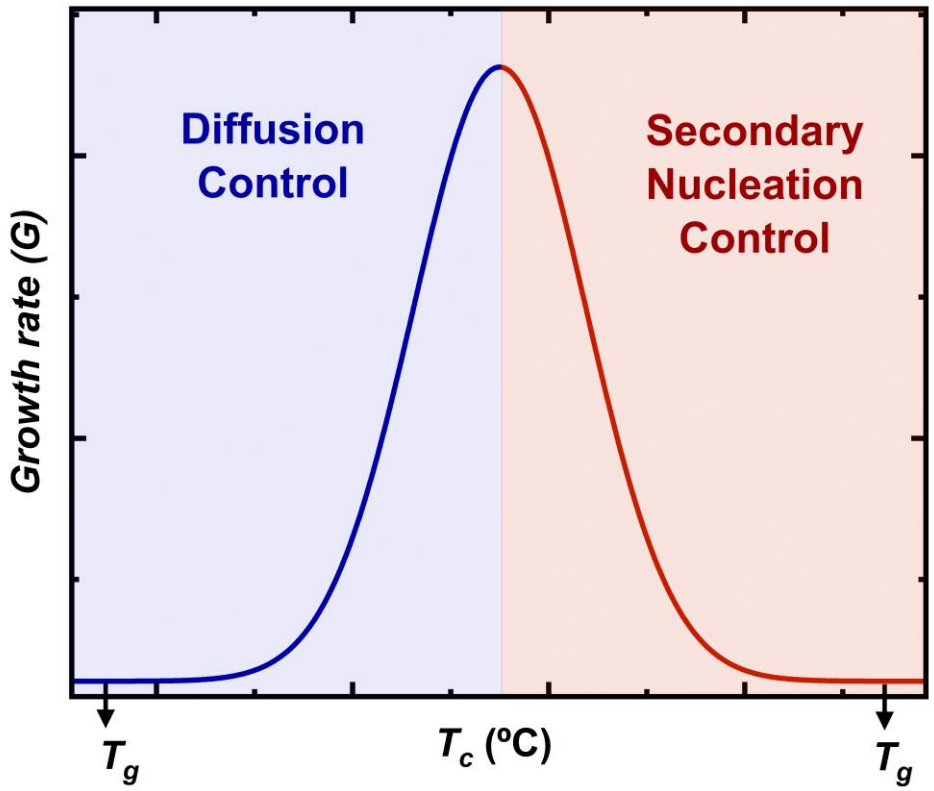

Figure 2.5 Crystal growth rate (G) as a function of the crystallization temperature[38].

2.4.2 Secondary Crystallization

After the spherulites have impinged on one another, secondary crystallization continues. During secondary crystallization, interspherulitic material crystallizes, and lamellar thickening and rearrangement can occur. Additionally, the nucleation of new nuclei and their subsequent growth can lead to the formation of new crystalline domains, increasing the overall crystallinity of the polymer material[39,40].

2.5 Crystallization theories

Numerous theories have been developed over the years to describe the

phenomenon of polymer crystallization, mainly thermodynamic and kinetic theories. While thermodynamic theories might offer some insight into certain aspects such as crystal thickness or the semicrystallinity of polymers. The consensus amongst experts is that kinetic theories and thus, kinetic parameters have a larger hold over determinant features of polymers such as the overall crystallization rate and morphology.

The kinetics of polymers can be described by different crystallization theories depending on which step of crystallization we want to study. That is, the overall crystallization kinetics, the kinetics of primary nucleation or of crystal growth (secondary crystallization).

2.5.1 Avrami Theory

The Avrami model also referred to as the Avrami theory or the Avrami equation is a mathematical model developed by Evans, Kolmogoroff, Johnson and Mehl, and Avrami around the 1930s to describe the kinetics of crystallization in polymers[36,41]. The Avrami theory describes the free growth of objects from random nucleation centers and is based upon the assumption that the volume remains constant. Moreover, this model is not capable of providing a complete description of the overall kinetics, *i.e.*, it does not consider the effects of secondary crystallization. Nonetheless, it provides insight into primary crystallization rates[1,38,42]. The model yields the expression below (Equation 2.1)[36]:

$$1 - V_c\,(t - t_o) = \exp(-k(t - t_o)^n) \qquad \text{Equation 2.1}$$

where V_c is the relative volumetric transformed fraction to the crystalline state, t is the crystallization time, t_o is the induction time, k is the overall crystallization rate constant which includes nucleation and growth components,

and n is the Avrami index. Moreover, V_c can be expressed as a function of mass fraction of the samples (W_c) as seen in Equation 2.2.

$$V_c = \frac{W_c}{W_c + \left(\frac{\rho_c}{\rho_a}\right)(1 - W_c)} \qquad \text{Equation 2.2}$$

where W_c is the mass fraction of the sample, ρ_c, the density of a 100% crystalline sample, and ρ_a the density of a 100% amorphous sample. Sometimes the values of ρ_c and ρ_a are unknown for some polymers and therefore we cannot apply Equation 2.1 in terms of volume fraction. However, V_c is proportional to W_c (see Equation 2.2 and Equation 2.3) and the overall crystallization kinetics can be fitted to the Avrami equation in terms of the mass fraction of crystals as an approximation.

From Equation 2.3, $\Delta H(t)$ is the enthalpy variation at a given crystallization temperature as a function of time, and ΔH_{total} is the maximum enthalpy value reached at the end of the isothermal crystallization process[38,43].

The enthalpies are obtained by integration of the experimental isothermal data when the mass of the sample is known. However, in cases were the sample measured is in the nanogram scale these values are given by the specific heat capacity (C_p) as a function of mass. These values are obtained from the normalized integrated area of each peak divided by the heating or cooling rate to determine the relative crystallinity mass fraction of the sample at a given *t* and describe the kinetics of the material at a constant mass.

$$W_c = \frac{\Delta H\ (t)}{\Delta H_{total}} \qquad \text{Equation 2.3}$$

To obtain the Avrami parameters, the data obtained from isothermal crystallization must be fitted to Avrami equation, for this, the equation must be linearized by applying logarithm in both sides as seen in Equation 2.4, and plotting $\log[-\ln[1 - V_c]$ as a function of $\log(t - t_o)$. This equation is used to construct the Avrami plot, from which the linear fit to the fitted range, usually between 3−20% conversion, the value of n can be obtained from the slope and k from the intercept. Correlation data (R^2) value close to 0.9999 is recommended to consider it a good fit.

$$\log[-\ln[1 - V_c\,(t - t_o)]] = \log(k) + n\log(t - t_o) \qquad \text{Equation 2.4}$$

Moreover, Müller *et al.* proposed that the Avrami index (n) can be considered in terms of the addition of two components: a nucleation rate component (n_n) and a growth dimensionally (n_d) component (Equation 2.5)[37,38],

$$n = n_n + n_d \qquad \text{Equation 2.5}$$

where, n_d represents the dimensionality of the growing crystals and can have values of 1, 2, and 3 depending on the dimensionality of the crystalline ensembles formed (*i.e.*, needles (1D), axialites (2D), and spherulites (3D)). The n_n value is proportional to the rate of nucleation with values ranging from 0 to 1, values equal to 1 are due to sporadic nucleation whereas values equal to 0 represent instantaneous nucleation or values in between these two[1,32,36,38,44]. A summary of the different combination of n_d and n_n are given below in Table 2.1, the sporadic nucleation es represented as (S) and instantanous nucleation as (I).

Table 2.1. Description of the different combination of n_d and n_n. Note that *I* is refer to instantaneous and *S* to Sporadic growth.

Avrami Index (n)	n_n	n_d	Crystals obtained
1	0	1	Rod (I)
2	1	1	Rod (S)
2	0	2	Axialite (I)
3	1	2	Axialite (S)
3	0	3	Spherulite (I)
4	1	3	Spherulite (I)

Additionally, t_o represents the induction time before any crystallization can be detected by the calorimeter, hence its inverse is proportional to the primary nucleation rate. Moreover, by applying the Avrami equation, it is also possible to obtain a theoretical value of the time needed to reach 50% conversion according to the Avrami parameters obtained *i.e.*, the half-crystallization time ($\tau_{50\%}$), see Equation 2.6, which can be compared to the experimentally observed quantity to see if the equation is able to describe the overall crystallization process until 50% conversion.

$$\tau_{50\%} = \left(\frac{-\ln(0.5)}{k}\right)^{\frac{1}{n}} \qquad \text{Equation 2.6}$$

As mentioned above, the range of conversion in which to perform the fitting when applying the Avrami equation is that recommended to be between

3 to 20% conversion this is because the Avrami equation provides information on the overall crystallization rate, that is, until the end of primary crystallization which is when the crystals impinge on one another at conversion range of 40−50%. Thus, a range of conversion which ensures the free growth of the crystals (no impingement occurs) and avoids deviations or errors due to secondary crystallization effects is of outmost importance to ensure a good fit.

2.5.2 Lauritzen-Hoffman Theory

The Lauritzen-Hoffman theory (LH) proposed by Lauritzen and Hoffman was developed in the 1960's[45]. The theory focuses on the kinetics of polymer crystallization and has been influential in understanding and predicting the behavior of polymers during crystallization[32,33,37,42,46]. In recent years the theory has received some criticism, however it is considered a widely accepted theory, since it provides a simple and analytical approach to provide insight into the crystallization behavior of polymer chains from the molten state to the solid crystalline state.

The LH theory revolves around two fundamental processes: nucleation and growth. According to the LH theory, the growth rate (G) as a function of time is described by the following expression[30,47]:

$$G = G_0 \, exp\left(\frac{-U^*}{R(T_c - T_\alpha)}\right) exp\left(\frac{-K_g^G}{T_c \Delta T_f}\right) \qquad \text{Equation 2.7}$$

Where G_o is a growth constant, the first exponential term is linked to molecular diffusion and the second exponential term refers to the secondary nucleation, R is the universal gas constant, T_α is the temperature at which the movement of the chains is frozen, and it is 30 °C degrees lower than the T_g, U^*

is the transport activation energy for the chain diffusion of the polymer (a value of 1500 cal/mol is usually employed), ΔT is the supercooling $(T_m^o - T_c)$ f is a temperature correction factor, and K_g^G is a constant proportional to the energy barrier for the spherulitic growth or secondary nucleation. At the same time, K_g^G is described by Equation 2.8:

$$K_g^G = \frac{j\, b_0\, \sigma\, \sigma_e\, T_m^0}{k\, \Delta h_f} \qquad \text{Equation 2.8}$$

Where j is dependent on the crystallization regime, b_0 is the polymer chain width, σ is the lateral surface free energy, σ_e is the fold surface energy, k is the Boltzmann constant (1.38 x 10^{-23} J/K) and Δh_f is the equilibrium melting enthalpy of the enthalpy of fusion of a 100% crystalline material.

On another note, there are three possible crystallization regimes depending on T_c and, thus, the supercooling according to LH[30,42].

- Regime I ($i << g$): the formation of secondary nuclei is slower than the growth, it occurs at low ΔT (high T_c).
- Regime II (the same order of magnitude for *i* and *g*): the formation and growth of secondary nuclei is comparable, occurs at intermediate ΔT.
- Regime III ($i > g$): the formation of secondary nuclei is faster than growth, occurs at high ΔT (low T_c).

Additionally, the primary nucleation rate (I) has been described by the Turnbull–Fisher model, the data – *i.e.*, the number of spherulites per cubic centimetre at different T_c – is fitted in the linear region of the following

expression:

$$log\, I = log\, I_0 - \frac{\Delta F^*}{2.3\, kT} \frac{16\, \sigma\, \sigma_e\, (\Delta\sigma) {T_m^0}^2}{2.3\, k\, T\, (\Delta T)^2 (\Delta H_v)^2} \qquad \text{Equation 2.9}$$

Where ΔH_v is the volumetric equilibrium melting enthalpy, ΔT is the supercooling ($\Delta T = T_m^o - T_c$), ΔF^* term is proportional to the free energy of the primary nucleation, T_m^o is the equilibrium melting point, I_o is related to the diffusion of polymeric chains, $\Delta\sigma$ is the free-energy difference, and σ is the lateral surface free energy and σ_e the fold surface energy are both obtained from the Lauritzen-Hoffman fit.

2.6 References for Chapter 2

(1) Van Krevelen, D. W.; Te Nijenhuis, K. *Properties of Polymers*; 2009.

(2) Cavallo, D.; Müller, A. J. Polymer Crystallization. In *Macromolecular Engineering*; John Wiley & Sons, Ltd, 2022; pp 1–57.

(3) Arif P., M.; Kalarikkal, N.; Thomas, S. Chapter 1 - Introduction on Crystallization in Multiphase Polymer Systems. In *Crystallization in Multiphase Polymer Systems*; Thomas, S., Arif P., M., Gowd, E. B., Kalarikkal, N., Eds.; Elsevier, 2018; pp 1–16.

(4) De Rosa, C.; Scoti, M.; Di Girolamo, R.; de Ballesteros, O. R.; Auriemma, F.; Malafronte, A. Polymorphism in Polymers: A Tool to Tailor Material's Properties. *Polym Cryst* **2020**, *3* (2), 1–29.

(5) Chung, H.; Diao, Y. Polymorphism as an Emerging Design Strategy for High Performance Organic Electronics. *J. Mater. Chem. C* **2016**, *4* (18), 3915–3933.

(6) F. Sousa, A.; Patrício, R.; Terzopoulou, Z.; N. Bikiaris, D.; Stern, T.; Wenger, J.; Loos, K.; Lotti, N.; Siracusa, V.; Szymczyk, A.; Paszkiewicz, S.; S. Triantafyllidis, K.; Zamboulis, A.; S. Nikolic, M.; Spasojevic, P.; Thiyagarajan, S.; Es, D. S. van; Guigo, N. Recommendations for Replacing PET on Packaging, Fiber, and Film Materials with Biobased Counterparts. *Green Chem.* **2021**, *23* (22), 8795–8820.

(7) Collings, P. J.; Hird, M. *Introduction to Liquid Crystals: Chemistry and Physics*; Taylor & Francis, 2017.

(8) An, J. G.; Hina, S.; Yang, Y.; Xue, M.; Liu, Y. Characterization of Liquid Crystals: A Literature Review. *Rev. Adv. Mater. Sci.* **2016**, *44* (4), 398–

406.

(9) Goodby, J. W.; Collings, P. J.; Kato, T.; Tschierske, C.; Gleeson, H.; Raynes, P.; Vill, V. *Handbook of Liquid Crystals, 8 Volume Set*; John Wiley & Sons, 2014.

(10) Mitov, M. Liquid-Crystal Science from 1888 to 1922: Building a Revolution. *ChemPhysChem* **2014**, *15* (7), 1245–1250.

(11) Margerum, J. D.; Miller, L. J. Electro-Optical Applications of Liquid Crystals. In *Plenary and Invited Lectures*; Kerker, M., Zettlemoyer, A. C., Rowell, R. L., Eds.; Academic Press, 1977; pp 593–614.

(12) Zhang, Z.; Yang, X.; Zhao, Y.; Ye, F.; Shang, L. Liquid Crystal Materials for Biomedical Applications. *Adv. Mater.* **2023**, *35* (36), 2300220.

(13) Andrienko, D. Introduction to Liquid Crystals. *J. Mol. Liq.* **2018**, *267*, 520–541.

(14) Ostroverkhova, O. Organic Optoelectronic Materials: Mechanisms and Applications. *Chem. Rev.* **2016**, *116* (22), 13279–13412.

(15) Kroon, R.; Lenes, M.; Hummelen, J. C.; Blom, P. W. M.; De Boer, B. Small Bandgap Polymers for Organic Solar Cells (Polymer Material Development in the Last 5 Years). *Polym. Rev.* **2008**, *48* (3), 531–582.

(16) Murad, A. R.; Iraqi, A.; Aziz, S. B.; Abdullah, S. N.; Brza, M. A. Conducting Polymers for Optoelectronic Devices and Organic Solar Cells: A Review. *Polymers* **2020**, *12* (11), 1–47.

(17) Pisula, W.; Feng, X.; Müllen, K. Organic Electronics: Tuning the Columnar Organization of Discotic Polycyclic Aromatic Hydrocarbons. *Adv. Mater.* **2010**, *22* (33).

(18) Brog, J.-P.; Chanez, C.-L.; Crochet, A.; Fromm, K. M. Polymorphism, What It Is and How to Identify It: A Systematic Review. *RSC Adv.* **2013**, *3* (38), 16905.

(19) Gabriele, B. P. A.; Williams, C. J.; Lauer, M. E.; Derby, B.; Cruz-Cabeza, A. J. Impact of Polymorphism on Mechanical Properties of Molecular Crystals: A Study of p -Amino and p -Nitro Benzoic Acid with Nanoindentation. *Cryst Eng Comm* **2021**, *23* (10), 2027–2033.

(20) Li, M.; Balawi, A. H.; Leenaers, P. J.; Ning, L.; Heintges, G. H. L.; Marszalek, T.; Pisula, W.; Wienk, M. M.; Meskers, S. C. J.; Yi, Y.; Laquai, F.; Janssen, R. A. J. Impact of Polymorphism on the Optoelectronic Properties of a Low-Bandgap Semiconducting Polymer. *Nat. Commun.* **2019**, *10* (1), 2867.

(21) Brittain, H. G. *Polymorphism in Pharmaceutical Solids*; Brittain, H. G., Ed.; CRC Press: Milford, 2009; Vol. 192.

(22) Gentili, D.; Gazzano, M.; Melucci, M.; Jones, D.; Cavallini, M. Polymorphism as an Additional Functionality of Materials for Technological Applications at Surfaces and Interfaces. *Chem Soc Rev* **2019**, *48* (9), 2502–2517.

(23) Gan, Z.; Abe, H.; Doi, Y. Temperature-Induced Polymorphic Crystals of Poly(Butylene Adipate). *Macromol. Chem. Phys.* **2002**, *203* (16), 2369–2374.

(24) Pan, P.; Inoue, Y. Polymorphism and Isomorphism in Biodegradable Polyesters. *Prog. Polym. Sci.* **2009**, *34* (7), 605–640.

(25) Zheng, Y.; Pan, P. Crystallization of Biodegradable and Biobased Polyesters: Polymorphism, Cocrystallization, and Structure-Property

Relationship. *Prog. Polym. Sci.* **2020**, *109*, 101291.

(26) Azzurri, F.; Flores, A.; Alfonso, G. C.; Baltá Calleja, F. J. Polymorphism of Isotactic Poly(1-Butene) as Revealed by Microindentation Hardness. 1: Kinetics of the Transformation. *Macromolecules* **2002**, *35* (24), 9069–9073.

(27) Gohn, A. M.; Rhoades, A. M.; Wonderling, N.; Tighe, T.; Androsch, R. The Effect of Supercooling of the Melt on the Semicrystalline Morphology of PA 66. *Thermochim. Acta* **2017**, *655*, 313–318.

(28) Mohammadi, H. On the Melting and Crystallization of Linear Polyethylene, Poly(Ethylene Oxide) and Metallocene Linear Low-Density Polyethylene, Virginia Polytechnic Institute and State University, Blacksburg, Virginia, 2018.

(29) Piorkowska, E.; Rutledge, G. C. *Handbook of Polymer Crystallization*; John Wiley & Sons, 2013.

(30) Mark, J. E. *Physical Properties of Polymers Handbook*; Springer Science & Business Media, 2007.

(31) Gedde, U. W.; Mattozzi, A. *Polyethylene Morphology*; Albertsson, A.-C., Ed.; Advances in Polymer Science; Springer: Berlin, Heidelberg, 2004.

(32) Mandelkern, L. *Crystallization of Polymers: Volume 2: Kinetics and Mechanisms*, 2nd ed.; Cambridge University Press: Cambridge, 2004; Vol. 2. https://doi.org/10.1017/CBO9780511535413.

(33) Schultz, J. *Polymer Crystallization: The Development of Crystalline in Thermoplastic Polymers*; An American Chemical Society Publication, 2001.

(34) Müller, A. J.; Balsamo, V.; Arnal, M. L. Nucleation and Crystallization in Diblock and Triblock Copolymers. *Adv. Polym. Sci.* **2005**, *190* (1), 1–63.

(35) Reiter, G.; Strobl, G. R. *Progress in Understanding of Polymer Crystallization*; Springer Science & Business Media, 2007.

(36) Lorenzo, A. T.; Arnal, M. L.; Albuerne, J.; Müller, A. J. DSC Isothermal Polymer Crystallization Kinetics Measurements and the Use of the Avrami Equation to Fit the Data: Guidelines to Avoid Common Problems. *Polym. Test.* **2007**, *26* (2), 222–231.

(37) Strobl, G. R. *The Physics of Polymers: Concepts for Understanding Their Structures and Behavior*; Springer Science & Business Media, 2007.

(38) Müller, A. J.; Michell, R. M.; Lorenzo, A. T. Isothermal Crystallization Kinetics of Polymers. *Polym. Morphol. Princ. Charact. Process.* **2016**, 181–203.

(39) Hay, J. N. Secondary Crystallization Kinetics. *Polym. Cryst.* **2018**, *1* (2).

(40) Wang, Z.-G.; Hsiao, B. S.; Sauer, B. B.; Kampert, W. G. The Nature of Secondary Crystallization in Poly(Ethylene Terephthalate). *Polymer* **1999**, *40* (16), 4615–4627.

(41) Tomellini, M.; Fanfoni, M. Connection between Phantom and Spatial Correlation in the Kolmogorov–Johnson–Mehl–Avrami-Model: A Brief Review. *Phys. Stat. Mech. Its Appl.* **2022**, *590*, 126748.

(42) Gedde, U. W. *Polymer Physics*; Chapman and Hall, 1995.

(43) Castillo, R. V.; Müller, A. J. Crystallization and Morphology of Biodegradable or Biostable Single and Double Crystalline Block Copolymers. *Prog. Polym. Sci.* **2009**, *34* (6), 516–560.

(44) Hiemenz, P. C.; Lodge, T. P. *Polymer Chemistry*, 2nd ed.; CRC Press: Boca Raton, 2007.

(45) Lauritzen, J. I.; Hoffman, J. D. Theory of Formation of Polymer Crystals with Folded Chains in Dilute Solution. *J. Res. Natl. Bur. Stand. Sect. Phys. Chem.* **1960**, *64A* (1), 73–102.

(46) Sperling, L. H. *Introduction to Physical Polymer Science*, Fourth.; John Wiley & Sons, Ltd, 2005.

(47) Lauritzen, J. I., Jr.; Hoffman, J. D. Formation of Polymer Crystals with Folded Chains from Dilute Solution. *J. Chem. Phys.* **1959**, *31* (6), 1680–1681.

Chapter 3

Materials & Methods

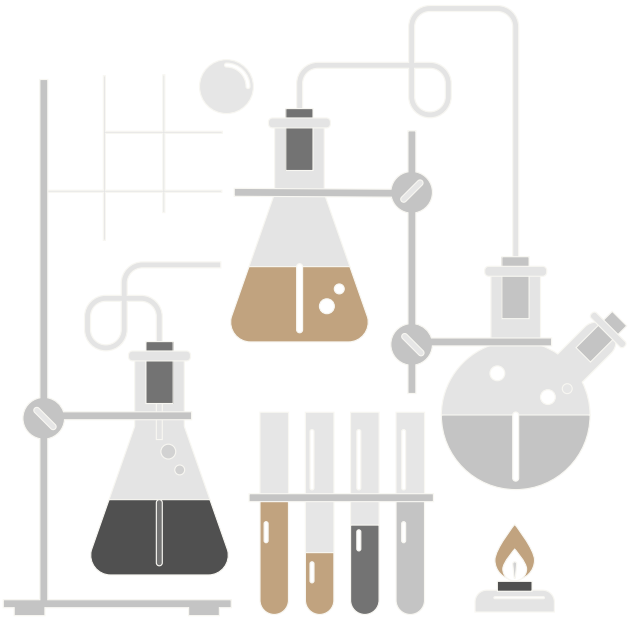

This chapter will describe the materials used during the different studies of this thesis and the techniques, methods, and protocols used throughout the work.

3.1 Materials

3.1.1 PFO

PFO was donated by the De Mello group and used without further purification. The polymer had a number-average molecular weight of $M_n =$ 13.04 kDa, and the polydispersity of $Đ = 2.03$, as determined by size exclusion chromatography in combination with multi-angle light scattering (SEC-MALS) and size exclusion chromatography calibrated with polystyrene (SEC-PS), respectively. Tetrahydrofuran (THF) was purchased from Sigma-Aldrich and used without further purification. PFO thin-films were prepared by depositing 20 μL from a 10 mg/mL solution of PFO in THF by spin-coating at 2,000 rpm for 60 s onto the FSC chip sensor.

3.1.2 PBTTT

PBTTT was obtained from 1−Materials without further purification. PBTTT had a molecular weight of $M_w = 65{,}000$ and a polydispersity of $Đ =$ 2.5, as determined by size exclusion chromatography in combination with multi-angle light scattering (SEC-MALS) and size exclusion chromatography calibrated with polystyrene (SEC-PS), respectively. Chlorobenzene (CB) was purchased from Sigma-Aldrich and used without further purification. Thin-films were deposited from 20 μL from 20 mg/mL solutions in CB at 90 ºC after 1 h of stirring at 1,000 rpm during 60 s via spin-coating of the sample onto a FSC sensor chip.

3.1.3 Polythioethers

DMDS-*alt*-DVE, DMDS-*alt*-TEGDVE and DMDS-*alt*-BDDVE are polythioethers based on the monomers 2,2'-dimercaptodiethyl sulfide (DMDS), di(ethylene glycol) divinyl ether (DVE), triethylene glycol divinyl ether (TEGDVE), and 1,4-butanediol divinyl ether (BDDVE), respectively. The polymers were synthesized and provided by Institut de Sciences des Matériaux de Mulhouse (IS2M), from the Université de Haute-Alsace, France.

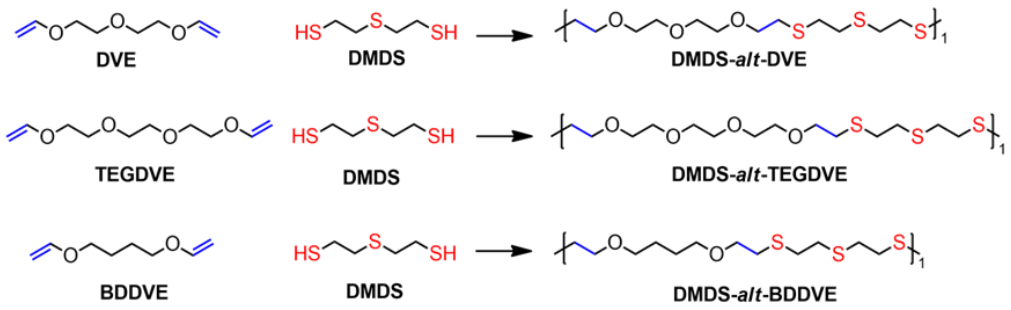

Figure 3.1 Chemical structures and reaction for the formation of polythioethers DMDS-*alt* DVE, DMDS-*alt*-TEGDVE and DMDS-*alt*-BDDVE.

The synthesis of these alternating copolymers was based on thiol-ene step-growth polymerization following the synthetic process they developed for the monomers DMDS and diallyl phthalate (DAP)[1]. This was performed between DMDS and diene monomers DVE, TEGDVE and BDDVE by Le *et al.*[1–4].

3.1.3.1 Synthesis of the Polythioethers

A mixture of 2,2'-dimercaptodiethyl sulfide (DMDS, 0.500 g, 3.2 mmol, 1 equiv.) and the diene monomer (diene, 0.516 g, 3.2 mmol) was added to a 20 mL soda-lime glass vial; with respect to the monomers, an aqueous phase containing a photo-catalyst (eosin disodium, 2 mg, 0.0026 mmol, 0.02% w/w monomer), a surfactant (sodium dodecyl sulfate (SDS), 35 mg, 3.5 wt%, 13.5

mM in water) and 9 mL of phosphate buffer 10 mM (pH = 8) was then added to the monomer mixture. To create an emulsion with an organic phase content of 10% w/w, a homogenizer (Ultra-Turrax, T25, IKA-Werke) was used to homogenize the mixture at 15,000 rpm for 10 min. Photopolymerization was initiated immediately after emulsification; the reaction was conducted at room temperature in a circular photochemical reactor with a green LED strip (530 nm, 3.0 $mW \cdot cm^{-2}$). The vial was continually stirred and irradiated using a magnetic stirrer (1,100 rpm) for 60 min. Table 3.1 provides information on the molar masses as reported by Elgoyhen et al.

Table 3.1. Molar masses of DMDS-*alt*-DVE, DMDS-*alt*-TEGDVE and DMDS-*alt*-BDDVE

Polythioether	M_n (g/mol)	M_w (g/mol)	Đ
DMDS-*alt*-DVE	9806	21871	2.23
DMDS-*alt*-TEGDVE	14145	32055	2.27
DMDS-*alt*-BDDVEa	17400b	-	-

[a] DMDS-*alt*-BDDVE it is not soluble neither in THF or DMF.
[b]Obtained from NMR measurements.

The molecular weight distribution of purified DMDS-*alt*-DVE was obtained by gel permeation chromatography (GPC) in N,N-dimethylformamide (DMF). The sample was prepared at 1.0 mg/mL and injected into a GPC (Agilent 1260 Infinity series with a set of three columns Polymer Laboratories ResiPore). A flow of eluent containing 10 mM lithium bromide was pumped at 0.9 mL/min through the columns controlled at 50 ºC. The system was calibrated using a set of narrow EasiVial poly(methyl methacrylate) standards. The M_w was calculated using Aligent SEC software.

3.2 Sample Preparation

The samples were deposited in the chip sensor by either one of two methods: spin-coating or bulk deposition.

1. **Bulk:** a small size of the sample (< 0.5 mm^2) is placed on the frontside of the chip sensor with the tip of hair.

2. **Spin-coating:** samples were prepared by (1) placing a drop of glucose solution on the reference part on the backside of the chip sensor and allowing it to solidify (2) the solution containing the sample is deposited by spin-coating between 10-20 µl of 20 mg/mL solutions of the sample at the desired spinning rate and time (the parameters used in this thesis vary for each material, however the standard parameters used are 2,000 rpm during 60s) (3) after the solution has been deposited onto the chip, the glucose dropped is removed carefully with distilled water (4) finally, the chip is allowed to dry before applying any thermal protocol. Figure 3.2 shows a scheme of the different steps.

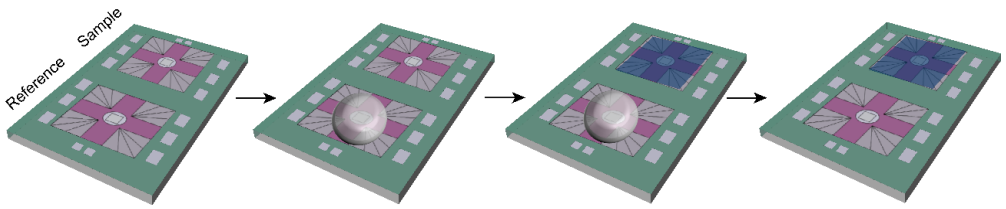

Figure 3.2 Thin-film deposition on an FSC sensor. A) Glucose deposition, B) Spin-coating of the sample C) Removing the glucose[5].

3.3 Thermal Characterization Techniques and Methods

These analytical methods are essential for understanding how temperature fluctuations influence the thermal behavior and properties of polymers. These techniques provide valuable information on various thermal transitions and properties of materials, including phase transitions such as the melting temperature (T_m), the glass transition temperature (T_g), the crystallization temperature (T_c), the cold crystallization temperature (T_{cc}), transitions between crystalline phases, degree of crystallinity, or the enthalpies associated with these thermal transitions. These analytical methods are essential for understanding how temperature fluctuations influence the thermal behavior and properties of polymers.

3.3.1 Differential Scanning Calorimetry (DSC)

Differential Scanning Calorimetry (DSC) measures the heat flow into or out of a sample as it is heated or cooled under controlled conditions. That is, the difference in heat capacity (C_p) of a sample and a reference is recorded as a function of temperature. In a typical DSC instrument, a sample and a reference material (typically an inert substance with known thermal properties) are placed in separate pans. These pans are subjected to controlled heating or cooling in a furnace. Two thermocouples control and measure the temperature difference between the sample and the reference, while a heat flow sensor monitors the heat flow variation between them[6,7].

The experiments were performed on a PerkinElmer DSC 8500 connected to an Intracooler III under a nitrogen atmosphere with 20 mL/min flow. The DSC 8500 was calibrated with indium and tin standards. The samples measured

were ca. 5 mg. The Pyris software was used to analyze the data.

3.3.1.1 DSC experimental protocols

(1) Heating/cooling ramps: during non-isothermal experiments, the rates used for this technique can vary between 1 ºC/min and 60 ºC/min. However, unless specified the samples were heated and cooled at 20 ºC/min (0.33 ºC/s). First, the samples were heated from 25 ºC to a T_m + 30 ºC to ensure erasing thermal history for 3 min, then cooled to a temperature below the glass transition temperature (T_g) and subsequently heated to T_m + 30 ºC.

(2) Isothermal experiments: for isothermal crystallization experiments, first, the study requires determining the minimum isothermal crystallization temperature ($T_{c,min}$). $T_{c,min}$ is the minimum temperature for which no melting peak is observed in the latter heating scan, attesting that no crystals were formed during the cooling scan to T_c. Having determined the $T_{c,min}$, the sample is heated to its molten state (T_m + 30 ºC) and kept there for 3 min to erase thermal history. Then, the sample is rapidly cooled down to a range of crystallization temperatures T_c with $T_c \geq T_{c,min}$, and kept at this temperature until saturation. Finally, the sample is heated to T_m + 30 ºC.

3.3.2 Fast Scanning Calorimetry (FSC)

Conventional DSC is widely used as a standard method for obtaining information on the thermal transitions occurring within a sample. However, the cooling and heating rates in these devices are limited to 1 ºC/min to 60 ºC/min,

and often do not allow for the study of other reorganization processes of some semicrystalline polymers. For this reason, a new type of DSC, known as fast scanning calorimetry (FSC), often referred to as Flash DSC, was created to allow for ultra-high cooling and ultra-high heating. It allows us to study both crystallization and reorganization processes that may occur during heating[8–10].

FSC Experiments were performed on a Mettler-Toledo Flash DSC 2+ device. The equipment is connected to a Huber TC-100 intracooler, permitting scans of up to 40,000 ºC/s. The MultiSTAR UFS1 (24×24×0.6 mm^3) chip sensors were conditioned and corrected prior to use according to the Flash DSC 2+ specifications. FSC measures a microchip embedded in a ceramic support. The chip contains a squared shaped sample sensor and a reference sensor made of silicon nitride membranes. These are equipped with 16 thermocouples distributed uniformly along the ceramic plate. Measurements were carried out under a nitrogen atmosphere, with a constant flow rate of 80 mL/min. The STARe software was used to analyze the data. The thermal protocols essentially consisted in recording heat flow rates during the heating, cooling, or isothermal steps as a function of temperature.

In general, throughout this thesis, we have employed three different isothermal step protocols and one non-isothermal protocol that were key to thoroughly characterize thermotropic behavior of different materials and to study their crystallization kinetics. As stated above, the FSC technique allows for very fast heating and cooling rates; hence, the thermal quenching of different phases of the materials could be isolated for their study. More complex protocols will be discussed and described in the corresponding chapters. Nevertheless, the general protocols designed and implemented are described here in detail and can be found in Figure 3.3.

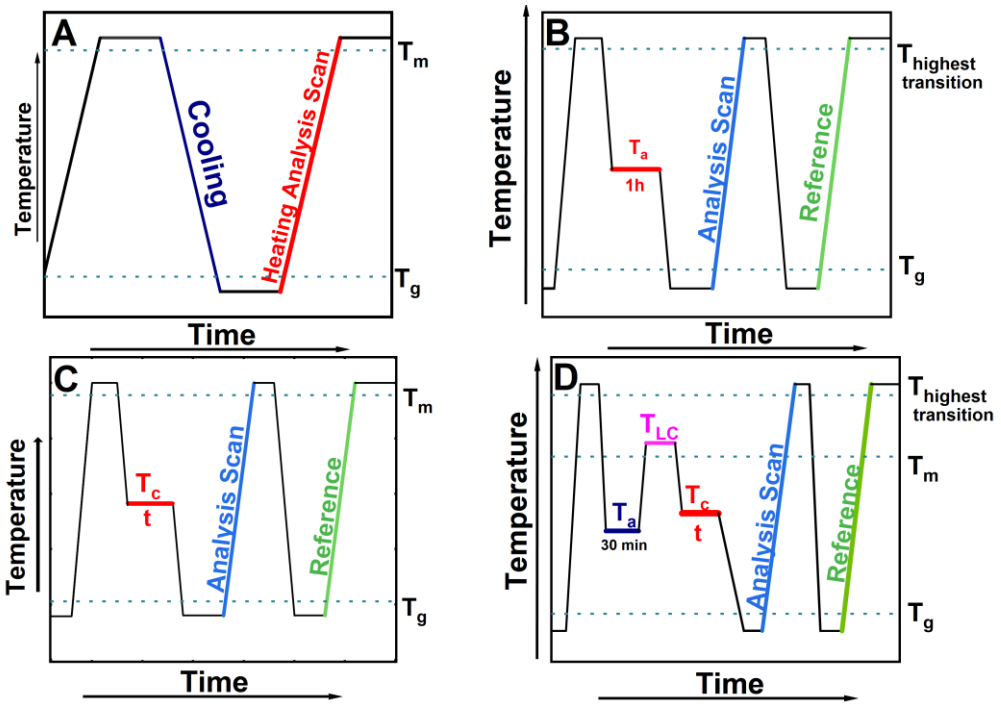

Figure 3.3. Thermal protocols in FSC. A) Non-isothermal B) Isothermal protocol for 1 h C) Isothermal protocol from an isotropic state D) Isothermal protocol from a liquid crystalline state.

(1) **Heating/cooling ramps:** non-isothermal crystallization experiments performed at various cooling rates from 1 ºC/s to 40,000 ºC/s and, unless otherwise specified at a constant heating rate of 1,000 ºC/s. The sample is heated from a temperature below T_g, typically −80 ºC, to a T_m + 30 ºC to erase any thermal history, then cooled to a temperature below T_g and heated again to temperatures well above T_m (see Figure 3.3A).

(2) **Isochronous experiments**: the samples were first heated well above the highest-temperature transition for 1 s to erase any previous thermal history while avoiding thermal degradation of the material. Then, the material was rapidly cooled to a range of isothermal

temperatures (T_a) and held at those $T_a s$ for 1h. During this time, the material had time to undergo the physical process that is relevant at that temperature. Subsequently, the material was cooled to a temperature well below T_g. From there, a heating scan was recorded up to a temperature above the highest-temperature transition. In some cases, the material is cooled to a temperature below T_g and a second heating scan was recorded which will serve as a reference scan. The heating and cooling rates vary according to the material, for this, the rates used are specified for each material in the corresponding chapters (see Figure 3.3B).

(3) Isothermal experiments: From an isotropic/melt state, the samples were first heated well above the highest-temperature transition to erase the thermal history for a short amount of time of 1s to avoid degradation. Then, samples are rapidly cooled down (at 4,000 ºC/s, unless otherwise specified) to the selected T_a where it is kept for a variable amount of time so that crystallization progresses. Samples are then rapidly cooled down to a temperature below T_g (at 4,000 ºC/s, unless otherwise specified), and lastly, they are heated to well above the highest-temperature transition (see Figure 3.3C). The endothermic peak appearing in this heating scan accounts for the melting of crystals formed during the isothermal step; hence, the enthalpy of this melting process can be employed to follow the isothermal crystallization kinetics. It is customary to assume that the values of melting enthalpy (measured under non-isothermal conditions, *i.e.*, during the heating scans after isothermal crystallization) are identical to the values of the crystallization enthalpy developed under isothermal conditions.

From a semi-ordered state, for those polymers exhibiting liquid crystalline phases (*i.e.*, PBTTT and PFO), a protocol was designed to follow the crystallization kinetics from this semi-ordered state while reducing the possibility of degradation of the sample by including a first step in which the mesophase is created. For this reason, the first step was to heat the material well above the highest temperature transition to erase the thermal history for a short amount of time of 1s to avoid degradation. Then, samples are rapidly cooled down (at 4,000 ºC/s, unless otherwise specified) to a selected T_a where it is kept for 30 min, the material is then rapidly heated to a temperature in which the mesophase is developed and kept there for 1 min. Then, the sample is cooled to the desired T_c and kept there for a variable amount of time. Finally, the sample is cooled rapidly below T_g and subsequently heated above the highest-transition temperature (see Figure 3.3D).

3.3.3 Differential Scanning Microcalorimetry (μ-DSC)

The measurements were conducted using a Setaram micro-DSC (Micro-Calvet) connected to an Intracooler III under a nitrogen atmosphere with 20 mL/min flow. The samples measured weighted ca. 10 mg. The relevant temperatures to consider are the crystallization temperature (T_c), the melting point (T_m) and the glass transition temperature (T_g).

3.3.3.1 μ-DSC protocols

(1) Heating/cooling ramps: the samples were heated and cooled at a rate of 0.2 ºC/min (0.0033 ºC/s). Samples were heated from 25 ºC to T_m + 30 ºC to ensure erasing thermal history for 3 min, then cooled to a temperature below T_g and subsequently heated to T_m + 30 ºC

3.3.4 Polarized Light Optical Microscopy (PLOM)

Polarized light optical microscopy (PLOM) is a powerful technique used to study anisotropic materials and their optical properties. The PLOM uses polarizers, which are filters that selectively allow light oscillating in a specific direction to pass through while blocking light with other orientations. Anisotropic materials are those whose optical properties vary depending on the direction in which light interacts with them. These materials often exhibit birefringence, which means they can split light into two separate rays, each with a different refractive index. Thermally induced phase transitions and crystallization kinetics of different materials were evaluated by PLOM.

Experiments were performed on a polarized light optical microscope, Olympus BX51 (Olympus, Tokyo, Japan), with an Olympus SC50 digital camera coupled to the microscope. The PLOM was equipped with a Linkam-15 TP-91 hot stage Linkam, Tadworth, U.K, connected to a liquid nitrogen cooling system that was used to observe the morphology of the sample.

(1) **Heating/cooling ramps:** during non-isothermal experiments, the rates used for this technique can vary between 1 ºC/min and 50 ºC/min. However, unless specified the samples were heated and cooled at 20 ºC/min (0.33 ºC/s). Samples were prepared by heating a small fraction of the polymer powder from 25 ºC to a T_m + 30 ºC to ensure erasing thermal history for 3 min, then cooled to a temperature below the glass transition temperature (T_g) and subsequently heated to T_m + 30 ºC.

(2) **Isothermal experiments:** samples were prepared by heating a small fraction of the polymer powder from 25 ºC to a T_m + 30 ºC to ensure erasing thermal history for 3 min, then cooled to the desired

crystallization temperature (T_c) at 50 ºC/min and allowed the polymer to crystallize at that temperature until saturation and subsequently heated to T_m + 30 ºC at 20 ºC/min. Films of around 10 μm thickness were prepared by melting the sample between two glass slides.

3.4 X-ray techniques and Synchrotron light sources

The complex structure of materials is often resolved with a combination of imaging techniques and scattering X-ray techniques. The most common for the detection of bulk structures in the molecular scale is wide angle x-ray scattering (WAXS) in transmission geometry. Additionally, due to the different applications requiring thin-films (*e.g.,* semiconducting polymers), a rise in interest for techniques able to study those conditions has occurred; the use of more conventional techniques such as WAXS is less suitable as the sample volume is significantly reduced. To overcome this, grazing incidence wide angle X-ray scattering (GIWAXS) is one of the techniques used for the structure determination in thin-films using synchrotron radiation.

In this thesis, some of the experiments have been carried out in synchrotron facilities from Elettra (Triestre), HZB (Berlin) and ALBA (Barcelona). Here a general overview of the basics of the Synchrotron will be given. However, we refer the reader to the following sources for a deeper understanding[11,12].

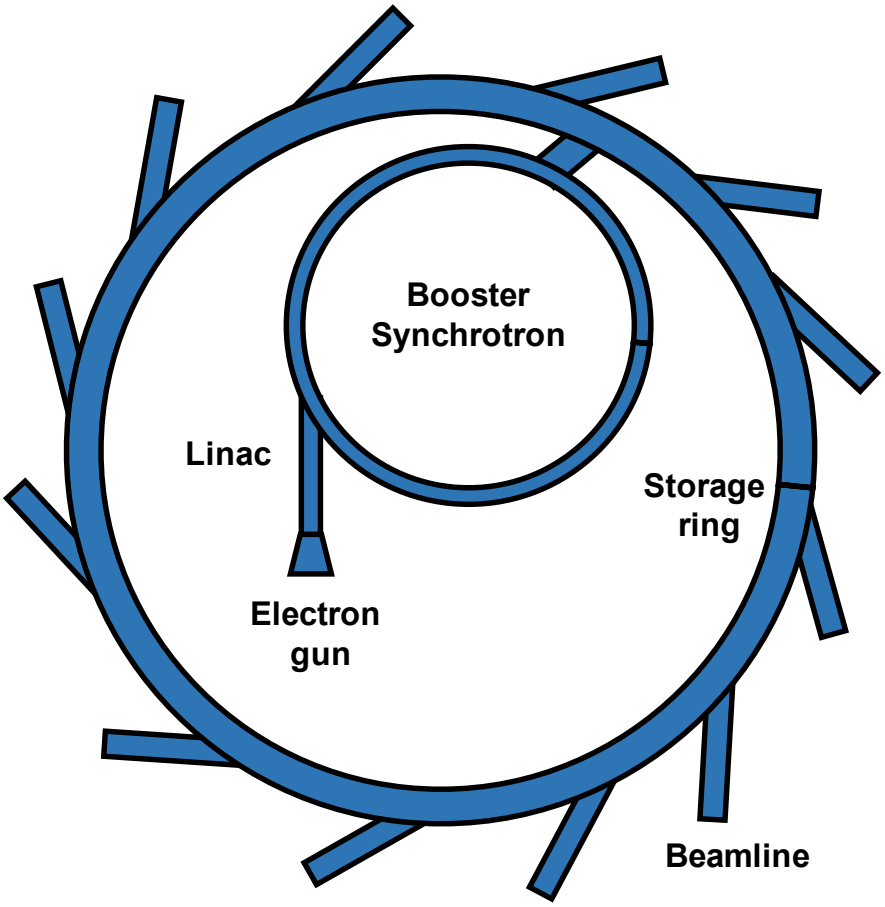

Figure 3.4. View of the main parts of a synchrotron radiation facility.

Figure 3.4 shows a scheme with the main parts of a synchrotron facility; the light generated in the synchrotron is radiated by electrons moving close to light speed inside the storage ring which are generated inside what is referred to as the electron gun by heating a metal (typically tungsten coated of barium oxide). After electron generation, these are accelerated in a linear accelerator ("Linac") and then injected into the booster synchrotron in which they are further accelerated and injected into the storage ring with the aid of magnets. Finally, the beamlines are the spaces in which the users will be able to place their samples and conduct their experiments. The beam is channeled through monochromators, mirrors and slits to obtain the desired wavelength[11–13].

3.4.1 Wide Angle X-ray Scattering (WAXS)

Light waves interact with matter in different ways. In crystalline structures, when the incident beam interacts with the regularly spaced atoms the wave will be scattered in different directions due to interference effects[14]. That is, scattering refers to wave interactions with atoms in which the scattered wave is redirected in many directions. Additionally, the scattering vector (q) represents the difference between the incident wave and the scattering wave which form an 2θ angle, also known as the scattering angle. The relation between the scattering vector, q, and the scattering angle, 2θ, can be found below in Equation 3.1.

$$q = \frac{4\pi}{\lambda} sin\theta \qquad \text{Equation 3.1}$$

Bragg's Law[15] was formulated by the physicist Sir W.H. Bragg and his son Sir W.L. Bragg in 1913, this law states the relation between the incident angle of the X-rays, the spacing between the crystal lattice planes and the direction of the scattering vector (see Equation 3.2)[13,15–17].

$$n\lambda = 2d \sin\theta \qquad \text{Equation 3.2}$$

where d is the distance between the crystal planes (interplanar spacing), 2θ is the angle formed between the incident and scattered wave, λ is the wavelength, and n denotes the reflection order (an integer number). Hence, a correlation between the crystal plane distances and the scattering vector can be found below Equation 3.3.

$$q = \frac{2\pi}{d} \qquad \text{Equation 3.3}$$

Wide angle X-ray scattering (WAXS) is an x-ray technique that as mentioned above is often used to determine the crystalline structure of different materials such as polymeric materials; the short sample to detector distance allows access to high resolution information in the 5–10 Å spatial range. One thing to note from these experiments is that the samples are often powders measured in aluminum pans. However, in this thesis, experiments on FSC sensor chips were also carried out with this technique. Figure 3.5 shows a schematic representation of an X-ray diffraction experiment where the sample is irradiated with the beam and the scattered light gives rise to a scattering pattern.

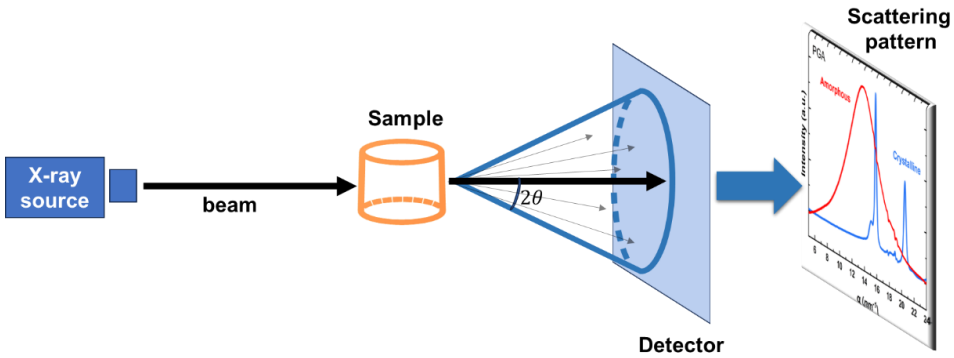

Figure 3.5. Schematic representation of and X-ray diffraction experiment.

As mentioned above, the crystalline materials will diffract the beam at a specific angles related to the distances between crystalline planes resulting in different scattering peaks often referred to as Bragg peaks. In contrast, amorphous materials will behave differently to crystalline materials and instead of defined peaks with varying intensity and width they will show a single broad scattering maximum, often referred to as “amorphous halo”. Figure 3.6 shows an example of a crystalline pattern and an amorphous pattern.

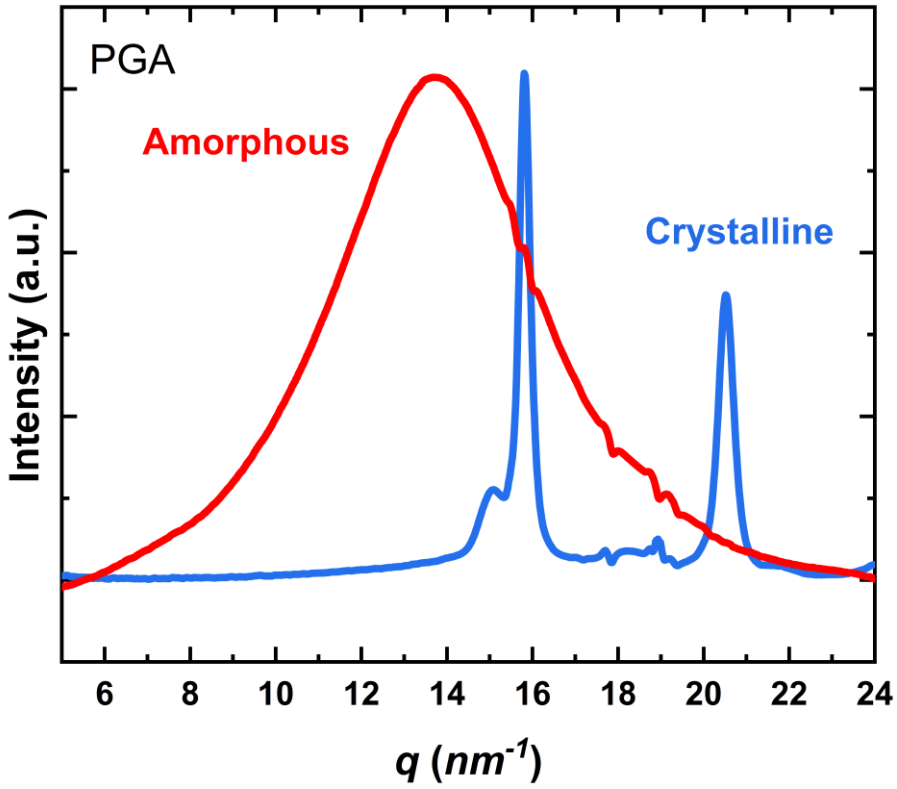

Figure 3.6 Scattering profiles material PGA as an example of an amorphous pattern (red) and a crystalline pattern (blue).

Some experiments in this thesis were carried out *in-situ* at ALBA Synchrotron Radiation Facility (Barcelona, Spain) at the beamline BL11 NCD-SWEET. DSC pans were employed to place samples in the beam path. A THMS 600 Linkam hot stage device was employed to first heat the samples from room temperature to the melt at 20 ºC/min and then from the melt to room temperature at the same rate, while data was been collected. The X-ray energy source amounted to 12.4 eV using a channel cut Si (1 1 1) monochromator (λ = 1.03 Å). The sample-detector distance was 132.6 mm with a 21.2° tilt angle, and chromium(III) oxide was employed to do the calibration. Rayonix LX255-HS detector, Evanston, IL, USA, with a resolution of 1920 × 5760 pixels and pixel size of 44 m^2 was employed.

In some of the experiments a synchrotron facility was not used, instead experiments were performed using a D500 X-ray powder diffractometer (Siemens, Germany) in reflection mode ($\theta-2\theta$ scans) with a Cu-Kα radiation source ($\lambda = 1.54$ Å) and a scintillation counter at an angular resolution slightly better than 0.1°. The diffractometer was equipped with an evacuated temperature-controlled TTK sample chamber (Paar, Austria). To achieve sub-ambient temperature ranges, the chamber was connected to a liquid nitrogen reservoir. The polymer powder scattered isotropically and was deposited on an aluminum plate (fabricated in the lab) and placed on a brass block. The temperature was varied by resistive heating through controlling the current. The temperature was measured by a thermometer at the bottom of the heated brass block. This temperature was calibrated to the sample temperature by measuring the actual temperature at the surface of the polymer samples in a control experiment using an external thermocouple (Mini Dual K/J Thermometer, Uni-T, Munich, Germany). Data points of the XRD patterns obtained from the polymers were collected over a range of the scattering angle between the incident beams and diffracted beam (2θ) from ≈ 1.8 ° to 30 ° at steps ($\Delta 2\theta$) of 0.04 °, each measured for 10 s. Changes in position and intensity of peaks of the diffracted X-rays were measured upon crystallization and melting of the polymers.

3.4.2 Grazing Incidence Wide Angle X-ray Scattering (GIWAXS)

Other experiments carried out in this thesis were grazing incidence wide angle X-ray scattering (GIWAXS). This technique mainly differs from WAXS in the fact that the samples measured here are deposited over rigid substrates (*e.g.*, glass or silicon wafers) as thin-films and not in bulk. More importantly, they differ in the geometry used; WAXS experiments are carried out in

transmission geometry contrary to GIWAXS where the x-ray beam reaches the sample at an incident angle, often between 0.12º and 0.4º from the substrate plane. These angles ensure that the beam can penetrate the thin-film sample but not the substrate is deposited on. Therefore, the X-ray beam is somehow confined in the plane of the sample, hence maximizing the scattering signal[17–20]. Below Figure 3.7 shows a schematic illustration of the GIWAXS geometry where α_i is the incident angle, *i.e.*, and the angle between the incident X-ray beam and the substrate plane of the sample and α_f is the exit angle[20,21].

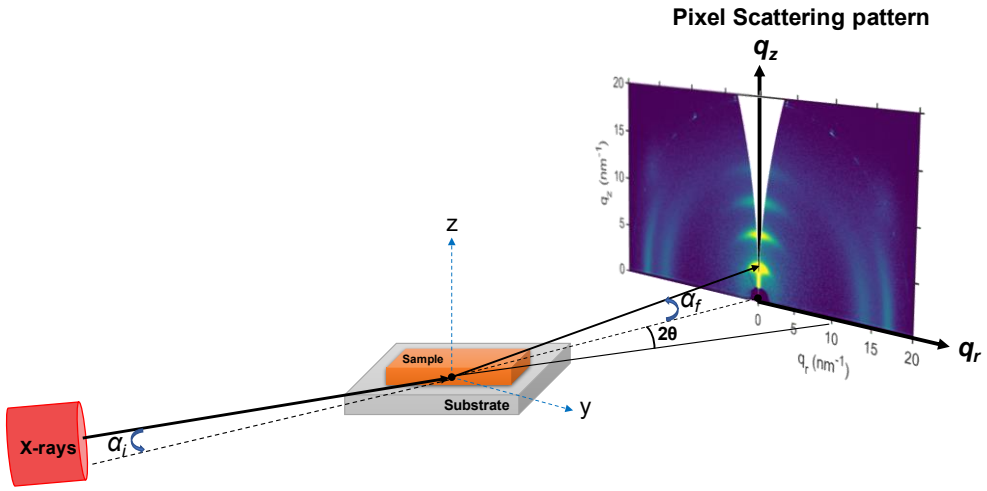

Figure 3.7. Schematic representation of the GIWAXS geometry.

GIWAXS measurements were performed at the BL11 NCD-SWEET at ALBA Synchrotron Radiation Facility (Barcelona, Spain). The incident X-ray beam energy was set to 12.4 eV using a channel cut Si (1 1 1) monochromator. 2D GIWAXS patterns were corrected as a function of the components of the scattering vector (q). 2D GIWAXS patterns were corrected as a function of the components of the scattering vector. The angle of incidence α_i was set between 0.1º and 0.2º to ensure surface sensitivity. Data are expressed as a function of the scattering vector, which was calibrated using Cr_2O_3, obtaining a sample-to-detector distance of 145.6 mm. The scattering patterns were recorded using a

Rayonix LX255-HS area detector, which consists of a pixel array of 1920 × 5760 pixels (H × V) with a pixel size of 44 × 44 μm^2. All the measurements were performed under N_2 atmosphere to minimize the damage of the films.

3.5 Atomic Force Microscopy (AFM)

Atomic Force Microscopy (AFM) is a powerful technique that allows the study of the morphological features of samples at the nanoscale. The technique consists on scanning the surface of a substrate with an AFM tip, this tip interacts with the surface via different forces (*e.g.,* Van der Waals) and retracts or lowers the tip according to the information received which is then translated by the software into a map of the height surface. This data can be used to identify different morphological features from spherulites, rods to terrace phases[22–24].

Measurements in Chapter 4 and Chapter 5 carried out in a dimension ICON with a Nanoscope V controller (Bruker) in a Peak-Force Tapping mode using ScanAsyst-Air tips by Bruker (nominal tip radius of 2 nm, nominal frequency of 70 kHz, nominal spring constant = 0.4 N/m) was used to obtain the images. The thin-films were deposited from a 10−20 mg/mL solution on the back side of the chip with a glucose cover on the reference cell, which was removed after deposition with water. The sample was heated above the highest transition and after melting it was rapidly cooled (at 4,000 ºC/s) to the annealing temperature (T_a). Subsequently, the sample was kept at T_a for 10h (the time it reaches maximum saturation), it was rapidly cooled to a temperature below the glassy state, T_g, and rapidly heated to room temperature and then measured by AFM.

Some measurements in this thesis, in Chapter 7, were conducted in collaboration with the CSIC Institute (Madrid,Spain), using a μTA 2990 Micro-Thermal Analyzer. Topography images were acquired in contact mode with a

current set point of − 5 nA. A feedback loop was employed to maintain constant cantilever deflection, which regulated the cantilever deflection to the chosen set point value during scanning. This was achieved by applying a constant voltage (50 V) to the Z-piezo. V-shaped silicon nitride probes (obtained from Applied NanoStructures, Inc., Mountain View, CA, U.S.A.), featuring a cantilever length of 200 μm and a spring constant of 0.046 $N \cdot m^{-1}$, were utilized. Scanning rates varied between 10 and 100 $\mu m \cdot s^{1}$ depending on the size of the images (ranging from 10 to 100 μm^2). Image processing was performed using the μTALab 1.01 and Gwyddion software packages. To correct for any tilting effects in height values, software levelling functions were applied. This involved fitting a surface to the observed topography and subsequently subtracting the height values of the fitted surface pixel by pixel from those of the initial image. For this study, a first-order plane was employed. Samples for observation were prepared by spin coating 20 μL of 5 mg/mL solutions of the copolymers in chloroform at 1,000 rpm for 60 seconds. Observations have been performed on samples crystallized in different conditions: (i) after cooling to room temperature and after heating to a preselected T_c that depended on the sample.

3.6 Computational methods: Simulation and analysis protocol

The field of computational simulations has become as important as theory and experiment. In this thesis, in Chapter 7 some simulations were conducted in collaboration with the CSIC Institute (Madrid,Spain).

3.6.1 Models and molecular dynamics parameters

The simulation setup involves 60 chains, each comprising ten polymer

monomers that are capped with terminal methyl groups (Figure 3.8). Initial topologies and structures for the molecular dynamics (MD) simulations were generated using Polyply software[25] at a density of 0.750 g/cm³. To eliminate surface effects and emulate the bulk state, periodic boundary conditions (PBC) were applied in all three directions. Subsequently, the simulation boxes underwent minimization with a fixed box length.

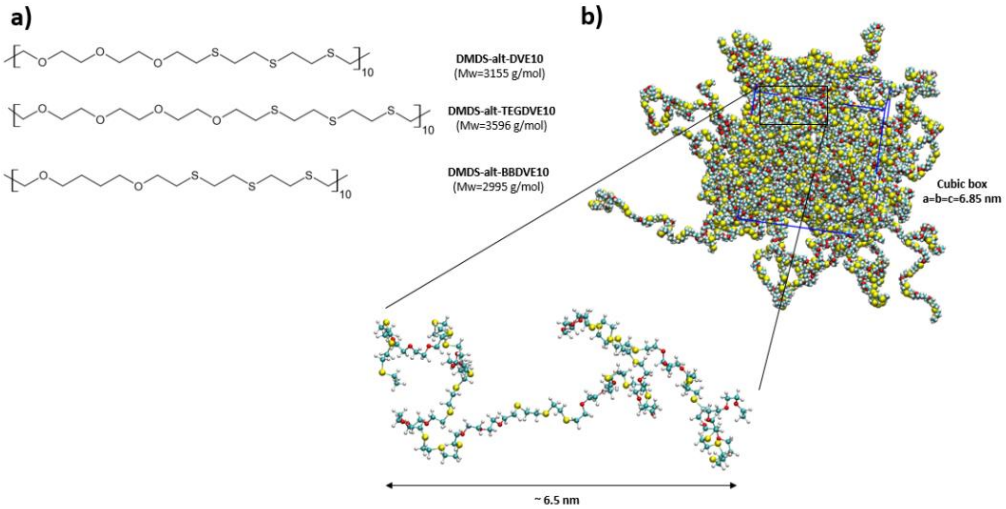

Figure 3.8. A) Chemical structures of the polymer models used in the molecular dynamic simulations. B) Simulation box of the equilibrated system DMDS-*alt*-DVE at 500 K (227 ºC), including a detailed chain representation. H, C, O and S atoms are indicated by white, gray, red and yellow colors, respectively. The simulation box comprises a total of 25680 atoms.

Further equilibration was conducted through 10 nanoseconds (ns) of NPT-MD runs at 550 K (277 ºC) and 1 bar, employing a time step of 1 femtosecond (fs). During the equilibration period, temperature coupling utilized the velocity-rescaling method ($\tau_T = 2$ ps), and the Berendsen barostat ($\tau_p = 2$ ps and compressibility = 4.5 x 10^{-5} bar^{-1}) was applied. This simulation duration proved sufficient for achieving system density equilibrium.

After equilibration, production NPT-MD simulations were extended to 1,000 ns (1 µs) at different temperatures (350, 400, 450, and 500 K). The bonds with hydrogen atoms were constrained using LINCS, resulting in a 2 fs time step. During production simulations, the C-rescale barostat ($\tau_p = 5$ ps) was employed, as the Berendsen barostat is known not to yield a correct thermodynamic ensemble. Short-range non-bonded interactions were truncated at a 1.2 nm cutoff using Verlet neighbor lists, and the particle mesh Ewald (PME) method was utilized for the treatment of long-range electrostatic interactions. Both energy and pressure dispersion corrections were applied.

All minimizations and molecular dynamics (MD) simulations were conducted using the GROMACS 2023 package[26], compiled for GPUs.

3.6.2 Force field

The Multiwfn[27] and Q-Force[28] toolkits were employed to parametrize the electrostatic atomistic charge (see in the following section) and bonded term (bonds, angles and dihedrals), see Figure 8.6 and Figure 8.7 in Appendix 2, located in Chapter 8) parametrization of the polymers, respectively. These toolkits facilitate the automated derivation of force field parameters through quantum mechanical calculations. The OPLS-AA force field served as base. To validate the *ad-hoc* force field, a specific force field for polyethylene(oxide) was developed using the same methodology, giving the absence of experimental information for polythioethers (see Figure 8.8 in Appendix 2, located in Chapter 8).

3.7 Photoluminescence (PL)

Photoluminescence is the emission of light by a material after being excited with light. It occurs when an electron returns to the ground state from

an electronic excited state, and the excess of energy is emitted in the form of a photon of lower energy. This phenomenon is often observed in certain materials like semiconductors, phosphors, and fluorescent dyes and can be used for applications such as opto-electronic devices.

In this thesis, the spectra are measured using a Witec equipment. We excited through a UV high transmission 40x objective using a solid-state laser with a peak wavelength at 355 nm, with a power of 60 µW. We made 500 µm x 500 µm images of the samples directly on the flash-DSC chips. We took a total of 2500 spectra per sample. Cluster analysis of the data revealed three different regions for each chip: (i) the inner part, likely very thick as deduced from the apparent self-absorption features in the spectra; (ii) the region above the heating resistance; (iii) the border between both. The data shown in the manuscript corresponds to the material fraction just over the resistances. Thin-films deposited from a 10 mg/mL solution on the back side of the chip with a glucose cover, after deposition, the drop was eliminated with water. The sample was heated above the highest transition to erase the thermal history, then rapidly cooled (at 4,000 ºC/s) from the melt to the selected isothermal crystallization temperature. Subsequently, the sample was kept at T_a for 10h (the time it reaches maximum saturation), and it was rapidly cooled to a temperature below T_g and rapidly heated to room temperature.

3.8 References for Chapter 3

(1) Le, C. M. Q.; Vidal, L.; Schmutz, M.; Chemtob, A. Droplet Nucleation in Miniemulsion Thiol–Ene Step Photopolymerization. *Polym Chem* **2021**, *12* (14), 2084–2094.

(2) Pirela, V.; Elgoyhen, J.; Tomovska, R.; Martín, J.; Le, C. M. Q.; Chemtob, A.; Bessif, B.; Heck, B.; Reiter, G.; Müller, A. J. Unraveling the Complex Polymorphic Crystallization Behavior of the Alternating Copolymer DMDS-Alt-DVE. *ACS Appl. Polym. Mater.* **2023**, *5* (7), 5260–5269.

(3) Bessif, B.; Heck, B.; Pfohl, T.; Minh, C.; Le, Q.; Chemtob, A.; Pirela, V.; Elgoyhen, J.; Tomovska, R.; Müller, A. J.; Reiter, G. Nucleation Assisted through the Memory of a Polymer Melt: A Different Polymorph Emerging from the Melt of Another One. *Macromolecules* **2023**, *56* (4), 1461–1470.

(4) Le, C. M. Q.; Schrodj, G.; Ndao, I.; Bessif, B.; Heck, B.; Pfohl, T.; Reiter, G.; Elgoyhen, J.; Tomovska, R.; Chemtob, A. Semi-Crystalline Poly(Thioether) Prepared by Visible-Light-Induced Organocatalyzed Thiol-Ene Polymerization in Emulsion. *Macromol Rapid Commun* **2022**, *43* (5), 2100740.

(5) Marina, S. Interplay between Microstructure/Morphology and the Opto-Electronic Properties of Materials for Organic Photovoltaics, EHU/UPV, 2021. https://www.ehu.eus/en/web/doktoregoa/-/tesis-marina-barbier-sara-luisa (accessed 2024-02-19).

(6) Höhne, G. W. H.; Hemminger, W. F.; Flammersheim, H.-J. *Differential Scanning Calorimetry*, 2nd ed.; Springer Berlin Heidelberg: Berlin, Heidelberg, 2003.

(7) *The Handbook of Differential Scanning Calorimetry*, 1st ed.; Joseph D. Menczel, Janusz Grebowicz, Eds.; Elsevier - Health Sciences Division, 2023.

(8) Mathot, V.; Pyda, M.; Pijpers, T.; Vanden Poel, G.; Van De Kerkhof, E.; Van Herwaarden, S.; Van Herwaarden, F.; Leenaers, A. The Flash DSC 1, a Power Compensation Twin-Type, Chip-Based Fast Scanning Calorimeter (FSC): First Findings on Polymers. *Thermochim. Acta* **2011**, *522* (1–2), 36–45.

(9) Schick, C.; Mathot, V. *Fast Scanning Calorimetry*; Schick, C., Mathot, V., Eds.; Springer Cham, 2016.

(10) Schick, C.; Androsch, R. New Insights into Polymer Crystallization by Fast Scanning Chip Calorimetry. In *Fast Scanning Calorimetry*; 2016; Vol. 91, pp 463–535.

(11) *Synchrotron Radiation Science and Applications*; Di Cicco, A., Giuli, G., Trapananti, A., Eds.; Springer Proceedings in Physics; Springer International Publishing: Cham, 2021; Vol. 220.

(12) Willmott, P. *An Introduction to Synchrotron Radiation: Techniques and Applications*; John Wiley & Sons, 2019.

(13) Roe, R.-J. X-Ray Diffraction by Polymers. *Encycl. Polym. Sci. Technol.* **2015**, 1–47.

(14) Cebe, P. *Scattering from Polymers: Characterization by X-Rays, Neutrons, and Light*; American Chemical Society, 2000.

(15) Cullity, B. D.; Stock, S. R. *Elements of X-Ray Diffraction, Third Edition*; Prentice-Hall: New York, 2001.

(16) Als-Nielsen, J.; McMorrow, D. *Elements of Modern X-Ray Physics*; John Wiley & Sons, Ltd, 2011.

(17) Chabinyc, M. L. X-Ray Scattering from Films of Semiconducting Polymers. *Polym. Rev.* **2008**, *48* (3), 463–492.

(18) Juraić, K.; Gracin, D.; Šantić, B.; Meljanac, D.; Zorić, N.; Gajović, A.; Dubček, P.; Bernstorff, S.; Čeh, M. GISAXS and GIWAXS Analysis of Amorphous-Nanocrystalline Silicon Thin Films. *Nucl. Instrum. Methods Phys. Res. Sect. B Beam Interact. Mater. At.* **2010**, *268* (3–4), 259–262.

(19) Manley, E. F.; Strzalka, J.; Fauvell, T. J.; Jackson, N. E.; Leonardi, M. J.; Eastham, N. D.; Marks, T. J.; Chen, L. X. In Situ GIWAXS Analysis of Solvent and Additive Effects on PTB7 Thin Film Microstructure Evolution during Spin Coating. *Adv. Mater.* **2017**, *29* (43), 1–9.

(20) Perlich, J.; Rubeck, J.; Botta, S.; Gehrke, R.; Roth, S. V.; Ruderer, M. A.; Prams, S. M.; Rawolle, M.; Zhong, Q.; Körstgens, V.; Müller-Buschbaum, P. Grazing Incidence Wide Angle X-Ray Scattering at the Wiggler Beamline BW4 of HASYLAB. *Rev. Sci. Instrum.* **2010**, *81* (10), 105105.

(21) Mahmood, A.; Wang, J. L. A Review of Grazing Incidence Small- and Wide-Angle X-Ray Scattering Techniques for Exploring the Film Morphology of Organic Solar Cells. *Sol. RRL* **2020**, *4* (10).

(22) Wu, X.; Shi, S.; Yu, Z.; Russell, T. P.; Wang, D. AFM Nanomechanical Mapping and Nanothermal Analysis Reveal Enhanced Crystallization at the Surface of a Semicrystalline Polymer. *Polymer* **2018**, *146* (6), 188–195.

(23) Voigtländer, B. *Atomic Force Microscopy*; NanoScience and Technology;

Springer International Publishing: Cham, 2019.

(24) Zhang, L.; Zhao, K.; Li, H.; Zhang, T.; Liu, D.; Han, Y. Liquid Crystal Ordering on Conjugated Polymers Film Morphology for High Performance. *J. Polym. Sci. Part B Polym. Phys.* **2019**, *57* (23), 1572–1591.

(25) Grünewald, F.; Alessandri, R.; Kroon, P. C.; Monticelli, L.; Souza, P. C. T.; Marrink, S. J. Polyply; a Python Suite for Facilitating Simulations of Macromolecules and Nanomaterials. *Nat. Commun.* **2022**, *13* (1), 68.

(26) Abraham, M. J.; Murtola, T.; Schulz, R.; Páll, S.; Smith, J. C.; Hess, B.; Lindahl, E. GROMACS: High Performance Molecular Simulations through Multi-Level Parallelism from Laptops to Supercomputers. *SoftwareX* **2015**, *1–2*, 19–25.

(27) Lu, T.; Chen, F. Multiwfn: A Multifunctional Wavefunction Analyzer. *J. Comput. Chem.* **2012**, *33* (5), 580–592.

(28) Sami, S.; Menger, M. F. S. J.; Faraji, S.; Broer, R.; Havenith, R. W. A. Q-Force: Quantum Mechanically Augmented Molecular Force Fields. *J. Chem. Theory Comput.* **2021**, *17* (8), 4946–4960.

Chapter 4

Influence of preexisting molecular order on the crystallization of semiconducting poly(9,9-di-n-octylfluorenyl-2,7-diyl (PFO)

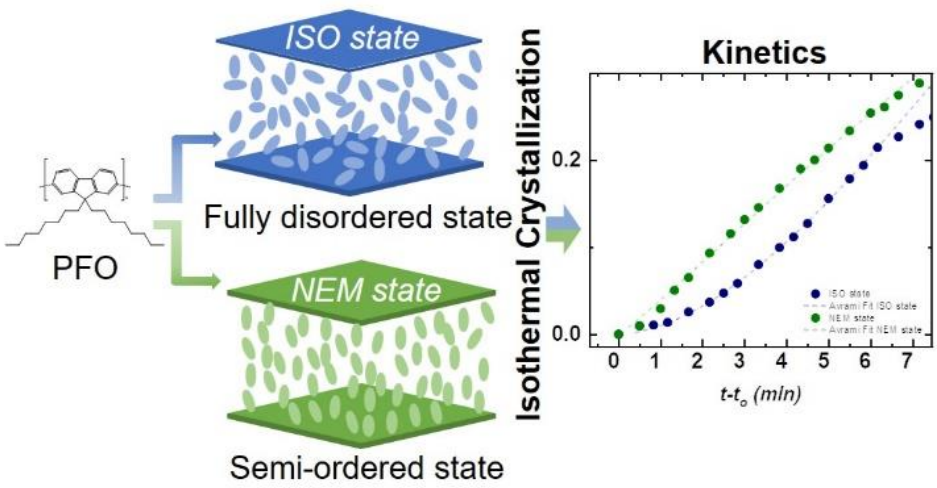

4.1 Abstract

Understanding the complex crystallization process of semiconducting polymers is vital for advancing organic electronic technologies, as the optoelectronic properties of these materials are intimately connected to their solid-state microstructure. These polymers often have semi-rigid backbones and flexible side chains, which results in a strong tendency to organize/order in the liquid state. Therefore, crystallization of these materials frequently occurs from liquid states that exhibit — at least partial — molecular order. However, the impact of preexisting molecular order on the crystallization process of semiconducting polymers — indeed, of any polymer — remained hitherto unknown. This study uses fast scanning calorimetry (FSC) to probe the crystallization kinetics of poly(9,9-di-n-octylfluorenyl-2,7-diyl (PFO) from both an isotropic disordered melt state ($ISO\ state$) and a liquid crystalline ordered state ($NEM\ state$). Our results demonstrate that preexisting molecular order profoundly impacts the crystallization of PFO. More specifically, it favors the formation of effective crystal nucleation centers, speeding up the crystallization kinetics at the early stages of phase transformation. However, samples crystallized from the $NEM\ state$ require longer times to reach full crystallization (during the secondary crystallization stage) compared to those crystallized from the $ISO\ state$, likely suggesting that preexisting molecular order slows down the advance in the latest stages of the crystallization, *i.e.*, those governed by molecular diffusion. The fitting of the data with the Avrami model reveals different crystallization mechanisms, which ultimately result in distinct semicrystalline morphology and photoluminescence properties. Therefore, this work highlights the importance of understanding the interrelationships between processing, structure, and properties of polymer semiconductors and opens the door for performing fundamental investigations via newly-developed FSC methodologies of such materials that otherwise are

not possible with conventional techniques.

4.2 Introduction

Motivated by the promise of low-cost production of conformable electronic devices, *e.g.*, organic solar cells (OSCs), organic light-emitting diodes (OLEDs), thermoelectric modules, and organic electrochemical transistors (OECTs), etc., semiconducting polymers are attracting significant interest from both academic and industrial sectors. The operation of these devices is typically based on the optical and electrical properties of semiconducting polymer thin-films, which are known to be intimately connected to their solid-state microstructure. More specifically, properties such as the mobility of charge carriers (either electronic or ionic) and the absorption and emission of light are profoundly affected by the presence of molecular domains with structural order, *e.g.*, crystals, in the material;[1–4] simply because they exhibit a greater overlap of π-orbitals and a reduced energetic disorder compared to amorphous/disordered domains. Consequently, the control over optical and electrical properties of polymer semiconductors — and hence, rational optimization of devices — stems from a precise understanding and control of their solid-state microstructure.

The solid-state microstructure of many semiconducting polymers is generated via crystallization in the thin-film deposition step. Thus, gaining an understanding of how crystallization is developed is of paramount importance to establishing accurate processing-structure-properties relationships. However, fundamental investigations of the crystallization process are scarce in the literature and are limited to congeners of the polythiophene family[5–13]. As a result, many important questions about the crystallization of semiconducting polymers remain unanswered.

Among these, one of the most important is how preexisting molecular order in the liquid state impacts crystallization and solid-state microstructure

development. Due to the rigidity of aromatic backbones and their amphiphilic nature, many high-performing, crystallizable semiconducting polymers exhibit liquid-crystalline behavior; therefore, crystallization in these polymers likely occurs via the stacking of polymer chain segments that exhibit a preexisting order in the liquid state[14–17]. Moreover, even non-liquid-crystalline polymer semiconductors are known to exhibit a strong tendency to form aggregates with local molecular order prior to crystallization[17–21]. Therefore, a major fundamental question in the field remains as to whether or not (and if so, how) the crystallization process of semiconducting polymers is affected by the presence of molecular order in the liquid state.

Crystallizable main-chain liquid-crystalline semiconducting polymers seem ideal materials-systems to investigate this scientific problem, as (i) they can crystallize and (ii) exhibit both ordered and disordered liquid phases. However, because the liquid phase that is thermodynamically stable at temperatures immediately above the crystallization temperature is the liquid-crystalline mesophase, these materials have a strong tendency to crystallize solely from the ordered mesophase. Conversely, the crystallization from the isotropic phase is strongly hampered in these materials. Most likely due to this experimental difficulty, the effect of the preexisting molecular order of an isotropic melt on the crystallization of polymers has been largely unexplored, not just for semiconducting polymers but for polymers in general[12,22–29].

Fortunately, the above-mentioned experimental difficulties in investigating crystallization from the isotropic phase may be overcome with advanced thermal characterization methods, such as fast scanning calorimetry (FSC). The extremely fast heating and cooling ramps (up to ~ 10^4 ºC/s) that can be applied in FSC are opening a plethora of new possibilities to investigate materials' thermal phase transitions, including those previously non-accessible. For example, potentially, one can design thermal treatments aimed at

suppressing liquid crystalline mesophases (at temperatures slightly above crystallization temperature) so that liquid-crystalline polymers can be crystallized from a disordered, isotropic liquid state.

To explore the hypothesis above, we selected poly(9,9-di-n-octylfluorenyl-2,7-diyl (PFO) as a model material system. PFO is a well-known crystallizable semiconducting polymer with relatively low thermal transition temperatures. Therefore, suitable thermal protocols can be designed to minimize the risk of significant degradation issues[21]. In addition to — at least — two crystalline forms, PFO exhibits a nematic liquid crystalline mesophase (hereafter referred to as $NEM\ state$) in the temperature range immediately above the crystalline phase(s) along with an isotropic liquid phase (hereafter referred to as $ISO\ state$) at higher temperatures[11,13,21,22,30–32].

Hence, in this paper, we unravel the impact of the preexisting molecular order on the isothermal crystallization kinetics of the semiconducting polymer PFO, which allows us to rationalize the resulting solid-state microstructure and the optical response (photoluminescence) of the solid material. We discover that the effect of the molecular order on crystallization is complex: the kinetics of the early stages of crystallization is faster when crystallization occurs from the ordered liquid state, likely because the preexisting molecular order facilitates crystal nucleation. However, liquid-crystalline order seems to slow down the advance of the later stages of the crystallization, *i.e.*, those governed by molecular diffusion, likely because the chain segments diffusing to the growing crystal front must distort the ordered molecular arrangement in the liquid mesophase, which has an associated free-energy penalty. The different crystallization kinetics result in a distinct dimensionality of the crystallization, which yields different crystal morphologies and, ultimately, a different optical response (photoluminescence) in the semiconducting solid material.

4.3 Results and discussion

4.3.1 Establishment of Suitable Thermal Protocols for the Study

Prior to our investigation, we wanted to scrutinize the possibility of crystallizing PFO from the disordered $ISO\ state$ by cooling the melt down from a temperature above the nematic-to-isotropic transition (T_{LC-I})[30] to the crystallization temperature, employing cooling rates like those typically applied in regular differential scanning calorimetry (DSC) or polarized light optical microscopy (PLOM) experiments, namely <100 ºC/min. PLOM experiments were performed to observe the microscopic morphology of the material as a function of temperature. PLOM micrographs were taken at different temperatures during cooling from the melt at 60 °C/min. The representative micrographs are shown in Figure 4.1.

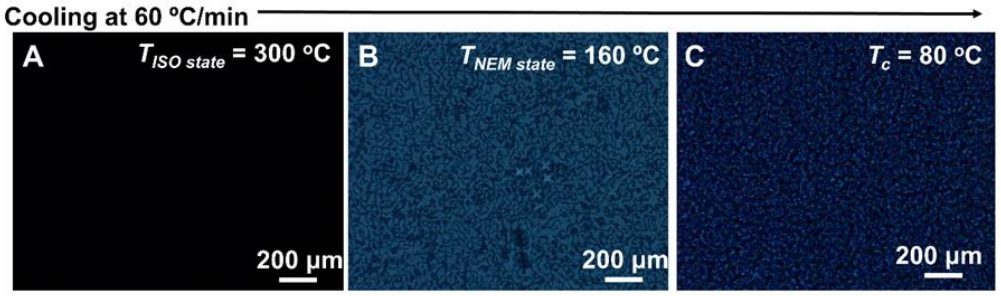

Figure 4.1 Polarized light optical micrographs of PFO during cooling at 60 ºC/min. A) 300 ºC, $ISO\ state$. B) 160 ºC, $NEM\ state$. C) 80 ºC, crystal phase.

The micrograph shown in Figure 4.1A was taken at a temperature above the clearing point at 300 °C, and as expected, a fully isotropic melt ($ISO\ state$) was observed, as no light can pass through the crossed polarizers. As the sample is cooled, the nematic liquid crystalline state ($NEM\ state$) can be identified, as

seen in Figure 4.1B, where a weakly birefringent texture can be observed. When the temperature decreases to 80 °C, small crystallites in Figure 4.1C were observed; however, their distinction in the micrograph is rather difficult due to their size.

This observation of the *NEM state* during cooling indicates that at a cooling rate of 60 °C/min, that is, the maximum cooling rate possible when using conventional PLOM and DSC techniques, the study of the kinetics of the material from a completely *ISO state* is not possible as the formation of the *NEM state* during cooling is unavoidable. Therefore, our data unambiguously proved that this range of cooling rates does not suffice to avoid the formation of the liquid-crystalline mesophase during cooling. Hence, in full accordance with our initial premises, conventional DSC and PLOM are not suitable for these studies, and methods enabling faster cooling rates, such as FSC, need to be used instead as this method enables to cool the sample at significantly faster rates.

Thus, we started our study by investigating the thermal conditions that allow us to compare crystallizations from the *ISO* and *NEM states*. More specifically, we need first to gain knowledge of the thermotropic phase behavior of PFO, including phase transition temperatures, and, secondly, to figure out the temperature range that allows isothermal crystallization from both the *ISO state* and the *NEM state*.

Figure 4.2A shows the FSC thermal protocol used to assess the thermotropic landscape of PFO. Firstly, PFO samples were heated to a temperature well above the T_{LC-I} transition to erase any thermal history (*e.g.*, at 300 ºC). Then, samples are rapidly cooled down (at 4,000 ºC/s) to various isothermal temperatures, T_a, ranging from 40 ºC to 160 ºC, and kept there for 1 h. During these isothermal steps, the PFO material will evolve according to its thermodynamic nature at that T_a. The evolution suffered by the material at

each T_a is probed in a subsequent heating scan (performed at 4,000 ºC/s, identified as "Analysis scan").

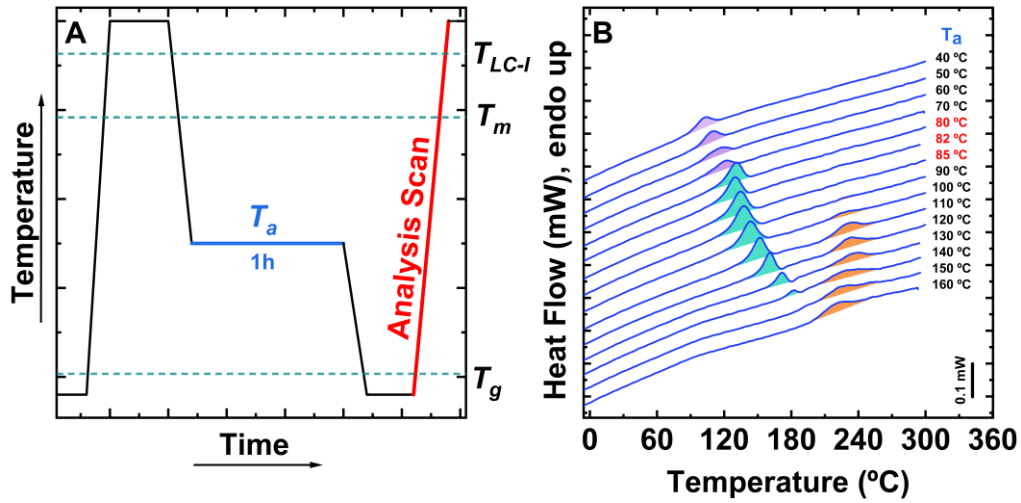

Figure 4.2. Thermotropic phase behavior of PFO. A) Thermal protocol employed for the experiment. Relevant temperatures: annealing temperature, T_a, melting temperature, T_m and nematic-to-isotropic transition temperature, T_{LC-I} . B) FSC heating traces (at 4,000 ºC/s) following the isothermal step of 1 h at temperatures ranging from $T_a = 40$ ºC to 160 ºC. Endothermic peaks shadowed in purple, cyan, and orange correspond to the enthalpic relaxation of the glassy phase, the melting of crystals, and the nematic-isotropic transition, respectively.

Figure 4.2B displays the calorimetric traces corresponding to the heating scans mentioned above (*i.e.*, "Analysis scans"). The T_a applied in the experiments is indicated on the right-hand side of the curves. Three different endothermic processes can be distinguished in the heating traces depending on the T_a applied. An aging glass tends to evolve towards an equilibrium state at temperatures well below their T_g. Hence, the area of the physical aging endotherm will decrease as the annealing temperature, T_a, increases, and approaches T_g. Based on this, below $T_a = 80$ °C, a broad

endotherm at low annealing temperatures (T_a < 80 ºC) is observed. The area of this endotherm decreases with increasing annealing temperature, indicating PFO is below T_g. That is, the observed endothermic peaks below $T_a = 80$ ºC correspond to the enthalpic overshoot as a physically aged glass undergoes the glass transition (this peak is shadowed in purple in Figure 4.2B). Moreover, in cyan color, at temperatures between $T_a = 80$ and 150 ºC, the overshoot due to the physical aging is no longer visible, and instead, a sharp bell-shaped endotherm associated to the melting process of the crystallites formed during the isothermal steps is observed[33,34,35].

Finally, the endothermic peaks colored in orange, from $T_a = 90$ °C onwards, feature the nematic-to-isotropic transition. Hence, this experiment directly informs about the thermodynamic phase behavior of the material, including relevant transition temperatures. The experiment above demonstrates that crystallization of PFO occurs between $T_a = 80$ and $T_a = 140$ ºC. Interestingly, curves obtained for T_as between 80 ºC and below 90 ºC feature solely the peak due to the melting of crystals, suggesting that no nematic phase is forming during the isothermal steps of 1 h at those temperatures. In other words, crystallization of PFO at $T_a = 80$ ºC occurs from the $ISO\ state$ when samples are cooled down from 300 ºC to 80 ºC at 4,000 ºC/s.

However, an isothermal step of 1 h is typically a short period for the crystallization of polymers to complete at temperatures so close to T_g. Therefore, to identify a suitable temperature range for our study, *i.e.*, the temperature range where crystals can develop from the $ISO\ state$, longer crystallization times need to be explored, *e.g.* 10 h.

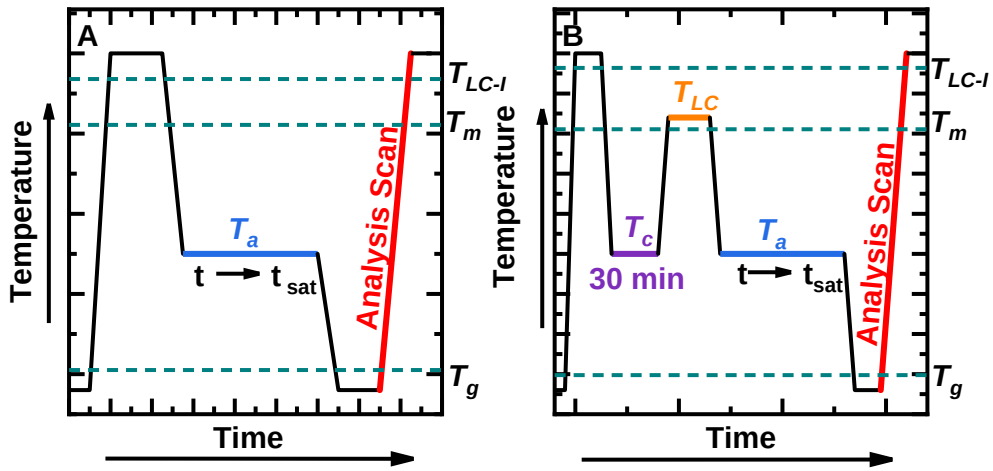

Figure 4.3. Thermal protocols used where T_a is the annealing temperature, T_{LC}, is a temperature at which the liquid crystal develops, T_m is the melting temperature, t is the annealing time and t_{sat} is the annealing time when the degree of crystallization reaches saturation. A) from an $ISO\ state$ and B) from a $NEM\ state$.

A suitable thermal protocol to investigate the crystallization of PFO from the $ISO\ state$ is shown in Figure 4.3A. The samples are first heated above T_{LC-I} to erase the thermal history for a short amount of time of 1s to avoid degradation. Then, samples are rapidly cooled down (at 4,000 ºC/s) to the selected T_a (between 80 and 85 ºC), where it is kept for a variable amount of time so that crystallization progresses. Samples are then rapidly cooled down to a temperature below T_g (at 4,000 ºC/s), and lastly, they are heated to 300 ºC (at 4,000 ºC/s) for 1 s. The endothermic peak appearing in this heating scan accounts for the melting of crystals formed during the isothermal step; hence, the enthalpy of this melting process can be employed to follow the isothermal crystallization kinetics.

It is customary to assume that the values of melting enthalpy (measured under non-isothermal conditions, *i.e.*, during the heating scans after isothermal crystallization) are identical to the values of the crystallization enthalpy

developed under isothermal conditions.

Having established the thermal conditions to investigate the isothermal crystallization of PFO from the $ISO\ state$, we determined a suitable thermal treatment to assess crystallization from the $NEM\ state$ between $T_a = 80$ and 85 ºC. The $NEM\ state$ can in principle, develop at any temperature above the T_m, but the higher the annealing temperature, the faster the development of the $NEM\ state$. However, high temperature also prompts undesired thermal degradation processes; hence we tried to minimize the exposure of samples to high temperatures. We found out that the PFO $NEM\ state$ was adequately forming when samples were first crystallized, and then crystals were molten without overpassing T_{LC-I}. Thus, the thermal protocol to study the crystallization of PFO from the nematic mesophase included two steps (Figure 4.3B): (i) an initial step in which the mesophase is formed (PFO is crystallized at $T_a = 80$ ºC for 30 min and then taken to 160 ºC for 1 min); and (ii) a second step that is equal to the one employed for the crystallization of samples from the $ISO\ state$.

Shown in Figure 4.4 are the calorimetric heating traces after samples were isothermally crystallized for 10 h at T_as of 80, 82, and 85 ºC from both the $ISO\ state$ and the $NEM\ state$ by applying the protocols described above (see Figure 4.3). As can be observed, neither of those traces crystallized from the $ISO\ state$ (see Figure 4.4A, Figure 4.4C and Figure 4.4E) exhibit the endothermic peak associated with T_{LC-I}, proving that PFO crystallizes solely from the $ISO\ state$ between $T_a = 80$ ºC and $T_a = 85$ ºC after being cooled down at 4,000 ºC/s from 300 ºC.

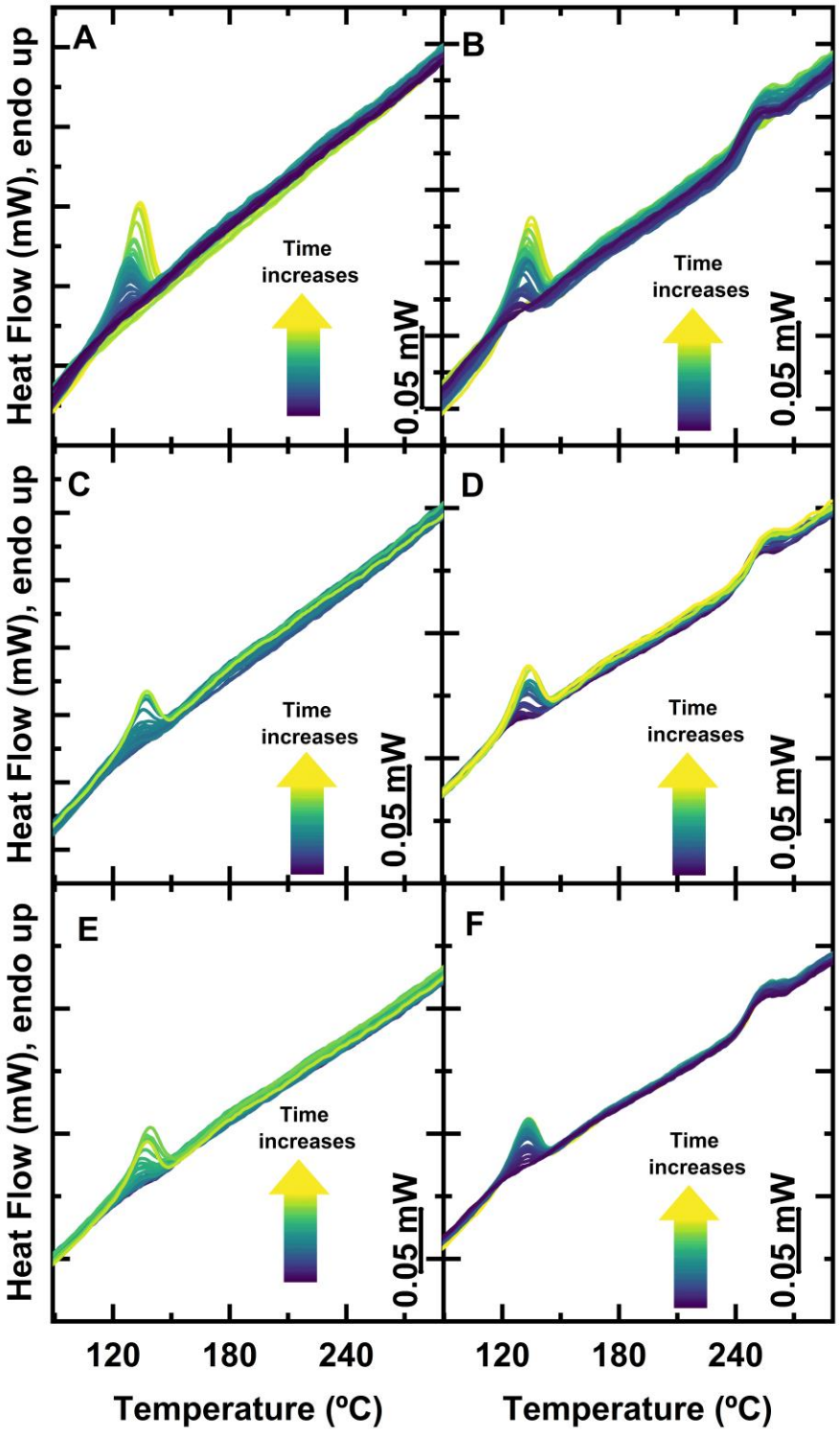

Figure 4.4 FSC heating traces (Analysis Scans), the progression of time is

illustrated by the color scale inside the arrow. A) For $T_a = 80$ ºC from $ISO\ state$. B) For $T_a = 80$ ºC from a $NEM\ state$. C) For $T_a = 82$ ºC from an $ISO\ state$. D) For $T_a = 82$ ºC from a $NEM\ state$. E) For $T_a = 85$ ºC from an $ISO\ state$. F) For $T_a = 85$ ºC from a $NEM\ state$.

4.3.2 Isothermal Crystallization Kinetics from the Isotropic and the Nematic Liquid States

Once we established the temperature conditions for our crystallization experiments, we endeavored to investigate the overall crystallization kinetics from the disordered $ISO\ state$ and the ordered $NEM\ state$.
Because polymer crystallization usually proceeds by nucleation and growth, it can be readily modeled with the Avrami framework, which describes the free growth of objects from random nucleation centers. The model yields the expression below (Equation 4.1) [36,37].

$$1 - V_c\,(t - t_o) = \exp(-k(t - t_o)^n) \qquad \text{Equation 4.1}$$

Where V_c is the relative volumetric transformed fraction to the crystalline state, t is the crystallization time, t_o is the induction time, k is the overall crystallization rate constant, which includes nucleation and growth components, and n is the Avrami index[36,37]. Moreover, V_c can be expressed as a function of mass fraction of the samples (W_c) as seen in Equation 4.2:

$$V_c = \frac{W_c}{W_c + \left(\frac{\rho_c}{\rho_a}\right)(1 - W_c)} \qquad \text{Equation 4.2}$$

where W_c is the mass fraction of the sample, ρ_c, the density of a 100%

crystalline sample, and ρ_a the density of a 100% amorphous sample. The values of ρ_c and ρ_a are unknown for PFO, and therefore we cannot apply Equation 4.1 in terms of volume fraction. However, V_c is proportional to W_c (see Equation 4.2 and Equation 4.3) and the overall crystallization kinetics determined by DSC can be fitted to the Avrami equation in terms of the mass fraction of crystals as an approximation. From Equation 4.3, $\Delta H\ (t)$ is the enthalpy at a given crystallization temperature, and ΔH_{total} is the maximum enthalpy value reached at the end of the isothermal crystallization process. The enthalpies are obtained from the specific heat capacity (C_p) as a function of mass. These values are obtained from the normalized integrated area of each peak divided by the scan rate to determine the relative crystallinity mass fraction of the sample at a given t and describe the kinetics of the material at a constant mass.

$$W_c = \frac{\Delta H\ (t)}{\Delta H_{total}} \qquad \text{Equation 4.3}$$

Moreover, Müller *et al.*[38,39] proposed that the Avrami index (n) can be considered in terms of the addition of two components: a nucleation rate component (n_n) and a growth dimensionally (n_d) component (Equation 4.4).[36,37]

$$n = n_n + n_d \qquad \text{Equation 4.4}$$

where, n_d can have values of 1, 2, and 3 depending on the dimensionality of the crystalline ensembles formed (*i.e.*, needles (1D), axialites (2D), and spherulites (3D)). The n_n value is proportional to the rate of nucleation with values ranging from 0 to 1; values equal to 1 are due to

sporadic nucleation, whereas values equal to 0 represent instantaneous nucleation.

For clarity, the experimental data obtained at a T_a of 80 °C is discussed here, while data for the rest of crystallization temperatures (the heating traces) employed for the study of the crystallization kinetics (denoted as "Analysis scan" in Figure 4.3A and Figure 4.3B) are included in Figure 4.4C−Figure 4.4F. We note here too, that the heating curves of PFO crystallized from the *ISO state* displayed a single endothermic feature associated with the crystal melting, while those of PFO crystallized from the *NEM state* exhibited a further peak associated with T_{LC-I} transition (see Figure 4.4).

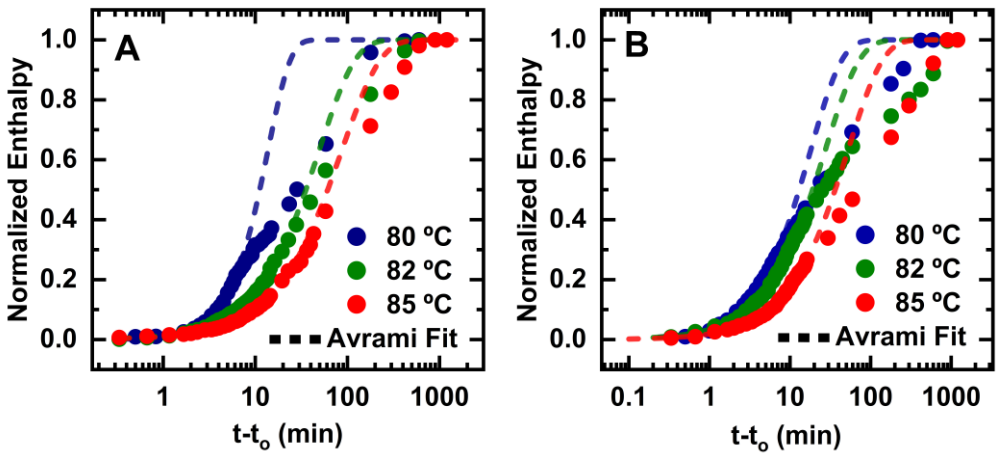

Figure 4.5. Advance of crystallization (from normalized enthalpy values) with time at the indicated temperatures and their corresponding Avrami fits. t and t_o are the annealing time and the induction time, respectively. A) from an *ISO state* and B) from a *NEM state*.

In order to study the crystallization kinetics, the crystal melting peaks were integrated, and the resulting enthalpy (normalized to the final value) was plotted against the crystallization time (Figure 4.5A and Figure 4.5B) and fitted with the Avrami model (dashed lines in Figure 4.5A and Figure 4.5B). The resulting Avrami parameters are given in Table 4.1, Table 4.2 and plotted in

Figure 4.6.

Table 4.1. Overall crystallization rate parameters (experimental and obtained through the Avrami theory fit)

T_c (ºC)	Initial State	$1/\tau_{20\%}$ exp. (min^{-1})	$1/\tau_{20\%}$ theo. (min^{-1})	$1/\tau_{50\%}$ exp. (min^{-1})	$1/\tau_{50\%}$ theo. (min^{-1})
80	ISO	0.166	0.169	0.035	0.089
80	NEM	0.223	0.229	0.042	0.077
82	ISO	0.075	0.074	0.017	0.028
82	NEM	0.159	0.160	0.034	0.052
85	ISO	0.049	0.049	0.0056	0.016
85	NEM	0.088	0.089	0.0055	0.027

Table 4.2. Overall crystallization rate parameters (experimental and obtained through the Avrami theory fit)

T_c (ºC)	Initial State	$1/t_o$ (min^{-1})	$k^{1/n}$ (min^{-1})	Avrami index (n)
80	ISO	0.630	0.073	1.7
80	NEM	0.857	0.055	1.1
82	ISO	0.480	0.020	1.1
82	NEM	2.00	0.036	1.0
85	ISO	0.46	0.011	1.0
85	NEM	2.22	0.019	0.99

As T_a increases, the overall crystallization rate becomes slower. This is reflected in a shift of the curves to higher crystallization times as T_a increases. In addition, the nucleation rate ($1/t_o$) when crystallizing from an $ISO\ state$ decreases with increasing T_a. t_o represents the induction time before any crystallization can be detected by the calorimeter; hence, its inverse is proportional to the primary nucleation rate. Therefore, a decrease in $1/t_o$ indicates that the rate of nucleation becomes slower with increasing T_a (values of $1/t_o$ can be found in Table 4.2).

Interestingly, the comparison of $1/t_o$ values for crystallizations from the $ISO\ state$ and the $NEM\ state$ at the same temperature reveafls that the preexisting molecular order in crystallizing PFO liquid accelerates the formation of effective nucleation centers. A faster nucleation process can explain why a faster overall crystallization rate is observed in the sample crystallized from the $NEM\ state$ both at 20% conversion ($1/\tau_{20\%}$) and at 50% conversion ($1/\tau_{50\%}$) (see Table 4.1 and Figure 4.6A).

It is important to note that samples crystallized from the $NEM\ state$ require longer times to reach the fully relative crystallized state in the sample, likely suggesting that liquid-crystalline order slows down the advance of the later stages of the crystallization, *i.e.*, those governed by molecular diffusion, after the crystallites impinged on one another during the growth process (*i.e.*, during the secondary overall crystallization process that typically occurs at relative conversions to the semicrystalline state larger than 50%).

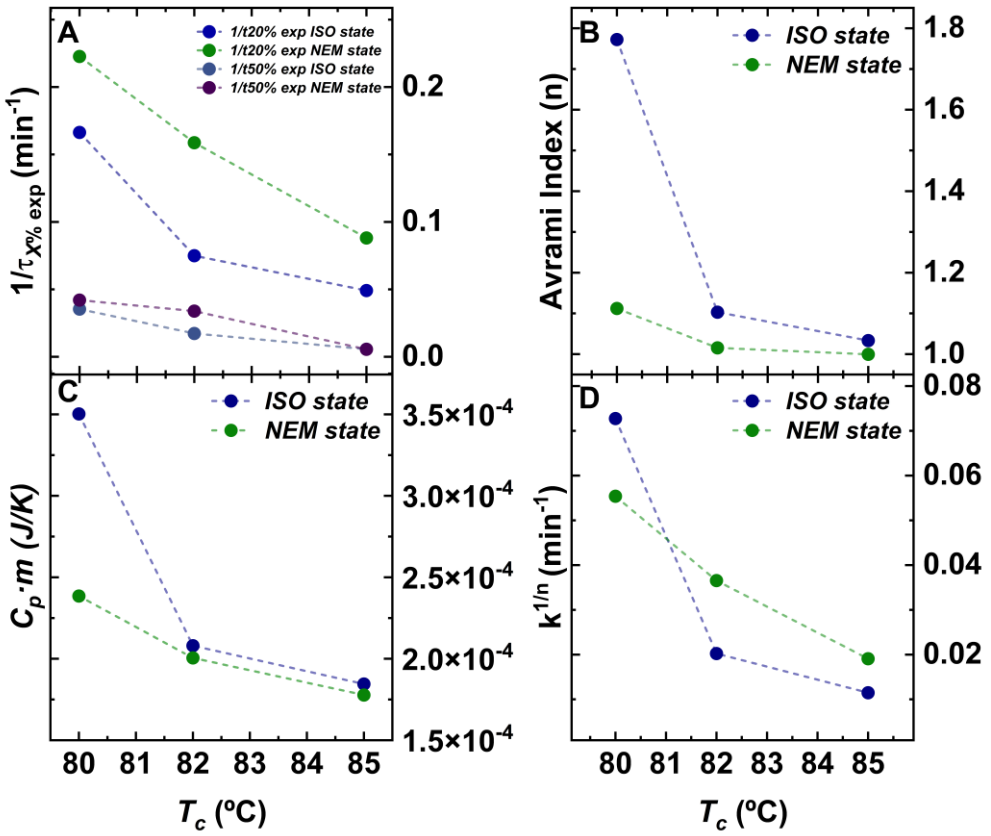

Figure 4.6 Experimental results and Avrami parameters as a function of crystallization temperature. A) Experimental values of the inverse of crystallization times ($1/\tau_{50\%}$ and $1/\tau_{20\%}$) for different conversions. B) Avrami index (n). C) Specific heat capacity for the longest crystallization time times the mass ($Cp \cdot m$) (*i.e.*, a proxy for the final degree of crystallinity because m is kept constant in the entire experiment). D) Isothermal crystallization rate obtained from the Avrami model ($k^{1/n}$).

We should consider that in the process of polymer crystallization, nucleation and mostly free growth from the activated nuclei first take place, and the overall crystallization kinetics accelerate with time (during the so-called primary crystallization). Then, a point is reached at which the kinetics slow down because the growing superstructures (spherulites or axialites, which are

semicrystalline entities or lamellar aggregates with 3 and 2 dimensions containing amorphous (molten) chains in between them) impinge on one another. This point usually coincides with or is close to 50% conversion to the semicrystalline state and is close to the time to peak when examining isothermal crystallization enthalpy values as a function of time. Secondary crystallization starts at this point when intra-spherulitic (or axialitic) and inter-spherulitic material that has not yet crystallized. If we crystallize from a pre-ordered state (*i.e.*, the nematic state), the energy barrier for overall primary crystallization (which includes both nucleation and growth) will most probably be lower than that needed to crystallize from the isotropic melt. We argue that the primary crystallization is dominated by nucleation when it occurs from the nematic state, and the overall crystallization kinetics is accelerated thanks to the enhanced nucleation with respect to the isotropic state. Then, during the secondary crystallization, as amorphous chains are embedded between the already formed crystallites, the diffusion rates are usually much lower than during primary crystallization, and the effect of nucleation at this stage can almost be neglected.

$NEM\ state$ exhibits orientational order but lacks the positional order that the crystalline motif has. Therefore, the crystallization of polymer molecules within the $NEM\ state$ must concur with some kind of translational motion that requires molecular or – at least – segmental relaxation. The slower kinetics is thus consistent with the fact that chain segments diffusing to the growing crystal front must distort the ordered molecular arrangement of the $NEM\ state$, which has an associated free-energy penalty. We must highlight, moreover, that our isothermal crystallization data from in situ wide angle X-ray scattering (WAXS), see Figure 4.7 and Table 4.3), agree well with the above-mentioned results and conclusions. Clearly, a realistic dynamic microscopic picture – at the molecular level – of how a polymer molecule within the nematic mesophase

transits into the crystalline state is required to fully understand the crystallization of PFO polymer.

We must note that the Avrami theory is used to describe the primary crystallization range (during the free growth of crystals without any impingement of one another), and fittings for large crystallization conversions are often unsuitable. Hence, to ensure the free growth approximation, the conversion range employed for the fittings was 3−20% of the relative crystallization conversion.

Figure 4.6B shows how the Avrami index (n) varies with T_a values depending on the initial liquid state, *i.e.*, $ISO\ state$ versus $NEM\ state$. The Avrami index was found to be larger at lower T_a values for crystallization from the $ISO\ state$. At $T_a = 80$ ºC, there is a significant change from n = 1.7 when the PFO is crystallized from the melt state to 1.1 when it is crystallized from the $NEM\ state$.

That is, the Avrami parameter is closer to 2 for the crystallization from an $ISO\ state$ and to 1 from a $NEM\ state$. One way to interpret these results is a change in the morphology and nucleation of the PFO. An Avrami index of 2 can be a result of the instantaneous nucleation of axialitic crystals (*i.e.*, two-dimensional aggregates of lamellar crystals), while n = 1 could be a result of the instantaneous growth of needle-like crystals. AFM results (see Figure 4.8) show some morphology changes that could correspond to the change in the Avrami index. Furthermore, $k^{1/n}$, is a rate crystallization constant whose values provide information on the overall crystallization rate obtained by the Avrami model, which correlate to the obtained experimental values.

Finally, as a proxy for the final degree of crystallinity reached in the samples, the product between the melting enthalpy for the longest crystallization time and the sample mass (m) was analyzed, where sample mass was constant

(but unknown) in the whole study (Figure 4.6C). Results indicate that samples crystallized from an $ISO\ state$ end up being more crystalline than those crystallized from a $NEM\ state$, especially for the lowest T_a analyzed. This, again, agrees with our interpretation that chain segment diffusion to the crystal growth front is more impeded in the $NEM\ state$ during the secondary crystallization process.

4.3.3 Isothermal Crystallization Kinetics from X-ray Scattering

In these experiments, the sensor with a previous thermal treatment done in the Flash DSC was placed perpendicular to the incident beam and in order to properly measure the sample and ensure a high S/N ratio, it was necessary to deposit the sample on the FSC sensor in the bulk, contrary to the FSC experiments which were measured in thin-films.

The kinetics were followed by measuring the relative crystallinity from the peak increase at q = 15 nm^{-1}, indexed to the crystalline plane [530], with increasing time (see Figure 4.7). The reflections found on the crystallized sample were able to be indexed to the orthorhombic unit cell of the α-crystal phase of PFO for both samples[40]. Results seen in Figure 4.7 reveal that for both methods (*i.e.*, FSC and WAXS) similar experimental results are obtained for both crystallization protocols. In addition, after applying the Avrami theory, overall crystallization kinetics ($k^{1/n}$) were significantly different for the two techniques.

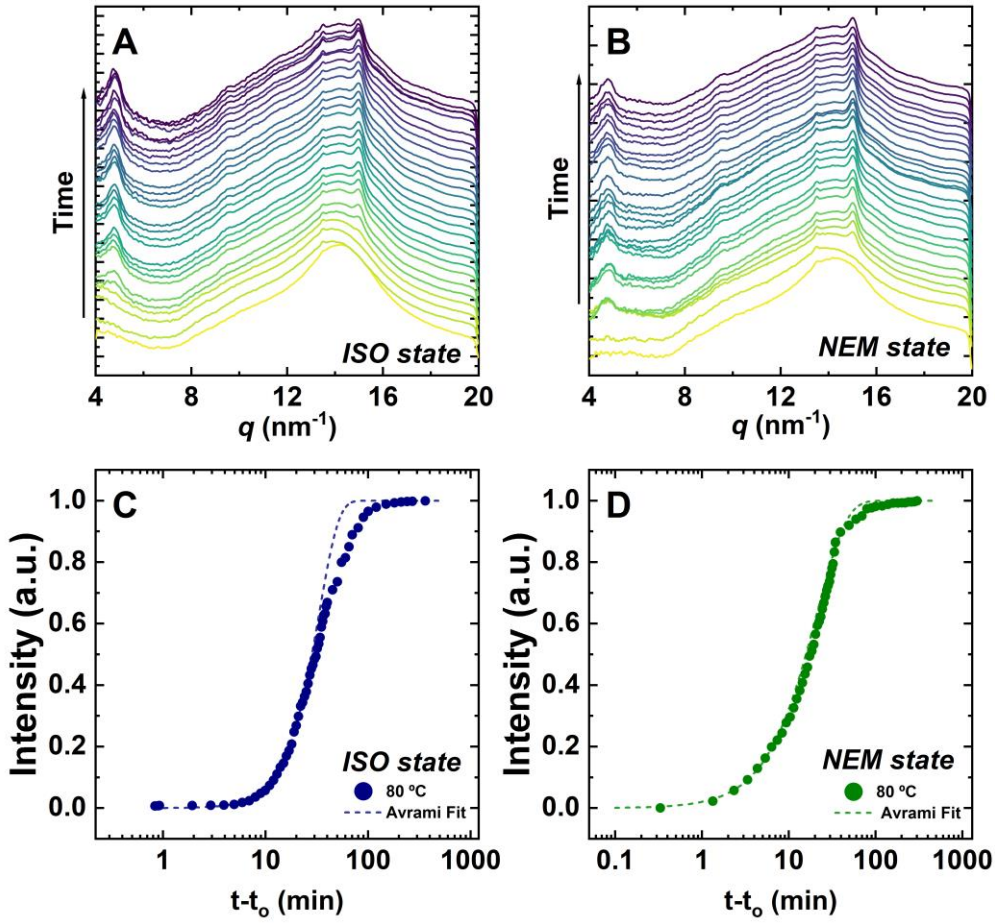

Figure 4.7. A and B) WAXS profiles after isothermal treatment for varying times at 80 °C for *ISO state* and *NEM state* crystallization, respectively. C and D) WAXS profiles after isothermal treatment and their corresponding Avrami fittings for an *ISO state* and for a *NEM state*, respectively.

This could be simply explained since the analysis of the kinetics is done by following a single peak, that is, only one direction of the crystal growth has been analyzed. or due to different sample shape, that is in the bulk compared to thin-film. This signal is in the region of π-π stacking (010) so it is possible the stacking is perpendicular to the growth of the crystal and is inhibited in this direction and growing in another, which is not able to be observed in that direction. However, it was found that the Avrami index gives the same pattern

for each initial crystallization state. That is, an Avrami index of 2 for an initial $ISO\ state$ and 1 for an initial $NEM\ state$. In Table 4.3, comparisons between the two techniques are presented to outline comparabilities and differences in the results.

Table 4.3. WAXS and FSC Avrami Parameters at T_a = 80 ºC.

Technique	Initial State	$1/\tau_{20\%}$ exp. (min^{-1})	$1/\tau_{20\%}$ theo. (min^{-1})	$1/\tau_{50\%}$ exp. (min^{-1})	$1/\tau_{50\%}$ theo. (min^{-1})	$k^{1/n}$ (min^{-1})	Avrami index (n)
FSC	*ISO*	0.166	0.167	0.035	0.089	0.073	1.7
WAXS	*ISO*	0.056	0.055	0.032	0.035	0.050	2.3
FSC	*NEM*	0.222	0.224	0.042	0.077	0.055	1.1
WAXS	*NEM*	0.159	0.158	0.053	0.061	0.12	1.3

4.3.4 Interplay between the crystallization kinetics and the morphology and the optical response (AFM and PL)

Having established that preexisting molecular order significantly influences the crystallization kinetics of polymers, we analyzed whether the distinct kinetics found, result in structural/morphological differences. Thus, samples crystallized both from the $ISO\ state$ and the $NEM\ state$ – thermally treated employing thermal protocols developed for kinetic studies with crystallization times of 10 h – were inspected by AFM (height images).

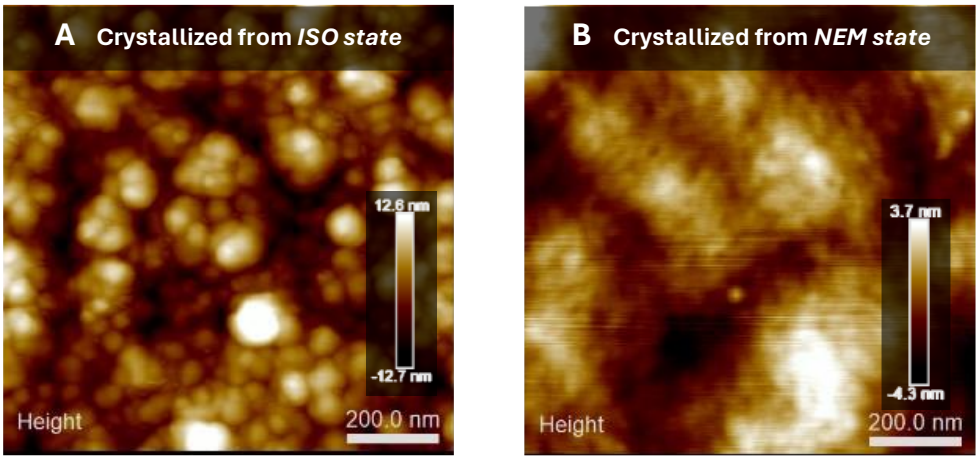

Figure 4.8. A) AFM-height images of PFO crystallized at $T_a = 80$ ºC from an $ISO\ state$. B) AFM-height images of PFO crystallized $T_a = 80$ ºC from a $NEM\ state$.

Tellingly, sample surfaces exhibit markedly different morphology/surface topography. AFM images (see Figure 4.8) revealed that PFO crystallized from the $ISO\ state$ develops round-sized nanoscopic features (*i.e.*, axialitic-like), whereas the sample crystallized from the $NEM\ state$ seems to comprise more-elongated features (*i.e.*, needle-like).

The height histograms for the sample crystallized from the $ISO\ state$ exhibit a broad distribution, denoting regions with large height variations, *i.e.*, large roughness, whereas histograms for the PFO samples crystallized from the $NEM\ state$ exhibit a narrow distribution of heights, corresponding to a more homogeneous surface (see Figure 4.9).

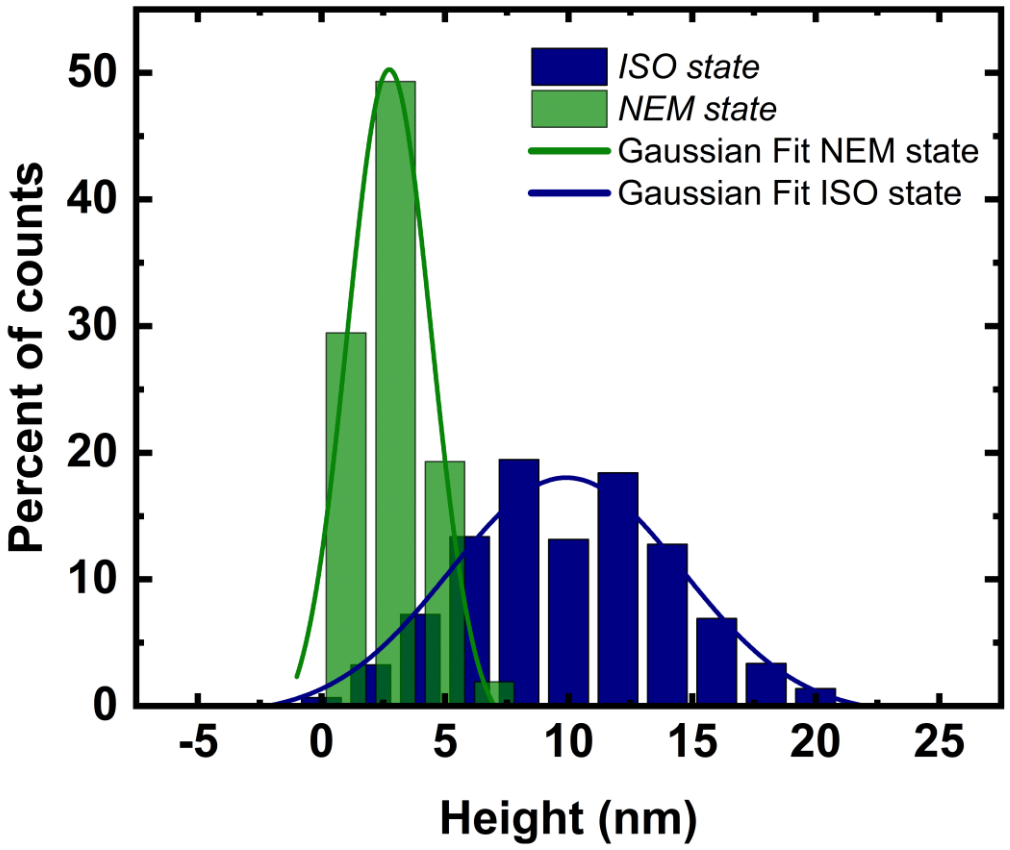

Figure 4.9. Height histograms distributions obtained from the AFM data of Figure 4.8 fitted to Gaussian curves.

Motivated by the aforementioned findings that preexisting order alters the crystallization and the resulting solid-state morphology, we explored whether these changes have in turn an impact on optoelectronic properties of the semiconducting polymer, *e.g.*, its optical emission properties (photoluminescence).

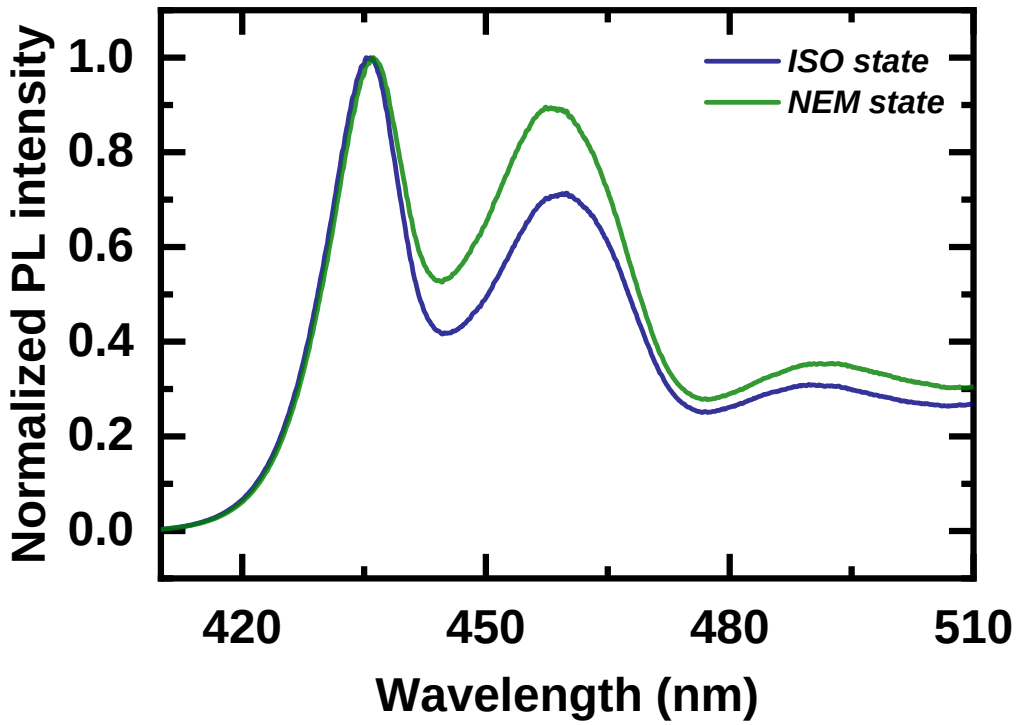

Figure 4.10. Photoluminescence spectra of crystallized FSC thin-film samples at $T_a = 80$ ºC from an $ISO\ state$ (blue), from a $NEM\ state$ (green).

Figure 4.10 compares the average photoluminescence (PL) spectrum excited at 355 nm for the two samples. The two spectra generally show the same shape: the main $0-0$ PL band followed by the first two phonon replicas. The most significant differences are in the relative intensity of the 00 and 01 transitions, being the ratio smaller for the liquid-crystalline sample and a small blue shift of the PL peaks of the liquid-crystalline sample with respect to the isotropic one. Both features suggest a larger fraction of PFO chain segments with planar conformations, hence a larger degree of energetic order for the sample processed from the $ISO\ state$. This is most likely associated with a higher degree of crystallinity[1] in this sample, as semiconducting polymers tend to crystallize in crystallites in which polymer chains adopt extended conformations.

4.4 Conclusions

In this work, we employ fast scanning chip calorimetry to study the crystallization kinetics from different states of a semiconducting semicrystalline material, PFO, opening new possibilities to investigate states of matter that would be otherwise inaccessible through conventional DSC techniques of other polymers in the field of organic electronics. We demonstrate that the pre-ordered molecular domains in the $NEM\ state$ facilitate the formation of effective nucleation sites for crystallization. However, they seem to hinder the diffusion of chain segments to the crystal growth front during the secondary crystallization stage, which slows down the crystal growth process. We argue that the different balance between nucleation and crystal growth between polymers crystallized from ordered and disordered liquids results in distinct solid-state morphologies and different degrees of crystallinity, which eventually impact the optical emission properties of materials. Therefore, our investigation clearly demonstrates a correlation between the preexisting molecular order in the crystallizable liquid, the crystallization kinetics, and the optoelectronic properties of solid semiconducting polymers. However, even more importantly, this work highlights that it is utterly important to conduct more fundamental investigations to gain full control over the optoelectronic properties of organic semiconductors.

4.5 References for Chapter 4

(1) Ariu, M.; Lidzey, D. G.; Lavrentiev, M.; Bradley, D. D. C.; Jandke, M.; Strohriegl, P. Study of the Different Structural Phases of the Polymer Poly(9,9′-Dioctyl Fluorene) Using Raman Spectroscopy. *Synth. Met.* **2001**, *116* (1–3), 217–221.

(2) Jimison, L. H.; Toney, M. F.; McCulloch, I.; Heeney, M.; Salleo, A. Charge-Transport Anisotropy Due to Grain Boundaries in Directionally Crystallized Thin Films of Regioregular Poly(3-Hexylthiophene). *Adv. Mater.* **2009**, *21* (16), 1568–1572.

(3) Yang, H.; Shin, T. J.; Yang, L.; Cho, K.; Ryu, C. Y.; Bao, Z. Effect of Mesoscale Crystalline Structure on the Field-Effect Mobility of Regioregular Poly(3-Hexyl Thiophene) in Thin-Film Transistors. *Adv. Funct. Mater.* **2005**, *15* (4), 671–676.

(4) Noriega, R.; Rivnay, J.; Vandewal, K.; Koch, F. P. V.; Stingelin, N.; Smith, P.; Toney, M. F.; Salleo, A. A General Relationship between Disorder, Aggregation and Charge Transport in Conjugated Polymers. *Nat. Mater.* **2013**, *12* (11), 1038–1044.

(5) Yu, L.; Davidson, E.; Sharma, A.; Andersson, M. R.; Segalman, R.; Müller, C. Isothermal Crystallization Kinetics and Time-Temperature-Transformation of the Conjugated Polymer: Poly(3-(2′-Ethyl)Hexylthiophene). *Chem. Mater.* **2017**, *29* (13), 5654–5662.

(6) Duong, D. T.; Ho, V.; Shang, Z.; Mollinger, S.; Mannsfeld, S. C. B.; Dacuña, J.; Toney, M. F.; Segalman, R.; Salleo, A. Mechanism of Crystallization and Implications for Charge Transport in Poly(3-Ethylhexylthiophene) Thin Films. *Adv. Funct. Mater.* **2014**, *24* (28),

4515–4521.

(7) Zhao, Y.; Yuan, G.; Roche, P.; Leclerc, M. A Calorimetric Study of the Phase Transitions in Poly(3-Hexylthiophene). *Polymer* **1995**, *36* (11), 2211–2214.

(8) Pal, S.; Nandi, A. K. Cocrystallization Mechanism of Poly(3-Hexyl Thiophenes) with Different Amount of Chain Regioregularity. *J. Appl. Polym. Sci.* **2006**, *101* (6), 3811–3820.

(9) Yang, G. Z.; Chen, X.; Wang, W.; Wang, M.; Liu, T.; Li, C. Z. Nonisothermal Crystallization and Melting Behavior of a Luminescent Conjugated Polymer, Poly(9,9-Dihexylfluorene-Alt-Co-2,5-Didecyloxy-1,4- Phenylene). *J. Polym. Sci. Part B Polym. Phys.* **2007**, *45* (8), 976–987.

(10) Chen, X. L.; Huang, H. L.; Shi, J. G.; Liu, Y. L.; Wang, L. M. Isothermal Crystallization Kinetics and Melting Behavior of a Luminescent Conjugated Polymer, Poly(9,9-Dihexylfluorene-Alt-2,5-Didodecyloxybenzene). *J. Macromol. Sci. Part B Phys.* **2012**, *51* (6), 1049–1056.

(11) Chen, S. H.; Wu, Y. H.; Su, C. H.; Jeng, U.; Hsieh, C. C.; Su, A. C.; Chen, S. A. Cold Crystallization of Poly(9,9-Di-n-Octyl-2,7-Fluorene). *Macromolecules* **2007**, *40* (15), 5353–5359.

(12) Yang, G. Z.; Chen, X.; Xu, Y.; Li, C. Z.; Wu, P.; Liu, T. Nonisothermal Crystallization Behavior of a Luminescent Conjugated Polymer, Poly(9,9-Dihexylfluorene-Alt-2,5-Didodecyloxybenzene). *Polym. Int.* **2007**, *56* (2), 245–251.

(13) Perevedentsev, A.; Stavrinou, P. N.; Bradley, D. D. C.; Smith, P. Solution-

Crystallization and Related Phenomena in 9,9-Dialkyl-Fluorene Polymers. I. Crystalline Polymer-Solvent Compound Formation for Poly(9,9-Dioctylfluorene). *J. Polym. Sci. Part B Polym. Phys.* **2015**, *53* (21), 1481–1491.

(14) Bridges, C. R.; Ford, M. J.; Bazan, G. C.; Segalman, R. A. Molecular Considerations for Mesophase Interaction and Alignment of Lyotropic Liquid Crystalline Semiconducting Polymers. *ACS Macro Lett.* **2017**, *6* (6), 619–624.

(15) Zhang, L.; Zhao, K.; Li, H.; Zhang, T.; Liu, D.; Han, Y. Liquid Crystal Ordering on Conjugated Polymers Film Morphology for High Performance. *J. Polym. Sci. Part B Polym. Phys.* **2019**, *57* (23), 1572–1591.

(16) McCulloch, I.; Heeney, M.; Bailey, C.; Genevicius, K.; MacDonald, I.; Shkunov, M.; Sparrowe, D.; Tierney, S.; Wagner, R.; Zhang, W.; Chabinyc, M. L.; Kline, R. J.; McGehee, M. D.; Toney, M. F. Liquid-Crystalline Semiconducting Polymers with High Charge-Carrier Mobility. *Nat. Mater.* **2006**, *5* (4), 328–333.

(17) Bridges, C. R.; Ford, M. J.; Popere, B. C.; Bazan, G. C.; Segalman, R. A. Formation and Structure of Lyotropic Liquid Crystalline Mesophases in Donor-Acceptor Semiconducting Polymers. *Macromolecules* **2016**, *49* (19), 7220–7229.

(18) Marina, S.; Gutierrez, E.; Gutierrez, J.; Gobbi, M.; Ramos, N.; Solano, E.; Rech, J.; You, W.; Hueso, L. E.; Tercjak, A.; Ade, H.; Martin, J. Semi-Paracrystallinity in Semi-Conducting Polymers. *Mater. Horiz.* **2022**, *9* (4), 1196–1206.

(19) Liu, X.; Huettner, S.; Rong, Z.; Sommer, M.; Friend, R. H. Solvent

Additive Control of Morphology and Crystallization in Semiconducting Polymer Blends. *Adv. Mater.* **2012**, *24* (5), 669–674.

(20) Liu, Y.; Zhao, J.; Li, Z.; Mu, C.; Ma, W.; Hu, H.; Jiang, K.; Lin, H.; Ade, H.; Yan, H. Aggregation and Morphology Control Enables Multiple Cases of High-Efficiency Polymer Solar Cells. *Nat. Commun.* **2014**, *5* (1), 1–8.

(21) Luzio, A.; Nübling, F.; Martin, J.; Fazzi, D.; Selter, P.; Gann, E.; McNeill, C. R.; Brinkmann, M.; Hansen, M. R.; Stingelin, N.; Sommer, M.; Caironi, M. Microstructural Control Suppresses Thermal Activation of Electron Transport at Room Temperature in Polymer Transistors. *Nat. Commun.* **2019**, *10* (1), 1–13.

(22) Padmaja, S.; Ajita, N.; Srinivasulu, M.; Girish, S. R.; Pisipati, V. G. K. M.; Potukuchi, D. M. Crystallization Kinetics in Liquid Crystals with Hexagonal Precursor Phases by Calorimetry. *Z. Naturforschung - Sect. J. Phys. Sci.* **2010**, *65* (8), 733–744.

(23) Carpaneto, L.; Marsano, E.; Valenti, B.; Zanardi, G. Crystallization and Melting Behaviour of a Semirigid Liquid-Crystalline Polyester. *Polymer* **1992**, *33* (18), 3865–3872.

(24) Katerska, B.; Exner, G.; Perez, E.; Krasteva, M. N. Cooling Rate Effect on the Phase Transitions in a Polymer Liquid Crystal: DSC and Real-Time MAXS and WAXD Experiments. *Eur. Polym. J.* **2010**, *46* (7), 1623–1632.

(25) Chen, X. L.; Huang, H. L.; Shi, J. G.; Liu, Y. L.; Wang, L. M. Isothermal Crystallization Kinetics and Melting Behavior of a Luminescent Conjugated Polymer, Poly(9,9-Dihexylfluorene-Alt-2,5-Didodecyloxybenzene). *J. Macromol. Sci. Part B Phys.* **2012**, *51* (6), 1049–1056.

(26) Androsch, R.; Soccio, M.; Lotti, N.; Cavallo, D.; Schick, C. Cold-Crystallization of Poly(Butylene 2,6-Naphthalate) Following Ostwald's Rule of Stages. *Thermochim. Acta* **2018**, *670*, 71–75.

(27) Ding, Q.; Soccio, M.; Lotti, N.; Cavallo, D.; Androsch, R. Melt Crystallization of Poly(Butylene 2,6-Naphthalate). *Chin. J Polym* **2020**, *38* (4), 311–322.

(28) Ding, Q.; Jehnichen, D.; Göbel, M.; Soccio, M.; Lotti, N.; Cavallo, D.; Androsch, R. Smectic Liquid Crystal Schlieren Texture in Rapidly Cooled Poly(Butylene Naphthalate). *Eur. Polym. J.* **2018**, *101*, 90–95.

(29) Cavallo, D.; Mileva, D.; Portale, G.; Zhang, L.; Balzano, L.; Alfonso, G. C.; Androsch, R. Mesophase-Mediated Crystallization of Poly(Butylene-2,6- Naphthalate): An Example of Ostwald's Rule of Stages. *ACS Macro Lett.* **2012**, *1* (8), 1051–1055.

(30) Martin, J.; Davidson, E. C.; Greco, C.; Xu, W.; Bannock, J. H.; Agirre, A.; De Mello, J.; Segalman, R. A.; Stingelin, N.; Daoulas, K. C. Temperature-Dependence of Persistence Length Affects Phenomenological Descriptions of Aligning Interactions in Nematic Semiconducting Polymers. *Chem. Mater.* **2018**, *30* (3), 748–761.

(31) Kawamura, T.; Misaki, M.; Koshiba, Y.; Horie, S.; Kinashi, K.; Ishida, K.; Ueda, Y. Crystalline Thin Films of β-Phase Poly(9,9-Dioctylfluorene). *Thin Solid Films* **2011**, *519* (7), 2247–2250.

(32) Elshaikh, M.; Marouf, A. A. S.; Modwi, A.; Ibnaouf, K. H. Influence of the Organic Solvents on the α and β Phases of a Conjugated Polymer (PFO). *Dig. J. Nanomater. Biostructures* **2019**, *14* (4), 1069–1077.

(33) Wang, W.; Fenni, S. E.; Ma, Z.; Righetti, M. C.; Cangialosi, D.; Di

Lorenzo, M. L.; Cavallo, D. Glass Transition and Aging of the Rigid Amorphous Fraction in Polymorphic Poly(Butene-1). *Polymer* **2021**, *226* (123830), 1–9.

(34) Cangialosi, D.; Alegría, A.; Colmenero, J. Cooling Rate Dependent Glass Transition in Thin Polymer Films and in Bulk. In *Fast Scanning Calorimetry*; 2016; pp 403–431.

(35) Martín, J.; Stingelin, N.; Cangialosi, D. Direct Calorimetric Observation of the Rigid Amorphous Fraction in a Semiconducting Polymer. *J. Phys. Chem. Lett.* **2018**, *9* (5), 990–995.

(36) Lorenzo, A. T.; Arnal, M. L.; Albuerne, J.; Müller, A. J. DSC Isothermal Polymer Crystallization Kinetics Measurements and the Use of the Avrami Equation to Fit the Data: Guidelines to Avoid Common Problems. *Polym. Test.* **2007**, *26* (2), 222–231.

(37) Pérez-Camargo, R. A.; Liu, G. M.; Wang, D. J.; Müller, A. J. Experimental and Data Fitting Guidelines for the Determination of Polymer Crystallization Kinetics. *Chin. J. Polym. Sci.* **2022**, *40* (6), 658–691.

(38) Müller, A. J.; Balsamo, V.; Arnal, M. L. Nucleation and Crystallization in Diblock and Triblock Copolymers. *Adv. Polym. Sci.* **2005**, *190* (1), 1–63.

(39) Balsamo, V.; Urdaneta, N.; Pérez, L.; Carrizales, P.; Abetz, V.; Müller, A. J. Effect of the Polyethylene Confinement and Topology on Its Crystallisation within Semicrystalline ABC Triblock Copolymers. *Eur. Polym. J.* **2004**, *40* (6), 1033–1049.

(40) Chen, S. H.; Chou, H. L.; Su, A. C.; Chen, S. A. Molecular Packing in Crystalline Poly(9,9-Di-n-Octyl-2,7-Fluorene). *Macromolecules* **2004**, *37*

(18), 6833–6838.

Chapter 5

Crystallization Kinetics of Semiconducting Poly(2,5-bis(3-alkylthiophen-2-yl)-thieno-[3,2-b]thiophene) (PBTTT) from its Different Liquid Phases

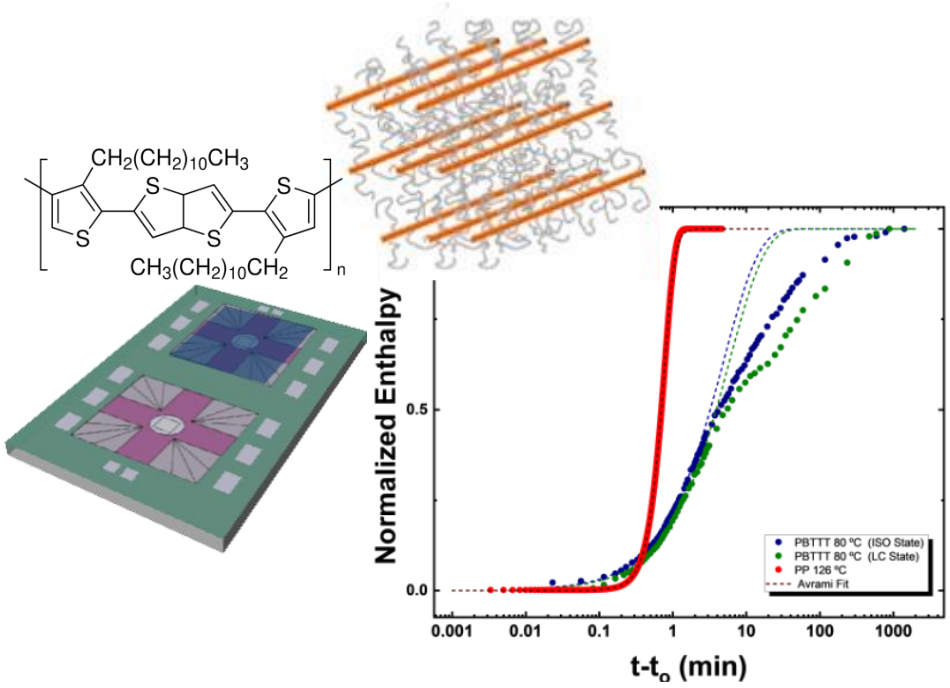

5.1 Abstract

Because the electronic properties of semiconducting polymers are inexorably linked to their solid-state microstructure, it is imperative to understand their complex crystallization processes fully. For example, Poly(2,5-bis(3-alkylthiophen-2-yl)-thieno-[3,2-b]thiophene) (PBTTT), which is frequently considered a model system for highly ordered semicrystalline semiconducting polymers, can exhibit two distinct semicrystalline thin-film morphologies: the so-called terrace-phase, which features high charge carrier mobility (> 1 cm^2/Vs), and the ribbon-phase with much poorer properties. The achievement of one or the other depends on the temperature at which the polymer is thermally annealed. Our results evidence that PBTTT is in the liquid state at those "annealing temperatures" and, therefore, the achievement of the terrace- or ribbon phases depends, in fact, on the distinct structural configuration of liquid PBTTT chains at each temperature (before crystallization). Motivated by this observation, we investigate the complex crystallization kinetics of spun cast PBTTT thin-films crystallized from those liquid states. We achieve this using a methodology that combines fast scanning calorimetry, X-ray scattering, and optical microscopy. We demonstrate that a preexisting smectic order enhances crystal nucleation rate, speeding up the crystallization kinetics at the early stages of phase transformation. More interestingly, our analysis reveals a complex crystallization kinetics in PBTTT, which differs from the typical crystallization behavior of commodity polymers. These results evidence that the crystallization of semiconducting polymers occurs quite differently to that of most commodity polymers, highlighting (once again) the necessity to conduct more fundamental investigations on the structure development of this important class of polymers.

5.2 Introduction

Conjugated polymers possessing semiconducting traits have great potential for a wide range of applications in the field of organic electronics, such as thin-film transistors (TFT), organic light-emitting diodes (OLEDs), thermoelectric modules, or organic solar cells[1–4], due to their easy processing, low weight, and mechanical flexibility.

Poly(2,5-bis(3-alkylthiophen-2-yl)-thieno-[3,2-*b*]thiophene) (PBTTT-C_{12}; hereafter termed PBTTT) is a well-studied conjugated polymer exhibiting a high degree of crystalline order at room temperature[5–8]. Upon heating, PBTTT is reported to undergo two main thermal transitions: a low-temperature transition at $T \approx 150$ °C and a high-temperature transition at $T \approx 250$ °C. Interestingly, a thermal annealing below or above the high-temperature transition permits tuning its solid-state morphology/microstructure and, more importantly, its electrical properties. For example, a crystalline ribbon-like morphology with only moderate charge carrier mobility results when PBTTT is thermally annealed above the high-temperature transition. In contrast, thermal annealing PBTTT thin-films at a temperature in between low-temperature and high-temperature transitions yields a semicrystalline terrace-like morphology[5–7] that exhibits remarkable charge carrier mobilities, frequently overpassing 1 $cm^2/ V \cdot s$[6,7,9,10]. This suggests that the distinct structural configuration of PBTTT chains (short- and long-range molecular order, conformation, etc.) at the annealing temperature leads to different structural rearrangement processes in the material that, eventually, result in solid-state microstructures/morphologies with different electrical performances. However, from the vast literature on PBTTT, it is rather unclear how are the structural rearrangement processes in the material that yield the terrace- and the ribbon- morphologies. On the one hand, this is motivated by the complex thermal behavior described above and,

on the other hand, by the fact that PBTTT is known to exhibit liquid crystalline order. More specifically, it has been proposed that PBTTT can form a smectic mesophase, *i.e.*, a liquid phase where polymer chains possess orientational and a certain positional order, which results in the formation of layered structures[11,12]. Therefore, it remains unclear whether the ribbon and the terrace phases result from an actual annealing process of the semicrystalline state, in which the quality of the crystalline domains is improved (like most of the typical thermal annealing processes) or whether they result through a crystallization process from the liquid states.

According to previous works, the kinetics of the crystallization process seem to have a profound impact on the resulting solid-state microstructure. For example, Kang *et al.*[13] reported that the crystallization rate has a severe impact on the solid-state morphology and the electrical properties of PBTTT crystallized from the mesophase. Employing X-ray diffraction, Vakshouri *et al.*[14] investigated how structural order developed at 100 and 150 ºC. However, as they mention in the manuscript, those temperatures are above the crystallization temperature for PBTTT and were chosen to anneal the liquid-crystal state. Recently, Qu *et al.* combined Raman spectroscopy and FSC, and investigated the structural evolution of PBTTT at various isothermal temperatures via the evolution of calorimetric peaks and Raman modes. The method is proven to be efficient, however their interpretation of the thermotropic behavior of the polymer contradicted previous literature[6,9,14]. For example, they claim crystallization of the backbones at 140 ºC, while that temperature is supposed to be above the melting temperature of crystals (according to most of the literature). Likewise, the associate an endothermic calorimetric peak showing up at ~30 ºC with the melting of side chains, which, according to our data (shown later on in the manuscript) it is likely due to physical ageing of glassy material regions.

Motivated by the apparent discrepancy in the literature related to the thermotropic phase behavior of PBTTT, in this paper, we first resolve the thermotropic phase behavior of PBTTT[15]. Then, we establish that, interestingly, both the terrace and the ribbon phases develop via crystallization processes from liquid states with different molecular order (a smectic liquid and an isotropic liquid). Ultimately, we study the crystallization kinetics of spun cast PBTTT thin-films from those different liquid states. These results reveal a complex crystallization kinetics that deviates from the typical crystallization behavior of polymers, being more accentuated in the crystallization from the smectic liquid.

5.3 Results and discussion

5.3.1 Thermotropic phase behavior of PBTTT

We begin our study by resolving the thermotropic phase behavior of PBTTT. For that, PBTTT ($M_w = 65{,}000$; $Đ = 2.5$) thin-films (~100 nm thick) were spun cast onto FSC chip sensors. The thermal protocol applied is shown in Figure 5.1A. PBTTT films were first heated well above the high-temperature transition, T_{LC}, (*e.g.*, 350 °C) for 1 s to erase any previous thermal history while avoiding thermal degradation of the material. Then, the material was rapidly cooled (at 4,000 ºC/s) to a range of isothermal temperatures (T_a) and held at those $T_a s$ for 1 h. During this time, the material had time to undergo the physical process that is relevant at that temperature, *e.g.*, crystallization, physical aging, ordering of the liquid mesophase, etc. Subsequently, the material was cooled at 4,000 ºC/s to a temperature well below T_g, (*e.g.*, −80 °C). From there, a heating scan at 4,000 ºC/s was recorded up to a temperature above T_{LC} (referred to as "Analysis Scan" in Figure 5.1A). Finally, the material is cooled to a temperature below T_g at 4,000 ºC/s and a second heating scan was recorded (also at 4,000 ºC/s), which will serve as a reference scan.

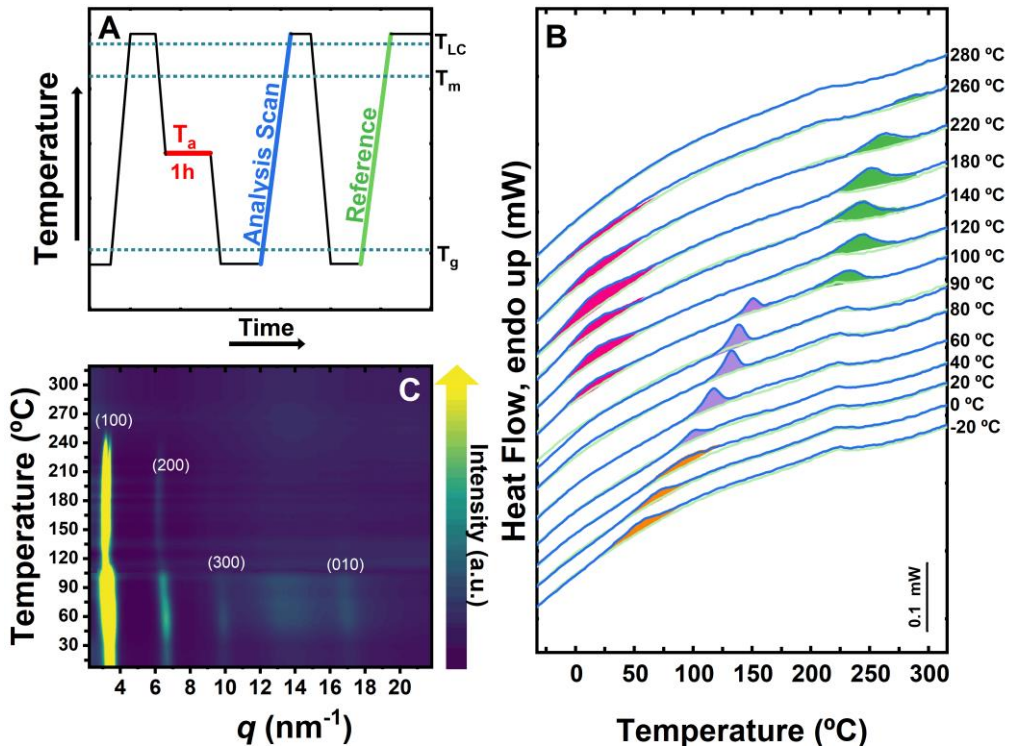

Figure 5.1. A) Thermal protocol employed for the experiments. B) FSC heating traces referred to as "Analysis Scans" and "Reference Scans" in A (conducted at 4,000 °C/s). Endothermic peaks are highlighted in orange, purple, pink and green. C) Temperature-resolved in situ grazing incidence wide angle X-ray scattering (GIWAXS) data during heating.

Figure 5.1B displays the calorimetric signals resulting from the heating traces referred to as "Analysis Scan" and "Reference Scan" for each T_a applied. The corresponding $T_a s$ are shown on the right-hand side of each curve. We note that any significant difference between the "Analysis Scan" and the "Reference Scan" results from the development of a specific physical process during the isothermal step at the indicated T_a, thereby reflecting the thermal response of PBTTT at that T_a. As a result, the analysis of the differences between the "Analysis Scan" and "Reference Scan" in the whole range of $T_a s$ informs about the thermotropic phase behavior of the material.

Our data shows at least four distinct endothermic processes in the "Analysis Scans" that are absent in the "Reference Scans" (these endothermic processes are shadowed in different colors). At low T_as, from $T_a = -70$ °C to approximately $T_a = 20-30$ °C, an endotherm corresponding to the enthalpic relaxation during the devitrification can be observed (shadowed in orange). Because enthalpic relaxations are linked to the physical aging of the material during the isothermal step, it can be concluded that PBTTT is in a glassy state in the temperature region below $20-30$ °C, which corresponds to the T_g of the material. Whether our data includes one or two distinct enthalpic relaxation processes is a question that needs to be investigated further.

At $T_a s$ immediately higher than T_g (T_a values ranging from 40 °C to 100 °C) PBTTT is a supercooled liquid and, therefore, it should be able to crystalize during the isothermal steps. The melting of crystals formed by cold crystallization at $T_a s$ between 40 and 100 ºC resulted in sharp endothermic peaks (highlighted in purple). Hence, within this temperature range, PBTTT is semicrystalline. Temperature-resolved grazing incidence wide angle X-ray scattering (GIWAXS) results shown in Figure 5.2 support this interpretation as it clearly demonstrates that the crystallization of PBTTT progresses at 80 ºC (the intensity of the (hk0) and the (010) peaks increase and a new peak centered at $q \approx 16$ nm^{-1} appears), which is incompatible with PBTTT being below T_g at that temperature. Interestingly, the area of the crystal melting endotherm in Figure 5.1B increases until it reaches a maximum at around $T_a = 80$ °C, which corresponds to the T_a at which the crystallization develops faster.

We associate the endothermic peak located at $T \approx 250$ ºC (shadowed in green) with the order-disorder transition of the liquid, *i.e.*, to the smectic-to-isotropic transition. Therefore, within the T_a range where this peak is visible in Figure 5.1B *(i.e.,* between $T_a = 110$ ºC and $T_a = 260$ ºC), the

thermodynamically stable phase in PBTTT is the liquid crystalline smectic mesophase (*LC state*). Above $T_a = 260$ ºC; therefore, PBTTT is in the disordered liquid state or isotropic state (*ISO state*).

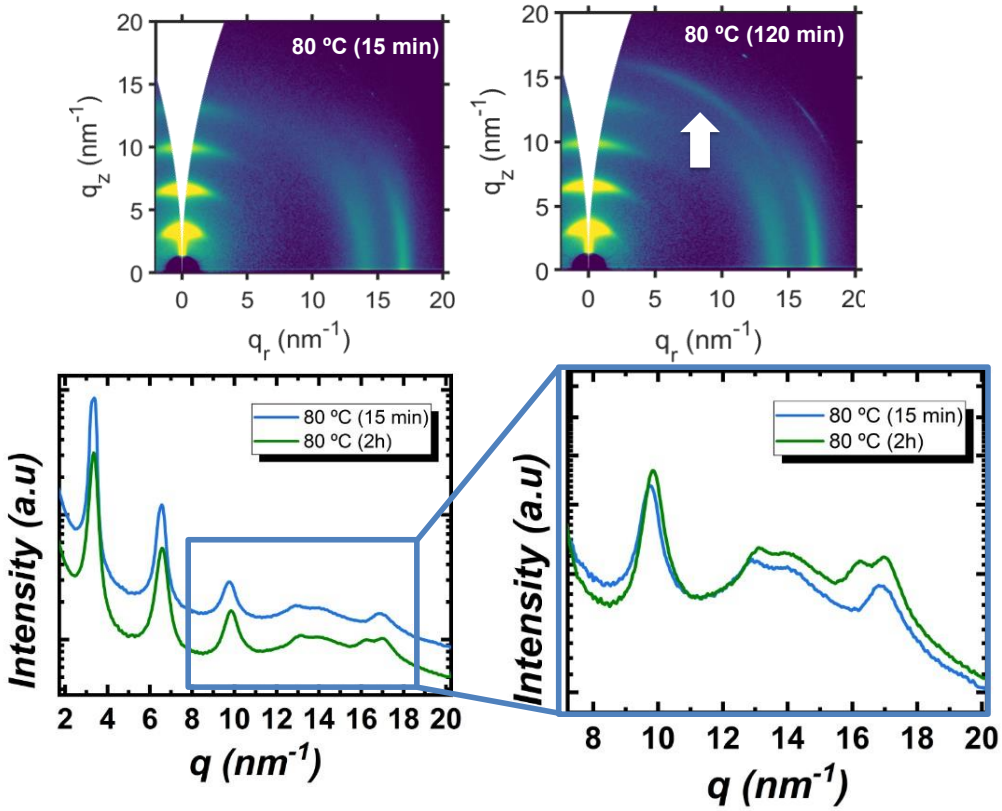

Figure 5.2. GIWAXS patterns for PBTTT films annealed at $T_c = 80$ ºC for 15 min and 120 min.

It should be noted that this endothermic peak (at $T \approx 250$ ºC) has often been associated with the melting of crystals, and therefore, PBTTT has been considered to be in the semicrystalline below 250 ºC. However, our data evidences that PBTTT is a liquid (crystal) between $T \approx 120$ ºC and $T \approx 250$ ºC. For example, temperature-resolved GIWAXS experiments shown in Figure 5.1C and in Figure 8.1 in Appendix 1, located in Chapter 8, reveal no (010) peak, thereby π-π stacking, at temperatures higher than ≈120 ºC.

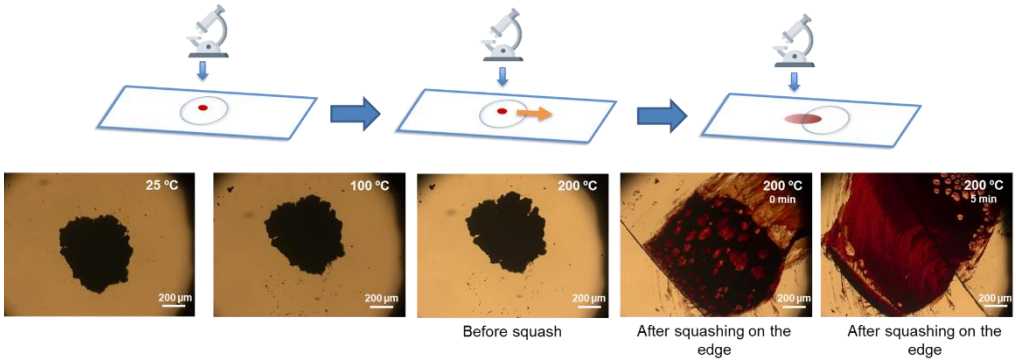

Figure 5.3. Optical microscopy images of a small piece of PBTTT acquired at the indicated temperatures. The images on the right hand side clearly show that PBTTT is a liquid at 200 ºC.

Moreover, the optical microscopy experiments included in Figure 5.3 and Figure 5.4 suggest that PBTTT is a flowable birefringent liquid at 200 ºC, while it is a rigid solid at 100 ºC.

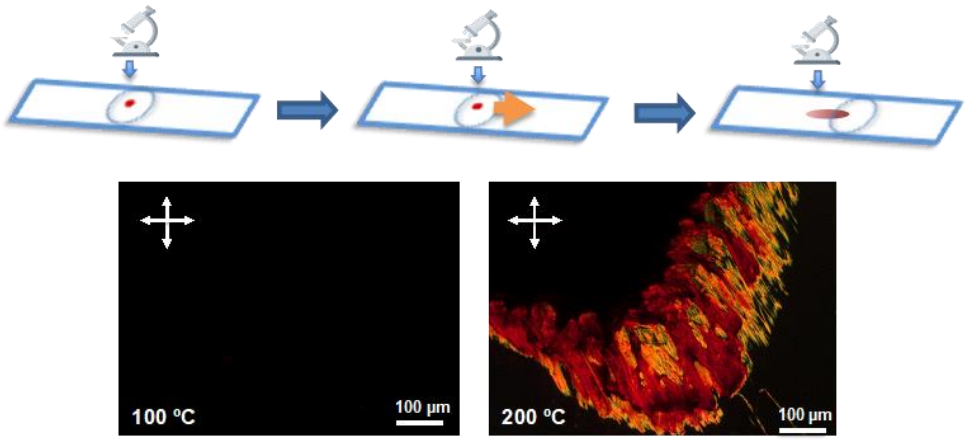

Figure 5.4. Optical microscopy images of a small piece of PBTTT acquired at the temperatures indicated. The images on the right hand side clearly show that PBTTT is a birefringent liquid at 200 ºC.

Lastly, we also found deviations in the "Analysis Scans" with respect to "Reference Scans" in the temperature region between 50 and 100 ºC when T_as

between 100 °C and 260 °C where applied, *i.e.,* when PBTTT was annealed at temperatures where the smectic mesophase is formed. While it cannot be ruled out the possibility that this broad endothermic overshoot results from the melting of side-chain crystals as it has been previously reported, we are more inclined to associate this signal with the increase of the enthalpy during the devitrification of the smectic glass. This could be explained by the fact that during a certain range of annealing temperatures, some of the amorphous fraction of PBTTT undergoes physical ageing, particularly when the temperature is lowered to −80 ºC, leading to an aged state in the amorphous fraction which is reflected as the low-temperature overshoot. We argue that any endothermic process showing up at such low temperatures must be related to a thermal process involving material regions that are rich in side chains. Therefore, the endothermic peak could result from two processes: the melting of crystallites formed by alkyl side chains and enthalpy relaxation from physically aged glassy domains that are rich in side chains. Our main rationales for associating this endothermic peak with the latter possibility are: (i) the peak is very broad, which is more compatible with enthalpy relaxation than with a melting peak (see *e.g.,* the comparison between the orange peak and the purple peak in Figure 5.1B). (ii) The little shift of the peak position with T_a is also more compatible with a glass transition process than with a melting process. (iii) Prior to the heating scan in which the endothermic peak appears, samples had been quenched at 4,000 ºC/s, which is expected to hinder (if not suppress) the crystallization.

Temperature-resolved GIWAXS experiments, shown in Figure 5.1C, agree well with our overall interpretation of the thermotropic behavior of PBTTT. In these experiments, spin-coated PBTTT thin-films were heated from room temperature to 30 ºC at 20 ºC/min while, simultaneously, GIWAXS patterns were recorded (see Figure 8.1 in Appendix 1, located in Chapter 8). The

thermal history applied to these samples is, therefore, different to that of the FSC experiments, but the information we obtain regarding the thermotropic phase behavior is highly complementary. Our GIWAXS data shows an overall decrease of the scattered intensity at ~120 ºC, coinciding with the melting of PBTTT crystals detected by FSC (*e.g.*, for a T_a = 20 ºC, which is comparable to a sample being stored at room temperature, like the one analyzed in GIWAXS). Moreover, at temperatures higher than 120 ºC, only the diffraction peaks associated with a layer ordering, *i.e.*, the set of (*h*00) peaks of the smectic mesophase, are visible, while the (010), associated with the π-π stacking of backbones, is missing, which also agrees with the absence of crystals. Eventually, at ~250 ºC, all reflections from the mesophase disappear when PBTTT transforms into a disordered liquid.

Hence, our analysis shows that — contrary to some previously reported works — PBTTT is in a liquid state at both "annealing temperatures" applied for the achievement of the terrace and the ribbon phases. This, first of all, means that such thermal treatment cannot be considered as actual annealing processes, as there are no crystals at those temperatures. The terrace-phase semicrystalline PBTTT is achieved when samples are "annealed" at 180 ºC, thereby within the temperature range where PBTTT is in the smectic mesophase. In contrast, for the achievement of the ribbon-phase, PBTTT should be "annealed" above the smectic-to-isotropic transition. A further conclusion from the above is that the formation of the semicrystalline terrace- or ribbon phases must occur via liquid-solid transition, *i.e.*, a crystallization processes. This is an important outcome as it means that terrace and ribbon morphologies can be further controlled/tuned via the experimental conditions in which crystallization occurs, *e.g.*, the cooling rate.

5.3.2 Crystallization kinetics and morphology of PBTTT

Motivated by these findings, we then investigated the crystallization kinetics of PBTTT thin-films starting from both the isotropic and the smectic liquids (a schematics of the crystallization process from each liquid state is included in Scheme 5.1).

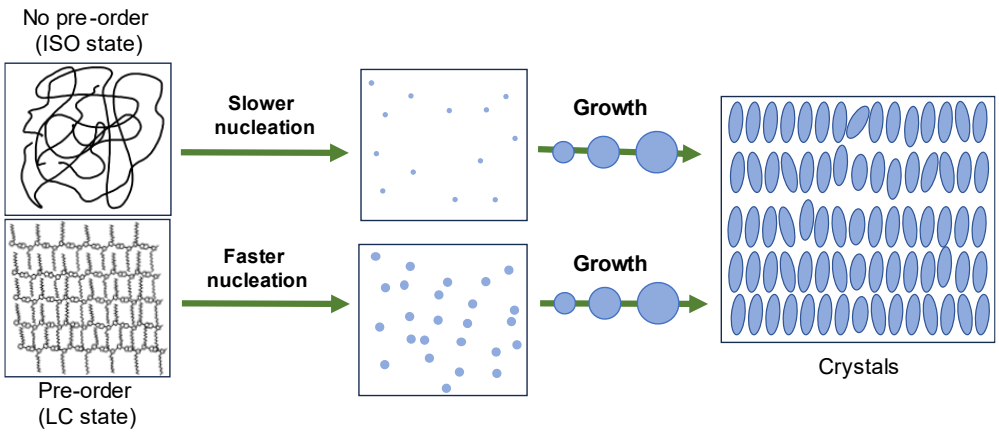

Scheme 5.1. Diagram of crystallization from an *ISO state* and a *LC state*.

For that, we needed to design adequate thermal protocols. Figure 5.5A and Figure 5.5B display the thermal protocols employed to investigate the crystallization kinetics from the isotropic melt and from the smectic mesophase, respectively. The former is similar to the previous section of the manuscript, but here, the length of the isothermal step (t) is varied from 1 to 86,400 s (24 h). In addition, T_as are limited to the range where the crystallization occurs, *i.e.*, between $T_c = 60$ ºC and $T_c = 90$ ºC. Hence, the "Analysis (heating) Scans" show the melting peak of the crystals isothermally formed within the time t at the selected T_c and so, the enthalpy of this peak can be used to monitor the advance of the crystallization, *i.e.*, the crystallization kinetics.

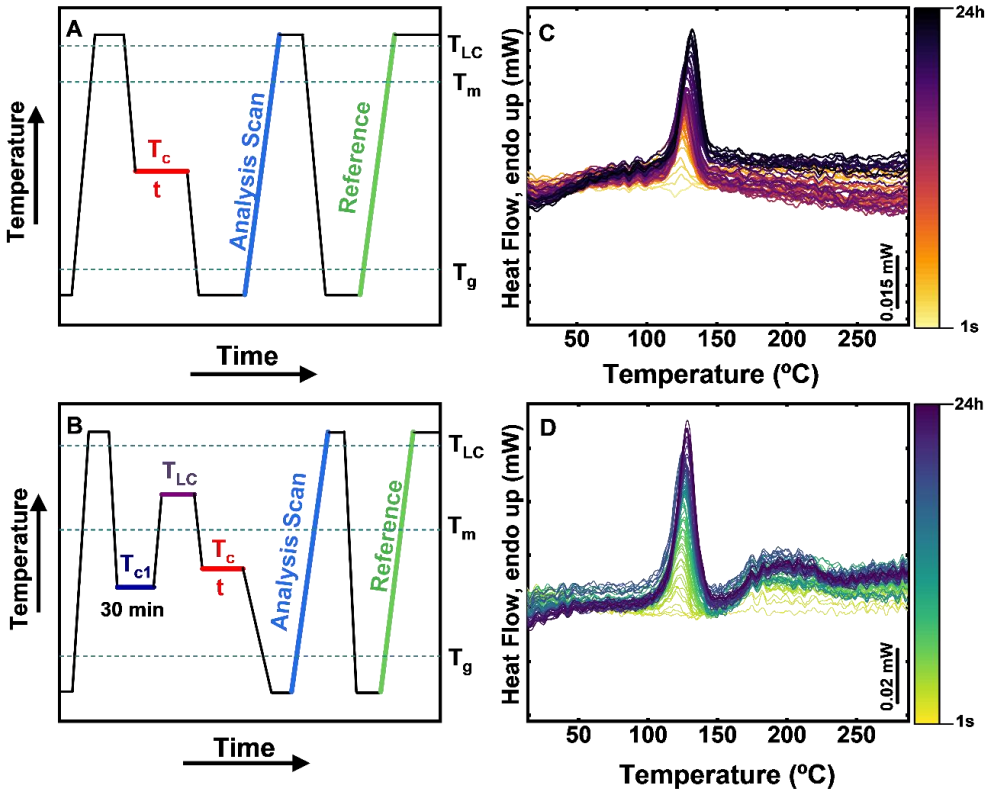

Figure 5.5. A) Thermal protocol used to study the crystallization kinetics from the disordered liquid state. B) Thermal protocol used to study the crystallization kinetics from the smectic liquid state. C) FSC Analysis Scans recorded when the thermal protocol in Figure 5.5A is applied (with $T_a = 80$ ºC). D) FSC Analysis Scans recorded when the thermal protocol in Figure 5.5B is applied (with $T_a = 80$ ºC).

We must note that the experiments shown in the previous section of the manuscript no signs of smectic mesophase when PBTTT was rapidly cooled down from 350 ºC (at 4,000 ºC) and then annealed between $T_a = 50$ °C and $T_a = 90$ °C, indicating that no mesophase was forming prior to crystallization at those temperatures and, hence, that PBTTT can be crystallized from a completely disordered liquid state (*ISO state*) at those T_as.

The thermal protocol designed to investigate the crystallization kinetics

from the smectic phase includes a first step in which the mesophase is created. We already showed that the development of the smectic mesophase occurs faster at 180 ºC (the application of a T_a of 180 °C results in the most intense smectic-to-isotropic transition peak). Thus, 180 ºC seems to be a suitable starting temperature for the crystallization of the smectic liquid. Moreover, preliminary studies showed that the smectic mesophase was more efficiently developed at 180 ºC upon heating from the solid crystalline phase than upon cooling from the isotropic melt to avoid degradation at high temperatures over time. Therefore, the thermal protocol included an initial isothermal step at a $T_c = 80$ °C for 30 min in which crystals are created, followed by a further isothermal step at $T = 180$ ºC for 1 min in which the smectic mesophase is developed. From this point on, the thermal history applied is equal to the above-mentioned protocol.

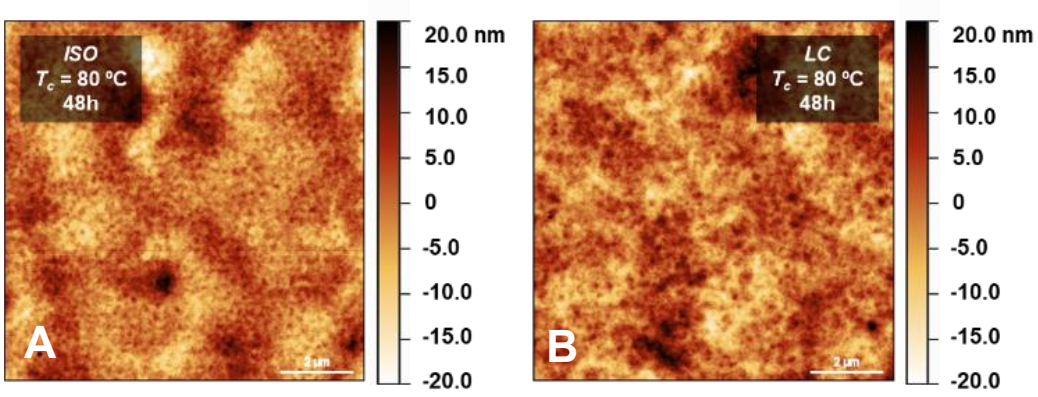

Figure 5.6 A) AFM-height images of PBTTT crystallized at $T_c = 80$ °C to form a ribbon phase after 48 h (*ISO state*). B) AFM-height images of PBTTT crystallized at $T_c = 80$ °C to form a terraced phase after 48h (*LC state*).

Atomic Force Microscopy (AFM) of the thin-films subject to the thermal protocols described above (shown in Figure 5.7) confirms the different solid-state morphologies of resulting thin-films. We must note, however, that AFM data do not unarguably show that resulting morphologies (after the thermal

treatment applied in FSC for the kinetics study) correspond to the terrace and the ribbon phases. It is well-known terrace and ribbon phases are better formed when films are slowly cooled down (*e.g.*, 20 ºC/min) from the suitable temperatures to room temperature, while here, samples are isothermically crystallized at T_c = 80 ºC (after extremely fast coolings from suitable temperatures).

Figure 5.5C and Figure 5.5D show the FSC heating traces referred to as "Analysis Scans" in the protocols displayed in Figure 5.5A and Figure 5.5B, respectively. These heating traces feature the melting peak of crystals formed at $T_c = 80$ ºC for the different crystallization times starting from the isotropic state (Figure 5.5C) and the mesophase (Figure 5.5D). The integration of these peaks and ulterior normalization to the integral value of the longest crystallization time (t = 24 h) yield normalized degree of crystallinity values were plotted in Figure 5.6A and Figure 5.6B. We note that the endothermic peak of the smectic-to-isotropic transition can also be seen at ~200 ºC in Figure 5.5D.

Figure 5.6A and Figure 5.6B indicate that none of the PBTTT samples are able to complete their crystallization in the maximum allowed time, *i.e.*, 24 h, as the isothermal crystallization curves do not reach a saturation point. Equally striking is that the analysis evidences a complex advance of the crystallization that deviates from the typical sigmoidal curves usually obtained during the isothermal crystallization of most semicrystalline polymers[16,17]. Plotted in a semi-log scale, curves shown in Figure 5.6B display an initial sigmoidal shape (up to a ~50% conversion) followed by an approximately linear trend. Although this behavior is observed in all curves, it is especially noteworthy for PBTTT crystallized from the $LC\ state$. We argue that this unusual behavior can occur when the crystallization process is complex and involves multiple stages.

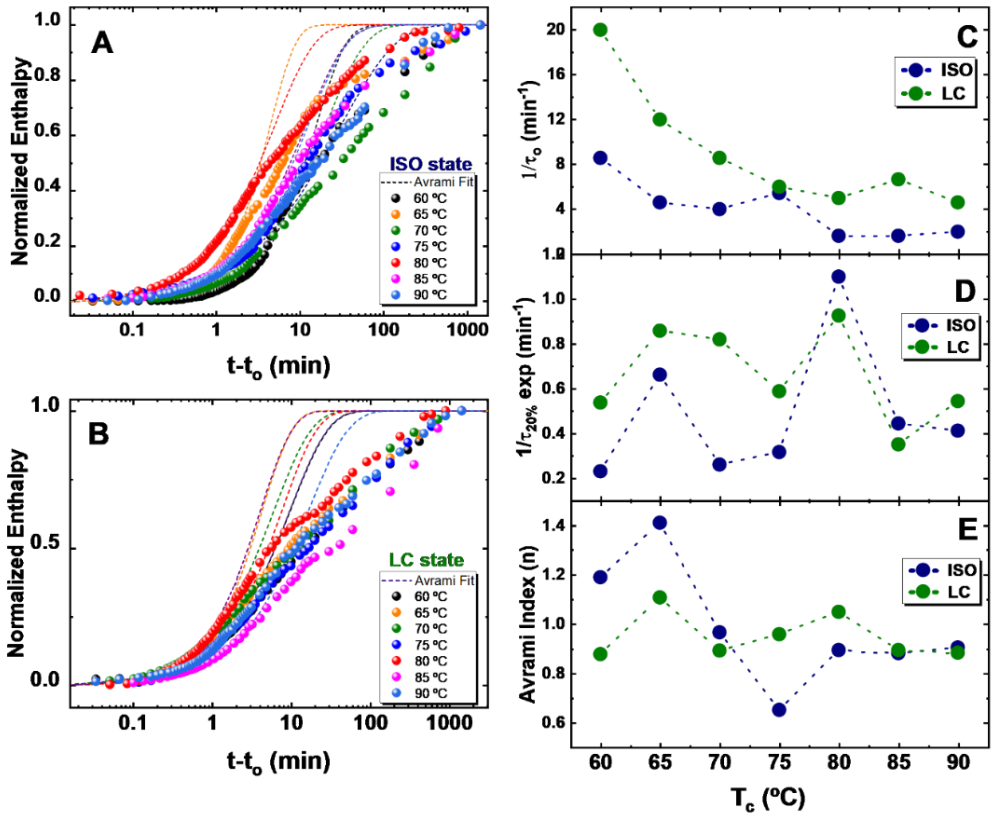

Figure 5.6. Crystallization kinetics from an *ISO state* and from a *LC state* for varying times at T_c = 80 °C. A) Advance of crystallization (from normalized enthalpy values) with time at the indicated temperatures and their corresponding Avrami fits from an *ISO state*. B) Advance of crystallization (from normalized enthalpy values) with time at the indicated temperatures and their corresponding Avrami fits from a *LC state*. C) Experimental values of the inverse of induction times ($1/t_o$). D) Experimental values of the inverse of crystallization times ($1/\tau_{20\%}$). E) Experimental values of the Avrami index (n); t and t_o are the crystallization time and the induction time, respectively.

In the crystallization process of polymers, primary nucleation occurs first, and it is immediately followed by the free growth of crystallites into semicrystalline superstructures (*i.e.*, 1D, 2D, or 3D structures composed of crystallites separated by amorphous intervening layers). Both steps constitute

the so-called primary crystallization process and typically extend over the initial 50% conversion. After primary crystallization, the semicrystalline superstructures impinge on one another, and the secondary crystallization starts, which develops with very different kinetics than the primary crystallization.

In this context, we explain the results in Figure 5.6A and Figure 5.6B by considering that the sigmoidal initial part of the isothermal curves of relative conversion versus time is associated with the primary crystallization process. In contrast, the second part of the kinetic curves corresponds to the secondary crystallization. Although these two crystallization stages occur in all semicrystalline polymers, both stages are partially overlapped in flexible thermoplastic materials like polyolefins, which is why the transition from the primary to the secondary crystallization occurs in succession with a smooth transition between them at approximately 50% conversion to the semicrystalline state (see the typical behavior, as an example, of polypropylene in Figure 5.7A and a comparison with our experimental data in Figure 5.7B).

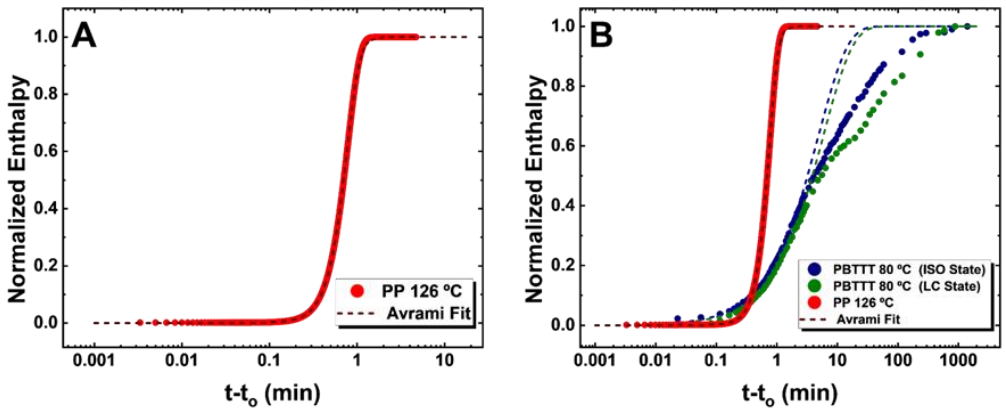

Figure 5.7. Crystallization kinetics. A) Example of Polypropylene (PP) normative crystallization kinetics. B) Comparison of PP kinetics with the data obtained of PBTTT at $T_c = 80$ ºC.

In the case of PBTTT, a sharp transition between the first and the secondary crystallization process is clearly observed. We note, moreover, that

this sharp transition is particularly noticeable when the crystallization occurs from the $LC\ state$. We argue that PBTTT chains may experience diffusion limitations during secondary crystallization by the surrounding crystallites because parts of the chains may be within neighboring crystals or at the interphase between the crystallites and the melt. Therefore, secondary crystallization, which can also involve the re-organization and alignment of the chains within crystalline domains, is especially slow in the crystallization of a relatively rigid molecule like PBTTT, particularly when the polymer is crystallized from the smectic state. As a result, PBTTT may not be able to reach a saturation point in its crystallization process (within the time frame explored here).

To further evaluate the crystallization kinetics, experimental data was fitted to the Avrami model. We note that this model adequately describes the overall crystallization kinetics of a material that includes both the primary nuclei formation and the free growth of crystalline features until they impinge with one another (*i.e.*, until secondary crystallization begins), which for regular polymers typically occurs within the initial 50% of the total conversion. Therefore, fittings for large crystallization conversions tend to be, in general, inadequate, and often, as is the case for PBTTT kinetics, much lower conversions, *e.g.*, of 3−20% are used to describe the kinetics within the primary crystallization range. It is noteworthy, though, that the conversion range that fits to the Avrami model is specially short for PBTTT (note the comparison with PP in Figure 5.7), which would also agree with a slightly different crystallization mechanism, compared to polyolefins, for example.

The model yields the expression below:[18,19]

$$1 - V_c\,(t - t_o) = \exp(-k(t - t_o)^n) \qquad \text{Equation 5.1}$$

where V_c is the relative volumetric transformed fraction to the crystalline

state, k is the overall crystallization rate constant that includes nucleation and growth components, n is the Avrami index, t is the crystallization time and t_o the induction time or the time for primary nucleation before growth has started. Hence, the inverse of the induction time ($1/t_o$) is proportional to the primary nucleation rate of PBTTT, before any growth starts.

The data shown in Figure 5.6C reveals that as T_c increases, the rate of primary nucleation decreases when crystallizing from both states. Interestingly, the nucleation rate is generally faster when crystallizing from a $LC\ state$ than when crystallizing from an $ISO\ state$. In agreement with previous results[15], this finding suggests that the preexisting molecular order in the liquid crystalline state accelerates the nucleation rate, most probably because the mesophase is acting as a precursor from which primary nuclei can form.

The overall crystallization kinetics of PBTTT when crystallizing from a $LC\ state$ and from an $ISO\ state$ can be further examined by comparing the experimental data to the fitted results of the Avrami equation. The results obtained at a 20% conversion (conversion at which a good fitting is obtained) show that the crystallization rate ($1/\tau_{20\%}$) from a $LC\ state$ is faster than when crystallizing from an $ISO\ state$ at low T_cs from $T_c = 60$ °C to $T_c = 75$ °C (see Figure 5.6D). Interestingly, at $T_c = 80$ °C the rate of crystallization suddenly increases when crystallizing from both states, with the rate of crystallization from the $ISO\ state$ being the fastest. Finally, as further increases from $T_c = 85$ ºC to $T_c = 90$ °C, the rate of crystallization becomes overall slower but similar from both states of crystallization.

The Avrami index (n) can provide information on the crystalline superstructural dimensionality and type of nucleation occurring during crystallization. Figure 5.6E shows that the Avrami index values found for PBTTT when crystallizing from both an $ISO\ state$ and an $LC\ state$ can be

approximated to 1 (the values for all crystallization temperatures and conditions can be found in Table 8.1 in Appendix 1, located in Chapter 8). A value of n = 1 suggests the development of instantaneously nucleated needle-like crystals (or 1D structures). Although the formation of ribbon-like and terrace-like morphologies should involve different growth geometries, both are primarily formed via the π-π stacking of chains, which is essentially a one-dimensional process.

5.3.3 Conclusions

In conclusion, our results firstly evidence that it is utterly important to resolve the thermotropic phase behavior semiconducting polymers in order to advance both structure/properties interrelationships and device optimization protocols based on thermal annealing. For example, our study highlights that the "thermal annealing" process yielding the high-mobility terrace phase cannot be consider a proper annealing, because PBTTT is a liquid at those temperatures. Hence, we argue that the terrace-phase is formed via a crystallization process.

Our isothermal crystallization studies demonstrate, moreover, that the crystal nucleation rate is faster when PBTTT crystallizes from the smectic mesophase compared to the isotropic liquid phase, which agrees with our previous study on poly(9,9-di-n-octylfluorenyl-2,7-diyl) (PFO)[15]. More interestingly, we observe a complex overall crystallization kinetics for PBTTT that differs from the general crystallization behavior of polymers, which highlights (once again) the necessity to conduct more fundamental investigations of the structure development of semiconducting polymers.

5.4 References

(1) Peng, Z.; Ye, L.; Ade, H. Understanding, Quantifying, and Controlling the Molecular Ordering of Semiconducting Polymers: From Novices to Experts and Amorphous to Perfect Crystals. *Mater Horiz* **2022**, *9* (2), 577–606.

(2) Murad, A. R.; Iraqi, A.; Aziz, S. B.; Abdullah, S. N.; Brza, M. A. Conducting Polymers for Optoelectronic Devices and Organic Solar Cells: A Review. *Polymers* **2020**, *12* (11), 1–47.

(3) Lim, J. A.; Liu, F.; Ferdous, S.; Muthukumar, M.; Briseno, A. L. Polymer Semiconductor Crystals. *Mater. Today* **2010**, *13* (5), 14–24.

(4) Furushima, Y.; Toda, A.; Schick, C. Effect of Multi-Step Annealing above the Glass Transition Temperature on the Crystallization and Melting Kinetics of Semicrystalline Polymers. *Polymer* **2020**, *202*.

(5) McCulloch, I.; Heeney, M.; Bailey, C.; Genevicius, K.; MacDonald, I.; Shkunov, M.; Sparrowe, D.; Tierney, S.; Wagner, R.; Zhang, W.; Chabinyc, M. L.; Kline, R. J.; McGehee, M. D.; Toney, M. F. Liquid-Crystalline Semiconducting Polymers with High Charge-Carrier Mobility. *Nat. Mater.* **2006**, *5* (4), 328–333.

(6) Delongchamp, D. M.; Kline, R. J.; Jung, Y.; Germack, D. S.; Lin, E. K.; Moad, A. J.; Richter, L. J.; Toney, M. F.; Heeney, M.; Mcculloch, I. Controlling the Orientation of Terraced Nanoscale "Ribbons" of a Poly(Thiophene) Semiconductor. *ACS Nano* **2009**, *3* (4), 780–787.

(7) DeLongchamp, D. M.; Kline, R. J.; Lin, E. K.; Fischer, D. A.; Richter, L. J.; Lucas, L. A.; Heeney, M.; McCulloch, I.; Northrup, J. E. High Carrier Mobility Polythiophene Thin Films: Structure Determination by

Experiment and Theory. *Adv. Mater.* **2007**, *19* (6), 833–837.

(8) Zhang, L.; Li, H.; Zhao, K.; Zhang, T.; Liu, D.; Wang, S.; Wu, F.; Zhang, Q.; Han, Y. Improving Crystallinity and Ordering of PBTTT by Inhibiting Nematic to Smectic Phase Transition via Rapid Cooling. *Polymer* **2022**, *256*, 125178.

(9) Delongchamp, D. M.; Kline, R. J.; Jung, Y.; Lin, E. K.; Fischer, D. A.; Gundlach, D. J.; Cotts, S. K.; Moad, A. J.; Richter, L. J.; Toney, M. F.; Heeney, M.; McCulloch, I. Molecular Basis of Mesophase Ordering in a Thiophene-Based Copolymer. *Macromolecules* **2008**, *41* (15), 5709–5715.

(10) McCulloch, I.; Heeney, M.; Chabinyc, M. L.; DeLongchamp, D.; Kline, R. J.; Cölle, M.; Duffy, W.; Fischer, D.; Gundlach, D.; Hamadani, B.; Hamilton, R.; Richter, L.; Salleo, A.; Shkunov, M.; Sparrowe, D.; Tierney, S.; Zhang, W. Semiconducting Thienothiophene Copolymers: Design, Synthesis, Morphology, and Performance in Thin-Film Organic Transistors. *Adv. Mater.* **2009**, *21* (10–11), 1091–1109.

(11) Percec, V.; Kawasumi, M. Synthesis and Characterization of a Thermotropic Nematic Liquid Crystalline Dendrimeric Polymer. *Macromolecules* **1992**, *25* (15), 3843–3850.

(12) Ding, Q.; Jehnichen, D.; Göbel, M.; Soccio, M.; Lotti, N.; Cavallo, D.; Androsch, R. Smectic Liquid Crystal Schlieren Texture in Rapidly Cooled Poly(Butylene Naphthalate). *Eur. Polym. J.* **2018**, *101*, 90–95.

(13) Kang, E. S. H.; Kim, E. Effect of Non-Isothermal Recrystallization on Microstructure and Transport in Poly(Thieno-Thiophene)Thin Films. *Org. Electron.* **2011**, *12* (10), 1649–1656.

(14) Vakhshouri, K.; Gomez, E. D. Effect of Crystallization Kinetics on Microstructure and Charge Transport of Polythiophenes. *Macromol. Rapid Commun.* **2012**, *33* (24), 2133–2137.

(15) Pirela, V.; Campoy-Quiles, M.; Müller, A. J.; Martín, J. Unraveling the Influence of the Preexisting Molecular Order on the Crystallization of Semiconducting Semicrystalline Poly(9,9-Di-n-Octylfluorenyl-2,7-Diyl (PFO). *Chem Mater* **2022**, *34* (23), 10744–10751.

(16) Conjugated Polymers. In *The Physics of Polymers: Concepts for Understanding Their Structures and Behavior*; Strobl, G., Ed.; Springer: Berlin, Heidelberg, 2007; pp 287–312.

(17) Piorkowska, E.; Rutledge, G. C. *Handbook of Polymer Crystallization*; John Wiley & Sons, 2013.

(18) Lorenzo, A. T.; Arnal, M. L.; Albuerne, J.; Müller, A. J. DSC Isothermal Polymer Crystallization Kinetics Measurements and the Use of the Avrami Equation to Fit the Data: Guidelines to Avoid Common Problems. *Polym. Test.* **2007**, *26* (2), 222–231.

(19) Pérez-Camargo, R. A.; Liu, G. M.; Wang, D. J.; Müller, A. J. Experimental and Data Fitting Guidelines for the Determination of Polymer Crystallization Kinetics. *Chin. J. Polym. Sci.* **2022**, *40* (6), 658–691.

Chapter 6

Crystallization behavior of polymorphic alternating copolymer DMDS-alt-DVE

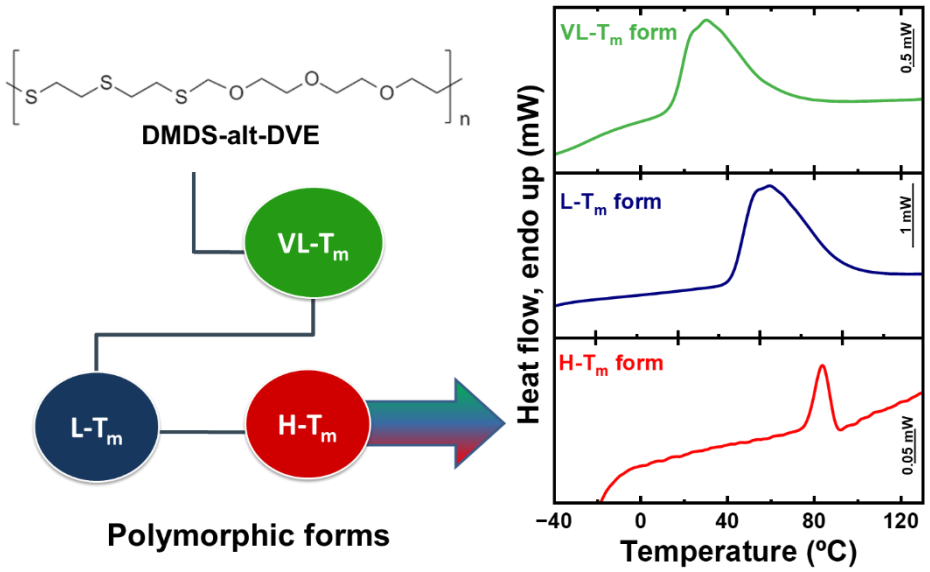

6.1 Abstract

A complex crystallization behavior was observed for the alternating copolymer DMDS-alt-DVE synthesized via thiol-ene step-growth polymerization. Understanding the underlying complex crystallization processes of such innovative polythioethers is critical for their application, for example, in polymer coating technologies. These alternating copolymers have polymorphic traits, resulting in different phases that may display distinct crystalline structures. The copolymer DMDS-alt-DVE was studied in an earlier work, where only two crystalline phases were reported: a low melting, $L-T_m$, and high melting, $H-T_m$ phase. Remarkably, the $H-T_m$ form was only achieved by the previous formation and melting of the $L-T_m$ form. We applied calorimetric techniques encompassing seven orders of magnitude in scanning rates to further explore this complex polymorphic behavior. Most importantly, by rapidly quenching the sample to temperatures well below room temperature, we detected an additional polymorphic form (characterized by a very low melting phase, denoted $VL-T_m$). Moreover, through tailored thermal protocols, we successfully produced samples containing only one, two, or all three polymorphs, providing insights into their interrelationships. Understanding polymorphism, crystallization, and the resulting morphological differences can have significant implications and potential impact on mechanical resistance and barrier properties.

6.2 Introduction

Polymerization technologies have recently focused on thiol-ene chemistry.[1–8] Historically, this polymerization approach has been used mainly in bulk or solution for applications such as coatings or surface modification.[2,3,5,7] Aiming to make the process more eco-friendly, there has been a growing interest in thiol-ene polymerization in aqueous dispersed media, such as emulsion and miniemulsion[4,6,8–11]. Le *et al*. reported the synthesis of polythioethers with high sulfur content. Such polymers have the ability to crystallize, yielding semicrystalline properties[9] which are directly related to their chemical and mechanical resistance[12]. The characterization of newly synthesized materials, mainly when specific applications are targeted, such as barrier coatings or materials with high mechanical resistance, requires a comprehensive understanding of their crystallization behavior.

The alternating copolymer DMDS-*alt*-DVE studied in this work is derived by alternatingly linking monomers of di(ethylene glycol) divinyl ether (DVE) and 2,2'-dimercaptodiethyl sulfide (DMDS) see Scheme 6.1. The synthesis and the determination of the molecular weight are given in Chapter 3. The number average molecular weight is reported in Table 3.1 located in Chapter 3.

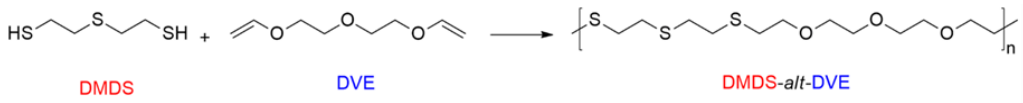

Scheme 6.1. Reaction for the formation of DMDS-*alt*-DVE.

This polythioether exhibits different polymorphic forms. In general, polymorphic materials are substances that can form several distinctly different crystalline phases[13–15]. Polymorphism can profoundly impact the mechanical, thermal, and functional properties of a material[15–17], and it is a highly researched topic in fields ranging from polymer science to electronics and biology[18]. The

crystallization behavior and phase transformations of polymorphic materials are influenced by an extensive array of factors, such as temperature variation, additives, solvents, or nucleating agents[14,17]. A specific crystal form will develop due to an interplay of thermodynamics and kinetics directly related to the processing conditions. For instance, kinetically-controlled solidification may generate metastable structures with high values in free energy, whereas thermodynamically-dominated crystallization typically leads to more stable structures[19]. Typically, the nucleation stage decides which phase will form. However, in some cases, a transformation from a metastable to a more stable form may be observed[17,20], a process often causing complications in industrial applications of these materials.

Materials exhibiting polymorphism are sometimes considered problematic, as controlling polymorph formation could be difficult[16,17]. However, in recent years, significant advances in implementing these materials in unprecedented applications have been achieved by exploiting and understanding the behavior of each polymorphic form[16–19]. The discovery of unknown, polymorphic forms with potentially different crystalline structures and a profound understanding of how they can be achieved and controlled allow for widening the spectrum of properties relevant to an array of applications[21]. For instance, isotactic poly(1-butene) (iPB) is a polymorphic material that can exist in different crystalline forms; when crystallized from the melt, it forms unstable tetragonal form II crystals. However, upon aging at room temperature, iPB will slowly transform into the more stable hexagonal form I crystals. The transformed crystals are reported to have enhanced elastic properties and a higher melting temperature, which makes iPB highly sought after for various applications, including tubes, water pipes, and pressurized tanks[22–26]. In addition, isotactic polypropylene (iPP) is known to exhibit a monoclinic α-phase, a trigonal β-phase, and the orthorhombic γ-phase. iPP mainly crystallizes into the

more thermodynamically stable α-form when crystallizing from the melt; however, by introducing β-nucleating agents, the β-form is obtained, which is reported to have higher ductility, higher impact resistance, and better weldability than the α-form[27–30].

In this work, we focus on the tunability of the alternating copolymer DMDS-*alt*-DVE by investigating the calorimetric behavior of its various polymorphs in depth. By employing experiments spanning seven orders of magnitude in scanning rates, we comprehensively understand the structural transitions within the copolymer. We utilize a microcalorimeter (μ-DSC) for low scanning rates, a conventional differential scanning calorimeter (DSC) for intermediate rates, and a fast scanning chip calorimeter (FSC) for very fast rates. The morphology is examined using polarized light optical microscopy (PLOM), while the crystalline structure is analyzed through wide angle X-ray scattering (WAXS). Our primary focus is to comprehensively understand all possible structural transitions of the DMDS-*alt*-DVE alternating copolymer and identify reliable thermal protocols that enable the tuning of properties by accessing different combinations of polymorphic phases. This knowledge is essential for maximizing the potential of this copolymer in various applications.

6.3 Results and Discussion

6.3.1 Investigating the crystallization of the H-T_m form of DMDS-*alt*-DVE alternating copolymer

Based on a combination of techniques such as a PLOM, X-ray scattering, and DSC employing scan rates of 5 ºC/min, the crystallization behavior of the alternating copolymer DMDS-*alt*-DVE was studied recently[31]. The polymorphic nature of this polymer was established, and two different polymorphic forms were identified, having distinctly different

melting temperatures (T_{m1} and T_{m2}, respectively). The low-melting temperature polymorph ($L-T_m$) was reported to have a T_{m1} of ca. 68 ºC, while the high-melting polymorph ($H-T_m$) had a T_{m2} of ca. 81 ºC. A table reporting approximate crystallization and melting temperatures obtained by the different calorimeters and the corresponding scan rates can be found in

Table **6.1**.

Table 6.1 Melting and crystallization temperatures of DMDS-alt-DVE for each technique.

Technique	T_m ($L-T_m$)	T_m ($H-T_m$)	T_m ($VL-T_m$)	T_{cc}	T_c
μ-DSC (0.2 ºC/min)	≈ 60[a]	≈ 80[b]	≈ 35[b]	≈ 65[a]	≈ 69[c]
DSC (5 ºC/min)	≈ 68[b]	≈ 81[b]	-	≈ 69[b]	≈ 40[c]
DSC (50 ºC/min)	≈ 66[b]	≈ 80[b]	-	≈ 68[b]	≈ 41[c]
FSC (1,000 ºC/s)	≈ 68[d]	≈ 83[d]	≈ 21[d]	≈ 45[a]	-

[a] Data obtained from the first heating scan of non-isothermal experiments.
[b] Data obtained from the 2nd heating scan ("Analysis Scan") of non-isothermal experiments.
[c] Data obtained from the cooling scan of non-isothermal experiments.
[d] Data obtained from the 2nd heating scan ("Analysis Scan") of isothermal experiments.

It is important to understand that these are not unique and precise values, as the scanning rates and the thermal protocol employed influence the melting point of each polymorph. This table is intended to illustrate orientative values.

In the present study, non-isothermal DSC experiments were carried out, employing heating and cooling scan rates of 20 ºC/min. The resulting scans presented no detectable differences from those obtained at a slower scan rate of 5 ºC/min[31]. The corresponding DSC results of the heating and cooling runs are reported in Figure 6.1A. During heating, the DMDS-*alt*-DVE alternating copolymer melted at $T_{m1} \approx 66$ ºC. Following this initial melting, the sample underwent a cold crystallization step at $T_{cc} \approx 68$ ºC, followed by a second melting at $T_{m2} \approx 81$ ºC.

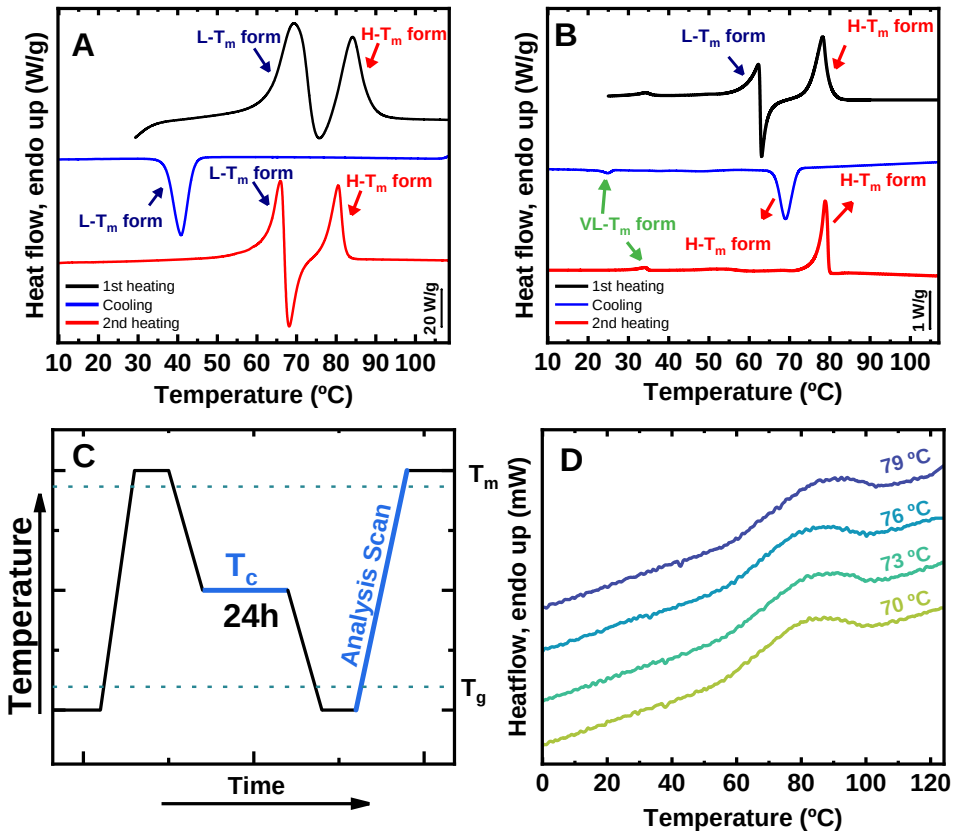

Figure 6.1. Thermal behavior of the DMDS-*alt*-DVE alternating copolymer determined via DSC, μ-DSC, and FSC. A) DSC scans at 20 ºC/min. B) μ-DSC scans at 0.2 ºC/min. C) Thermal protocol employed for isothermal crystallization in FSC. D) FSC heating scans ("Analysis Scan") after isothermal crystallization for 24 h at varying T_c. The arrows point to the peaks

corresponding to $H-T_m$, $L-T_m$, or $VL-T_m$ forms, respectively and the curves correspond to: first heating (black), cooling (blue), and second heating (red).

According to the data reported in Figure 6.1A, the first endotherm (*i.e.*, T_{m1}) is attributed to the melting of the low-melting temperature polymorph, the $L-T_m$ form. After the $L-T_m$ has melted, the sample re-crystallized at T_{cc} (in a cold-crystallization process) into the high-melting temperature polymorph, the $H-T_m$ form, which melted at higher temperatures (*i.e.*, at T_{m2}). Interestingly, when cooling from the molten state, only a single crystallization peak was observed at a crystallization temperature, at $T_c \approx 40$ ºC, indicating that only one of the polymorphs, *i.e.*, the $L-T_m$ form, crystallized during cooling, as demonstrated in our previous work[31].

Thus, by cooling from the molten state at 20 ºC/min, only the $L-T_m$ form was generated. The second heating scan in Figure 6.1A further supports this conclusion, showing similar behavior to that observed during the first heating. Upon heating, the $L-T_m$ phase melted, the sample re-crystallized (cold-crystallization) and transformed into the $H-T_m$ phase, and finally, the $H-T_m$ phase melted. This sequential behavior occurred because the molten $L-T_m$ phase provided a non-equilibrated melt with the memory of the previous ordered state, which assisted nucleation of the $H-T_m$ form[31,32]. That is, from the memory of the molten $L-T_m$ form. Interestingly, when using a conventional DSC, identical results were obtained for all scanning rates ranging from 1 ºC/min to 50 ºC/min. That is, crystallization of the $H-T_m$ form was not achieved at any of these scanning rates when cooling the sample from the molten state at $T > T_{m2}$[31]. Furthermore, our findings are consistent with Ostwald's rule of stages, which describes the sequential transformation of DMDS-alt-DVE as crystallization progresses. This phenomenon suggests that the first polymorph to crystallize from a polymer melt is the closest in structure to the amorphous state and differs the least in energy, eventually

transforming into the more stable form[33,34].

It is crucial to study the influence of the scanning rate on the formation of the $H-T_m$ form to understand if its direct formation from the melt is impossible even at an extremely slow cooling rate or if the formation of the $H-T_m$ form can also be initiated from the molten state at $T > T_{m2}$, for example, by heterogeneous nucleation. In this work, complementary experiments have been performed at rates slower than 1 ºC/min. By employing differential scanning micro-calorimetry (μ-DSC), we performed non-isothermal experiments at a cooling rate of 0.2 ºC/min in the same manner as a conventional DSC. The sample was heated for 3 min to a temperature thirty degrees above T_{m2}, slowly cooled to a temperature below T_g, and subsequently reheated above T_{m2}. Figure 6.1B shows the results of these μ-DSC experiments. The first heating scan did not exhibit any significant differences compared to the results obtained by standard DSC for rates between 1 ºC/min to 50 ºC/min (see also Figure 6.1A). The lower observed melting peak corresponds to the $L-T_m$ form, and the higher melting peak corresponds to the $H-T_m$, as indicated by arrows in Figure 6.1B. During cooling the sample at 0.2 ºC/min, a single crystallization peak was observed at a rather high temperature, with an exothermic peak at $T_c \approx 69$ ºC. Strikingly, this crystallization temperature is higher than T_{m1} measured for the $L-T_m$ phase, indicating that this crystallization peak cannot correspond to the crystallization of the $L-T_m$ form. Thus, it can only be due to the crystallization of the $H-T_m$ phase. This conclusion is further supported by the absence of any melting peak associated with the $L-T_m$ during the second μ-DSC heating scan in Figure 6.1B. A single melting point was observed during the second heating, which coincided with the melting temperature of the $H-T_m$ phase, confirming that the $H-T_m$ form crystallized at ca. 69 ºC. The results of Figure 6.1B indicate that in the μ-DSC experiments, the $H-T_m$ form of the alternating copolymer DMDS-alt-DVE can

be obtained through slow cooling (*i.e.,* at 0.2 ºC/min) of the molten sample.

In light of these results, a series of experiments were carried out to explore if the $H-T_m$ form can also be achieved by isothermal crystallization. To this end, we used FSC, a technique that allows changing temperatures so rapidly that any crystallization can be excluded during the temperature change[35–41]. For such experiments, we used a rate of 1,000 ºC/s. At such a cooling rate, we did not detect any crystallization, as will be shown later in the section on the influence of the cooling rate. To erase thermal history, the sample was first heated above the maximum melting point. Next, the sample was rapidly cooled to various values of T_c above the T_{m1} of the $L-T_m$ form. At $T_c > T_{m1}$, only the $H-T_m$ form can crystallize. At these various values of T_c, the sample was then kept for a long time, *i.e.,* 24 h. Subsequently, the sample was rapidly cooled to a temperature below T_g and heated again above the highest melting temperature of the material. The applied thermal protocol is presented schematically in Figure 6.1C. Each of these FSC heating scans (the "Analysis Scan") after isothermal crystallization at various values of T_g (see Figure 6.1D) showed a single melting endotherm at $T_m > 80$ ºC, which we associated with the melting temperature T_{m2} of the $H-T_m$ form. Thus, we have demonstrated that by providing sufficiently long times for crystallization, the $H-T_m$ form of DMDS-alt-DVE can also be obtained via isothermal crystallization.

6.3.2 Morphology of the H-T_m form of the DMDS-*alt*-DVE alternating copolymer

The morphology and structure of a crystalline phase can be influenced by several factors, including nucleation and growth kinetics and the thermal protocol applied to the sample. As a result, depending on the thermal protocol used, the same crystallographic phase can reveal different

morphologies. To generate the $H-T_m$ crystalline phase directly from the melt, an experiment was carried out using PLOM on a thick film of ca. 50 µm.

To erase thermal history, the sample was first heated thirty degrees above the maximum T_m and then cooled at 50 ºC/min to $T_c = 70$ ºC, where it was allowed to crystallize for ca. 32 h. Interestingly, as shown in Figure 6.2A, a single large spherulite was obtained within an area of ca. 1 mm^2. Such large spherulites require an extremely low nucleation probability, *i.e.*, very few nucleation sites were generated at $T_c = 70$ ºC when cooling the sample from the molten state according to the procedure described above.

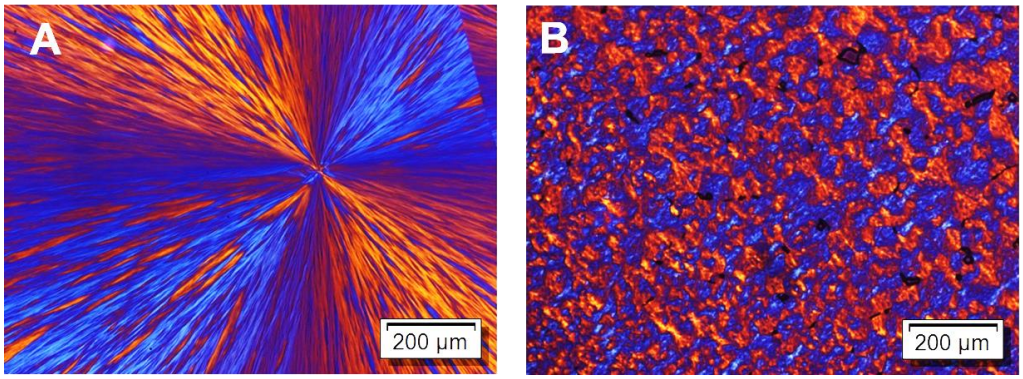

Figure 6.2. PLOM images of the $H-T_m$ form of the alternating copolymer DMDS-alt-DVE after A) isothermal crystallization at $T_c = 70$ ºC for ca. 32 h, and B) after self-seeding from the $L-T_m$ form and isothermal crystallization at $T_c = 70$ ºC for 30 min.

For comparison, Figure 6.2B shows the $H-T_m$ form obtained with the help of the melt memory of the previous crystalline state of the $L-T_m$ form for an assisted generation of the $H-T_m$ form. First, the sample was heated to erase thermal history, then cooled at 50 ºC/min to $T_c = 40$ ºC for 30 min, where the $L-T_m$ form crystallized. Subsequently, the temperature was increased in order to melt the $L-T_m$ form and to crystallize the $H-T_m$ form at $T_c = 70$ ºC for 30

min, yielding the different morphology shown in Figure 6.2B. In this case, a large number of very small impinged spherulites was observed. This nucleation density was comparable with the one previously reported for thin-films of ca. 100 nm[31]. Due to the melt memory of the molten $L-T_m$ form, a large number density of self-nucleation sites was provided, resulting in a large number of small crystallites of the $H-T_m$ form. Tentatively, we attribute the very few nucleation sites observed when cooling the sample directly from the molten state at $T > T_{m2}$ to heterogeneous nuclei with a number proportional to the sample volume. We note that in thin-films, upon cooling from the molten state at $T > T_{m2}$, we never observed crystallization of the $H-T_m$ form. Assuming that thin and thick films contain the same number of heterogeneous nuclei per unit volume, we expect that, compared to the previous examined thin-films, the here studied thick films contain 1,000 times more heterogeneous nuclei.

It should be noted that the spherulites have a positive sign, as indicated by the colors generated when a lambda plate (*i.e.,* a red-sensitive plate) is inserted at a 45º angle with respect to the polarization direction, as done in the present case. A positive spherulite has a larger refractive index (n_r) in the radial direction than in the tangential direction ($n_t < n_r$). Most polymers exhibit negative spherulites, but there are a few examples where polymers can display, depending on the crystallization conditions, positive spherulites, like isotactic polypropylene, poly(ethylene terephthalate), and poly(hydroxy butyrate)[42,43]. The exact origin of the sign of the spherulite is further explored in Chapter 7

6.3.3 Forming and characterizing the *VL*-T_m form of the DMDS-*alt*-DVE alternating copolymer

To further investigate the influence of the cooling rate on the

crystallization behavior of the alternating copolymer DMDS-alt-DVE, FSC experiments were conducted, as this technique allows for very fast cooling rates. Noteworthy results were obtained by such non-isothermal crystallization experiments performed at various cooling rates but for a constant heating rate of 1,000 ºC/s. The samples were initially heated thirty degrees above the maximum T_m to erase any thermal history, then cooled to a temperature below T_g and heated again to temperatures well above T_m. Figure 6.3 shows the FSC heating scans (obtained at a constant heating rate of 1,000 ºC/s) after cooling the samples at different rates, as indicated next to each heating curve. For cooling rates faster than 100 ºC/s, no signs of crystallization were detected during cooling, corroborated by the absence of melting peaks in the heating scans. Curves corresponding to cooling rates faster than 100 ºC/s only showed a glass transition below ca. –40 ºC. Thus, for such fast cooling rates, the material remained amorphous.

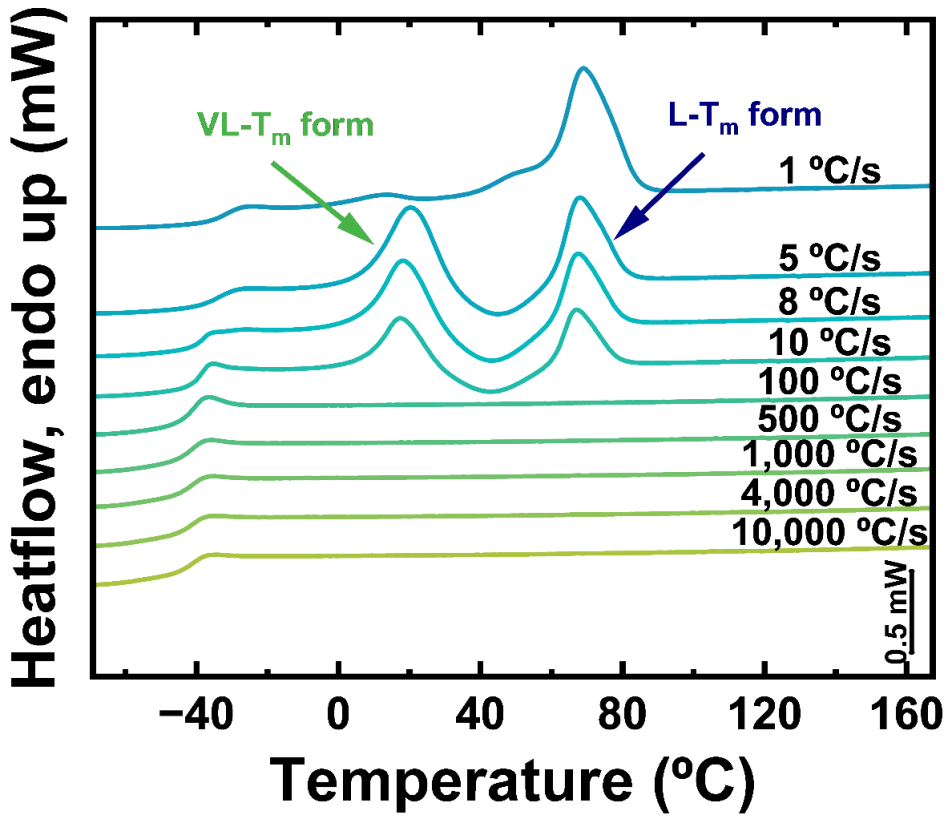

Figure 6.3. Thermal behavior of alternating copolymer DMDS-alt-DVE under non-isothermal conditions via FSC. The arrows indicate the distinct phases found during heating at a constant rate of 1,000 ºC/s, pointing to the peaks corresponding to the $L{-}T_m$ and $VL{-}T_m$ forms, respectively.

For cooling rates of 10 ºC/s, 5 ºC/s and 2.5 ºC/s, the heating scans of the samples showed a sequence of melting-recrystallization-melting processes. During the second heating scan, two distinct melting peaks, separated by a crystallization peak, were observed. A first melting peak was detected around 25 ºC, followed by a crystallization peak around 45 ºC and a second melting peak around 69 ºC. The latter two peaks coincide approximately with the crystallization and melting of the $L{-}T_m$ form observed with both DSC and μ-DSC, consistent with a previous study.[31] Outstandingly, an additional polymorphic form could be observed that is

distinct from the already identified $H-T_m$ and $L-T_m$ forms. The endotherm at $T_{m,VL} \approx 25$ ºC does not correspond to any previously reported phase, suggesting the existence of a third polymorphic form for the alternating copolymer DMDS-alt-DVE.

When cooling at rates faster than 1 ºC/s and slower than 100 ºC/s, the newly discovered very low-temperature form melts and re-crystallizes into the $L-T_m$ form, which subsequently melts. We refer to this additional phase as the very-low melting temperature form ($VL-T_m$ form or crystalline $VL-T_m$ phase). For a cooling rate of 1 ºC/s, the peak at $T_{m,VL} \approx 25$ ºC became smaller, and the one at $T_{m1} \approx 69$ ºC became more prominent. This behavior is consistent with the results shown above, for example, in Figure 6.1B. Micro-calorimetry results indicated a tiny peak at $T_m \approx 20$ ºC, suggesting that a very small amount of the $VL-T_m$ form was generated during slow cooling.

After identifying this additional polymorphic phase ($VL-T_m$ form), experiments were conducted to generate each of the three phases individually and to explore whether they can co-exist. To generate each phase individually, the samples were initially heated well above the maximum T_m to erase any thermal history (*e.g.*, to 170 ºC).

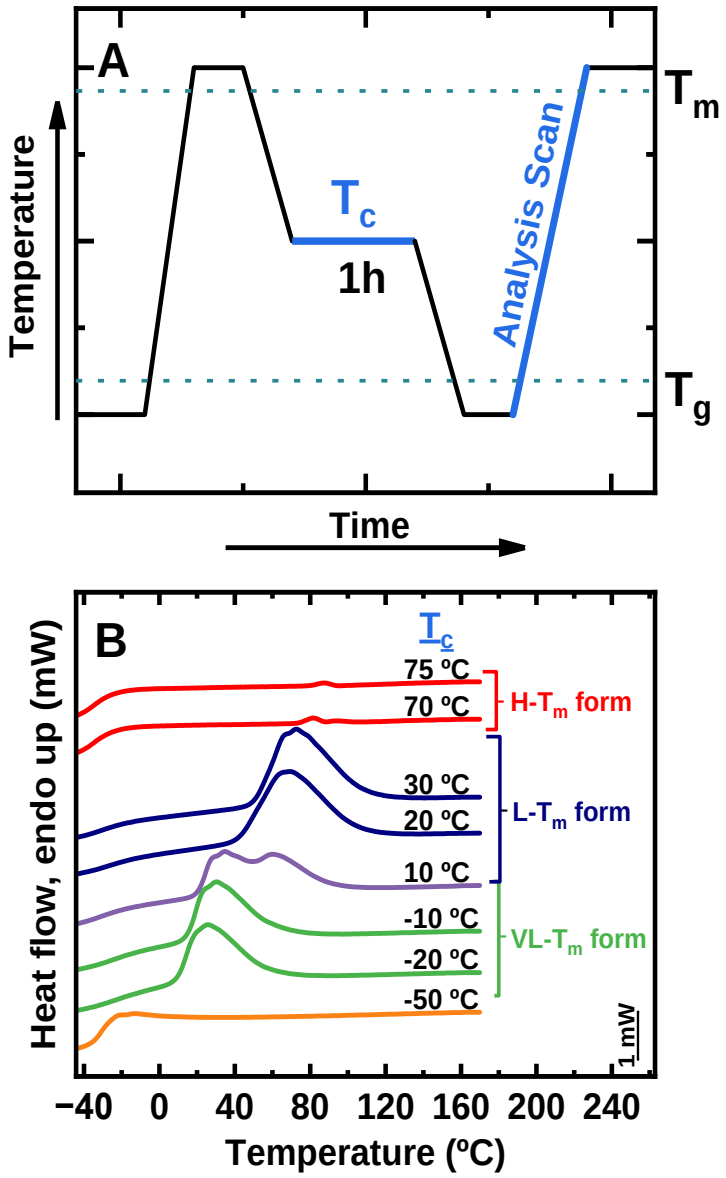

Figure 6.4. A) Thermal protocol for isothermal crystallization experiments employed at varying T_c. B) FSC heating scans at a heating rate of 4,000 ºC/s, after 1 h isothermal crystallization at the indicated values of T_c. The brackets point to the range of temperatures corresponding to the $H-T_m$, $L-T_m$, or $VL-T_m$ forms, respectively.

To avoid crystallization during cooling, samples were then rapidly cooled to different T_c values, where they were allowed to isothermally

crystallize for 1 h. Finally, the samples were rapidly cooled below T_g (*e.g.*, −80 °C). For each T_c, the subsequent FSC heating scan, denoted as "Analysis Scan" in Figure 6.4A, revealed the melting of the crystals formed during the 1 h crystallization at T_c. We have chosen heating and cooling rates of 4,000 ºC/s for the thermal protocol of Figure 6.4A.

Figure 6.4B shows the FSC heating curves measured after 1 h isothermal crystallization at the values of T_c indicated next to each curve. At $T_c = -50$ ºC, the sample was below T_g; no crystallization occurred. Upon heating at 4,000 °C/s, only the glass transition was observed at approximately −37 ºC. For a T_c range from −20 °C to −10 ºC, a broad melting endotherm around $T_{m,VL} \approx 25$ ºC could be observed. For a T_c range from 20 °C to 30 ºC, another endotherm with a higher melting point of $T_{m1} \approx 68$ ºC was found. The peak at around 25 ºC corresponds to the melting of $VL-T_m$ crystals, and that at about 68 ºC corresponds to the melting of $L-T_m$ crystals, as these values align well with previously found ones. Finally, for $T_c = 10$ ºC, we could observe the convolution of two endotherms; hence, both $VL-T_m$ and $L-T_m$ polymorphs crystallized at that temperature. Interestingly, at a first glance on Figure 6.4B, no significant endotherms could be detected after isothermal crystallization at $T_c = 70$ ºC. However, if the curve was magnified, a weak endotherm could be observed with a melting point of around 81 ºC, associated with melting of crystals of the $H-T_m$ form.

To summarize, the individual generation of each of the phases was accomplished. Through isothermal crystallization at appropriate values of T_c, samples with only one or two crystalline forms can be produced. Individual generation of the $VL-T_m$ form and the $L-T_m$ form can be mainly achieved by isothermal crystallization after rapidly cooling the sample (*e.g.*,

at rates faster than 100 ºC/s) to a very low T_c. Exclusive generation of the $H-T_m$ form can be achieved either by slow cooling from the melt or by isothermal crystallization over long periods at $T_c > T_{m1}$.

Having accomplished the generation of each phase individually by employing the protocols described above, we shift the focus to observing all three distinct forms simultaneously within the same sample. The ability of the material to adopt different crystalline structures under various thermal conditions, potentially leading to different properties, is of interest for tailoring the material properties required for specific applications. To this particular purpose, we devised a complex thermal protocol. However, it is worth noting that there are multiple alternative protocols suitable for accomplishing three distinct forms simultaneously within a sample. Nonetheless, the protocol described here is illustrative of the tunable thermal properties of this alternating copolymer.

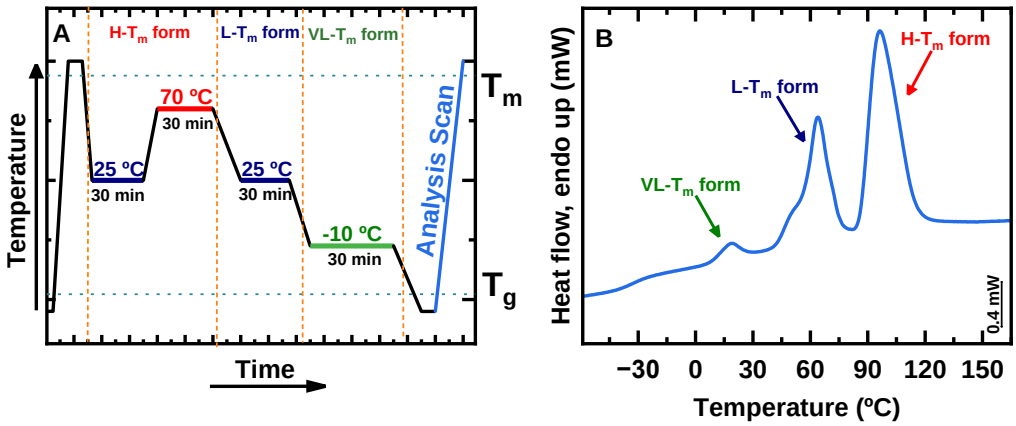

Figure 6.5. FSC experiments on alternating copolymer DMDS-*alt*-DVE. A) Thermal protocol employed to achieve all three polymorphs of this alternating copolymer within the same sample. B) FSC results obtained during the analysis (heating) scan shown in the protocol described in A. All heating and cooling rates for this experiment were 1,000 ºC/s. The arrows point to the endothermic peaks corresponding to melting of the $VL-T_m$, $L-T_m$ and $H-T_m$ forms,

respectively.

In the protocol outlined in Figure 6.5A, depending on the desired outcome, the indicated crystallization temperatures can be adjusted. To achieve all forms within the same sample, the key requirement is that the highest melting phase ($H-T_m$) has to be formed first. In the following, the form with an intermediate melting temperature ($L-T_m$), and finally, the one with the lowest melting temperature ($VL-T_m$) can be generated.

For the employed thermal protocol, we have chosen 1,000 ºC/s for all heating and cooling rates. Following the protocol of Figure 6.5A, the sample was first heated thirty degrees above the maximum T_m to erase thermal history, then rapidly cooled (at 1,000 ºC/s) to $T_c = 25$ ºC and kept at that temperature for 30 min. During this isothermal crystallization step, we generated the $L-T_m$ form. The sample was then rapidly heated to $T_c = 70$ ºC where it was kept for 30 min, and part of the sample was crystallized in the $H-T_m$ form. The $L-T_m$ crystals formed in the previous step melted during heating, but the memory of the previous crystalline state assisted generation of the $H-T_m$ form at $T_c = 70$ ºC. To re-generate the $L-T_m$ form, the sample was rapidly cooled to $T_c = 25$ ºC and kept there for 30 min. After this stage, both the $H-T_m$ and $L-T_m$ have been formed within the same sample. However, the sample was not yet crystallized completely, and crystallization of the $VL-T_m$ form was achieved by rapidly cooling to $T_c = -10$ ºC and keeping the sample at this low isothermal crystallization temperature for 30 min. Finally, the sample was rapidly quenched (at 1,000 ºC/s) below T_g. After all three forms were generated in the same sample, an FSC heating scan (denoted as "Analysis Scan", in Figure 6.5A) was performed to determine the individual melting temperatures.

Figure 6.5B shows the corresponding FSC analysis scan performed at a rate of 1,000 °C/s, where three melting peaks can be observed. The peak at

$T_{m,VL} \approx 20$ ºC corresponds to the melting of the $VL-T_m$ form, the peak at $T_{m1} \approx 65$ ºC corresponds to the melting of the $L-T_m$ form, and finally, the peak at $T_{m2} \approx 95$ ºC corresponds to the melting of the $H-T_m$ form. We note that due to the fast heating scan, the values of the melting peaks are somewhat higher than those observed for slow heating rates. We conclude that by applying properly-tailored thermal protocols, we can generate each phase individually or produce a sample where two or all three of them co-exist.

6.3.4 Crystalline structures of the alternating copolymer DMDS-*alt*-DVE at various low temperatures and related changes in time

Our wide angle X-ray scattering experiments (WAXS) aimed to explore differences in crystalline structures between the $VL-T_m$ and $L-T_m$ forms. The scattering patterns for the $L-T_m$ and $H-T_m$ forms have been reported previously[31]. Samples were prepared as described in the experimental section. First, thermal history was erased by heating the sample to 100 °C for 1 min, which is above the maximum T_{m2}. Subsequently, the sample was quenched by rapidly depositing it onto a brass block cooled to –20 °C, where it was kept for 5 min. According to the FSC results discussed above, the $VL-T_m$ form was generated by this thermal treatment. To identify the anticipated crystalline structures, the sample was mounted in the diffractometer's holder, which had been previously cooled to -10°C. Starting at this low temperature, ten isothermal WAXS spectra were measured in steps of 5 °C up to 35 °C. Two of these spectra are shown in Figure 6.6A. The sample was eventually cooled back to room temperature (r.t $= 20$ °C) and measured again after being kept at r.t for 4 days.

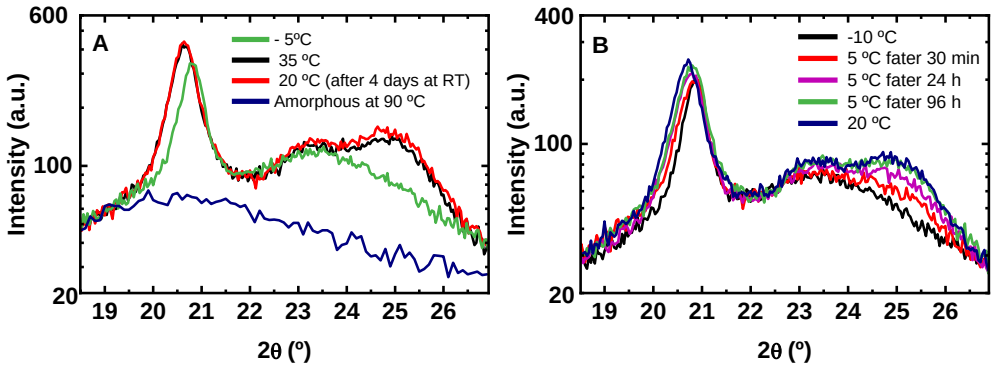

Figure 6.6. Isothermal WAXS diffractograms measured at: A) –5 °C (green curve) and 35 °C (black curve), by increasing the temperature in steps of 5 °C, after being stored for four days at r.t = 20 °C (red curve) and at 90 °C, (amorphous background, blue curve). B) –10 °C (black curve) in steps of 5 °C up to 5 °C and left for four days (after 30 min = red curve; 24 h = purple curve; 96 h = green curve) and after heating it to 20 °C (blue curve).

As shown in Figure 6.6A, the spectrum measured at 20 °C did not differ from the one measured before at 35 °C, indicating the stability of the underlying crystalline $L-T_m$ phase. Notably, at temperatures below ca. 5 °C, the measured spectra showed clear differences from the ones observed at temperatures above ca. 5 °C. As an example, we show in Figure 6.6A the spectrum measured at –5 °C. In particular, the position of the dominant peak differed by about (0.2 ± 0.05) and the peak at ca. 25° was not observed at temperatures below ca. 5 °C. We conclude that the $VL-T_m$ form generated at –20 °C has transformed into the $L-T_m$ form at temperatures above 5 °C.

In order to explore if this transformation was a rapid or a slow process, we examined the temporal evolution of the spectrum measured at 5 °C. As can be seen in Figure 6.6B, the transformation of the $VL-T_m$ form into the $L-T_m$ form was slow and required more than ca. 30 h. Besides the progressive shifting of the dominant peak to lower scattering angles, two distinguishable peaks emerged out of the initially "broad" peak located at

around 23.5°. We tentatively conclude that the $VL-T_m$ form is probably metastable and contains less perfectly ordered crystalline structures. While the similarities of the peak positions may indicate similar unit cell parameters, the difference in the scattering intensities may result from differences in chain packing. For the $VL-T_m$ form, which has the lowest melting temperature, we may expect a rather imperfect or less ordered structure. However, at present, all details of the crystalline structure of the three detected polymorphs are still not resolved.

6.4 Conclusions

This work explored the different polymorphic forms generated by the alternating copolymer DMDS-*alt*-DVE at low temperatures. We demonstrated that under specific thermal protocols, this polymer has the ability to crystallize into up to three polymorphic forms. Besides the previously presented $L-T_m$ and $H-T_m$ forms[31], the alternating copolymer DMDS-*alt*-DVE possesses an additional polymorphic form that can be generated at temperatures well below room temperature (*i.e.,* the $VL-T_m$ polymorph). Due to clear differences in their melting temperatures and certain microstructural features, these polymorphs are easily distinguishable.

Interestingly, as shown here, the most stable crystallographic form (the $H-T_m$ form) of DMDS-*alt*-DVE can also be established directly from the molten state. Given that there exist appropriate heterogeneous nuclei, the $H-T_m$ form can be generated by either cooling the sample very slowly from the melt (*e.g.,* at a rate of 0.2 ºC/min or less) or by cooling the sample rapidly to a temperature above the melting temperature of the $L-T_m$ form and keeping it there for long times (*e.g.,* 24 h or longer). However, even without any heterogeneous nuclei, the $H-T_m$ form can be generated rapidly by first preparing the $L-T_m$ form and employing the melt memory of the previous crystalline state of the $L-T_m$ form for an assisted nucleation of the $H-T_m$ form.

Finally, based on the knowledge of the melting temperatures of the different polymorphs and the corresponding nucleation probability, including concepts of melt memory and self-nucleation, we have successfully devised an appropriate thermal protocol, which allows to generate samples that contain only one, two, or all three crystalline forms. Thus, our results demonstrate the tunability and controlled formation of different crystalline polymorphs with potentially different properties within a single polymer sample. Further studies

on each polymorph generated individually may reveal differences in mechanical or optical properties, opening a promising avenue for the exploitation of the specific properties of each polymorph.

6.5 References

(1) Cramer, N. B.; Scott, J. P.; Bowman, C. N. Photopolymerizations of Thiol-Ene Polymers without Photoinitiators. *Macromolecules* **2002**, *35* (14), 5361–5365.

(2) Hoyle, C. E.; Bowman, C. N. Thiol–Ene Click Chemistry. *Angew. Chem. Int. Ed.* **2010**, *49* (9), 1540–1573.

(3) Kade, M. J.; Burke, D. J.; Hawker, C. J. The Power of Thiol-Ene Chemistry. *J Polym Sci Part Polym Chem* **2010**, *48* (4), 743–750.

(4) Quoc Le, C. M.; Schmutz, M.; Chemtob, A. Ab Initio Batch Emulsion Thiol-Ene Photopolymerization. *Macromolecules* **2020**, *53* (7), 2369–2379.

(5) Resetco, C.; Hendriks, B.; Badi ab, N.; Du Prez, F. Thiol-Ene Chemistry for Polymer Coatings and Surface Modification-Building in Sustainability and Performance. *Mater Horiz* **2017**, *4* (6), 1041–1053.

(6) Jasinski, F.; Lobry, E.; Tarablsi, B.; Chemtob, A.; Croutxé-Barghorn, C.; Nouen, D. L.; Criqui, A. Light-Mediated Thiol-Ene Polymerization in Miniemulsion: A Fast Route to Semicrystalline Polysul Fide Nanoparticles. *ACS Macro Lett.* **2014**, *3* (9), 958–962.

(7) Lowe, A. B. Thiol–Ene "Click" Reactions and Recent Applications in Polymer and Materials Synthesis: A First Update. *Polym Chem* **2014**, *5* (17), 4820–4870.

(8) Jasinski, F.; Schweitzer, J.; Fischer, D.; Lobry, E.; Croutxe, C.; Schmutz, M.; Nouen, D. L.; Criqui, A.; Chemtob, A. Thiol−Ene Linear Step-Growth Photopolymerization in Miniemulsion: Fast Rates, Redox-

Responsive Particles, and Semicrystalline Films. *Macromolecules* **2016**, *49* (4), 1143–1153.

(9) Le, C. M. Q.; Schrodj, G.; Ndao, I.; Bessif, B.; Heck, B.; Pfohl, T.; Reiter, G.; Elgoyhen, J.; Tomovska, R.; Chemtob, A. Semi-Crystalline Poly(Thioether) Prepared by Visible-Light-Induced Organocatalyzed Thiol-Ene Polymerization in Emulsion. *Macromol Rapid Commun* **2022**, *43* (5), 2100740.

(10) Le, C. M. Q.; Vidal, L.; Schmutz, M.; Chemtob, A. Droplet Nucleation in Miniemulsion Thiol–Ene Step Photopolymerization. *Polym Chem* **2021**, *12* (14), 2084–2094.

(11) Durham, O. Z.; Krishnan, S.; Shipp, D. A. Polymer Microspheres Prepared by Water-Borne Thiol-Ene Suspension Photopolymerization. *ACS Macro Lett.* **2012**, *1* (9), 1134–1137.

(12) Piorkowska, E.; Rutledge, G. C. *Handbook of Polymer Crystallization*; John Wiley & Sons, 2013.

(13) De Rosa, C.; Auriemma, F. *Crystals and Crystallinity in Polymers: Diffraction Analysis of Ordered and Disordered Crystals*; Claudio De Rosa, Finizia Auriemma, Eds.; Wiley, 2013.

(14) Kitamura, M. Strategy for Control of Crystallization of Polymorphs. *CrystEngComm* **2009**, *11* (6), 949–964.

(15) De Rosa, C.; Auriemma, F.; Malafronte, A.; Scoti, M. Crystal Structures and Polymorphism of Polymers: Influence of Defects and Disorder. *Polym Cryst* **2018**, *1* (4), 1–21.

(16) Gentili, D.; Gazzano, M.; Melucci, M.; Jones, D.; Cavallini, M.

Polymorphism as an Additional Functionality of Materials for Technological Applications at Surfaces and Interfaces. *Chem Soc Rev* **2019**, *48* (9), 2502–2517.

(17) De Rosa, C.; Scoti, M.; Di Girolamo, R.; de Ballesteros, O. R.; Auriemma, F.; Malafronte, A. Polymorphism in Polymers: A Tool to Tailor Material's Properties. *Polym Cryst* **2020**, *3* (2), 1–29.

(18) Brittain, H. G. *Polymorphism in Pharmaceutical Solids*; Brittain, H. G., Ed.; CRC Press: Milford, 2009; Vol. 192.

(19) Liu, C.; Brandenburg, J. G.; Valsson, O.; Kremer, K.; Bereau, T. Free-Energy Landscape of Polymer-Crystal Polymorphism. *Soft Matter* **2020**, *16* (42), 9683–9692.

(20) Keller, A.; Cheng, S. Z. D. The Role of Metastability in Polymer Phase Transitions. *Polymer* **1998**, *39* (19), 4461–4487.

(21) Zheng, Y.; Pan, P. Crystallization of Biodegradable and Biobased Polyesters: Polymorphism, Cocrystallization, and Structure-Property Relationship. *Prog. Polym. Sci.* **2020**, *109*, 101291.

(22) Wu, X.; Shi, S.; Yu, Z.; Russell, T. P.; Wang, D. AFM Nanomechanical Mapping and Nanothermal Analysis Reveal Enhanced Crystallization at the Surface of a Semicrystalline Polymer. *Polymer* **2018**, *146* (6), 188–195.

(23) Marigo, A.; Marega, C.; Cecchin, G.; Collina, G.; Ferrara, G. Phase Transition II → I in Isotactic Poly-1-Butene: Wide- and Small-Angle X-Ray Scattering Measurements. *Eur. Polym. J.* **2000**, *36* (1), 131–136.

(24) Azzurri, F.; Flores, A.; Alfonso, G. C.; Baltá Calleja, F. J. Polymorphism

of Isotactic Poly(1-Butene) as Revealed by Microindentation Hardness. 1: Kinetics of the Transformation. *Macromolecules* **2002**, *35* (24), 9069–9073.

(25) Cavallo, D.; Kanters, M. J. W.; Caelers, H. J. M.; Portale, G.; Govaert, L. E. Kinetics of the Polymorphic Transition in Isotactic Poly(1-Butene) under Uniaxial Extension. New Insights from Designed Mechanical Histories. *Macromolecules* **2014**, *47* (9), 3033–3040.

(26) Qiao, Y.; Wang, Q.; Men, Y. Kinetics of Nucleation and Growth of Form II to I Polymorphic Transition in Polybutene-1 as Revealed by Stepwise Annealing. *Macromolecules* **2016**, *49* (14), 5126–5136.

(27) Xiao, W.; Wu, P.; Feng, J.; Yao, R. Influence of a Novel β-Nucleating Agent on the Structure, Morphology, and Nonisothermal Crystallization Behavior of Isotactic Polypropylene. *J. Appl. Polym. Sci.* **2009**, *111* (2), 1076–1085.

(28) Marco, C.; Gómez, M. A.; Ellis, G.; Arribas, J. M. Activity of a β-Nucleating Agent for Isotactic Polypropylene and Its Influence on Polymorphic Transitions. *J. Appl. Polym. Sci.* **2002**, *86* (3), 531–539.

(29) Garbarczyk, J.; Paukszta, D.; Borysiak, S. Polymorphism of Isotactic Polypropylene in Presence of Additives, in Blends and in Composites. *J Macromol Sci Phys B* **2007**, *41* (4–6), 1267–1278.

(30) Horváth, Z.; Sajó, I. E.; Stoll, K.; Menyhárd, A.; Varga, J. The Effect of Molecular Mass on the Polymorphism and Crystalline Structure of Isotactic Polypropylene. *Express Polym. Lett.* **2010**, *4* (2), 101–114.

(31) Bessif, B.; Heck, B.; Pfohl, T.; Minh, C.; Le, Q.; Chemtob, A.; Pirela, V.; Elgoyhen, J.; Tomovska, R.; Müller, A. J.; Reiter, G. Nucleation Assisted

through the Memory of a Polymer Melt: A Different Polymorph Emerging from the Melt of Another One. *Macromolecules* **2023**, *56* (4), 1461–1470.

(32) Sangroniz, L.; Cavallo, D.; Müller, A. J. Self-Nucleation Effects on Polymer Crystallization. *Macromolecules* **2020**, *53* (12), 4581–4604.

(33) Hedges, L. O.; Whitelam, S. Limit of Validity of Ostwalds Rule of Stages in a Statistical Mechanical Model of Crystallization. *J Chem Phys* **2011**, *135* (16), 164902.

(34) Tavassoli, Z.; Sear, R. P. Homogeneous Nucleation near a Second Phase Transition and Ostwald's Step Rule. *J. Chem. Phys.* **2002**, *116* (12), 5066–5072.

(35) Schick, C.; Mathot, V. *Fast Scanning Calorimetry*; Schick, C., Mathot, V., Eds.; Springer Cham, 2016.

(36) Schick, C.; Androsch, R. New Insights into Polymer Crystallization by Fast Scanning Chip Calorimetry. In *Fast Scanning Calorimetry*; 2016; Vol. 91, pp 463–535.

(37) Schawe, J. E. K.; Ag, M.; Schwerzenbach, C.-. Flash DSC 1 : A Novel Fast Differential Scanning Calorimeter. *Processing* **2011**, *27*, 1–4.

(38) Toda, A.; Androsch, R.; Schick, C. Insights into Polymer Crystallization and Melting from Fast Scanning Chip Calorimetry. *Polymer* **2016**, *91*, 239–263.

(39) Sangroniz, L.; Ocando, C.; Cavallo, D.; Müller, A. J. Melt Memory Effects in Poly(Butylene Succinate) Studied by Differential Fast Scanning Calorimetry. *Polymers* **2020**, *12* (12), 1–18.

(40) Schawe, J. E. K. Influence of Processing Conditions on Polymer

Crystallization Measured by Fast Scanning DSC. *J. Therm. Anal. Calorim.* **2014**, *116* (3), 1165–1173.

(41) Furushima, Y.; Schick, C.; Toda, A. Crystallization, Recrystallization, and Melting of Polymer Crystals on Heating and Cooling Examined with Fast Scanning Calorimetry. *Polym. Cryst.* **2018**, *1* (2), e10005.

(42) Caputo, M. R.; Tang, X.; Westlie, A. H.; Sardon, H.; Chen, E. Y. X.; Müller, A. J. Effect of Chain Stereoconfiguration on Poly(3-Hydroxybutyrate) Crystallization Kinetics. *Biomacromolecules* **2022**, *23* (9), 3847–3859.

(43) Gedde, U. W.; Hedenqvist, M. S. Morphology of Semicrystalline Polymers. In *Fundamental Polymer Science*; Springer Nature: Cham,Switzerland, 2019; pp 251–372.

Chapter 7

Effect of chemical structure on the crystallization kinetics and polymorphism of high-sulfur-content polythioethers

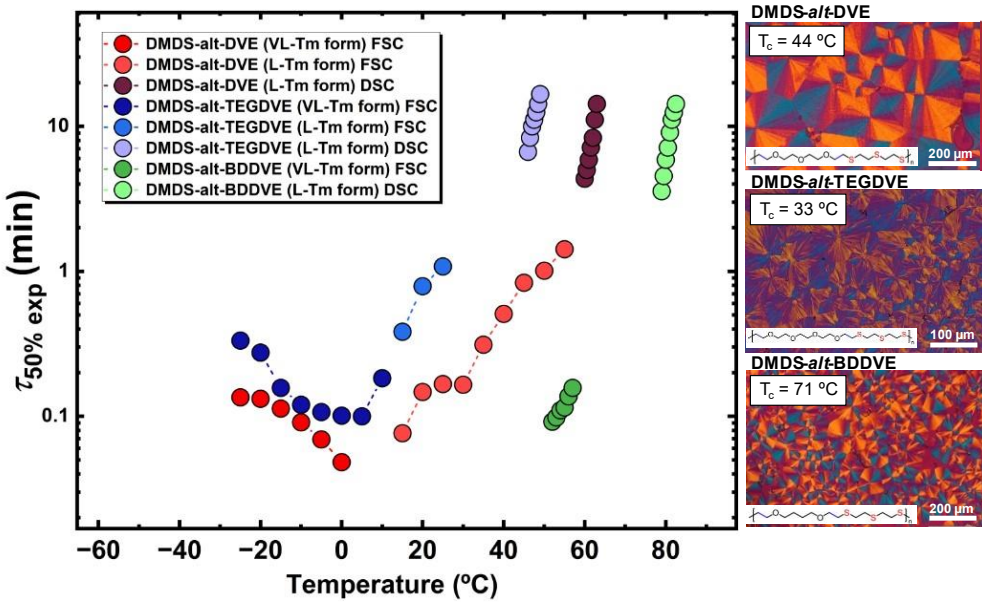

7.1.1 Abstract

This study focuses on understanding how the chemical structure of relatively similar high-sulfur alternating polythioether homopolymers (DMDS-alt-DVE, DMDS-alt-TEGDVE, and DMDS-alt-BDDVE) affects their structural properties, morphology, polymorphism, and crystallization kinetics. Differential scanning calorimetry (DSC) and polarized light optical microscopy (PLOM) experiments revealed a complex crystallization for the samples in which up to three different polymorphic phases were identified: the $VL-T_m$ form, the $L-T_m$ form and the $H-T_m$ form, characterized by their corresponding melting temperature ranges. A coexistence of negative and positive spherulites was found, and their origin was revealed by atomic force microscopy (AFM), which showed how the lamellar arrangement varied in the samples from predominantly radial to a cross-hatched morphology. Additionally, the overall crystallization kinetics were investigated using a combination of PLOM, DSC, and fast scanning calorimetry (FSC) experiments in which DMDS-alt-BDDVE exhibited the fastest overall crystallization kinetics among the three homopolymers, followed by DMDS-alt-DVE and then DMDS-alt-TEGDVE. These behaviors were explained by molecular dynamic simulations in which the diffusion capabilities of each homopolymer along their density, characteristic ratio, and chain diffusion effects were simulated to understand the polymer backbone flexibility and chain mobility, revealing differences among the homopolymers. DMDS-alt-BDDVE demonstrated the fastest diffusion in the melt, potentially explaining its exceptionally rapid crystallization kinetics.

7.1.2 Introduction

Polymorphism is the ability of many materials, including semicrystalline polymers, to crystallize into different crystallographic forms that differ in thermodynamic stability[1–4]. Historically, achieving precise control over the formation of each polymorph has posed significant challenges[2,4,5]. However, in recent years, a growing interest has emerged in understanding the mechanical and physical properties of these polymorphic materials. Understanding solidification and crystallization processes is crucial for developing tailored materials with varying mechanical, thermal, and electrical properties[3–5]. These advancements open the avenue for optimizing production methods for enhanced efficiency and sustainability, broadening the spectrum of potential applications. As an illustrative example, polyvinylidene fluoride (PVDF) exhibits different crystalline phases used in various applications; PVDF can exist in at least four phases depending on the crystallization temperature and processing conditions. Two of these phases can exhibit piezoelectric and ferroelectric properties, while the others are non-polar insulating phases[6–8]. Therefore, understanding the crystallization is critical in determining which polymorphic phase will develop.

In recent years, developments in thiol-ene polymerization have shifted from cross-linking reactions, generally in bulk or solution to its application in aqueous-dispersed media, such as emulsion and miniemulsion[9–14]. This transition aims to make the polymerization process more environmentally friendly and versatile [9–11,15–19]. Thiol-ene polymerization in aqueous-dispersed media is an approach to synthesize polymer particles used for diverse applications such as coatings, as demonstrated by Elgoyhen *et al.*[20] by achieving water-borne emulsion polymerization of high-sulfur-content polythioethers[16–19]. Additionally, these newly synthesized polythioethers have been the focus of our recent work, in which we have shown that they can form polymorphic

materials. Notably, the tunability of DMDS-*alt*-DVE alternating homopolymer was demonstrated as it can solidify into multiple polymorphs under specific thermal treatments[21,22]. These forms are referred to as the very-low melting phase ($VL-T_m$), the low-melting phase ($L-T_m$) and the high-melting phase ($H-T_m$). They can be distinguished based on their melting points and microstructural characteristics. Therefore, the ability to control and modify the formation of different polymorphic forms through thermal treatments within a single polymer can potentially lead to distinct mechanical or optical properties. For this, it is essential to study the crystallization kinetics of each phase.

In this work, we study for the first time the influence of the chemical structure of a series of high-sulfur-content alternating polythioether homopolymers, *i.e.,* DMDS-*alt*-DVE, DMDS-*alt*-TEGDVE, and DMDS-*alt*-BDDVE (see Scheme 7.1 and the text above it for the acronyms definitions) on their structure, morphology, polymorphism, and crystallization kinetics. As shown in Scheme 7.1, they are linear polymers which have some similarities with traditional polyethers (*e.g.*, poly(ethylene oxide)) but incorporate sulfur atoms in the main chain, so in principle they should be able to crystallize. However, their structure and crystallization should be a function of their chemical repeat units. The overall crystallization kinetics was measured by employing a combination of FSC and DSC covering a wide range of temperatures. Additionally, the nucleation and spherulitic growth kinetics of the materials were examined using PLOM. Furthermore, the morphology of each polymorphic phase of the material was studied via atomic force microscopy (AFM), revealing a cross-hatched lamellar morphology that explains the positive sign frequently encountered in these polythioether materials. Using molecular dynamic simulations, we have found that macromolecular diffusion in the melt is the dominant parameter determining the studied homopolymers'

overall crystallization rate.

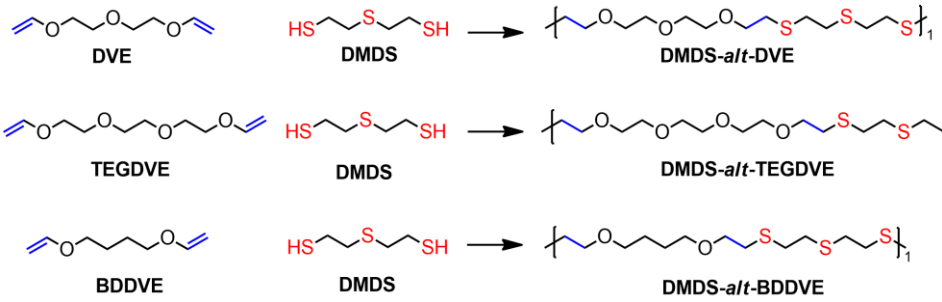

Scheme 7.1. Chemical structures and reaction for the formation of polythioethers DMDS-*alt*-DVE, DMDS-*alt*-TEGDVE and DMDS-*alt*-BDDVE.

The synthesis and the determination of the molecular weight are described in Chapter 3, and the number average molecular weight is reported in Table 3.1 located in Chapter 3. It should be noted that all three homopolymers have one part of their repeating unit, which is identical, as it comes from DMDS (see Scheme 7.1).

7.2 Results and Discussion

7.2.1 Characterization of DMDS-*alt*-DVE, DMDS-*alt*-TEGDVE and DMDS-*alt*-BDDVE polymorphic forms via DSC, PLOM, and WAXS

The crystallization process is highly dependent on thermodynamic and kinetic factors. Thermodynamics can determine whether a polymorph can exist under specific conditions, whereas kinetics dictates whether a polymorph can be formed at a particular rate over a period of time. Our previous studies[22], (see

also Chapter 6) established that DMDS-alt-DVE exhibits three polymorphic phases, easily identified by their distinct melting temperatures. As stated above, the polymorphic phases of the DMDS-alt-DVE homopolymer have been designated as very low-melting temperature ($VL-T_m$), low-melting temperature ($L-T_m$) and high-melting temperature ($H-T_m$) forms. In addition, we also showed reliable thermal protocols to combine or isolate the different polymorphic forms[22]. Furthermore, we determined that at a rate of 0.2 ºC/min, the high-melting temperature polymorph ($H-T_m$) can directly form from the melt without self-seeding[22].

In this work, we first investigate the thermal behavior of the three polythioethers. Figure 7.1 shows non-isothermal DSC results for experiments performed at different rates in a range between 1 ºC/min and 50 ºC/min, respectively, for all three alternating homopolythioethers. The identification of the different polymorphs (see labels in Figure 7.1) was performed by comparison with our previous works[21,22] but also by parallel PLOM and isothermal crystallization DSC experiments, to be discussed below.

It is essential to understand that as the melting temperatures vary from one polythioether to another, the phases were assigned from the lowest to the highest melting temperature found for each polythioether. That is, each phase ($VL-T_m$, $L-T_m$ or $H-T_m$ phase) was assigned according to the first-order transition temperatures of each polythioether (*e.g.*, the $VL-T_m$ polymorph corresponds to the lowest melting temperature found for that polymer), which could vary in range from one polymer to another.

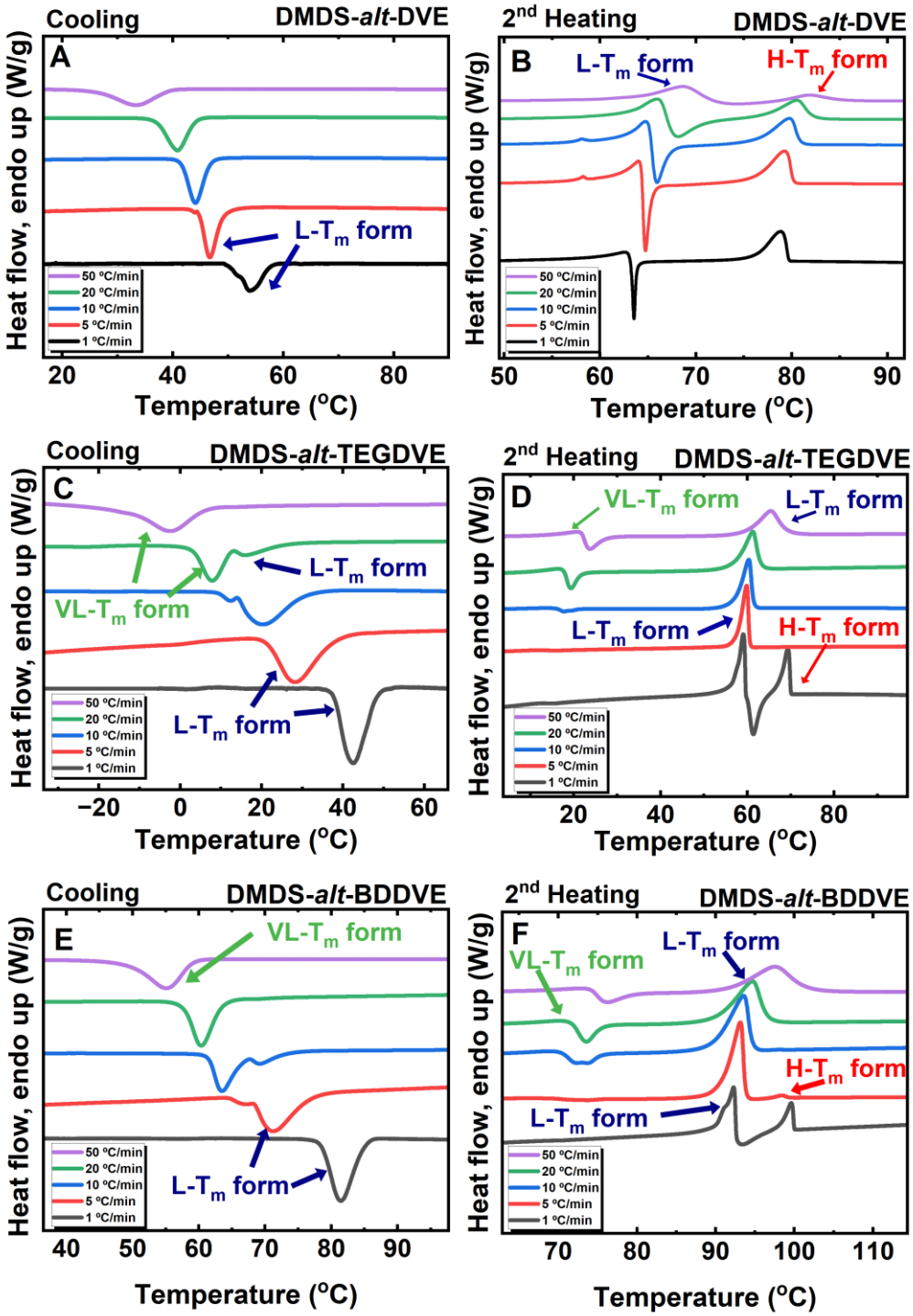

Figure 7.1. Calorimetric behavior at the indicated scan rates, from 1 ºC/min to 50 ºC/min for all three homopolymers via standard DSC. A) Cooling DSC scans

for DMDS-*alt*-DVE B) Subsequent heating DSC scans for DMDS-*alt*-DVE C) Cooling DSC scans for DMDS-*alt*-TEGDVE D) Subsequent heating DSC scans for DMDS-*alt*-TEGDVE E) Cooling DSC scans for DMDS-*alt*-BDDVE F) Subsequent heating DSC scans for DMDS-*alt*-BDDVE .

Figure 7.1A shows that a single crystallization peak is observed upon cooling for the DMDS-*alt*-DVE homopolymer, at all explored rates, from 1 ºC/min to 50 ºC/min. This exothermic peak corresponds to the crystallization of the $L-T_m$ form, as previously demonstrated[22]. Upon subsequent heating, as seen in Figure 7.1B, a first melting (T_{m1}) is observed, followed by immediate re-crystallization (T_{cc}), and a second melting (T_{m2}). It has been shown[22] that the first endothermic peak at $T_{m1} \approx 65$ ºC corresponds to fusion of the $L-T_m$ form crystals, which re-crystallize at $T_{cc} \approx 70$ ºC into the $H-T_m$ form crystals, which melt at around $T_{m2} \approx 80$ ºC. Interestingly, further studies demonstrated that this polymer exhibits a third polymorph (*i.e.*, the $VL-T_m$ form) when the material is under extremely fast cooling and heating rates achieved by FSC experiments (see Figure 7.2).

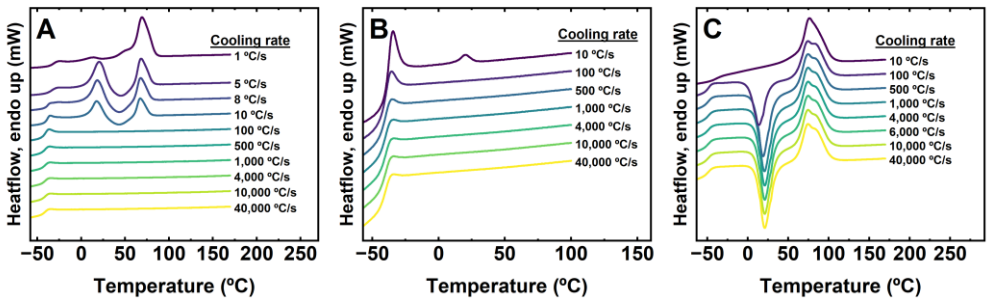

Figure 7.2. FSC second heating scans after cooling at different rates. A) DMDS-*alt*-DVE. B) DMDS-*alt*-TEGDVE. C) DMDS-*alt*-BDDVE.

DMDS-*alt*-TEGDVE displays a similar behavior when lower scanning rates are employed. Figure 7.1C shows that DMDS-*alt*-TEGDVE, upon cooling

at 1 ºC/min, only displays a single exothermic peak at a crystallization temperature of $T_{c1} \approx 42$ ºC indicating that only one of the polymorphs crystallized during cooling, which we attribute to the crystallization of the $L-T_m$ form. During the subsequent second heating, DMDS-alt-TEGDVE undergoes a first melting (T_{m1}), followed by re-crystallization (T_{cc}), and a second melting (T_{m2}). The first endotherm at $T_{m1} \approx 59$ ºC is attributed to the fusion of the low-melting temperature polymorph, the $L-T_m$ form. After the $L-T_m$ crystals have melted, the sample re-crystallizes at $T_{cc} \approx 61$ ºC (in a cold-crystallization process) into the high-melting temperature polymorph, the $H-T_m$ form, which melts at higher temperatures, *i.e.*, $T_{m2} \approx 70$ ºC. Interestingly, at a rate of 5 ºC/min, a similar behavior is observed during cooling as at a rate of 1 ºC/min. However, during the subsequent heating a single melting process at $T_{m1} \approx 60$ ºC takes place, corresponding to the melting of the $L-T_m$ form; that is, no re-crystallization takes place. Additionally, DMDS-alt-TEGDVE behaves quite differently when it is cooled and heated at higher rates (see Figure 7.1C and Figure 7.1D), during cooling at 10 ºC/min, two crystallization peaks appear at $T_{c1} \approx 20$ ºC and at $T_{c2} \approx 12$ ºC. When the material is cooled at a higher rate of 20 ºC/min the higher-crystallization peak, T_{c1}, decreases in intensity while the lower-crystallization, T_{c2}, increases indicating that the crystallization of one of the polymorphs is becoming more prominent compared to the other polymorph. Finally, as the rate increases to 50 ºC/min again a single crystallization exotherm at much lower temperatures, close to $T_{c2} \approx -5$ ºC is observed. We attribute the higher crystallization peak, T_{c1}, to the $L-T_m$ form while the peak at T_{c2} we attribute to the $VL-T_m$ form, as in the subsequent heating from 10 ºC/min to 50 ºC/min, DMDS-alt-TEGDVE undergoes a melting-recrystallization-melting process. However, the first melting occurs at $T_{m1} \approx 16$ ºC which can be attributed to the melting of a very low-melting temperature polymorph, the $VL-T_m$ form. After the $VL-T_m$ crystals melt, the sample immediately re-

crystallizes at $T_{cc} \approx 16$ ºC into the $L-T_m$ form. Finally, the $L-T_m$ form melts at around $T_{m2} \approx 64$ ºC.

Finally, Figure 7.1E shows that DMDS-alt-BDDVE, upon cooling at 1 ºC/min, exhibits only a single exothermic peak at $T_c \approx 82$ ºC, where only one of the polymorphs crystallized. Upon heating, the first endotherm at $T_{m1} \approx 92$ ºC is attributed to the melting of the low-melting temperature polymorph, the $L-T_m$ form. After the $L-T_m$ has melted, the sample re-crystallizes at $T_{cc} \approx 94$ ºC into the $H-T_m$ form, which melts at $T_{m2} \approx 99$ ºC. At higher cooling rates, from 10 to 50 ºC/min, DMDS-alt-BDDVE presents a similar behavior to that observed for DMDS-alt-TEGDVE (Figure 7.1C - Figure 7.1D). For DMDS-alt-BDDVE at 5 ºC/min initially two exothermic peaks are observed and as the cooling rate increases the lower-T_c peak increases in enthalpy while the higher-T_c peak decreases. Additionally, upon heating the material also undergoes a melting-recrystallization-melting process (see Figure 7.1F). However, from 10 ºC/min to 50 ºC/min, the first melting occurs at $T_{m1} \approx 73$ ºC, attributed to the melting of the very low-melting temperature polymorph, $the\ VL-T_m$ form. After the $VL-T_m$ has melted, the sample immediately re-crystallizes at $T_{cc} \approx 76$ ºC into the $L-T_m$ form. Finally, the $L-T_m$ form melts at around $T_{m2} \approx 98$ ºC.

A direct crystallization of the $H-T_m$ form upon cooling from the melt in the cases of DMDS-alt-TEGDVE and DMDS-alt-BDDVE was never observed even using slow cooling rates in a microcalorimeter (*i.e.,* 0.1 ºC/min).

After describing the correlation between the non-isothermal crystallization and melting behavior with the polymorphic nature of the DMDS-alt-DVE, DMDS-alt-TEGDVE, and DMDS-alt-BDDVE alternating homopolymers, we will focus on the nucleation and growth kinetics of each polymorph; the overall crystallization will be studied and discussed in sections below.

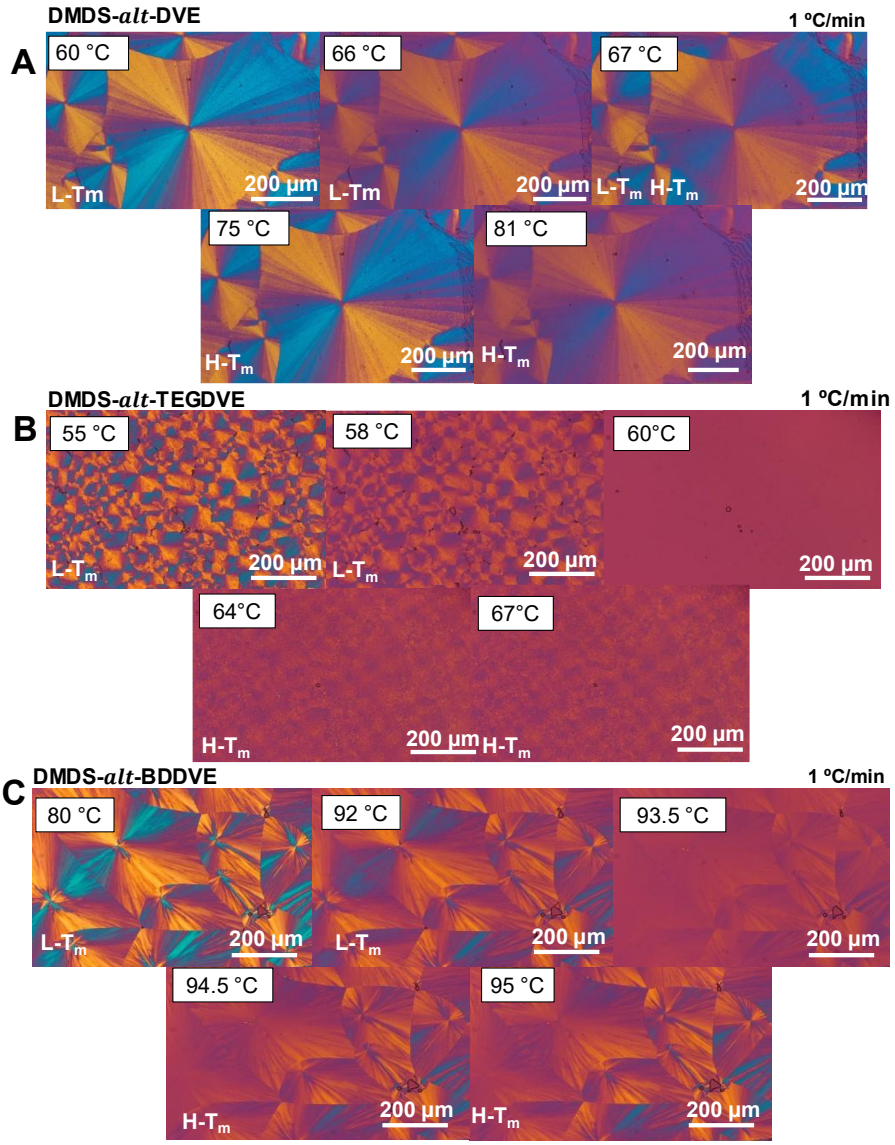

Figure 7.3. PLOM images of DMDS-*alt*-DVE, DMDS-*alt*-TEGDVE, and DMDS-*alt*-BDDVE during heating, at 1 ºC/min, taken at different temperatures after a previous cooling at 1 ºC/min (during which the samples crystallized); the temperature at which the image was taken is indicated in each micrograph. The image shows the melting of the $L-T_m$ form (produced during the previous cooling from the melt), its melting and recrystallization into the $H-T_m$ form and start of the final melting for all polymers. A) DMDS-*alt*-DVE; B) DMDS-*alt*-

TEGDVE and C) DMDS-alt-BDDVE.

The polymorphic phases revealed by DSC were studied by performing analogous non-isothermal experiments using a polarized light optical microscope (PLOM). Thus, the same heating and cooling rates were employed to visualize the phase changes. DMDS-alt-DVE exhibits similar behavior at low and high rates (see Figure 7.1B); hence, similar results are expected to those conducted in the DSC.

Figure 7.3A shows PLOM images taken during heating of DMDS-alt-DVE at 1 °C/min after the samples were crystallized during cooling at the same rate. Although the changes in the spherulitic morphology are less pronounced, the material undergoes a sequence similar to that registered by the DSC experiments in Figure 7.1B. As DMDS-alt-DVE homopolymer is being heated at 1 ºC/min, the micrographs show large positive spherulites that have a change in the intensity of the transmitted light as they undergo a melting-recrystallization-melting process (see Figure 7.1B and compare with Figure 7.3A). That is, at $T_{m1} \approx 66$ ºC, the partial melting corresponds to the $L-T_m$ form, which re-crystallizes at $T_{cc} \approx 67$ ºC into the $H-T_m$ form, and then starts to melt at around $T_{m2} \approx 81$ ºC. The brightest images correspond to the samples before any melting: see Figure 7.3A micrographs corresponding to the temperatures 60 ºC ($L-T_m$ form spherulites) and 75 ºC ($H-T_m$ form spherulites).

Similarly, Figure 7.3B shows that by heating DMDS-alt-TEGDVE at 1 °C/min after crystallizing from the melt at the same rate, the micrographs show small positive spherulites that undergo a similar melting-crystallization-melting sequence in which $T_{m1} \approx 58$ ºC corresponds to the start of the melting of the $L-T_m$ form (at 60 ºC, the spherulitic texture almost disappears, indicating that the $L-T_m$ form has completely melted and is cold-crystallizing simultaneously),

which then re-crystallizes at $T_{cc} \approx 64$ ºC into the $H-T_m$ form, characterized by lower intensity spherulitic morphology, which then starts melting at around $T_{m2} \approx 67$ ºC. In this sample, the images after the first melting and cold-crystallization are not as clear as it seems that the melting process is overlapping with the cold-crystallization, which in turn overlaps with the second melting process.

Finally, the DMDS-alt-BDDVE homopolymer crystallizes into the $L-T_m$ form (see Figure 7.1F and Figure 7.3C), which starts to melt at $T_{m1} \approx 92$ ºC then re-crystallizes at $T_{cc} \approx 93.5$ ºC into the $H-T_m$ form which starts to melt at around $T_{m2} \approx 100$ ºC. Hence, these results clearly indicate that, in fact, these DMDS-alt-TEGDVE and DMDS-alt-BDDVE exhibit at least two distinct crystalline phases. Here, we also note that in most polymers, the spherulites are often negative; in the case of all three copolymers under study here, the spherulites obtained are positive or a mixture of positive and negative spherulites; this phenomenon will be discussed in sections below. Another interesting observation that can be made from the images shown in Figure 7.3 is the much lower nucleation density of DMDS-alt-DVE, as indicated by the large sizes of the spherulites obtained. DMDS-alt-BDDVE is characterized by an intermediate nucleation density, and finally, DMDS-alt-TEGDVE has the highest nucleation density of active nuclei produced during cooling at 1 ºC/min. At this rate, the previous crystallization only produces the $L-T_m$ form for the three samples.

Similar experiments were conducted at 50 ºC/min for all three homopolymers, *i.e.*, the homopolymers were first melted and crystallized at 50 ºC/min. Images taken by PLOM during heating at 50 ºC/min can be found in Figure 7.4. First, Figure 7.4A shows the melting-recrystallization-melting process for DMDS-alt-DVE, in which we can clearly see the melting of the $L-T_m$ phase and the re-crystallization into the $H-T_m$ phase and subsequent

start of melting.

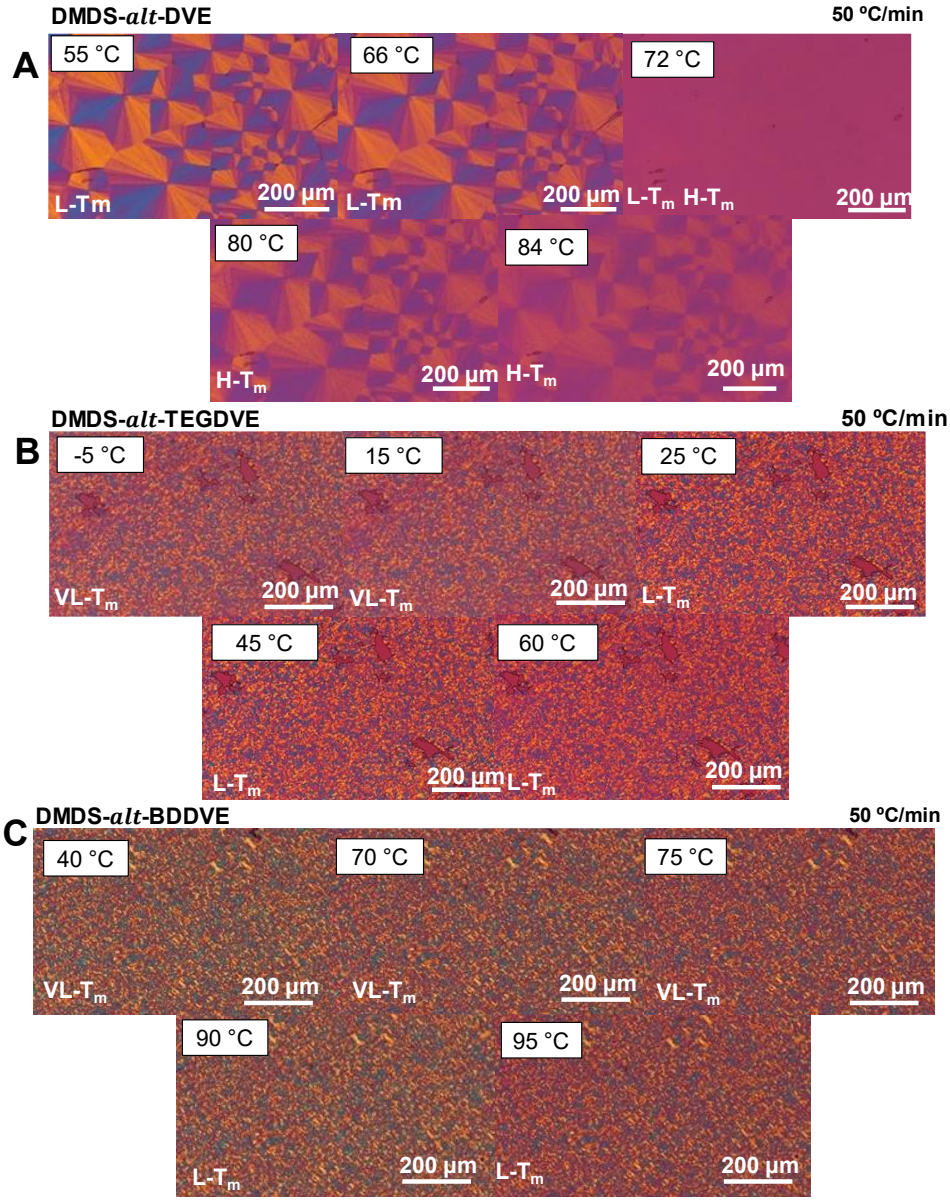

Figure 7.4. PLOM images of DMDS-*alt*-DVE, DMDS-*alt*-TEGDVE and DMDS-*alt*-BDDVE during heating taken at different temperatures after non-isothermal crystallization; the temperature at which the image was taken is indicated in each micrograph. The image shows the melting of one form ($VL-T_m$ in the case of DMDS-*alt*-TEGDVE and DMDS-*alt*-BDDVE and

$L-T_m$ of DMDS-alt-DVE) and the recrystallization into the $H-T_m$ form followed by the start of its melting for all polymers. A) DMDS-alt-DVE at 50 ºC/min B) DMDS-alt-TEGDVE at 50 ºC/min C) DMDS-alt-BDDVE at 50 ºC/min.

A more complex behavior is observed for the other two copolymers (*i.e.*, DMDS-alt-TEGDVE and DMDS-alt-BDDVE). The phase changes are more subtle than when performing the same experiment at 1 ºC/min. This is due to the much higher number of active nuclei that were produced during the formation of the $VL-T_m$ phase, which occurs at higher supercoolings.

Figure 7.4B shows the evolution of DMDS-alt-TEGDVE as the sample is heated. Although total melting of the $VL-T_m$ phase ($T_{m1} \approx 15$ ºC) is not clearly discernable, a change in birefringence is indicative that a phase changed (*i.e.*, re-crystallization of the $VL-T_m$ into the $H-T_m$ form) has occurred at a $T_{cc} \approx 25$ ºC which subsequently starts to melt at $T_{m2} \approx 60$ ºC. Furthermore, DMDS-alt-BDDVE undergoes a similar phase transformation (Figure 7.4C) in which the full melting of the $VL-T_m$ form is not distinguishable but rather a change in birefringence as the sample re-crystallizes into the $H-T_m$ form. That is, the $VL-T_m$ form of DMDS-alt-BDDVE melts at $T_{m1} \approx 75$ ºC and re-crystallizes at $T_{cc} \approx 80$ ºC and subsequently starts melting at $T_{m2} \approx 95$ ºC.

Additionally, for DMDS-alt-TEGDVE and DMDS-alt-BDDVE, as the materials are being heated, complete melting of the lower melting phase ($L-T_m$ form) before recrystallization (cold-crystallization) into the higher melting phase ($H-T_m$ form) is not observed.

The reason for this could be that as the high-temperature phase forms from the low-temperature phase (*i.e.*, self-seeding occurs[21]), their crystal structures could be similar, and thus, the transformation from one phase to the other would

require a lower amount of energy. Additionally, nuclei density measurements as a function of time (performed by quantifying the number of spherulites before impingement on one another) were carried out. The results are reported in Figure 8.2−Figure 8.5 in Appendix 2, located in Chapter 8.

Results shown in Figure 7.5 support the interpretation given above, as the intensity of transmitted light through the crossed polarizers was measured during heating and plotted against the temperature, in which the increase or decrease in intensity correlates to the crystallization or melting of the phases, respectively.

Some of the non-isothermal experiment results only showed a slight difference in birefringence upon the second melting of the melting-recrystallization-melting process. The same experiments were performed to measure the light intensity, which will be later analyzed using the "*ImageJ*" program. For these experiments, it was essential to remove the sensitive tint plate that gives color to the spherulites under crossed polarizers and obtain black-and-white images. The micrographs obtained were then analyzed measuring the color intensity of each image.

The intensity varies depending on the crystallization of the sample, showing low values when the sample is molten and increasing values as crystallization occurs. The experiments were at 1 °C/min, 20 °C/min and 50 °C/min for DMDS-alt-DVE and 20 °C/min and 50 °C/min for DMDS-alt-TEGDVE and DMDS-alt-BDDVE. The intensity values were then plotted as a function of temperature. Results are shown below (Figure 7.5).

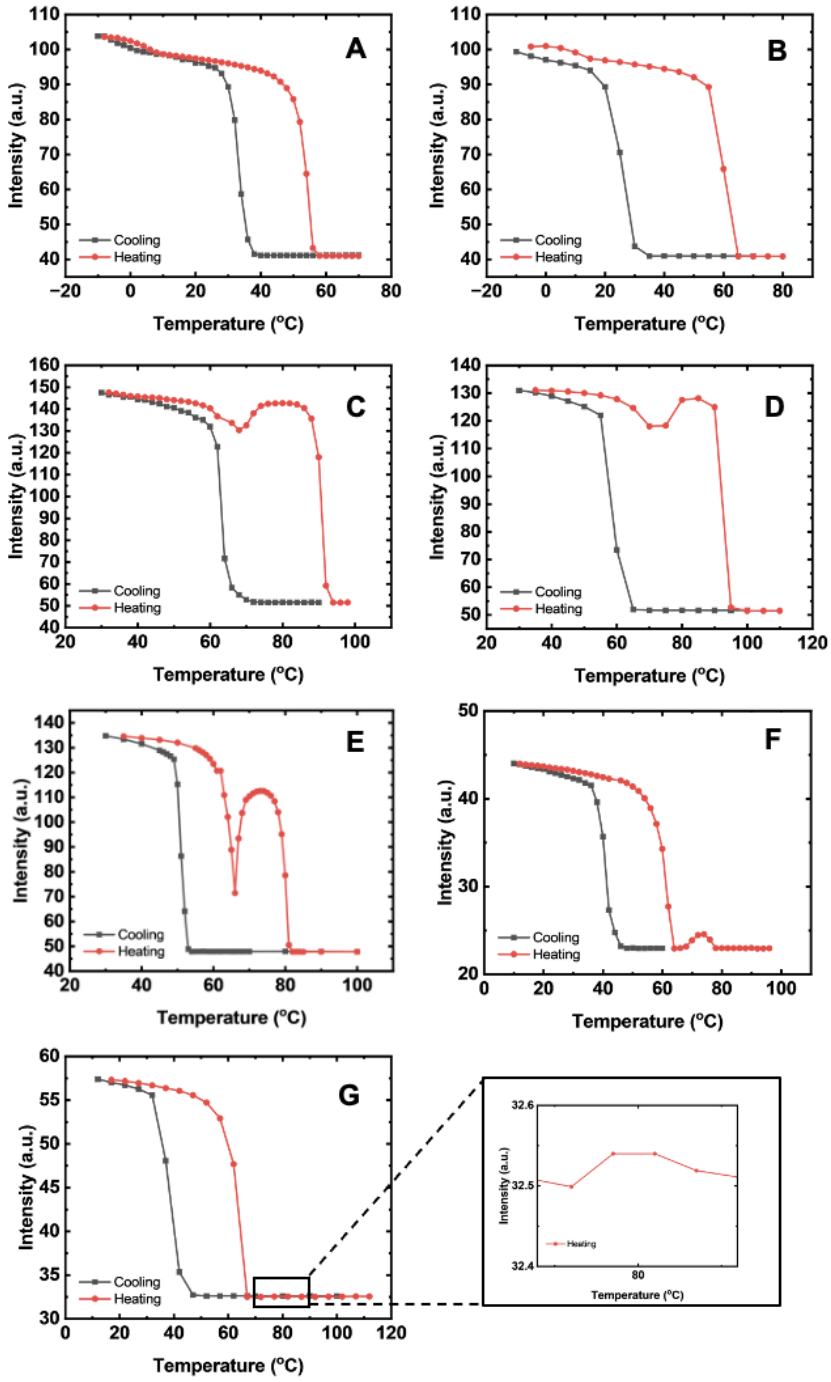

Figure 7.5. Birefringence intensity as a function of temperature. A) DMDS-*alt*-TEGDVE performed at 20 °C/min. B) DMDS-*alt*-TEGDVE performed at 50 °C/min. C) DMDS-*alt*-BDDVE performed at 20 °C/min. D) DMDS-*alt*-

BDDVE performed at 50 °C/min. E) DMDS-alt-DVE performed at 1 °C/min. F) DMDS-alt-DVE performed at 20 °C/min. G) DMDS-alt-DVE performed at 50 °C/min.

The cooling (black line) shows, in all cases a single crystallization process: as temperature decreases, the intensity of the micrographs increases. The second heating (red line) of the DMDS-alt-TEGDVE shows a small increase in intensity at lower temperatures that may be due to the melting of the $VL-T_m$ polymorph. As temperature increases, a sharp decrease in intensity is observed, corresponding to the melting of the $H-T_m$ form. Regarding DMDS-alt-BDDVE, both experiments performed at 20 and 50 °C/min (Figure 7.5C and Figure 7.5D) clearly show a melting-recrystallization-melting process during the heating: intensity slightly decreases first, representative of the melting of the $VL-T_m$ form, then increases due to the recrystallization of the $H-T_m$ polymorph and finally decreases again as the latter polymorph melts. Lastly, experiments performed on DMDS-alt-DVE at 20 and 50 °C/min (Figure 7.5F and Figure 7.5G), similarly to the previous copolymer, show a melting-recrystallization-melting process during the second heating. However, the first melting and recrystallization occur so quickly that the intensity peak is very small, for which it was deemed necessary to repeat the experiment at 1 °C/min (Figure 7.5E). Figure 7.5E clearly shows the first melting that corresponds to the $L-T_m$ polymorphic form, and the recrystallization and second melting that belong to the $H-T_m$ form.

Additionally, the range of T_cs from which we can follow the isothermal crystallization of each of the three copolymers (DMDS-alt-TEGDVE, DMDS-alt-BDDVE and DMDS-alt-DVE) was estimated from preliminary DSC scans.

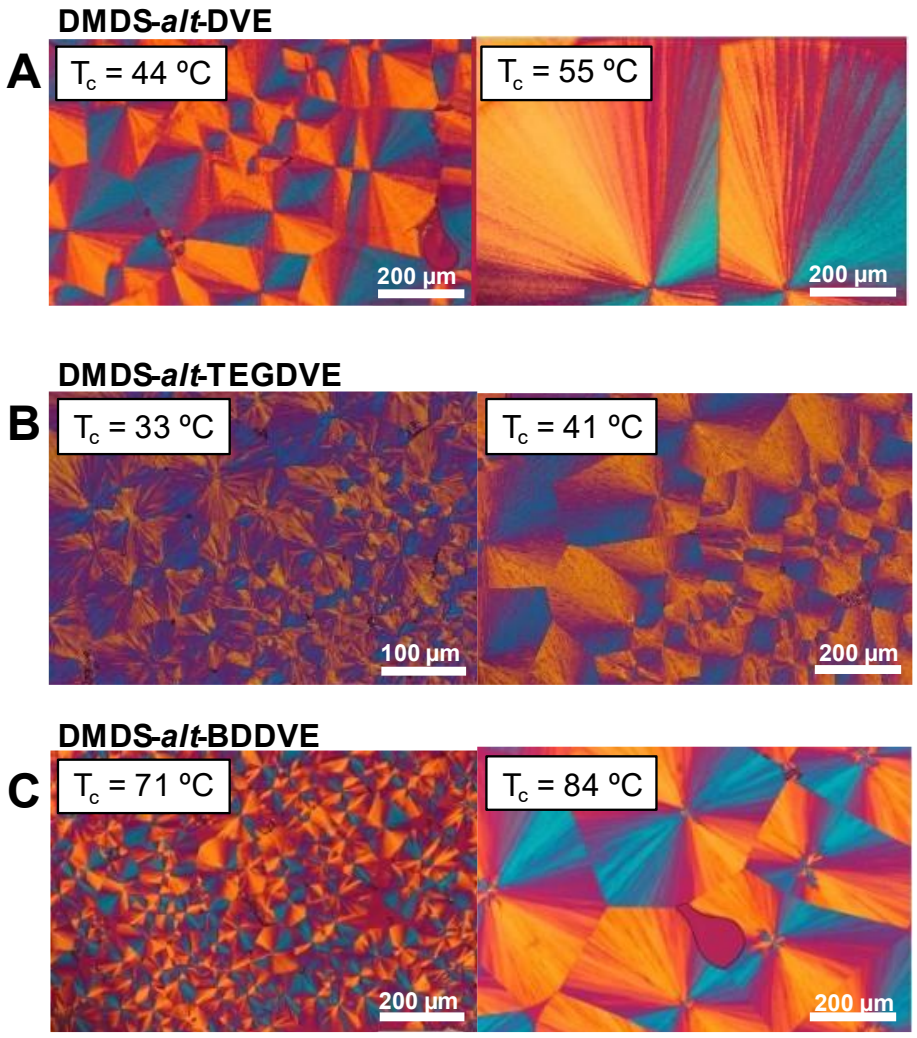

Figure 7.6. PLOM images of DMDS-*alt*-DVE, DMDS-*alt*-TEGDVE and DMDS-*alt*-BDDVE after isothermal crystallization at the indicated T_c. A) DMDS-*alt*-DVE at low $T_c = 48$ ºC and high $T_c = 55$ ºC. B) DMDS-*alt*-TEGDVE at low $T_c = 33$ ºC and high $T_c = 41$ ºC. C) DMDS-*alt*-TEGDVE at low $T_c = 71$ ºC and high $T_c = 84$ ºC.

The lowest T_c used was determined as the lowest temperature that could be reached without onset of crystallization during cooling at 50 ºC/min while the highest T_c was the highest temperature at which neither nucleation nor

growth could be followed (due to a very small number of spherulites and/or a very slow growth process). Hence, it was not possible to study the nucleation kinetics for all polymorphs exhibited by the three copolymers. The range of $T_c s$ at which it was possible to study DMDS-alt-DVE was determined to be from $T_c = 44$ °C to $T_c = 55$ °C, the T_c range of DMDS-alt-TEGDVE was from $T_c =$ 33 °C to $T_c = 41$ °C and, lastly, DMDS-alt-BDDVE was determined to be studied from $T_c = 71$ °C to $T_c = 84$ °C. The distinct melting point of each polymorphic phase was used to determine which polymorph had been crystallized and subsequently melted.

In Figure 7.6, for clarity, while multiple crystallization temperatures were examined, we will hereby refer to a $T_c = 44$ °C to allude to a low crystallization temperature for DMDS-alt-DVE, a $T_c = 33$ °C to refer to a low crystallization temperature for DMDS-alt-TEGDVE and a $T_c = 71$ °C to allude to a low crystallization temperature for DMDS-alt-BDDVE. Additionally, a $T_c = 55$ °C will be used to reference a high crystallization temperature for DMDS-alt-DVE, a $T_c = 41$ °C will be used to refer to a high crystallization temperature for DMDS-alt-TEGDVE and a $T_c = 84$ °C will be used to allude to a high crystallization temperature for DMDS-alt-BDDVE (see Figure 7.6). The morphology observed varies from small spherulites at lower T_cs (high supercooling) to larger spherulites at higher T_cs (low supercooling). The changes in the size of the spherulite can be explained by knowing that higher supercooling increases the nucleation rate by enhancing the thermodynamic driving force for crystallization, and assuming that each spherulite is generated by one nucleus, a higher nucleation rate leads to the formation of smaller crystalline structures, and a slower nucleation rate leads to larger crystalline structures as is the case here (see Figure 7.6).

7.3 Structure determination for all three homopolymers via WAXS experiments

Analogous *in-situ* experiments similar to those performed in the DSC and PLOM were carried out using synchrotron wide angle X-ray scattering (WAXS). Due to experimental conditions at the ALBA synchrotron facility, these *in-situ* WAXS experiments were carried out at 20 ºC/min. It is important to notice that experiments carried out at 20 ºC/min by DSC and PLOM exhibited very similar results as those carried out at 50 ºC/min. DSC experiments carried out at 20 ºC/min can be found in Figure 7.1.

Previous studies[21] revealed, under analogous thermal protocols, differences in the scattering curves which indicated the formation of two different crystalline structures by the same polymer with slight variations in unit cell parameters; for DMDS-*alt*-DVE the $L-T_m$ form exhibited three prominent diffraction peaks at q = 14.5 nm^{-1}, 16.4 nm^{-1}, and 17.6 nm^{-1}, while the $H-T_m$ form showed four peaks at q = 14.5 nm^{-1}, 15.9 nm^{-1}, 16.7 nm^{-1}, and 17.7 nm^{-1}, with similar uncertainties. Our studies yielded similar results which are described in detail below.

The WAXS patterns measured at two distinct temperatures taken during the second heating for each alternating copolymer are shown in Figure 7.7. In Figure 7.7A, three distinct diffraction peaks can be identified at 14.6 nm^{-1}, 16.2 nm^{-1}, and 17.6 nm^{-1} for DMDS-*alt*-DVE at T_1 = 40 ºC for the $L-T_m$ form. The diffraction pattern for the $H-T_m$ form at T_2 = 76 ºC shows a fourth low-intensity peak that appears at 15.9 nm^{-1}, which is not observed for the $L-T_m$ form. Additionally, we can observe a slight shift in the position of the peaks initially at 16.2 nm^{-1} and 17.6 nm^{-1} (at 40 ºC) to higher q values at 76 ºC, see Table 7.1, where the scattering patterns and the exact position of each maximum

for each homopolymer are reported.

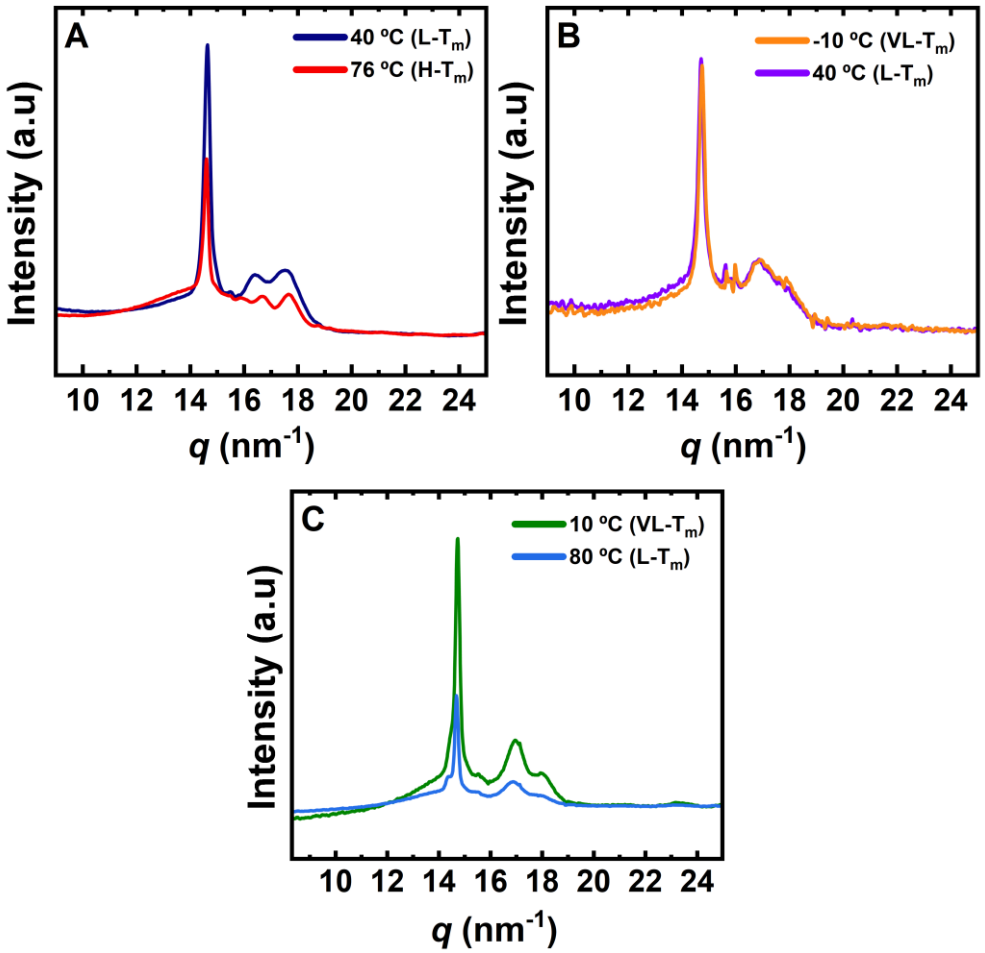

Figure 7.7. Comparison of the WAXS profiles obtained during heating at 20 ºC/min for DMDS-*alt*-DVE, DMDS-*alt*-TEGDVE, DMDS-*alt*-BDDVE. A) DMDS-*alt*-DVE at 40 ºC ($L-T_m$ form is present) and at 76 ºC ($H-T_m$ form is present) B) DMDS-*alt*-TEGDVE at −10 ºC ($VL-T_m$ form is present) and at 40 ºC ($H-T_m$ form is present) C) DMDS-*alt*-BDDVE at 10 ºC ($VL-T_m$ form is present) and at 80 ºC ($H-T_m$ form is present). The labeling of the polymorphs present has been done based on the DSC and PLOM results.

Table 7.1. Scattering q values of all polythioethers.

Polythioether	q (nm^{-1}) $VL-T_m$	q (nm^{-1}) $L-T_m$	q (nm^{-1}) $H-T_m$
DMDS-alt-DVE	-	14.6	14.6
	-	-	15.9
	-	16.2	16.7
	-	17.6	17.7
DMDS-alt-TEGDVE	14.8	-	14.6
	16.8	-	16.7
DMDS-alt-BDDVE	14.7	-	14.6
	17.0	-	16.8
	18.0	-	17.8

The WAXS pattern for DMDS-alt-TEGDVE for the $VL-T_m$ form at $T_1 = -10$ ºC shows two distinct peaks: a sharp peak at 14.8 nm^{-1} and a broader peak with a slight shoulder at 16.8 nm^{-1}. A small shift to lower q occurs (see Table 7.1) when the $VL-T_m$ form of DMDS-alt-TEGDVE at $T_2 = 40$ ºC transforms into the $H-T_m$ form.

Finally, in Figure 7.7C, the $VL-T_m$ form ($T_1 = 10$ ºC) of DMDS-alt-BDDVE exhibits three distinct peaks one at 14.7 nm^{-1}, 17.0 nm^{-1} and 18.0 nm^{-1} while the $H-T_m$ form ($T_2 = 80$ ºC) shows prominently two peaks which have slightly shifted to lower qs at 14.6 nm^{-1} and 16.8 nm^{-1} and a small peak at 17.8 nm^{-1}. These results support our interpretation that the different phases have similar crystalline structures, and hence, the transformation from one to the other could occur via self-nucleation of the lower-melting phase, making the transition from one phase to the other difficult to discern through PLOM

experiments.

In general, all the results obtained by WAXS support the DSC findings as differences could be found in the WAXS patterns corresponding to each polymorph. However, the differences between the crystalline unit cells of the different polymorphs should be quite small, as indicated by the small changes detected in the WAXS results.

7.3.1 The origin of positive spherulites revealed by AFM

The nucleation and growth kinetics were studied via PLOM after identifying the polymorphs for all three alternating homopolymers employed here. As mentioned in the above sections, the resulting spherulites of these different polymorphs of all three homopolymers are either negative, positive or often a mixture of both. Interestingly, when performing non-isothermal experiments at various rates, we observed a change in birefringence as one phase transformed into another. For this, experiments were carried out in which we achieved the $L - T_m$ and $H - T_m$ form of each polymorph and AFM experiments were performed to determine the nature of this phenomenon and gain a deeper insight into the morphology of each phase.

The spherulites in this work exhibit the typical Maltese cross pattern (as seen in Figure 7.3 and Figure 7.4) when observed between crossed polarizers[23,24]. Birefringence is a phenomenon in which a material exhibits different refractive indices along different axes, splitting light into two polarized components as it passes through the material[25] and generally speaking, the birefringence of spherulites is mainly dependent on the orientation of lamellar crystals within them (and concomitantly the chain orientation in crystallographic registry inside the lamellae)[23,25,26]. Spherulite lamellar crystals

grow radially from a central nucleation point extending outward symmetrically.

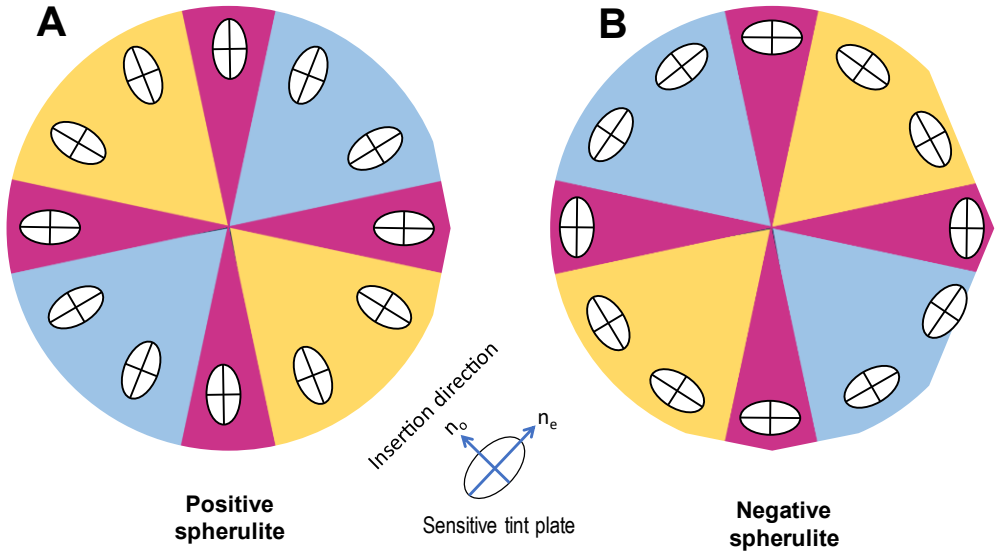

Figure 7.8. Illustration of two types of spherulites under PLOM. A) Positive Spherulite. B) Negative Spherulite.

To understand the optical properties of these spherulites, an indicatrix is defined[26,27]. For this, we are using a biaxial crystal model, where the refractive indices along the *a* and *b* crystal dimensions have the same magnitude ($n_a = n_b$), while the refractive index along the chain axis *c* has a different value normally expected to be larger ($n_c > n_a = n_b$). Depicted in Figure 7.8 is an ellipsoid whose axes are proportional to the principal refractive indices of a crystal (defined as ordinary ray, n_o and extraordinary ray, n_e)[26,29]. That is, a long axis representing the chain axis, n_e, and a minor axis perpendicular to the chain axis, n_o. The reason we need two refractive indexes is that when light interacts with the polymer chains along the chain axis, n_e, (parallel to the long axis of the ellipsoid), it experiences a different refractive index compared to when it interacts with the polymer chains perpendicular to the chain axis, n_o. Therefore, $n_e = n_c$ and $n_o = n_a = n_b$.

Figure 7.8A shows the case of a positive spherulite in which the largest refractive index is in the radial direction of the spherulite, which in the majority of cases indicates that the chain axis (*i.e.,* the long axis) is parallel to the radius of the spherulite and the smallest refractive index (*i.e.,* perpendicular to the long axis) is tangential to the spherulite. That is, $n_e < n_o$ and when observed through PLOM with a sensitive tint plate, the 1st and 3rd quadrant appear blue in color[26,29]. For negative spherulites, see Figure 7.8B, where $n_e > n_o$ and when observed by PLOM with a sensitive tint plate, the 1st and 3rd quadrant appear yellow[26,29]. That is, the largest refractive index is tangential to the spherulite.

Typically, in most polymeric spherulites, the crystalline lamellae grow radially with their chains folded; therefore, the chain axis is tangential to the spherulite, and the *b* axis is parallel to the radius; hence, most spherulites tend to be negative[26,29,31]. However, in the case of DMDS-alt-DVE, DMDS-alt-TEGDVE and DMDS-alt-BDDVE as seen in Figure 7.3, when non-isothermal crystallization takes place the spherulites obtained are primarily positive, that is, the highest refractive index is located along the radius of the spherulite. This can be seen in the PLOM images as positive spherulites show quadrants two and four of yellow color and the first and third quadrants of blue color[26,29].

On the other hand, during isothermal experiments the situation is different for each homopolymer. DMDS-alt-DVE presents positive spherulites during non-isothermal and isothermal experiments. However, although DMDS-alt-TEGDVE generally presents positive spherulites, it is important to note that at lower T_cs the spherulites appear to be more mixed (the quadrants are not so well defined) which can be seen clearly in Figure 7.6B in the section above. For DMDS-alt-BDDVE both positive and negative spherulites are formed. While some are positive as soon as they are formed, others change from negative to positive as they grow. This can be observed particularly as a mixture of positive

and negative spherulites appears to be present as there are more nuclei which can only grow to a certain extent (see Figure 7.6). At higher T_cs, as there are fewer nuclei, the spherulites can grow more, and as a result, most transform and change signs to form positive spherulites. This change in sign from negative to positive can be observed by taking a closer look at the center of the spherulites (the nucleus) in Figure 7.6C, as there you can see that they started as negative and switched to positive. More details on the optical properties of spherulites can be found in references[23,24,26–28].

Figure 7.9 to Figure 7.11 present the topographical images captured by AFM, showcasing the crystallization behavior of the homopolymers under various conditions.

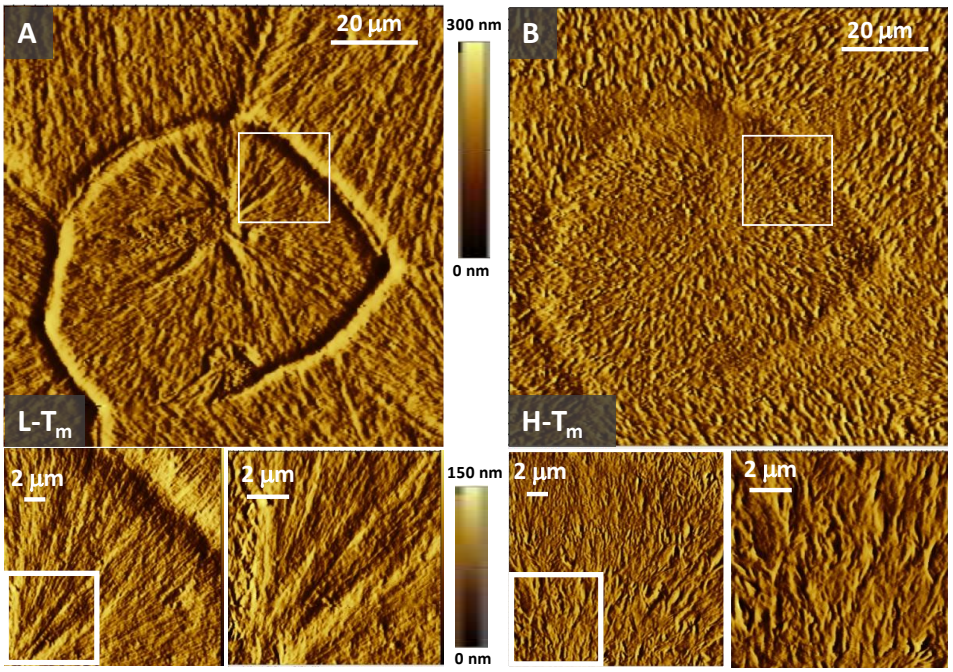

Figure 7.9. AFM images of the $L-T_m$ (cooling at 10 ºC/min to room temperature) and $H-T_m$ (heating at 10ºC/min to 73 ºC) phases in DMDS-alt-DVE sample. A) $L-T_m$ form of DMDS-alt-DVE. B) H$-T_m$ form of DMDS-alt-DVE.

Notably, the images reveal the presence of large spherulites, some exceeding 100 μm in diameter, as observed by PLOM. Within these spherulites, the radial growth of lamellae is evident, with distinct patterns indicative of their formation process and crystalline structure.

Figure 7.9 shows the topographical features obtained for DMDS-alt-DVE after non-isothermal crystallization during cooling at 10 ºC/min from 100 ºC to 25 ºC, thus the crystallization of the $L - T_m$ form is taking place. The sample was subsequently heated from 25 ºC to 73 ºC and quenched (Figure 7.9B), thus creating the $H - T_m$ form. The images include a 100 μm x 100 μm area covering the same spherulite in both panels and different magnifications (indicated by the white squares). The morphological features are clearly different, in agreement with previous results obtained by PLOM in this sample[21,22].

The $L - T_m$ form (Figure 7.9A) shows large spherulites, which exhibit long lamellae with the typical radial growth. The subsequent heating and crystallization at T_c = 73 ºC ($H - T_m$ polymorph) retain the previous spherulitic template but with new anisotropic crystalline structures that emerge within the template, thus retaining the crystalline memory (Figure 7.9B). For DMDS-alt-TEGDVE and DMDS-alt-BDDVE there is also a change in the morphological features, but in these samples, it has been more difficult to locate the previous crystalline templates (see Figure 7.10 below).

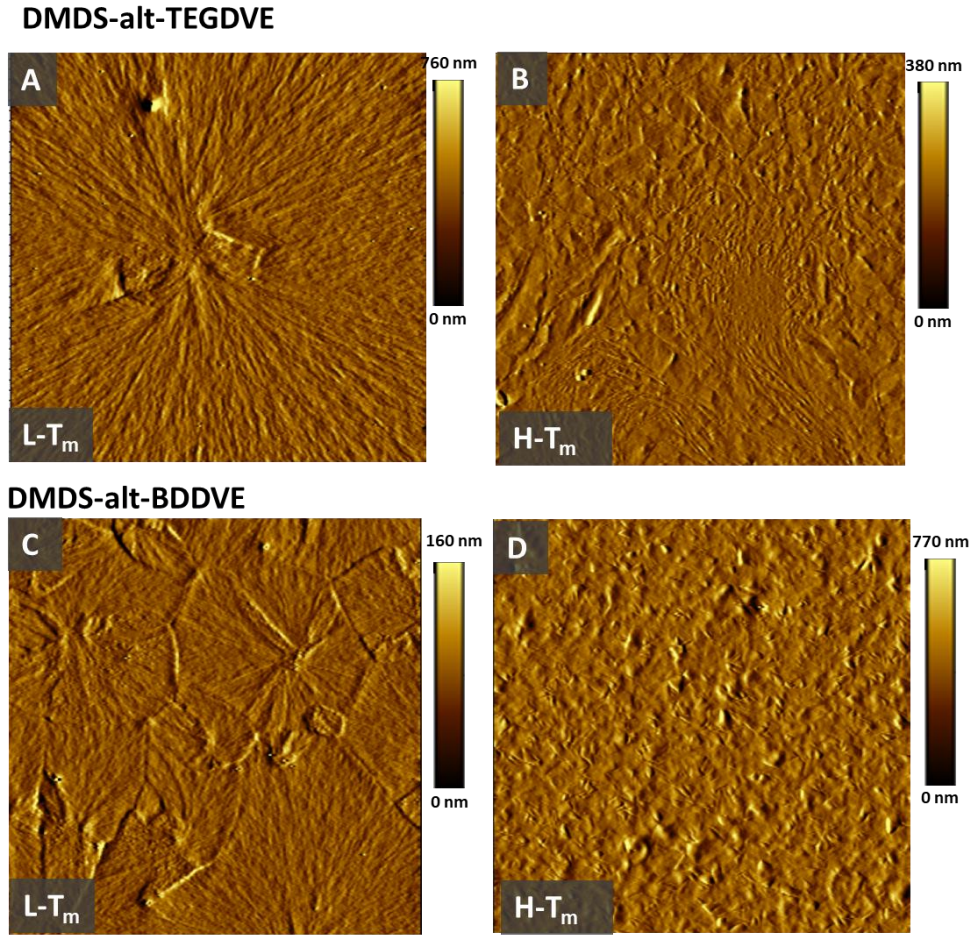

Figure 7.10. AFM images of the $L-T_m$ and $H-T_m$ phases in DMDS-alt-TEGDVE and DMDS-alt-BDDVE copolymers. A) $L-T_m$ form of DMDS-alt-TEGDVE. B) $H-T_m$form of DMDS-alt-TEGDVE. C) $L-T_m$ form of DMDS-alt-BDDVE. D) $H-T_m$ form of DMDS-alt-BDDVE.

A detailed examination of the morphologies obtained for each polymorph (the $L-T_m$ and $H-T_m$ form) are depicted in the AFM images in Figure 7.11. The images clearly reveal the morphological differences between the two polymorphs, with the presence of parent lamellae that grow along the radius of the spherulites (with the c-axis tangential to the spherulites), but also daughter lamellae that are more difficult to see (at the magnification presented in Figure

7.11, a close-up of the cross-hatched morphology marked in Figure 7.11C can be better seen in Figure 7.12 below) that grow perpendicularly to the dominant parent lamellae (with their c-axis parallel to the spherulites radii).

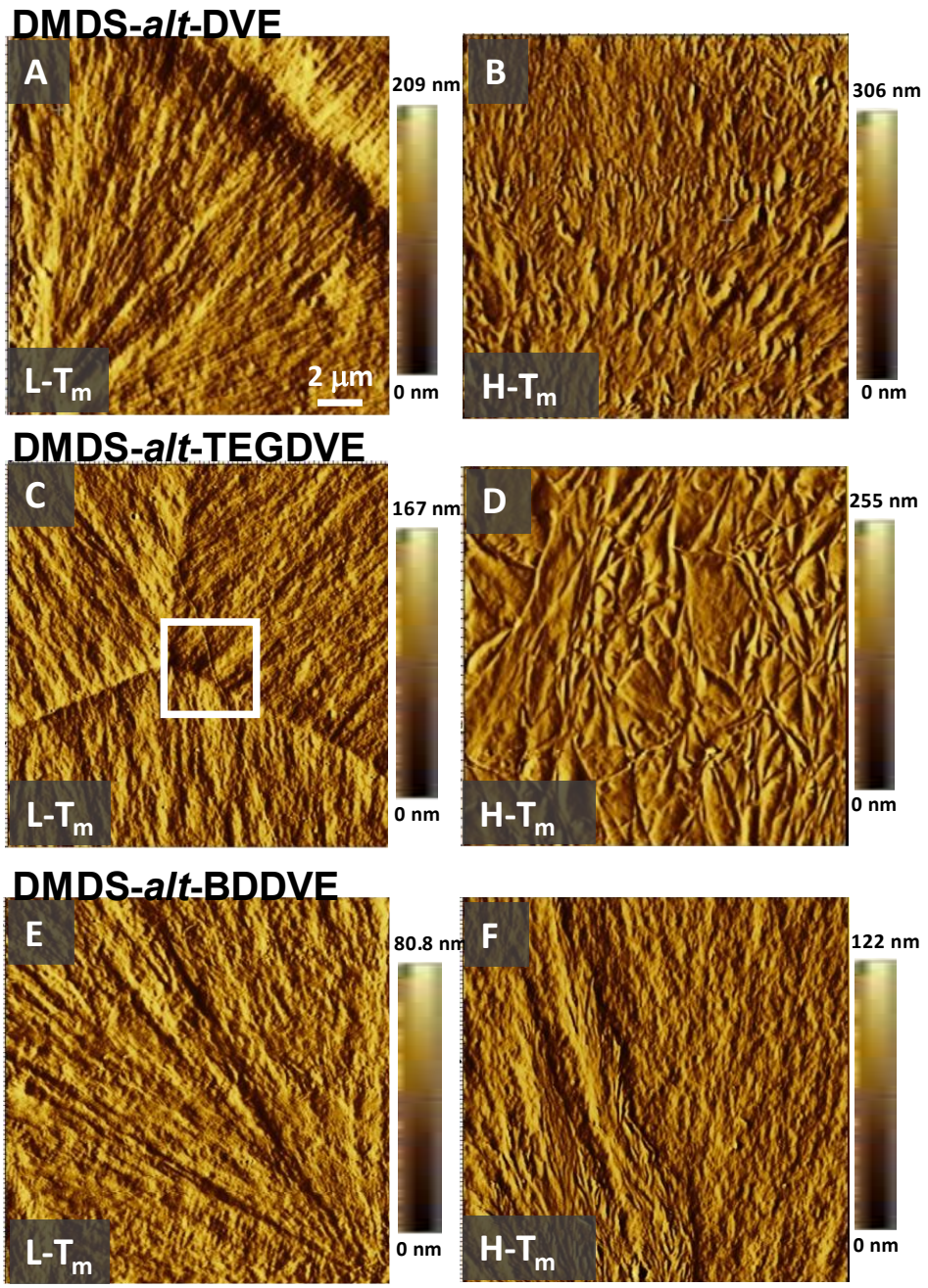

Figure 7.11. AFM images of DMDS-*alt*-DVE, DMDS-*alt*-TEGDVE and

DMDS-*alt*-BDDVE of the $L-T_m$ and $H-T_m$ phases. A) $L-T_m$ form of DMDS-*alt*-DVE B) H$-T_m$ form of DMDS-*alt*-DVE C) $L-T_m$ form of DMDS-*alt*-TEGDVE D) H$-T_m$ form of DMDS-*alt*-TEGDVE E) $L-T_m$ form of DMDS-*alt*-BDDVE F) H$-T_m$ form of DMDS-*alt*-BDDVE.

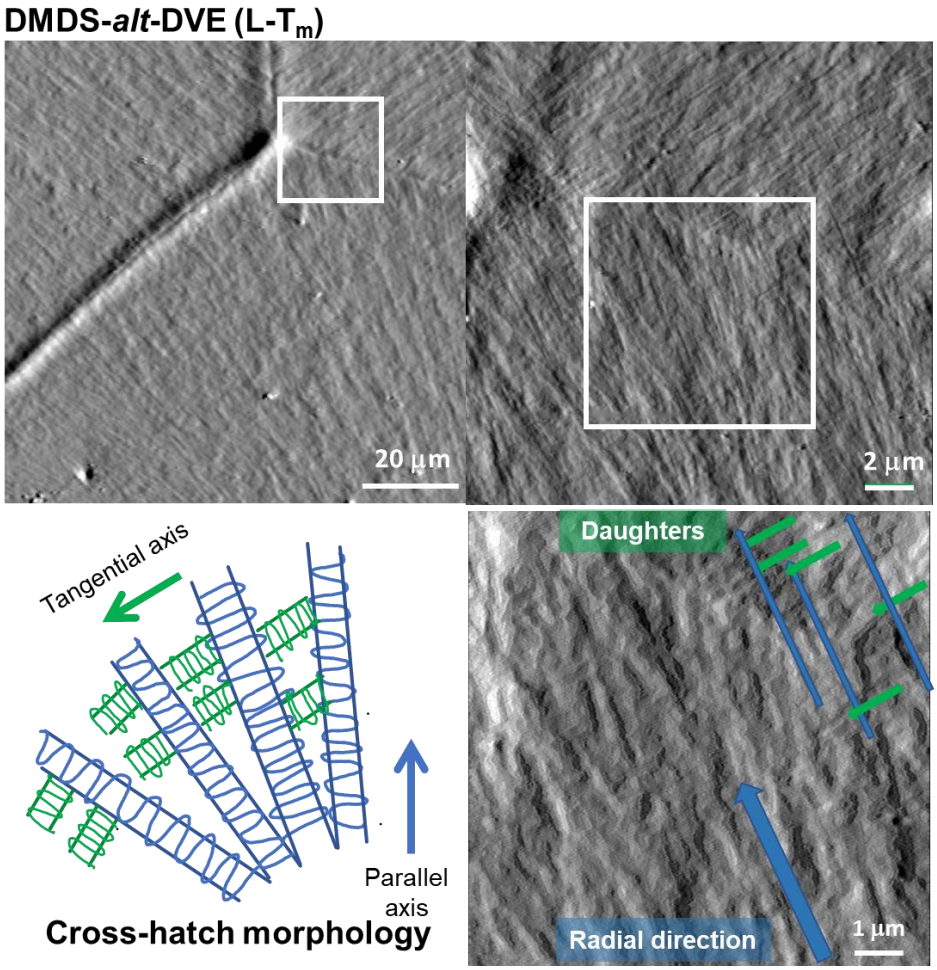

Figure 7.12. AFM images of the $L-T_m$ phase in DMDS-*alt*-DVE copolymer at different magnifications. The arrows indicate the direction of the main (radial) and daughter (perpendicular) lamellae.

This peculiar lamellar branching generates a morphology usually termed "cross-hatched" similar to that observed in isotactic polypropylene[29]. The

spherulites may be positive, negative, or mixed depending on the parent versus daughter lamellae ratio.

While the AFM only probes the surface of the film prepared, PLOM averages the optical properties of the entire film, as the light is transmitted through the thickness of the sample. Thanks to observing the cross-hatching morphology via AFM at the surface of the films in Figure 7.9 and Figure 7.11, we can explain the peculiar finding of positive spherulites, which is uncommon in most polymers[23]. The formation of the cross-hatched morphology depends on the exact secondary nucleation of the daughter lamellae on the parent lamellae. It could also rely on the specific polymorph that is formed by the conditions for its development (*i.e.,* from the melt or upon cold-crystallization).

7.3.2 Overall crystallization kinetics of all three homopolymers via DSC and FSC

We measured separately the primary nucleation and the spherulitic growth kinetics of the $L-T_m$ phase of DMDS-alt-DVE, DMDS-alt-TEGDVE and DMDS-alt-BDDVE and the results are presented and discussed in Appendix 2 located in Chapter 8. In the present section we focus on the DSC overall crystallization kinetics (which include both primary nucleation and growth kinetics) of these homopolymers. DSC isothermal crystallization experiments were carried out in a small range of temperatures, as limited by the maximum cooling rate of the calorimeter employed under temperature control (*i.e.,* 60 ºC/min).

For DMDS-alt-DVE the $T_{c,min}$ was determined to be T_c = 60 ºC, this temperature represents the threshold at which the material can be rapidly cooled without undergoing crystallization. Knowing the $T_{c,min}$, the sample was heated to its molten state and kept there for 3 min to erase thermal history. Then, the

sample was rapidly cooled down to a range of T_c values with $T_c \geq T_{c,min}$, and kept at this temperature until saturation. Finally, the sample was heated to T_m + 30 ºC.

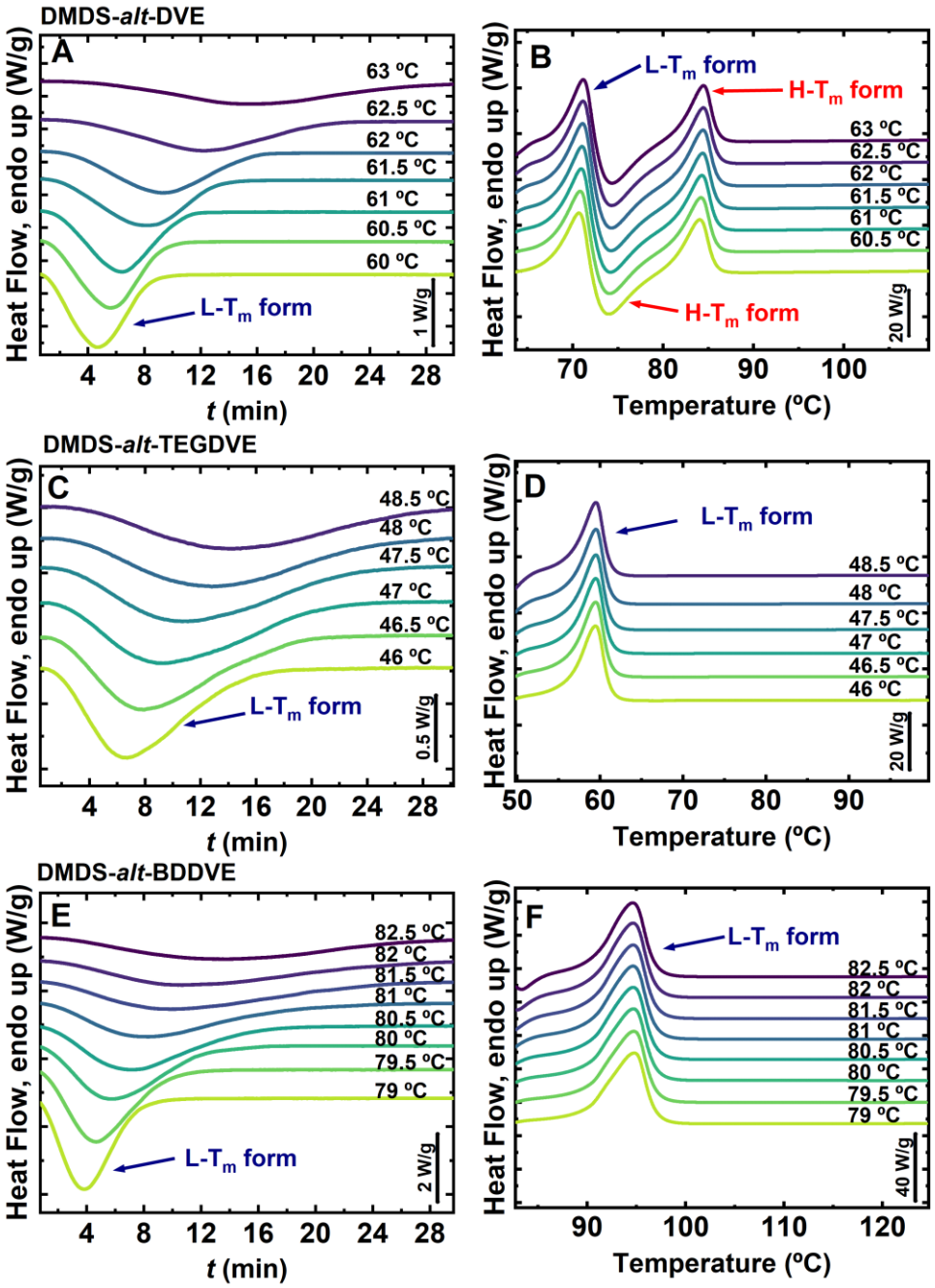

Figure 7.13. DSC scans for DMDS-*alt*-DVE, DMDS-*alt*-TEGDVE and

DMDS-*alt*-BDDVE at the indicated T_c A) DSC scans measured during isothermal crystallization of DMDS-*alt*-DVE at the indicated T_c values. B) Subsequent heating scans at 20 ºC/min of DMDS-*alt*-DVE after the isothermal crystallization scans shown in A. C) DSC scans measured during isothermal crystallization of DMDS-*alt*-TEGDVE at the indicated T_c values. D) Subsequent heating scans at 20 ºC/min of DMDS-*alt*-TEGDVE after the isothermal crystallization scans shown in C. E) DSC scans measured during isothermal crystallization of DMDS-*alt*-BDDVE at the indicated T_c values. F) Subsequent heating scans at 20 ºC/min of DMDS-*alt*-BDDVE after the isothermal crystallization scans shown in E.

Figure 7.13A through Figure 7.13E show that during isothermal crystallization in the DSC at the employed T_c values, a single polymorph crystallized for each alternating homopolymer as deduced by the presence of a single crystallization isotherm (Figure 7.13A, Figure 7.13C and Figure 7.13E). Results in Figure 7.13B for DMDS-*alt*-DVE show that the heating scan immediately after the isothermal crystallization allows us to determine that the $L-T_m$ polymorphic phase was the one formed during the isothermal crystallization. This is because, its first melting peak upon heating from T_c, is in the right T_m range, and is followed by successive cold crystallization (to form the $H-T_m$ form) and a second melting, as previously demonstrated[21,22] and also seen in Figure 7.1B.

For DMDS-*alt*-TEGDVE and DMDS-*alt*-BDDVE, the polymorph that crystallized during isothermal crystallization was the $L-T_m$ form, as indicated by the melting temperatures seen in Figure 7.13D and Figure 7.13F, respectively. Additionally, no other melting peak was observed in the heating scans after isothermal crystallization.

Figure 7.13A, Figure 7.13C and Figure 7.13E show the crystallization of

the materials as a function of time. The data can be integrated and expressed as a relative conversion as a function of time (see analogous data derived from Flash DSC experiments in Figure 7.18 below), from which we can determine when the experimental overall crystallization reaches 50% conversion, this provides a measure of the overall crystallization rate. The data obtained was fitted to the Avrami theory which can be expressed as (Equation 7.1) below[30]

$$1 - V_c\,(t - t_o) = \exp(-k(t - t_o)^n) \qquad \text{Equation 7.1}$$

The theory is described in detail in Chapter 2; the parameters obtained from applying the Avrami theory can also be found in Table 8.2−Table 8.4 in Appendix 2, located in Chapter 8. The Avrami theory successfully described the overall crystallization kinetics (especially during the primary crystallization, up to 50% conversion, as detailed in the data presented in Appendix 2, located in Chapter 8). The overall crystallization kinetics data obtained by DSC for the three homopolymers will be discussed below, together with complementary data obtained by Flash DSC (see Figure 7.19 and its discussion).

A protocol was designed to isolate each polymorphic phase in these alternating homopolymers, as it has been established that through conventional rates such as those used in DSC and PLOM experiments, all of the present polymorphs cannot be isolated. For this, an FSC technique that can apply rates of up to 40,000 ºC/s was employed.

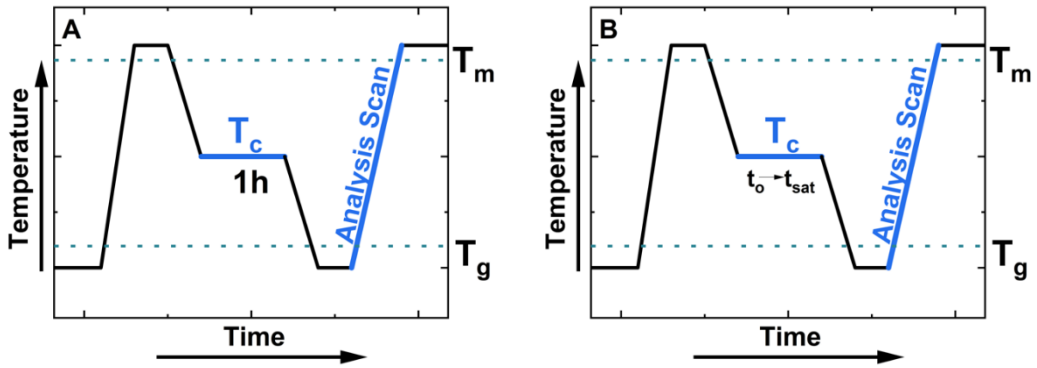

Figure 7.14. A) Protocol used to isolate each polymorphic phase via FSC. B) Protocol used to study the crystallization kinetics via FSC of DMDS-*alt*-DVE and DMDS-*alt*-TEGDVE.

The FSC protocol created for DMDS-*alt*-DVE and DMDS-*alt*-TEGDVE consisted in, first, the materials were heated thirty degrees above T_m to erase any thermal history. Then, they were rapidly cooled to various isothermal temperatures, T_c, and kept there for 1 h. The samples were then cooled rapidly to a temperature below T_g, then subsequently heated to a temperature $T_m + 30$ ºC. The subsequent heating scans show the melting endotherm after the applied crystallization procedure for each T_c (The protocol described above can be found in a schematic plot in Figure 7.14A). The T_c used is indicated on top of each curve in Figure 7.15A and Figure 7.15B.

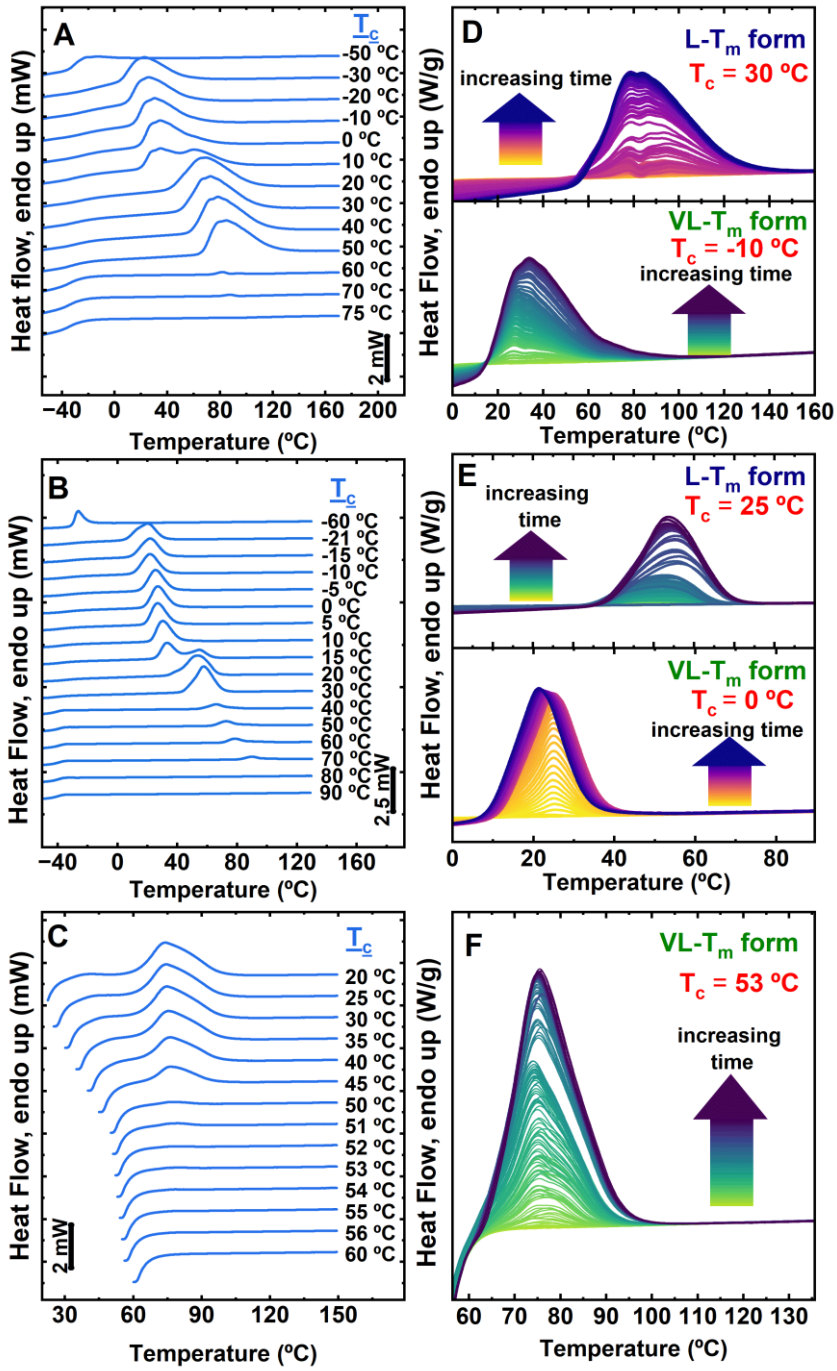

Figure 7.15. FSC heating scans of DMDS-*alt*-DVE, DMDS-*alt*-TEGDVE and DMDS-*alt*-BDDVE. Heating scans at a rate of 1,000 °C/s, after 1 h isothermal crystallization at the indicated T_c for: A) DMDS-*alt*-DVE, B) DMDS-*alt*-

TEGDVE and C) DMDS-*alt*-BDDVE. FSC heating traces at different times after isothermal crystallization until saturation at the indicated T_c for: D) DMDS-*alt*-DVE, E) DMDS-*alt*-TEGDVE and F) DMDS-*alt*-BDDVE.

The heating and cooling rates chosen for DMDS-*alt*-DVE and DMDS-*alt*-TEGDVE for these experiments were 1,000 ºC/s, as it was determined that at this rate, the materials do not crystallize during cooling or heating.

Interestingly, for DMDS-*alt*-DVE in Figure 7.15A at T_c = 60 ºC, it would seem that no crystallization processes are taking place. However, this is not the case, Figure 7.16, as well as previous studies[22] showed that when taking a close-up look at the heating curves, another very weak endotherm with a melting point at around $T_m \approx 82$ ºC associated with the melting of the $H-T_m$ form can be found. As previously reported in our recent study[22] and in Chapter 6, this result indicates that the formation of the $H-T_m$ form is highly dependent on the cooling rate and the duration of the annealing step during isothermal crystallization. That is, DMDS-*alt*-DVE can exhibit a $H-T_m$ form; however, the formation of the $H-T_m$ form via isothermal crystallization at rates above 1 ºC/s can only be achieved through excessively long periods (>24 h); therefore, it is out of our experimental window, and determining crystallization kinetics of this form is not suitable via this methodology.

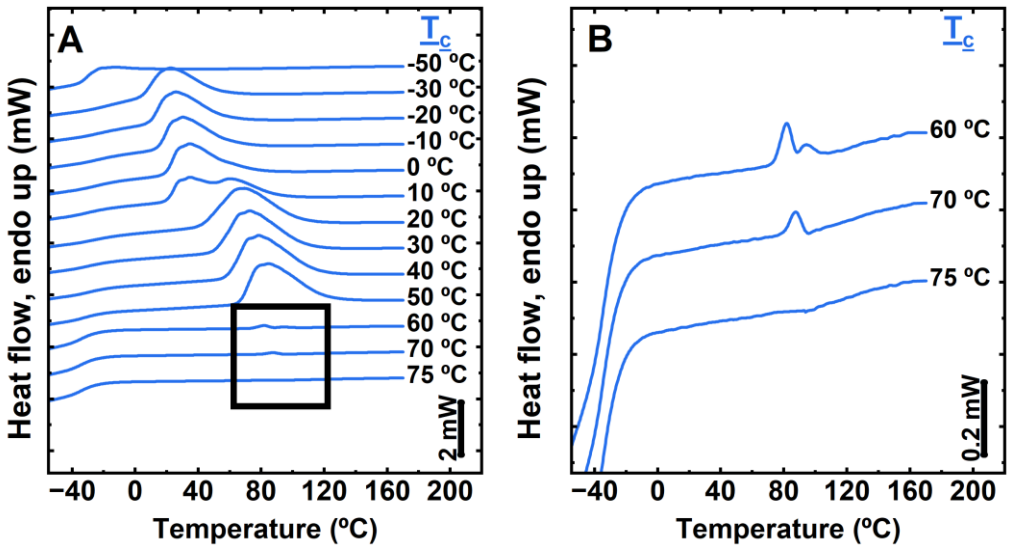

Figure 7.16. FSC heating scans of DMDS-*alt*-DVE, heating scans at a rate of 1,000°C/s, after 1 h isothermal crystallization at the indicated T_c for: A) DMDS-*alt*-DVE all temperatures B) close-up of high crystallization temperatures.

Similarly, the resulting scans for DMDS-*alt*-TEGDVE (see Figure 7.15B) showed that up to four endothermic processes can be observed in the heating traces depending on the different T_c values applied to the material. At T_c = −60 °C, no endotherms can be observed; however, we can distinguish a glass transition temperature at ca. −30 °C. Furthermore, between T_c = −21 °C to T_c = 10 °C, we can observe an endotherm at ca. T_m ≈ 25 °C, associated with the melting of the $VL-T_m$ form.

At T_c = 15 °C, in Figure 7.15B, we observe two convoluted endotherms indicating that two types of crystallites are being melted. One with a T_m ≈ 25 °C and another T_m ≈ 60 °C. The first endotherm, as previously mentioned, is associated with the melting of the $VL-T_m$ form, while the second endotherm is associated with the melting of the $L-T_m$. For a T_c = 20 °C to a T_c = 30 °C, another broad endotherm associated with the melting of the $L-T_m$ form at ca. T_m ≈ 60 °C can be found. Finally, for a T_c = 40 °C to a T_c = 70 °C, another

broad endotherm associated with the melting of the $H-T_m$ form at ca. $T_m \approx$ 75 ºC can be observed. Therefore, in the range of temperatures from −21 ºC to 10 ºC, we can follow the kinetics for the $VL-T_m$ form, and in the range of 15 ºC to 55 ºC that of the $L-T_m$ form.

On the other hand, DMDS-alt-BDDVE required a different protocol for non-isothermal experiments at various cooling rates as it was observed that even when using cooling rates of 40,000 ºC/s, the material upon heating experienced a sharp cold-crystallization (see Figure 7.2C). Because of this, the $T_{c,min}$ of the material was determined, and the crystallization kinetics of the $VL-T_m$ form was followed by firstly, heating the material up to $T_m +$ 30 ºC to erase the thermal history. Then, it was rapidly cooled down to a T_c above the $T_{c,min}$ (at which the material does not crystallize upon cooling) and kept there for 1 h. The sample was directly heated from T_c to a temperature of $T_m +$ 30 ºC. The subsequent heating scans show the evolution of the melting of the material that previously crystallized during the thermal treatment for each T_c. The detailed protocol employed can be found in a schematic plot in Figure 7.17. The $T_{c,min}$ was determined to be 50 ºC, and the range of T_c studied was from 50 to 60 ºC for the $VL-T_m$. Having established the temperature and rate conditions via FSC; here we investigated the overall crystallization kinetics for both $VL-T_m$ and $L-T_m$ forms of DMDS-alt-DVE and DMDS-alt-TEGDVE and the $VL-T_m$ form of DMDS-alt-BDDVE via isothermal crystallization. The protocol employed was chosen based on previous kinetic studies[31,32] and can be found in a schematic plot in Figure 7.14B and Figure 7.17.

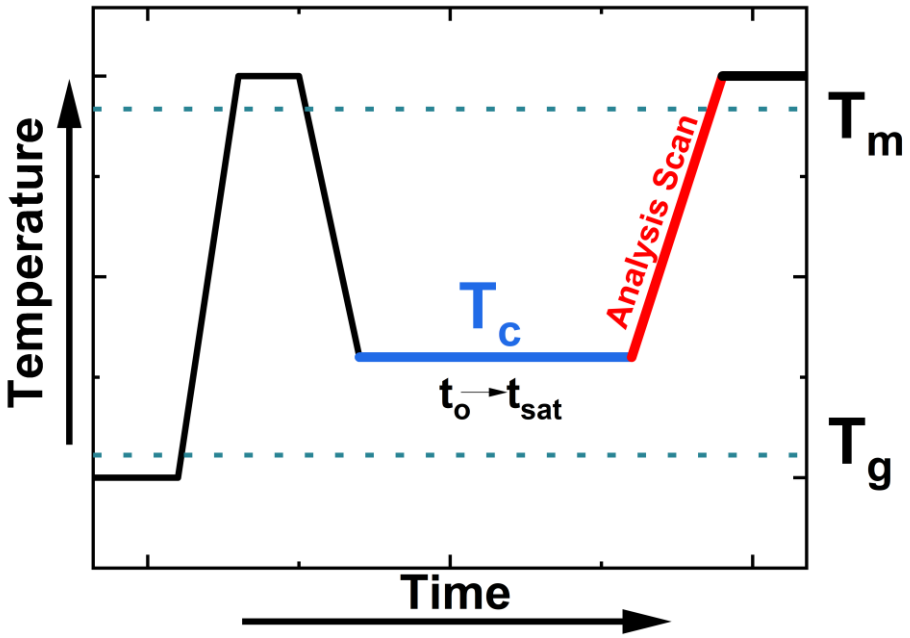

Figure 7.17. B) Protocol used to study the crystallization kinetics via FSC of DMDS-*alt*-BDDVE.

For clarity, only one temperature for each polymorph of the different homopolymers is shown in Figure 7.15D, Figure 7.15E and Figure 7.15F. However, all temperatures exhibited a similar consistent trend. For DMDS-*alt*-DVE, T_c = 30 ºC corresponds to the crystallization of the $L-T_m$ form, and T_c = −10 ºC corresponds to the $VL-T_m$ form. An endothermic peak corresponding to the melting of each polymorph after the applied isothermal crystallization protocol is shown in Figure 7.15D.

Similarly, for DMDS-*alt*-TEGDVE, the crystallization of the $L-T_m$ form occurred at a T_c = 25 ºC, while at T_c = 0 ºC the $VL-T_m$ form was developed (see Figure 7.15E). Finally, Figure 7.15F shows the evolution of the crystallization of the $VL-T_m$ form as a function of time at a $T_c = 53$ ºC for DMDS-*alt*-BDDVE.

For this, it is important to establish that the overall polymer crystallization kinetics process, measured by DSC or FSC, contains both nucleation and growth components.

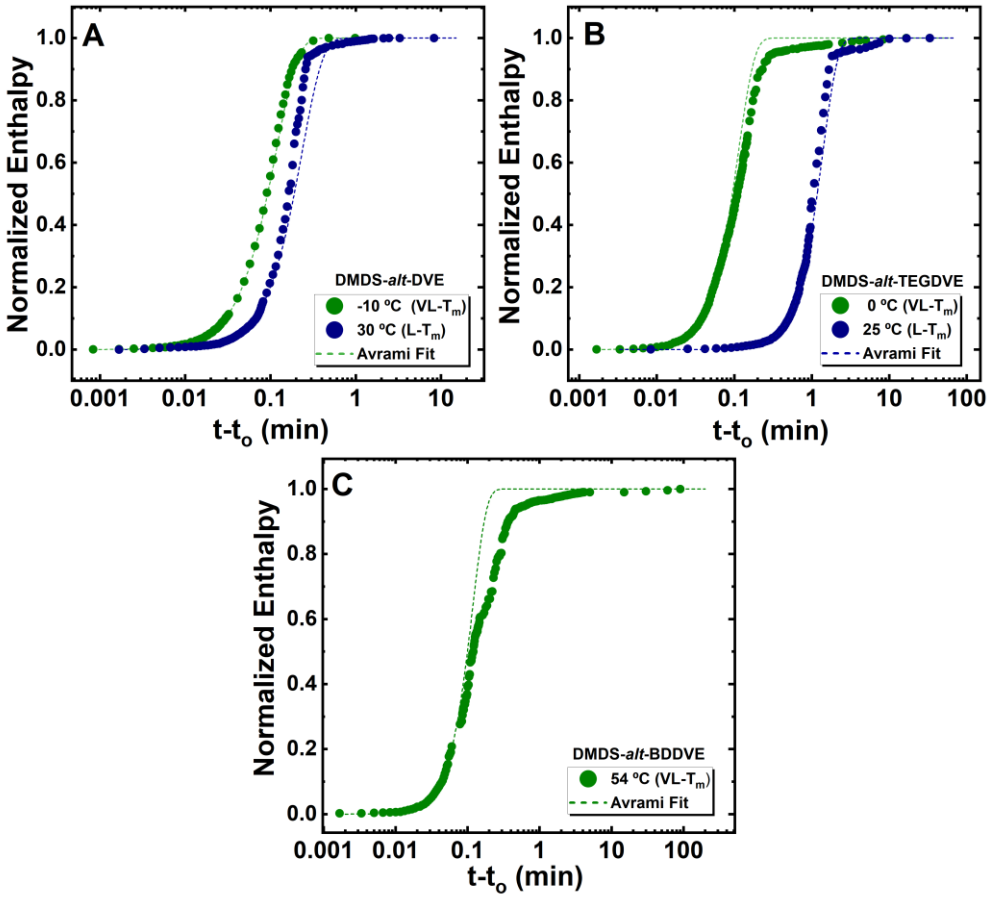

Figure 7.18. Crystallization kinetics of DMDS-*alt*-DVE, DMDS-*alt*-TEGDVE and DMDS-*alt*-BDDVE at the indicated T_c. A) Evolution of crystallization extracted from normalized enthalpy values with time for DMDS-*alt*-DVE and their corresponding Avrami fits B) Evolution of crystallization extracted from normalized enthalpy values with time for DMDS-*alt*-TEGDVE and their corresponding Avrami fits C) Evolution of crystallization extracted from normalized enthalpy values with time for DMDS-*alt*-BDDVE and their corresponding Avrami fits.

The normalized enthalpies obtained from the integration of the FSC curves (such as those reported in Figure 7.15) were plotted against the crystallization times (t) and their corresponding Avrami Fits for DMDS-alt-DVE, DMDS-alt-TEGDVE and DMDS-alt-BDDVE in Figure 7.18A, Figure 7.18B and Figure 7.18C, respectively (see Table 8.2 - Table 8.4 in Appendix 2, located in Chapter 8). As can be seen in Figure 7.18A-Figure 7.18C, the fits to the Avrami theory are very good in the primary crystallization range, *i.e.*, until about 50% conversion to the semicrystalline state, or just before any impingement of most of the spherulites occurs during crystallization.

In Figure 7.19, all the values of experimental half-crystallization times obtained by isothermal DSC and FSC experiments for all three homopolymers are plotted versus T_c. We can see that the overall kinetics are faster as T_c increases for the $VL-T_m$ form of DMDS-alt-DVE and DMDS-alt-TEGDVE as the time needed to reach 50% conversion decreases. In turn, for the $L-T_m$ of DMDS-alt-DVE and DMDS-alt-TEGDVE as T_c increases, the crystallization rate decreases; hence, the half-crystallization time increases.

This trend can be observed in the results obtained from both FSC and DSC experiments for DMDS-alt-DVE. Therefore, the overall crystallization kinetics of $VL-T_m$ forms are faster; this could be attributed to the fact that this phase is the less thermodynamically stable phase, and thus, it is kinetically favored[33,34].

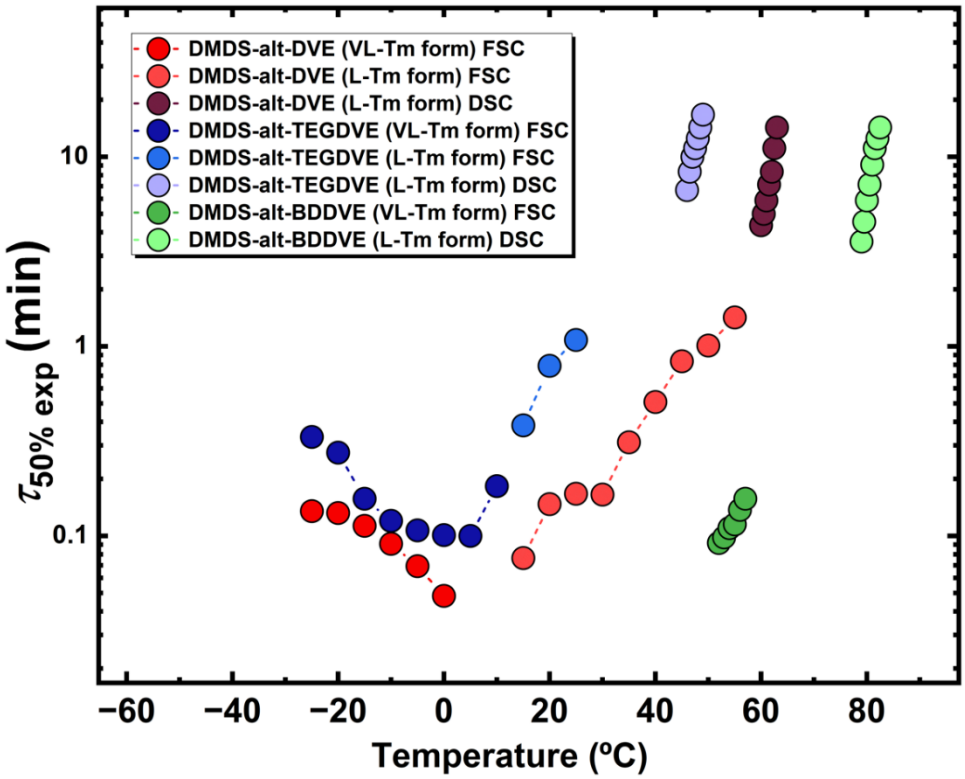

Figure 7.19. Half-crystallization time ($\tau_{50\%}$) as a function of crystallization temperature for DSC and FSC for all three polymers.

Since the $L-T_m$ form is more thermodynamically stable than the $VL-T_m$, its overall crystallization kinetics should be slower, as is the case here. In the case of DMDS-*alt*-DVE, this is further supported by the fact that the $H-T_m$ form has such slow kinetics that it was not possible to measure its crystallization kinetics even with FSC.

On the other hand, for DMDS-*alt*-TEGDVE during DSC experiments, the overall crystallization of the $L-T_m$ form follows the same trend; that is, as T_c increases the half-crystallization time increases. For DMDS-*alt*-BDDVE, a smaller range of temperatures was able to be studied due to the fast kinetics of this homopolymer in which we observed that for the $VL-T_m$ form, the crystallization rate follows a different trend in the same form for DMDS-*alt*-

TEGDVE and DMDS-*alt*-DVE; here, as T_c increases, the half-crystallization time also increases, and hence, the rate becomes slower.

In summary, Figure 7.19 shows the general expected trend for the overall crystallization rates of polymers (if all polymorphs are considered), where the rate first increases with supercooling up to a maximum value (*i.e.,* minimum half-crystallization time in Figure 7.19) and then decreases as temperatures become low and approach vitrification. However, there are several interesting novel features in Figure 7.19: (i) It was possible to follow for the first time the overall crystallization kinetics of alternating homopolythioethers; (ii) the crystallization rate of isolated polymorphs was also measured for these types of homopolymers by matching FSC and DSC results depending on the crystallization temperature range of the 3 different crystalline phases; (iii) we were able to measure a trend regarding the relative crystallization rate of the three different homopolymers.

Regarding the crystallization rates, the homopolymer with the fastest overall crystallization kinetics (considering all polymorphs) among the 3 studied here is DMDS-*alt*-BDDVE, followed by DMDS-*alt*-DVE and then DMDS-*alt*-TEGDVE. This order is consistent with the separate measurements performed of primary nucleation (where the order in Figure 8.5A in Appendix 2, located in Chapter 8, can also be considered as DMDS-*alt*-BDDVE > DMDS-*alt*-DVE > DMDS-*alt*-TEGDVE by extrapolating the curves in the 40-90 ºC range).

The homopolymers' chemical repeating units are relatively similar to one another, see Scheme 7.1. As the homopolymers include heteroatoms like oxygen and sulfur, explaining the order of the overall crystallization rate by considering the differences in the chemical structure of the repeating units of the homopolymers is not easy. The overall crystallization kinetics is influenced

by chain flexibility, molecular diffusion, nucleation, and intermolecular interactions. We assume that the molecular weight differences can be ignored, as the three polymers have a similar range of 10-17 kg/mol.

We decided to perform molecular dynamic simulations to predict the diffusion capabilities of these alternating homopolymer molecules in the melt as a function of their molecular structures. The predicted values could be used as a first guideline to interpret the differences in crystallization rates experimentally determined. Specifically, a polymer chain tends to crystallize more rapidly when it possesses greater diffusive properties. That is, the ability of the polymer chains to diffuse in the melt plays a pivotal role in the transport of chains from the melt to the crystallization front. The molecular dynamic simulations were carried out, and will be discussed in a separate section below.

The Avrami index (n) predicts the type of superstructures and their evolution with time. However, these predictions have to be corroborated by separate experiments to observe the generated morphology (usually PLOM or AFM), as the order of the kinetics may not accurately reflect the type of microstructures formed. Table 8.2−Table 8.4 in Appendix 2, located in Chapter 8, shows how n can vary with T_c for each polymorph formed. For the $VL-T_m$ form, at all T_cs, the Avrami index can be approximated to 2. This result can be interpreted by considering that instantaneously nucleated axialites were formed. Similarly, for the $L-T_m$ polymorph, at low T_cs, the growing structures can be described as axialites according to the Avrami index values close to 2.

For DMDS-alt-DVE, PLOM and AFM studies showed that the $T_{c,min}$ at which the sample could be crystallized isothermally was above 35 ºC; therefore, we cannot determine under conventional rates if the material's morphology coincides with the results obtained from fitting to the Avrami

model. Nevertheless, at high T_cs (*i.e.*,> 35 ºC), the parameter n describes spherulitic growth obtained from FSC and DSC experiments[22]. AFM results (see Figure 7.9 to Figure 7.11) show this spherulitic morphology.

Unfortunately, it was impossible to observe the morphology of $VL{-}T_m$ as it crystallizes at very low-crystallization temperatures, and the melting point is close to room temperature (the temperature at which our AFM studies could be conducted). Similar results were obtained for DMDS-alt-TEGDVE and DMDS-alt-BDDVE, in which for most T_cs, the Avrami index was close to 2. However, as seen in PLOM and AFM experiments, the resulting morphology for all forms of DMDS-alt-TEGDVE and DMDS-alt-BDDVE homopolymers were spherulites, a fact that does not match in this case the predictions of the Avrami index.

7.3.3 Density, characteristic ratio and chain diffusion simulation

Figure 7.20 shows the dependence of the melt density and characteristic ratio (C_n) with the temperature for each polymer.

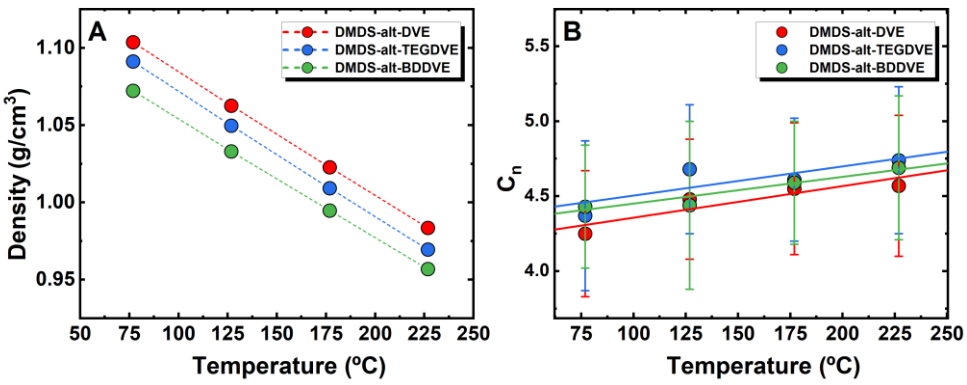

Figure 7.20. A) Melt density and B) Stiffness (characteristic ratio) as a function of the temperature for the three simulated polymers.

Polythioethers were found to have a higher density than poly(ethylene oxide), PEO (see Figure 8.9 in Appendix 2 located in Chapter 8). DMDS-*alt*-DVE has the higher density among the three polythioethers. In addition, the decrease in density can be observed with increasing temperature for all systems (Figure 7.20A).

In terms of polymer backbone flexibility, all polythioethers (Figure 7.20B) display a lower C_n value compared to PEO (Figure 8.8 in Appendix 2, located in Chapter 8). Significantly, the chain dimensions exhibit a positive temperature-dependent expansion, contrary to the negative expansion observed in PEO. This distinctive behavior is attributed to the incorporation of the bulky sulfur atom in the backbone. While variations in C_n values are subtle, it suggests that among the three homopolymers, DMDS-*alt*-DVE may indeed display higher flexibility. The diffusion of polymer chains is an important aspect to consider during crystal growth. Faster diffusion facilitates polymer chains to reach the crystal front, thereby increasing the crystallization rate. In Figure 7.21, the atomistic mean square displacement at two different temperatures is presented. At long times, the polymer dynamics are governed by chain diffusion.

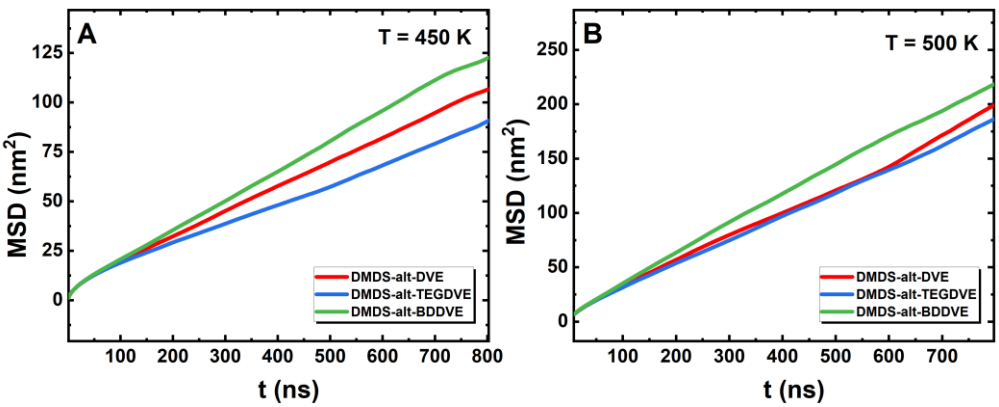

Figure 7.21. Atomistic mean-square displacements (MSD) of the backbone atoms for each of the three homopolymers studied here at different temperatures

A) 450 K (177 ºC) and B) 500 K (227 ºC).

The DMDS-alt-BDDVE homopolymer exhibits the fastest diffusion, while the DMDS-alt-TEGDVE has the slowest. This disparity in chain mobility in the melt may account for the observed slower crystallization rate in the DMDS-alt-TEGDVE homopolymer. Conversely, the high chain mobility of DMDS-alt-BDDVE homopolymer can justify its exceptionally high overall crystallization rate, as indicated in Figure 7.21.

7.4 Conclusions for Chapter 7

DMDS-*alt*-DVE, DMDS-*alt*-TEGDVE, and DMDS-*alt*-BDDVE homopolymers exhibit distinct non-isothermal crystallization behaviors and polymorphic phases. Our study successfully identified the different polymorphic phases and investigated their nucleation and growth kinetics for DMDS-*alt*-DVE, DMDS-*alt*-TEGDVE, and DMDS-*alt*-BDDVE using a combination of DSC, FSC and PLOM experiments. The DSC and PLOM results showcase their unique melting, recrystallization, and melting sequences in which we resolve the thermal behavior for $VL-T_m$, $L-T_m$ and $H-T_m$ forms. We also showed that the nucleation density varies among homopolymers, influencing spherulite sizes. Furthermore, in-situ WAXS experiments compared the crystalline structures in the three homopolymers, showing minor but distinct diffraction peaks. Most homopolymers exhibit some positive spherulites (as indicated by PLOM) whose origin is connected to the cross-hatched morphology that was observed by AFM. In terms of nucleation, growth, and overall crystallization, we were able to determine the kinetics associated with each process for some of the phases within each homopolymer. The overall crystallization kinetics was studied with DSC and FSC for the different polymorphs. The results clearly indicated an order in crystallization rate: DMDS-*alt*-BDDVE > DMDS-*alt*-DVE > DMDS-*alt*-TEGDVE. These differences were attributed to the different chemical repeating units of these homopolymers. Molecular dynamic simulations identified differences in the diffusion of the chains in the melt that can explain the order found in the crystallization rate.

7.5 References for Chapter 7

(1) De Rosa, C.; Auriemma, F. *Crystals and Crystallinity in Polymers: Diffraction Analysis of Ordered and Disordered Crystals*; Claudio De Rosa, Finizia Auriemma, Eds.; Wiley, 2013.

(2) Kitamura, M. Strategy for Control of Crystallization of Polymorphs. *CrystEngComm* **2009**, *11* (6), 949–964.

(3) De Rosa, C.; Auriemma, F.; Malafronte, A.; Scoti, M. Crystal Structures and Polymorphism of Polymers: Influence of Defects and Disorder. *Polym Cryst* **2018**, *1* (4), 1–21.

(4) De Rosa, C.; Scoti, M.; Di Girolamo, R.; de Ballesteros, O. R.; Auriemma, F.; Malafronte, A. Polymorphism in Polymers: A Tool to Tailor Material's Properties. *Polym Cryst* **2020**, *3* (2), 1–29.

(5) Gentili, D.; Gazzano, M.; Melucci, M.; Jones, D.; Cavallini, M. Polymorphism as an Additional Functionality of Materials for Technological Applications at Surfaces and Interfaces. *Chem Soc Rev* **2019**, *48* (9), 2502–2517.

(6) Dallaev, R.; Pisarenko, T.; Sobola, D.; Orudzhev, F.; Ramazanov, S.; Trčka, T. Brief Review of PVDF Properties and Applications Potential. *Polymers* **2022**, *14* (22), 4793.

(7) Algarni, F.; Zapsas, G.; María, N.; Maiz, J.; Müller, A. J.; Hadjichristidis, N. The Effect of Chain Topology on the Crystallization and Polymorphism of PVDF: Linear versus Star Molecules. *Macromol. Chem. Phys.* **2023**, *224* (1), 2200268.

(8) Silva, M. P.; Sencadas, V.; Botelho, G.; Machado, A. V.; Rolo, A. G.;

Rocha, J. G.; Lanceros-Mendez, S. α- and γ-PVDF: Crystallization Kinetics, Microstructural Variations and Thermal Behaviour. *Mater. Chem. Phys.* **2010**, *122* (1), 87–92.

(9) Quoc Le, C. M.; Schmutz, M.; Chemtob, A. Ab Initio Batch Emulsion Thiol-Ene Photopolymerization. *Macromolecules* **2020**, *53* (7), 2369–2379.

(10) Jasinski, F.; Lobry, E.; Tarablsi, B.; Chemtob, A.; Croutxé-Barghorn, C.; Nouen, D. L.; Criqui, A. Light-Mediated Thiol-Ene Polymerization in Miniemulsion: A Fast Route to Semicrystalline Polysul Fide Nanoparticles. *ACS Macro Lett.* **2014**, *3* (9), 958–962.

(11) Jasinski, F.; Schweitzer, J.; Fischer, D.; Lobry, E.; Croutxe, C.; Schmutz, M.; Nouen, D. L.; Criqui, A.; Chemtob, A. Thiol−Ene Linear Step-Growth Photopolymerization in Miniemulsion: Fast Rates, Redox-Responsive Particles, and Semicrystalline Films. *Macromolecules* **2016**, *49* (4), 1143–1153.

(12) Le, C. M. Q.; Schrodj, G.; Ndao, I.; Bessif, B.; Heck, B.; Pfohl, T.; Reiter, G.; Elgoyhen, J.; Tomovska, R.; Chemtob, A. Semi-Crystalline Poly(Thioether) Prepared by Visible-Light-Induced Organocatalyzed Thiol-Ene Polymerization in Emulsion. *Macromol Rapid Commun* **2022**, *43* (5), 2100740.

(13) Le, C. M. Q.; Vidal, L.; Schmutz, M.; Chemtob, A. Droplet Nucleation in Miniemulsion Thiol–Ene Step Photopolymerization. *Polym Chem* **2021**, *12* (14), 2084–2094.

(14) Durham, O. Z.; Krishnan, S.; Shipp, D. A. Polymer Microspheres Prepared by Water-Borne Thiol-Ene Suspension Photopolymerization. *ACS Macro Lett.* **2012**, *1* (9), 1134–1137.

(15) Cramer, N. B.; Scott, J. P.; Bowman, C. N. Photopolymerizations of Thiol-Ene Polymers without Photoinitiators. *Macromolecules* **2002**, *35* (14), 5361–5365.

(16) Hoyle, C. E.; Bowman, C. N. Thiol–Ene Click Chemistry. *Angew. Chem. Int. Ed.* **2010**, *49* (9), 1540–1573.

(17) Kade, M. J.; Burke, D. J.; Hawker, C. J. The Power of Thiol-Ene Chemistry. *J Polym Sci Part Polym Chem* **2010**, *48* (4), 743–750.

(18) Resetco, C.; Hendriks, B.; Badi ab, N.; Du Prez, F. Thiol-Ene Chemistry for Polymer Coatings and Surface Modification-Building in Sustainability and Performance. *Mater Horiz* **2017**, *4* (6), 1041–1053.

(19) Lowe, A. B. Thiol–Ene "Click" Reactions and Recent Applications in Polymer and Materials Synthesis: A First Update. *Polym Chem* **2014**, *5* (17), 4820–4870.

(20) Elgoyhen, J.; Pirela, V.; Müller, A. J.; Tomovska, R. Synthesis and Crystallization of Waterborne Thiol–Ene Polymers: Toward Innovative Oxygen Barrier Coatings. **2023**.

(21) Bessif, B.; Heck, B.; Pfohl, T.; Minh, C.; Le, Q.; Chemtob, A.; Pirela, V.; Elgoyhen, J.; Tomovska, R.; Müller, A. J.; Reiter, G. Nucleation Assisted through the Memory of a Polymer Melt: A Different Polymorph Emerging from the Melt of Another One. *Macromolecules* **2023**, *56* (4), 1461–1470.

(22) Pirela, V.; Elgoyhen, J.; Tomovska, R.; Martín, J.; Le, C. M. Q.; Chemtob, A.; Bessif, B.; Heck, B.; Reiter, G.; Müller, A. J. Unraveling the Complex Polymorphic Crystallization Behavior of the Alternating Copolymer DMDS-Alt-DVE. *ACS Appl. Polym. Mater.* **2023**, *5* (7), 5260–5269.

(23) Crist, B.; Schultz, J. M. Polymer Spherulites: A Critical Review. *Prog.*

Polym. Sci. **2016**, *56*, 1–63.

(24) Cavallo, D.; Müller, A. J. Polymer Crystallization. In *Macromolecular Engineering*; John Wiley & Sons, Ltd, 2022; pp 1–57.

(25) Piorkowska, E.; Rutledge, G. C. *Handbook of Polymer Crystallization*; John Wiley & Sons, 2013.

(26) Wunderlich, B. *Macromolecular Physics, Volume 1: Crystal Structure, Morphology, Defects*; Academic Press, 1973.

(27) Schultz, J. M. *Polymer Materials Science*; Prentice-Hall, 1974.

(28) Kabe, T.; Sato, T.; Kasuya, K.; Hikima, T.; Takata, M.; Iwata, T. Transition of Spherulite Morphology in a Crystalline/Crystalline Binary Blend of Biodegradable Microbial Polyesters. *Polymer* **2014**, *55* (1), 271–277.

(29) Olley, R. H.; Bassett, D. C. On the Development of Polypropylene Spherulites. *Polymer* **1989**, *30* (3), 399–409.

(30) Lorenzo, A. T.; Arnal, M. L.; Albuerne, J.; Müller, A. J. DSC Isothermal Polymer Crystallization Kinetics Measurements and the Use of the Avrami Equation to Fit the Data: Guidelines to Avoid Common Problems. *Polym. Test.* **2007**, *26* (2), 222–231.

(31) Pirela, V.; Campoy-Quiles, M.; Müller, A. J.; Martín, J. Unraveling the Influence of the Preexisting Molecular Order on the Crystallization of Semiconducting Semicrystalline Poly(9,9-Di-n-Octylfluorenyl-2,7-Diyl (PFO). *Chem Mater* **2022**, *34* (23), 10744–10751.

(32) Pirela, V.; Muller, A.; Martin, J. Crystallization Kinetics of Semiconducting Poly(2,5-Bis(3-Alkylthiophen-2-Yl)-Thieno-[3,2-

b]Thiophene) (PBTTT) from Its Different Liquid Phases. *J. Mater. Chem. C* **2024**.

(33) Van Westen, T.; Groot, R. D. Effect of Temperature Cycling on Ostwald Ripening. *Cryst. Growth Des.* **2018**, *18* (9), 4952–4962.

(34) Vetter, T.; Iggland, M.; Ochsenbein, D. R.; Hänseler, F. S.; Mazzotti, M. Modeling Nucleation, Growth, and Ostwald Ripening in Crystallization Processes: A Comparison between Population Balance and Kinetic Rate Equation. *Cryst. Growth Des.* **2013**, *13* (11), 4890–4905.

Chapter 8

Final Remarks, Appendix and Publications

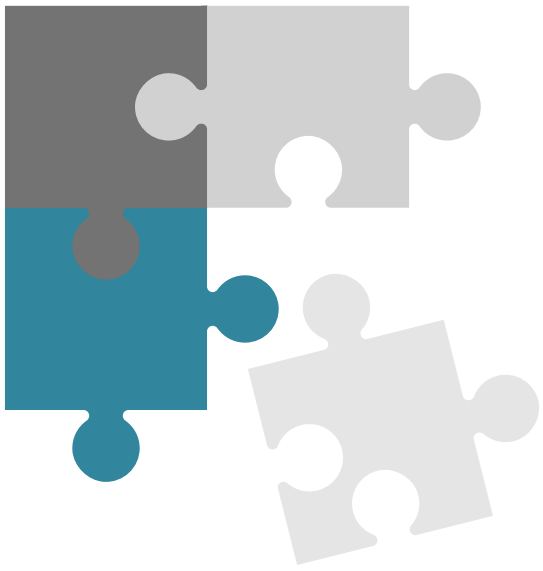

8.1 Final Remarks

This thesis emphasizes the critical importance of understanding the intricate processes underlying crystallization processes occurring in polymer materials as understanding these processes is paramount for the advancing of polymer technologies for a range of applications. By investigating the complex solidification behavior semiconducting polymers and polymorphic polythioethers, this work aimed to fill the gap regarding crystallization kinetics, phase transitions and microstructure on both bulk and thin-film methodologies.

The study of conjugated polymers, PFO and PBTTT, highlights the influence of preexisting molecular arrangement in the resulting crystallization kinetics and solid-state morphology. The findings in this thesis show the importance of resolving the thermotropic behavior of these polymers to forward our understanding of structure-property relationships and optimize device fabrication protocols. Our findings on the crystallization dynamics of PFO from both isotropic and liquid crystalline states have demonstrated that preexisting molecular order profoundly influences the behavior of this polymer. While preexisting molecular order accelerates the formation of active nucleation centers, which in turns leads to faster crystallization kinetics in the early stages of primary crystallization, diffusion of the chains during the secondary crystallization stage is hindered. This hindrance slows down the crystal growth process, leading to longer times required for samples crystallized from the liquid crystalline ordered state to reach full crystallization compared to those crystallized from the isotropic disordered melt state. This suggests a complex interplay between molecular order and crystallization dynamics, which in turn, have implications for the morphology and optical emission properties of PFO.

Similarly to our PFO study, the presence of a preexisting order in PBTTT

enhances crystal nucleation rates compared to the isotropic liquid phase. Notably, our study challenges the conventional understanding of PBTTT transitions. We provide evidence suggesting that at the temperatures conventionally used for thermal annealing of the high mobility terrace phase, PBTTT exists in a liquid state rather than a solid, implying that the formation of the terrace phase occurs through a crystallization process from a semi-ordered liquid crystalline state. Moreover, the results showed a complex overall crystallization kinetics for PBTTT, diverging from the general crystallization behavior observed in commodity polymers. This complexity underscores the unique nature of crystallization in semiconducting polymers and highlights the need for further fundamental investigations into their structure development.

Similarly, the exploration of polymers with high sulfur content such as alternating copolymers DMDS-alt-DVE, by employing advanced calorimetric techniques and tailored thermal protocols showed that these polymers can exhibit up to three polymorphic forms, known as the $VL-T_m$, $L-T_m$ and $H-T_m$ forms. This work highlights the direct relationship between processing conditions and the microstructure of the material. By designing a series of thermal protocols, the isolation of the individual phases or a combination of two or three phases was achieved.

Motivated by these findings further analysis on DMDS-alt-DVE, DMDS-alt-TEGDVE and DMDS-alt-BDDVE novel polythioethers provided further insights into the complex solidification behaviors and the tunability and controlled formation of different crystalline polymorphs of these materials. The results showed that DMDS-alt-TEGDVE and DMDS-alt-BDDVE also possess three distinct polymorphic phases with distinct structural and morphological characteristics. A series of characterization and calorimetric techniques, such as DSC and PLOM, helped shed light into the varying

crystallization and melting sequences of all polymorphs at different rates. The presence of the uncommon positive spherulites found for these materials were correlated with the cross-hatched morphology observed through AFM. Additionally, the overall crystallization kinetics revealed a clear order in crystallization rate: DMDS-*alt*-BDDVE > DMDS-*alt*-DVE > DMDS-*alt*-TEGDVE. With the aid of molecular dynamic simulations this order was explained by the distinct repeating units of each copolymer; results help identifying variances in the diffusion of the chains in the melt, thus providing the underlying factors contributing to the observed order in crystallization rate. That is, a higher diffusivity will yield an overall faster crystallization rate.

In summary, the findings shown throughout this thesis offer new insights into the complex crystallization behavior of semiconducting and non-semiconducting polymers by explaining in depth the interrelations between thermal processing, structure and properties.

8.2 Future Work

Moving forward, further research in this area holds the potential to unlock new frontiers in organic electronic technologies and beyond, driving innovation and technological advancement in the field of polymer science. Particularly, similar work conducted here for PFO and PBTTT should be conducted on other semiconducting polymers exhibiting similar characteristics as to show if there is a common kinetic, structural or any other type of trend amongst this class of polymers.

Moreover, although here we have delved into the crystallization kinetics of these high-sulfur containing copolymers. Further studies need to be conducted, as preliminary studies have shown that all three copolymers DMDS-*alt*-DVE, DMDS-*alt*-TEGDVE and DMDS-*alt*-BDDVE seem to be able to

generate a vary order structure below T_g. The implications and reasoning behind this phenomena will be further explored in future work.

8.3 List of Publications

(1) Pirela, V.; Campoy-Quiles, M.; Müller, A. J.; Martín, J. Unraveling the Influence of the Preexisting Molecular Order on the Crystallization of Semiconducting Semicrystalline Poly(9,9-Di-n-Octylfluorenyl-2,7-Diyl (PFO). *Chem Mater* **2022**, *34* (23), 10744–10751.

(2) Pirela, V.; Elgoyhen, J.; Tomovska, R.; Martín, J.; Le, C. M. Q.; Chemtob, A.; Bessif, B.; Heck, B.; Reiter, G.; Müller, A. J. Unraveling the Complex Polymorphic Crystallization Behavior of the Alternating Copolymer DMDS-Alt-DVE. *ACS Appl. Polym. Mater.* **2023**, *5* (7), 5260–5269.

(3) Pirela, V.; Muller, A. J; Martin, J. Crystallization Kinetics of Semiconducting Poly(2,5-Bis(3-Alkylthiophen-2-Yl)-Thieno-[3,2-b]Thiophene) (PBTTT) from Its Different Liquid Phases. *J. Mater. Chem. C* **2024**.

(4) Pirela, V.; Unanue, L; Elgoyhen, J; Ramos, J; Vega, JF; Mugica, A; Zubitur, M; Minh Quoc Le, C; Chemtob, A; Tomovska, R; Reiter, G; Müller, A. J.; Martin, J. A Comprehensive Study of Crystallization Kinetics and Polymorphism of High-sulfur-content Polythioethers [*Under Review*]

(5) Aniés, F.; Furlan, F.; Qiao, Z.; Pirela, V.; Bidwell, M.; Rimmele, M.; Martín, J.; Gasparini, N.; Heeney, M. A Comparison of Para, Meta, and Ortho -Carborane Centred Non-Fullerene Acceptors for Organic Solar Cells. *J. Mater. Chem. C* **2023**, *11* (12), 3989–3996.

(6) Bessif, B.; Heck, B.; Pfohl, T.; Minh, C.; Le, Q.; Chemtob, A.; Pirela, V.; Elgoyhen, J.; Tomovska, R.; Müller, A. J.; Reiter, G. Nucleation Assisted through the Memory of a Polymer Melt: A Different Polymorph Emerging from the Melt of Another One. *Macromolecules* **2023**, *56* (4), 1461–1470.

(7) Elgoyhen, J.; Pirela, V.; Müller, A. J.; Tomovska, R. Synthesis and Crystallization of Waterborne Thiol–Ene Polymers: Toward Innovative Oxygen Barrier Coatings. *ACS Appl. Polym. Mater.* **2023**, *5* (11), 8845–8858.

(8) Liu, P.; Pirela, V.; Ocando, C.; Müller, A. J.; Hadjichristidis, N. High Trans-Selectivity in Boron-Catalyzed Polymerization of Allylic Arsonium Ylide and Its Contribution to Thermal Properties of C3-Polymers. *Macromolecules* **2020**, *53* (24), 10718–10724.

(9) Aniés, F.; Hamilton, I.; Castro, C. S. P. D.; Furlan, F.; Marsh, A. V.; Xu, W.; Pirela, V.; Patel, A.; Pompilio, M.; Cacialli, F.; Martín, J.; Durrant, J. R.; Laquai, F.; Gasparini, N.; Bradley, D. D. C.; Heeney, M. A Conjugated Carboranyl Main Chain Polymer with Aggregation-2 Induced Emission in the Near-Infrared. *J. Am. Chem. Soc.* **2024**.[*Accepted*]

8.4 Appendix 1: supplementary information for Chapter 5

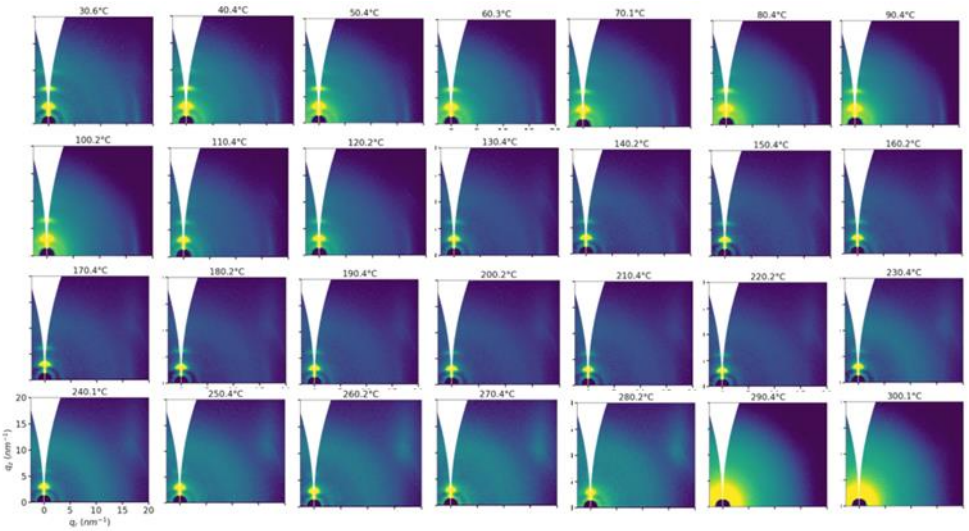

Figure 8.1. *In situ* GIWAXS patterns for PBTTT films acquired during heating from 30 ºC to 300 ºC.

Table 8.1 Values obtained from applying the Avrami theory to the experimental data

T_c (ºC)	State	$1/t_{20\%exp}$ (min^{-1})	$k^{1/n}$ (min^{-1})	Avrami Index (n)
60	ISO	0.23	0.06	1.2
	LC	0.54	0.1	0.89
65	ISO	0.66	0.23	1.4
	LC	0.86	0.24	1.1
70	ISO	0.26	0.06	0.97
	LC	0.82	0.17	0.89
75	ISO	0.32	0.03	0.65
	LC	0.59	0.13	0.96
80	ISO	1.10	0.20	0.89
	LC	0.93	0.23	1.05
85	ISO	0.44	0.09	0.88
	LC	0.35	0.07	0.89
90	ISO	0.41	0.08	0.90
	LC	0.740	0.11	0.88

8.5 Appendix 2: supplementary information for Chapter 7

8.5.1 Nuclei density (N)

The nuclei density (N) was followed as a function of time (t) by quantifying the number of nuclei before impingement on one another. It was important to measure the thickness of the film within the area observed in the microscope to accurately determine the number of nuclei per cubic centimetre, *i.e.*, the nucleation density (N). Figure 8.2, Figure 8.3, and Figure 8.4 shows N as a function of t at different T_c of all three copolymers. For DMDS-alt-DVE, the point of saturation for N at $T_c = 44$°C is much higher as it saturates after 30 s, while at higher crystallization temperatures, *i.e.*, $T_c = 55$°C, longer times of up to 6 min are required to reach saturation. Furthermore, in the lower $T_c s$ range (from $T_c = 44$ °C to $T_c = 51$ °C), the number of spherulites increases with decreasing T_c due to a much higher nucleation density because of faster nucleation. Consequently, similar trends are observed for other T_cs. That is, as T_c increases, the nucleation density decreases.

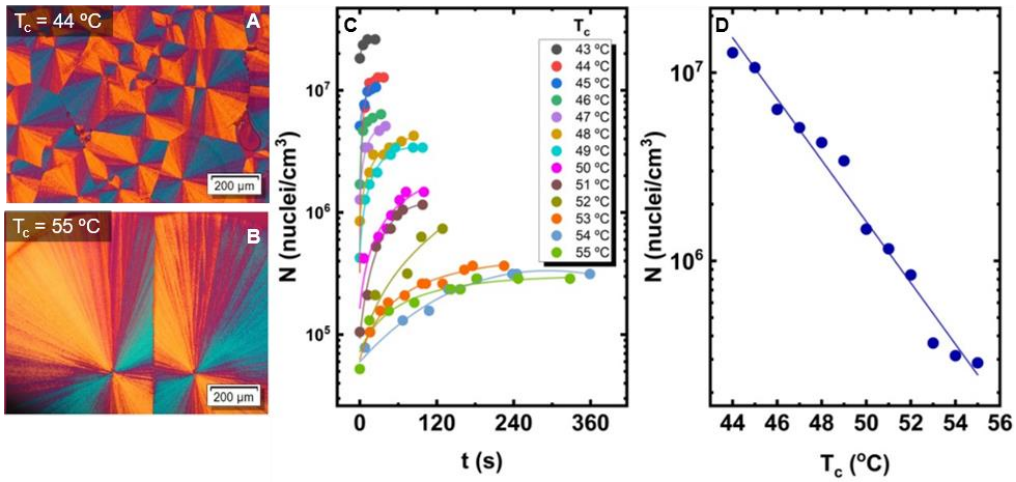

Figure 8.2. Nucleation density of DMDS-*alt*-DVE. A) PLOM images taken at $T_c = 44$ ºC after reaching saturation B) PLOM images taken at $T_c = 55$ ºC after reaching saturation C) Nucleation density for different T_c as a function of time (t) D) Nucleation density as function of T_c.

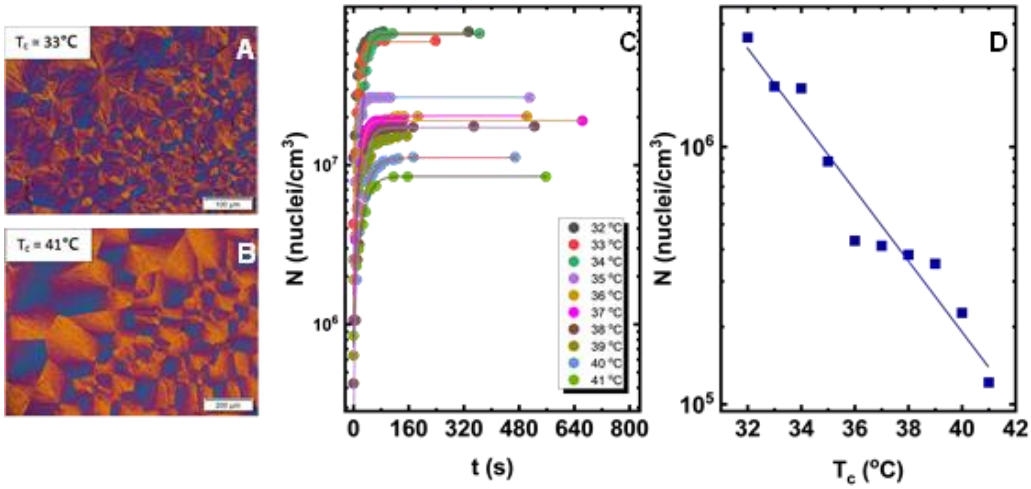

Figure 8.3. Nucleation density of DMDS-*alt*-TEGDVE. A) PLOM images taken at $T_c = 33$ ºC after reaching saturation B) PLOM images taken at $T_c = 41$ ºC after reaching saturation C) Nucleation density for different T_c as a function of time (t) D) Nucleation density as function of T_c.

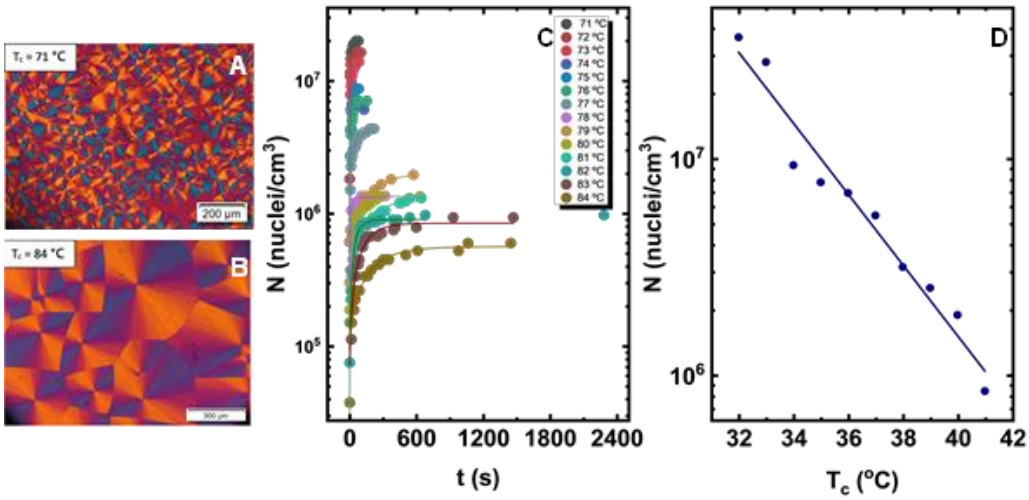

Figure 8.4. Nucleation density of DMDS-*alt*-BDDVE. A) PLOM images taken at $T_c = 71$ ºC after reaching saturation B) PLOM images taken at $T_c = 84$ ºC after reaching saturation C) Nucleation density for different T_c as a function of time (t) D) Nucleation density as function of T_c.

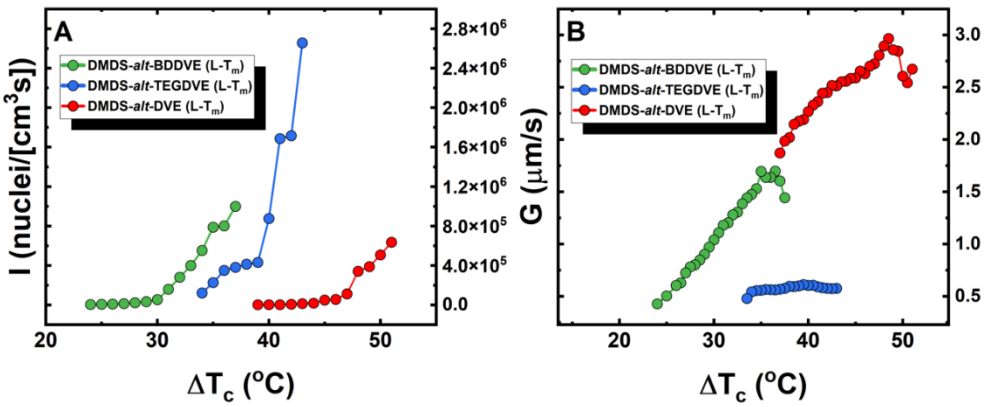

Figure 8.5. Primary nucleation and superstructural growth kinetics of DMDS-*alt*-DVE, DMDS-*alt*-TEGDVE and DMDS-*alt*-BDDVE after isothermal crystallization as a function of supercooling. A) Primary nucleation rate (I) B) Spherulitic growth rate (G); red (DMDS-*alt*-DVE), blue (DMDS-*alt*-TEGDVE), green (DMDS-*alt*-BDDVE).

Table 8.2. Avrami parameters for DMDS-*alt*-DVE

DMDS-*alt*-DVE

Technique	T (ºC)	$1/\tau_{50\%}$ exp (min^{-1})	$k^{1/n}$ (min^{-1})	Avrami index (n)
FSC	-30	7.7	6.5	2.4
	-25	4.6	2.9	1.7
	-20	7.6	5.7	1.6
	-15	7.5	6.0	1.6
	-10	11.0	8.7	1.7
	-5	14.5	10.2	1.5
	0	20.7	18.1	2.5
	15	13.1	8.6	2.0
	20	6.8	5.9	1.9
	25	6.0	5.4	2.0
	30	6.1	4.3	1.8
	35	3.2	3.1	3.7
DSC	60	0.23	0.21	2.83
	60.5	0.20	0.18	2.8
	61	0.17	0.15	3.08
	61.5	0.14	0.12	3.07
	62	0.12	0.11	3.32
	62.5	0.09	0.08	3.17
	63	0.07	0.06	3.41

Table 8.3 Avrami parameters for DMDS-*alt*-TEGDVE

DMDS-*alt*-TEGDVE

Technique	T (ºC)	$1/\tau_{50\%}$ exp (min^{-1})	$k^{1/n}$ (min^{-1})	Avrami index (n)
FSC	-30	2.40	2.08	2.8
	-25	3.00	2.29	2.2
	-20	3.64	2.14	1.5
	-15	6.37	4.05	1.7
	-10	8.33	5.75	1.7
	-5	9.35	6.89	1.9
	0	9.90	8.87	2.1
	5	10.00	10.02	2.2
	10	5.46	5.69	3.1
	15	2.61	2.33	2.9
	20	0.88	0.71	2.1
	25	0.93	0.56	2.2
DSC	46	0.15	0.13	2.74
	46.5	0.12	0.11	3.05
	47	0.10	0.09	3.06
	47.5	0.09	0.08	3.04
	48	0.08	0.07	3.28
	48.5	0.07	0.07	3.31

	49	0.06	0.06	3.88

Table 8.4. Avrami parameters for DMDS-*alt*-BDDVE

DMDS-*alt*-BDDVE

Technique	T (ºC)	$1/\tau_{50\%}$ exp (min^{-1})	$k^{1/n}$ (min^{-1})	Avrami index (n)
FSC	53	10.17	11.66	1.93
	54	9.09	8.57	2.24
	55	8.70	8.39	1.83
	56	6.54	6.52	1.99
	57	6.37	4.88	1.87
DSC	79	0.28	0.24	2.6
	79.5	0.22	0.19	2.7
	80	0.17	0.15	2.69
	80.5	0.14	0.12	2.91
	81	0.11	0.10	2.86
	81.5	0.09	0.08	2.72
	82	0.08	0.08	2.7

8.5.1.1 Derivation of an *ad-hoc* force field for polymers

The force field employs Lennard Jones (LJ) parameters sourced from the OPLS-AA force field[1]. Atomistic charges were computed using the monomer of each polymer through the following procedure:

3. In Materials Studio 2022, a polymer chain consisting of a single monomer capped with methyl groups is constructed. Subsequently, 60 chains are assembled in a simulation box at a density of 0.8 g/cm^3 using the Amorphous builder module. After minimizing the simulation box, a short 1 ns NPT simulation is conducted with the COMPASS force field. This simulation duration proves sufficient for density equilibration in the initial stages. The structures at 0.7, 0.8, 0.9, and 1.0 ns are then exported to PDB format for use in the subsequent step.

4. The open-sourced in-house GeCos toolkit(https://github.com/jrdcasa/gecos) is utilized for extracting, optimizing, and analyzing monomer conformers. GeCos is specifically designed to obtain conformers using MD trajectories and optimize them at the quantum molecular level with the Gaussian package. This toolkit supports distributed calculations and recovery through a computing cluster. The DFT theory level employed for optimization and electrostatic charge determination is CAM-B3LYP/cc-PVTZ//CAM-B3LYP/6-31G* in Gaussian 16. Numerous conformers are generated, with only the ten most stable conformers selected for deriving the electrostatic charges.

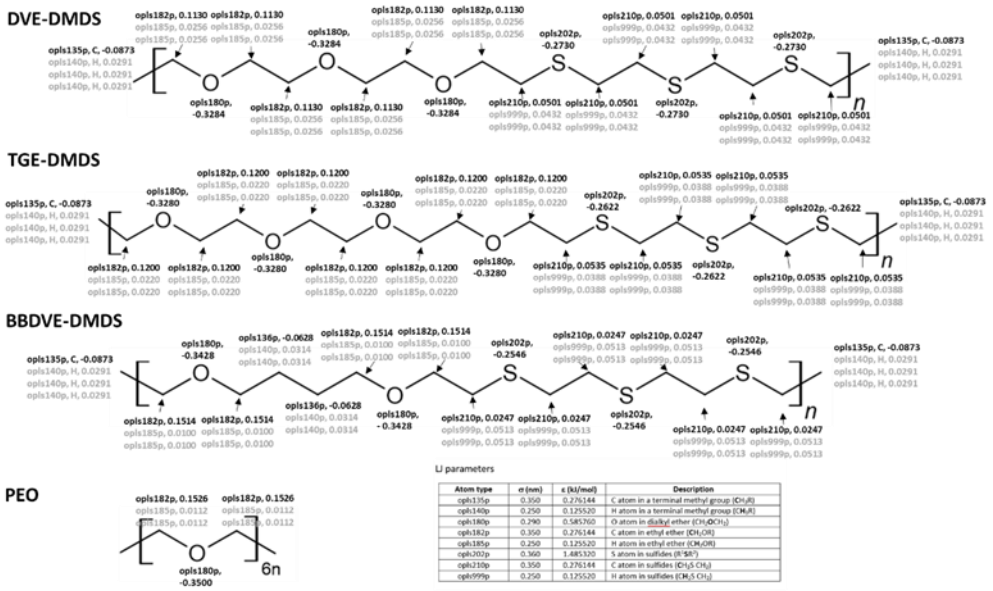

Atom type	σ (nm)	ε (kJ/mol)	Description
opls135p	0.350	0.276144	C atom in a terminal methyl group (CH_3R)
opls140p	0.250	0.125520	H atom in a terminal methyl group (CH_3R)
opls180p	0.290	0.585760	O atom in dialkyl ether (CH_3OCH_3)
opls182p	0.350	0.276144	C atom in ethyl ether (CH_3OR)
opls185p	0.250	0.125520	H atom in ethyl ether (CH_3OR)
opls202p	0.360	1.485320	S atom in sulfides (R^1SR^2)
opls210p	0.350	0.276144	C atom in sulfides ($CH_2S\,CH_2$)
opls999p	0.250	0.125520	H atom in sulfides ($CH_2S\,CH_2$)

Figure 8.6. Electrostatic charges at each atom for DMDS-*alt*-DVE, DMDS-*alt*-TEGDVE, DMDS-*alt*-BDDVE and PEO polymers. The fitting process in RESP was carried out with $n = 1$. Equivalent groups exhibit identical charges, resulting in a total charge of zero. The accompanying inset table compiles the Lennard-Jones (LJ) parameters derived from the OPLS-AA force field. Additionally, these parameters are available in the accompanying topology files associated with this paper.

5. The restrained electrostatic potential (RESP) module of the Multiwfn package[2] was employed to calculate electrostatic charges, utilizing both charge and equivalence constraints. Specifically, the groups CH_2-O-CH_2, CH_2-S-CH_2, CH_2-CH_2 and terminal CH_3 were constrained to be equivalents, with a total charge equal to zero in all polymers. The electrostatic charges for each polymer and the corresponding atom type names are illustrated in Figure 8.6. Additionally, the Lennard Jones parameters are taken from OPLS-AA, and the specific values are presented in the inset table.

6. The bonded parameters (bond, bend and dihedral terms) were derived utilizing the QForce toolkit, incorporating the electrostatic charges and LJ parameters derived in prior steps. Employing quantum mechanical calculations, each monomer was fragmented, as illustrated in Figure 8.7, to enhance computational efficiency. The dihedral energy profiles for individual flexible bonds are presented in Figure 8.7 Comprehensive details of these parameters are accessible in the accompanying topology files linked to this paper.

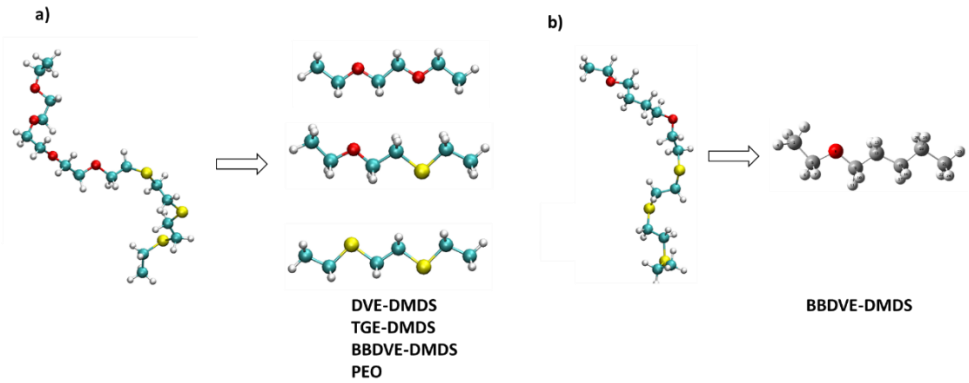

Figure 8.7. Fragments utilized in then Q-Force toolkit to derive the bonded parameters, encompassing all necessary bond, angle and dihedral terms.

8.5.1.2 Validation of the force field

Validating force fields for polythioethers presents a difficulty as direct experimental data is lacking. To assess the reliability of the obtained force field, an indirect validation approach has been adopted by applying the same methodology to develop a force field for polyethylene oxide polymer (PEO), for which experimental data is readily available in the literature. In this validation process, two characteristic features have been considered: (i) Melt density from PVT measurements[3,4] and (ii) Characteristic ratios (C_∞) in PEO melts via SANS (Small Angle Neutron Scattering) experiments[5].

In Figure 8.9A, the melt density of PEO is shown as a function of temperature, revealing a very good agreement between experimental[3,4] and simulated values. The calculated thermal expansion coefficient at constant pressure ($\alpha = (d\ln v/dT)_P$, where v is the specific volume) stands at 1.0×10^3 K^{-1}, closely to the experimental one of 0.7×10^3 K^{-1}. Chain stiffness is calculated from MD simulations (Figure 8.9B), demonstrating excellent agreement between simulated $C\infty$ values for PEO and experimental data. Furthermore, the observed negative temperature coefficient of chain dimensions in the melt chains is well captured in the simulations, aligning precisely with the experimental behavior[5]. Hence, drawing from this indirect validation, it may be suggested that the force field shows a reasonable level of accuracy.

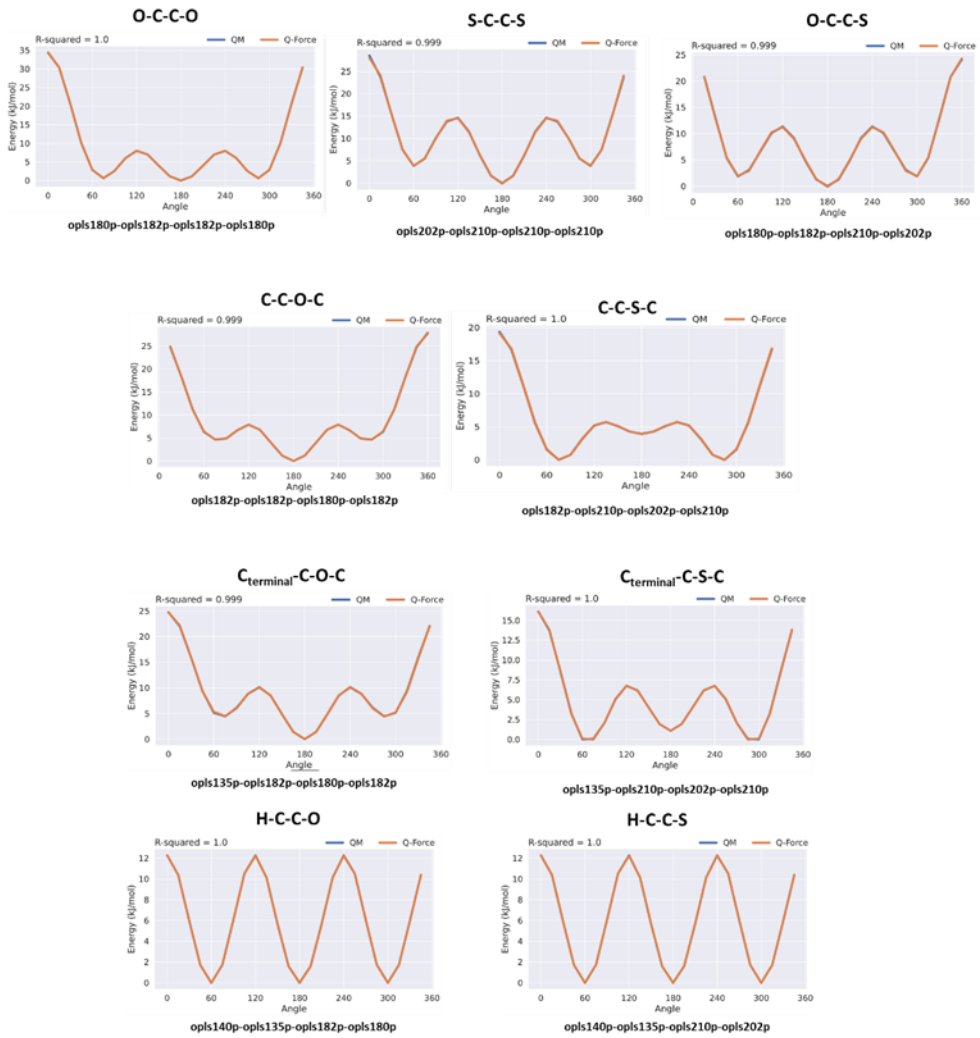

Figure 8.8. QM vs Q-force torsional energy profiles for all flexible torsions of DMDS-*alt*-DVE, DMDS-*alt*-TEGDVE, DMDS-*alt*-BDDVE and PEO polymers.

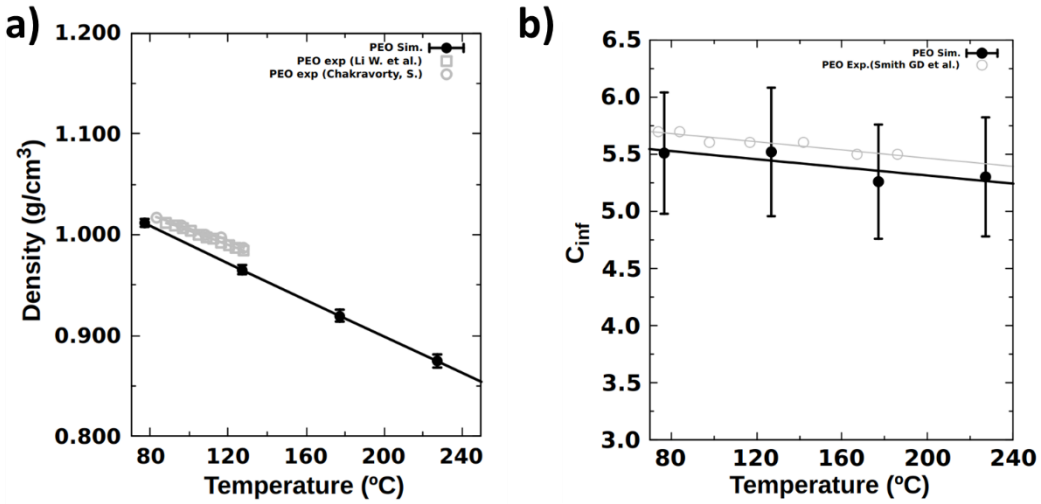

Figure 8.9. A) Melt density and B) Stiffness (characteristic ratio) as a function of the temperature for polyethylene(oxide) (PEO).

8.6 References for Chapter 8

(1) Jorgensen, W. L.; Maxwell, D. S.; Tirado-Rives, J. Development and Testing of the OPLS All-Atom Force Field on Conformational Energetics and Properties of Organic Liquids. *J. Am. Chem. Soc.* **1996**, *118* (45), 11225–11236.

(2) Lu, T.; Chen, F. Multiwfn: A Multifunctional Wavefunction Analyzer. *J. Comput. Chem.* **2012**, *33* (5), 580–592.

(3) Chakravorty, S. *Specification of Pressure-Volume-Temperature (PVT) Measurements Relevant to Industrial Polymer Processing.*; NPL; Teddington, 1999.

(4) Li, W.; Radosz, M. Pressure-Induced Melting and Crystallization of Poly(Ethylene Oxide). *Macromolecules* **1993**, *26* (6), 1417–1423.

(5) Smith, G. D.; Yoon, D. Y.; Jaffe, R. L.; Colby, R. H.; Krishnamoorti, R.; Fetters, L. J. Conformations and Structures of Poly(Oxyethylene) Melts from Molecular Dynamics Simulations and Small-Angle Neutron Scattering Experiments. *Macromolecules* **1996**, *29* (10), 3462–3469.